BED DYNAMICS AND HEAT TRANSFER IN SHALLOW VIBRATED PARTICULATE BEDS

by

Mark O. Mason

Dissertation submitted to the Faculty of the

Virginia Polytechnic Institute and State University

in partial fulfillment of the requirements for the degree of

DOCTOR OF PHILOSOPHY

in

Chemical Engineering

APPROVED:

Arthur M. Squires, Co-Chairman

Y. A. Liu, Co-Chairman

Thomas E. Diller

Henry A. McGee, Jr.

George B. Wills

March, 1990

Blacksburg, Virginia

BED DYNAMICS AND HEAT TRANSFER IN SHALLOW BEDS OF VIBRATED PARTICLES

by

Mark O. Mason

Arthur M. Squires, Co-Chairman

Y. A. Liu, Co-Chairman

Chemical Engineering

(ABSTRACT)

A vibrated bed is a mobile layer of solid particles contained in a vessel that is vibrated vertically. This study investigates bed dynamics and heat transfer from a vertical surface in shallow vibrated beds in absence of aeration. In general, "shallow" means a depth-to-width ratio less than one. In this study, bed depth is 30 mm, and this ratio is about 0.2. All experiments are at 25 hertz and at vibrational amplitudes affording peak accelerations between 2 and 7 times gravity. The study uses spherical glass beads of two densities and "Master Beads," nearly spherical particles of a crude, dense alumina, in size fractions from 63 to 707 micrometers.

A disc embedded in the vessel floor, vibrated at 4.5 kilohertz, gives data on bed-vessel separation, showing it to occur later than predicted by plastic, single-mass models. The delay is attributed to bed expansion, monitored by piezoelectric force gauges mounted on floor and wall of the vessel. In large-particle beds, bed-vessel collision occurs simultaneously everywhere. In small-particle beds, exhibiting an uneven top surface, collision occurs first at the side walls and moves toward the center.

In small-particle beds, pressure gradients appearing during the bed's free flight drive a horizontal component of particle circulation from the vessel's side walls toward its center. An apparent viscosity of the bed, estimated crudely by pulling a rod through it, influences this component's velocity. In beds of large particles, circulation is almost entirely vertical, a layer of two or three particles moving downward at a wall, and a slow return flow moving upward elsewhere. The study confirms the downward wall motion to be driven by friction.

Heat transfer closely follows trends in rate of circulation. Greater dependence upon vibrational intensity is seen in small-particle beds. Values as high as 578 W/m^2-K are measured.

Comparison of vertical-surface heater geometry with an earlier horizontal tube shows the former to be generally superior for surface-to-bed heat transfer.

Acknowledgments

I would like to thank the National Science Foundation, the Department of Energy, and the Virginia Mining and Minerals Resource Research Institute for supporting this work at different times during my stay at VPI&SU. I would also like to thank the Chemical Engineering Department for the Southeastern Regional and Pratt Fellowships which provided supplemental support. Thanks also go to the Norton-Alcoa Company for supplying the Master Beads which have been used in the vibrated beds in this study.

I am grateful to my committee co-chairmen, Drs. Arthur M. Squires and Y. A. Liu, for their assistance and guidance during this effort. Dr. Squires deserves thanks for discussions of the meaning of results, and Dr. Liu for a careful editing of the final version of the manuscript. I would like to thank the other members of my committee, Drs. Diller, McGee and Wills, for their timely assistance and helpful comments. I am also deeply indebted to Dr. Conger for greatly expediting the final process.

Many of my colleagues through the years have contributed greatly to my educational experience during the course of this work. ,

, and all have laid groundwork for this study, and I have benefited immeasurably from discussions with each. deserves thanks also for patiently allowing me to discuss ideas with him as I was analyzing results and formulating theories late at night down the stretch.

I especially appreciate the assistance of and who built and modified the vessels used in this study. I have learned much from both about machining and things mechanical, as well as things which are

important in life. deserves credit for the electronic circuitry and discussions on instrumentation. His ideas and assistance made several of the measurement devices possible. I would also like to acknowledge , , , and , staff of the Department of Chemical Engineering, who have assisted in many ways over the course of my tenure here. A very special thanks goes to for taking on the mountainous task of typing this dissertation. Her patience and willing availability have been greatly appreciated and surely cut several very important days off of the final preparation of this document.

I am glad to acknowledge the friendship and support of many of the graduate students in this department who have enriched this experience at Virginia Tech. Notable among these are , who also assisted in preparation of the figures, and , who assisted with final preparation of the manuscript.

Finally, I would like to thank my family whose love and support guided me down a long and often dark road. My wife especially carried the burden through many long nights alone with patience and understanding. I will never forget her unfailing support and love in the difficult times. This dissertation would not have been possible without her, and it is dedicated to her.

Table of Contents

List of Figures

List of Tables

Chapter 1 Introduction

The application of vertical vibration to a particulate bed of solids significantly improves heat and mass transfer in the bed. The vibration increases the mobility of the particles, which develop circulation patterns if the vibrational intensity is sufficiently high. Vibration also increases the porosity of the bed, which takes on fluid-like properties. For this reason, these types of beds have often been referred to in the literature as vibrofluidized beds. The properties of such beds are similar in some respects to gas-fluidized beds, but there are also differences.

The term "vibrofluidized bed" as it appears in the literature is confusing because it is used for several different situations. If the base plate of a vibrated vessel is porous, a flow of gas can be forced upward through the bed to create particle mobility in addition to that due to vibration. Both this type of bed, as well as the bed mobilized purely by vibration, have been termed "vibrofluidized" by various authors. Other terms, such as vibroboiling and vibromobile, have been used without adequate description [Chlenov and Mikhailov, 1964]. For the sake of consistency, this study refers to beds mobilized through vibration alone as *vibrated beds*. For the case of forced gas flow as well as vibration, the bed is termed an *aerated vibrated bed* if the gas flow is below the minimum fluidization velocity of the particles, and a *vibrated fluidized bed* if it is above. *Vibrofluidized bed* and *vibrofluidization* are used here only as generic terms for all vibrated beds, with or without forced gas flow.

A large vertical component of vibration in vibrated beds differentiates between these beds, which are used primarily to promote heat and mass transfer,

from vibratory conveyors. The main goal of the conveyor is to efficiently transport solids, and so there is a large horizontal component of vibration. Although some continuous or flowing vibrated beds have a horizontal component [Hirt, 1984; Cheah, 1986], the main component is vertical. In fact, most vibrated beds are strictly vertical.

Vibrofluidized beds appear to have gained widespread use only in the last two decades. Pakowski *et al.* [1984] did an extensive review of the literature and cite 135 references. They estimate that 90 percent of all the current commercial applications are in drying of granular solids. Also, it is apparent from their list of references that much of the work has been done in the Soviet Union and the eastern European countries.

1.1 Observed Vibrated-Bed Behavior

The displacement of a vertically, sinusoidally vibrated vessel can be described by an equation for simple harmonic motion:

$$a = a_o \sin(2\pi ft) = a_o \sin(\omega t) = a_o \sin(\theta) \qquad [1.1]$$

where a is the displacement, a_0 is the amplitude or maximum displacement from rest position, f is the frequency of vibration, t is time, ω is the angular frequency, and θ is the phase angle. The velocity and acceleration of the vessel are the first and second time derivatives of the displacement, respectively. This leads to

$$\frac{da}{dt} = \dot{a} = a_o \omega \cos(\omega t) \qquad [1.2]$$

and

$$\frac{d^2a}{dt^2} = \ddot{a} = -a_o\omega^2 \sin(\omega t) \qquad [1.3]$$

The dimensionless vibrational intensity parameter, K, a useful quantity often found in the vibrated bed literature, is defined as the ratio of the *maximum, positive* vessel acceleration to gravitational acceleration, g. This is expressed as:

$$K = \frac{\text{Max } |-a_o\omega^2 \sin(\omega t)|}{g} = \frac{a_o\omega^2}{g} \qquad [1.4]$$

Vibrational frequencies between 10 and 100 Hz give the best results for vibrofluidization, and most investigators work between 15 and 60 Hz. Vibrational amplitudes are varied between 0 and 4 mm so that K-values up to 10 are reported, but most investigations are conducted at lower values with a maximum K-value of 5 or 6.

If a few particles are placed in a vessel and vibrations are imposed, the particles remain on the floor of the vessel as long as the K-value is less than one. If the intensity of vibration is increased such that the K-value exceeds one, there is a point in each vibrational cycle where the acceleration of the vessel is less than -1 (the vessel is accelerated downward at a value greater than gravitational acceleration). When this occurs, the particles separate from the floor since they can accelerate downward no faster than gravity. The particles experience a period of free-flight and then collide with the vessel at some later point.

For the case of a few particles, this later collision leads to a situation of apparently randomly bouncing particles [Sprung *et al.*, 1986]. The behavior of

individual particles is determined primarily by the Newtonian mechanics of the collisions with the vessel floor and walls as well as with other particles. For this reason, Thomas *et al.* [1989] have described this case as the "Newtonian state." As more particles are added to the vessel, aerodynamic forces on the particles become more important and they begin to move in concert. Bachmann [1940] noted that the bed behaved as a coherent mass if the depth exceeded about six particle diameters, although Thomas *et al.* [1989] found this to be true at much shallower depths.

When the bed acts as a coherent mass, its collision with the vessel base is typically plastic; that is, the bed collides with the base and does not bounce but rather travels with the vessel until the lift-off point in the next cycle. Figure 1.1 schematically depicts this type of behavior. Based on these observations, several investigators [Bachmann, 1940; Kroll, 1954, 1955; Yoshida and Kousaka, 1967; Takahashi, *et al.* 1968; Gutman, 1974, 1976a] have modeled the vibrated bed as a single, coherent, plastic body. Some of these models are discussed in the literature review chapter which follows.

For large particles (particle diameter greater than 0.5 mm), the surface of the bed stays relatively flat and the particles display a slight bulk circulation pattern, down at the walls and upward at the center. The cyclic gap which forms beneath the bed causes gas to rush down through the bed as the gap grows. As the gap closes and the bed collides, this gas is forced back up out of the bed. Since the permeability of the bed is high for these large solids, this gas flow encounters little resistance and the particles experience relatively little drag.

As the particle size is decreased, the bed is less permeable, and the cyclic flow of gas begins to play a larger part in bed behavior. The surface of the bed no longer remains level, but tends to pile up or "bunker." The overall particle

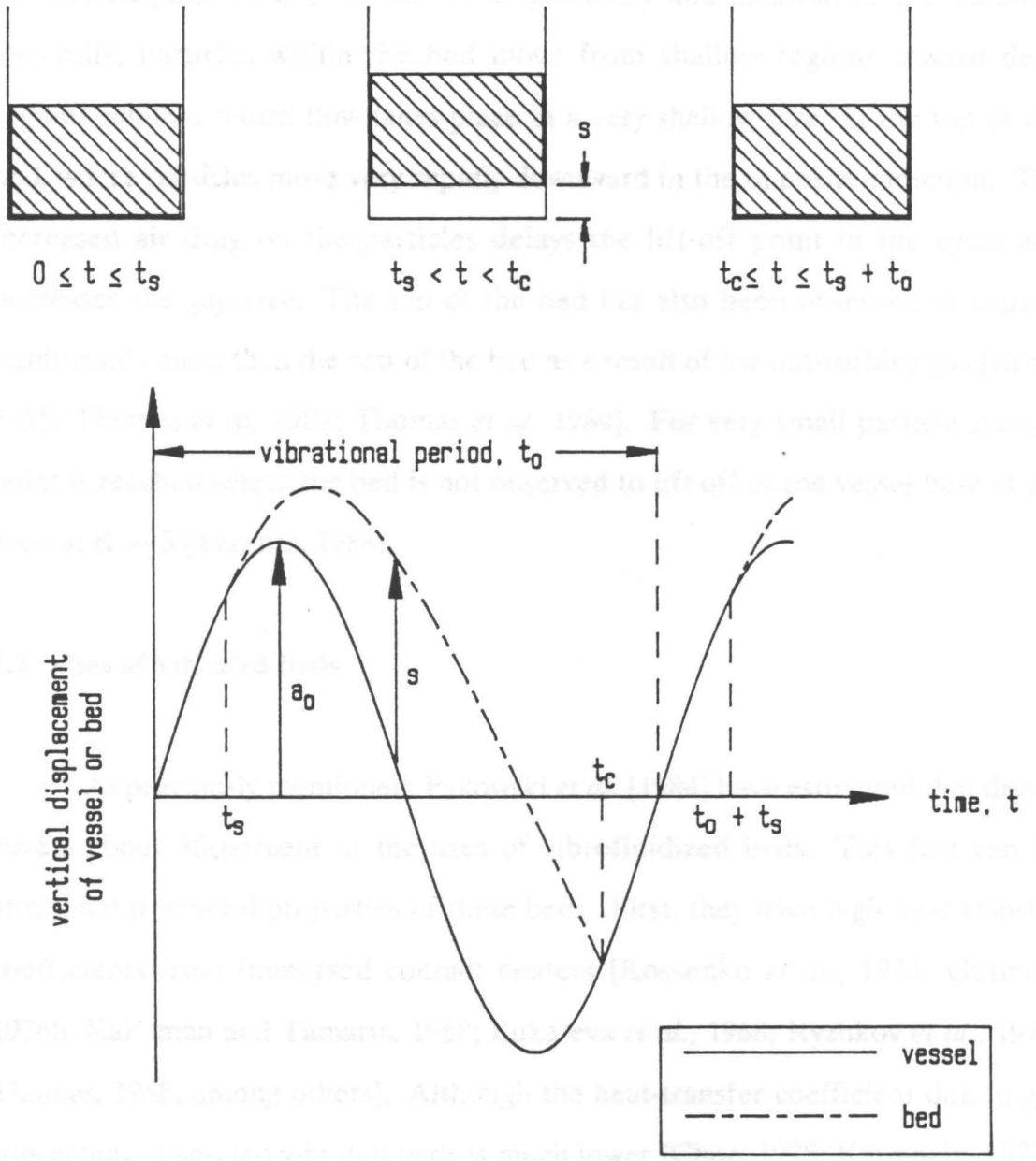

Figure 1.1. Schematic illustration of periodic bed motion: The bed is depicted as a single, coherent, plastic mass which separates from and collides with the vessel periodically. Notation: t_s = time at which the bed and vessel separate; t_c = time at which the bed and vessel collide; t_0 = the period of vibration; a_0 = the amplitude of vibration; s = thickness of the air gap between bed and vessel. From Thomas [1988].

circulation patterns depend on vessel geometry and location of the bunkers. Typically, particles within the bed move from shallow regions toward deep regions, while a return flow takes place in a very shallow layer at the top of the bed, where particles move very rapidly downward in the opposite direction. The increased air drag on the particles delays the lift-off point in the cycle and decreases the gap size. The top of the bed has also been observed to expand significantly more than the rest of the bed as a result of the out-rushing gas [Kroll, 1955; Thomas *et al.* 1987; Thomas *et al.* 1989]. For very small particle sizes, a point is reached where the bed is not observed to lift off of the vessel base at all, even at K = 5 [Thomas, 1988].

1.2 Uses of Vibrated Beds

As previously mentioned, Pakowski *et al.* [1984] have estimated that drying covers about 90 percent of the uses of vibrofluidized beds. This fact can be attributed to several properties of these beds. First, they have high heat-transfer coefficients from immersed contact heaters [Kossenko *et al.*, 1975; Gutman, 1976b; Kal'tman and Tamarin, 1968; Bukareva *et al.*, 1968; Ryzhkov *et al.*, 1976; Thomas, 1988; among others]. Although the heat-transfer coefficient due to gas convection in aerated vibrated beds is much lower [Choc, 1975; Karmagin, 1977], these beds have been investigated for use in drying due to the tendency of wet, sticky particles to adhere to heater surfaces. Choc [1975, 1976] has found heat transfer to be appreciably increased by vibration for gas flows up to the minimum fluidization velocity, at which point the effect of vibration was minimal. Osinskii *et al.* [1969], however, have found the drying rate to be increased five to seven

times in a vibrated fluidized bed compared to a stationary gas-fluidized bed under similar conditions.

Vibrofluidized beds have other advantages over gas-fluidized beds which make them desirable in certain situations. The mechanical action of vibration creates solid mixing which increases heat and mass transfer, allowing fluidizing gas velocity through the bed to be decreased. This results in a reduction or elimination of elutriation of fines from the bed [Bukareva *et al.*, 1970]. Suzuki *et al.* [1980a] note that this reduction in air flow is also desirable for drying of oxygen-sensitive materials such as medicines and foods. Furthermore, vibrofluidized-bed drying has been successfully applied to cohesive particles which agglomerate when wet, making gas-fluidization difficult or impossible [Zaitsev *et al.*, 1976; Suzuki *et al.*, 1980b; Danielsen and Hovmand, 1980]. Thermally-unstable materials, which are degraded by high temperatures caused by thermal gradients, also are good candidates for vibrofluidized drying [Ginzburg and Syroedov, 1965; Shvetsov *et al.* 1976]. In the extremely heat-sensitive case of pharmaceuticals such as antibiotics, Volovik *et al.* [1975] have found that vibration improves the drying in their radiant vacuum dryer. Attrition of crystalline materials is lower in vibrated beds than in gas-fluidized beds [Pakowski *et al.*, 1984]. Also, a well-defined residence time can be achieved in a vibrated bed [Danielsen and Hovmand, 1980]. Finally, Chlenov and Mikhailov [1972] cite examples and Gutman [1974] provides a theoretical analysis, which show the power consumption for a vibrofluidized-bed system can be significantly less than that for a gas-fluidized system. This is primarily due to the reduction in gas-compression requirements, and is especially significant if the vibration equipment is operated at its resonant frequency.

Although most of the work on vibrofluidization to date has centered on drying, several other applications have been investigated. Much is done with transport of solids by vibratory conveying, but that is really a separate topic and will not be discussed here. Vibration of particles of different sizes tends to segregate the particles, with smaller particles moving toward the bottom of the vessel and larger ones toward the top under certain conditions [Harwood, 1976; Williams and Shields, 1967]. Williams and Shields [1967] have used this property to separate fertilizer granules by size. Lawrence and Beddow [1968], however, have studied this phenomenon to optimize homogeneity and density in vibratory die filling. Ripple *et al.* [1973] have performed a similar study to reduce the radial segregation of particles in a cylindrical column packed using vibration. Vibration is used in compaction because a denser, more effective packing can be obtained.

The high heat transfer between an immersed surface and the particles in a vibrated bed has led to several other applications. Tamarin *et al.* [1968] have studied the use of a vibrated bed to quench-harden hot metal parts. They found the product to be as hard and to require less processing than oil-quenched metals. More recently, Hirt *et al.* [1988] and Cheah *et al.* [1988] have proposed and demonstrated a vibrated-bed heat exchanger for the recovery of heat from hot waste gases. Their concept encompasses a design for counter-current flow of solids and supernatant gas, and a design for a non-flowing bed of solids. In both cases, heat is transferred from a hot gas to the solid by convection (the vessel is baffled to improve contact between the solids and supernatant gas), and from the solid to cooling water flowing in tubes immersed in the bed.

Vibrated beds have also found limited application as chemical reactors. Lyul'ko *et al.* [1979] have investigated the final annealing of iron powders in a vibrated furnace. The process involves reduction from the oxides to the product

powder in a flowing vibrated bed. Vibration has also been found to increase the rate of carbonization and improve the coke quality in the coking process [Konyakhin *et al.*, 1979]. Several investigators from this laboratory have used vibrated beds to develop microreactors. Whiting [1985] has developed a vibrated microreactor in which he studied the Fischer-Tropsch reaction. In related work, he has developed a second microreactor system which operates at ambient temperature and atmospheric pressure and allows for study of the effect of rapid gas switching on the gas mixing in a vibrated bed. A further investigation on unsteady-state gas and solid mixing in an ambient microreactor has been made by Briggs [1987], who induced gas-solid mixing in a vibrated bed by baffle movement. Most recently, Thomas and Squires [1989] and Benge [1990] have performed experiments in an ultra-shallow vibrated bed (settled bed depth of less than 1 mm) aimed at modeling gas-fluidized bed kinetics in a vibrated microreactor.

Chapter 2 Literature Review and Scope of Study

This chapter presents a review of previous work in the field of vibrated particulate beds. The first section deals with work done in the area of vibrated-bed dynamics, and the second deals with work on heat transfer. Following this historical perspective, the scope of this study is presented.

2.1 Vibrated-Bed Dynamics

There are many parameters which affect the particle dynamics in a vibrated bed. The following subsections present the findings of previous researchers on the effect of these parameters, as well as their attempts to model the bed.

2.1.1 Solid Circulation

Circulation patterns which develop in a bed of vibrated particles depend on the intensity of vibration, particle size, bed depth, and method of vibration. Chlenov and Mikhailov [1964] divided vibrated-bed dynamics into two "states": the "vibropseudoliquid" state and the "vibrofluidized" state. The "vibropseudoliquid" state represents the case in which the bed undergoes compaction and corresponds to vibrational intensities less than $K = 1$ for large particles. Particle circulation in this state is essentially non-existent once the initial compaction of particles has been achieved and thus the term is confusing. In the "vibrofluidized" state, however, vigorous particle circulation and mixing is

observed. Figure 2.1 gives their findings on the transition between the two states. Other researchers have investigated this transition from a "static" bed to a "mobile" bed. Typically, they report a "critical" K-value, K_{CR}, at which the transition takes place. Kapustin *et al.* [1980] and Thomas *et al.* [1989] give K = 1 as the transition for particles larger than 100 μm. Thomas *et al.* [1989] state that K_{CR} increases as particle size decreases below 100 μm, but also note a dependence on the cohesiveness of the solid. They quote a value of K_{CR} as high as 4.95 for cohesive, fine-ground flour. Ur'ev [1978] has also noted a dependence of K_{CR} on the cohesiveness of the solid. He has demonstrated the effect by reducing K_{CR} for very fine solids from about K_{CR} = 7 to 2 through the addition of a surfactant which reduces the interparticle forces. Since the "vibropseudoliquid" state of Chlenov and Mikhailov does not appreciably enhance heat or mass transfer due to its marked lack of particle circulation, nearly all work on vibrated beds has concentrated on what they term the "vibrofluidized" state, where the bed is much more active.

Kroll [1955], in his early work on vibrated beds, described a particle motion in which particles flow up at the center of the bed and down at the walls, as shown in Figure 2.2. This general pattern has been confirmed by other investigators [Bretsznajder *et al.*, 1963; Ratkai, 1976; Muchowski, 1980; Kapustin *et al.*, 1980; Savage, 1988], although the reason for the circulation pattern is not clear. These investigators used two markedly different methods of inducing vibrations. Kroll, Muchowski, and Kapustin vibrated the entire vessel, whereas Bretsznajder, Ratkai, and Savage employed a vessel with fixed sidewalls and a vibrating base plate. (Bretsznajder used a cloth membrane for a base, and Ratkai vibrated only a section of the base plate).

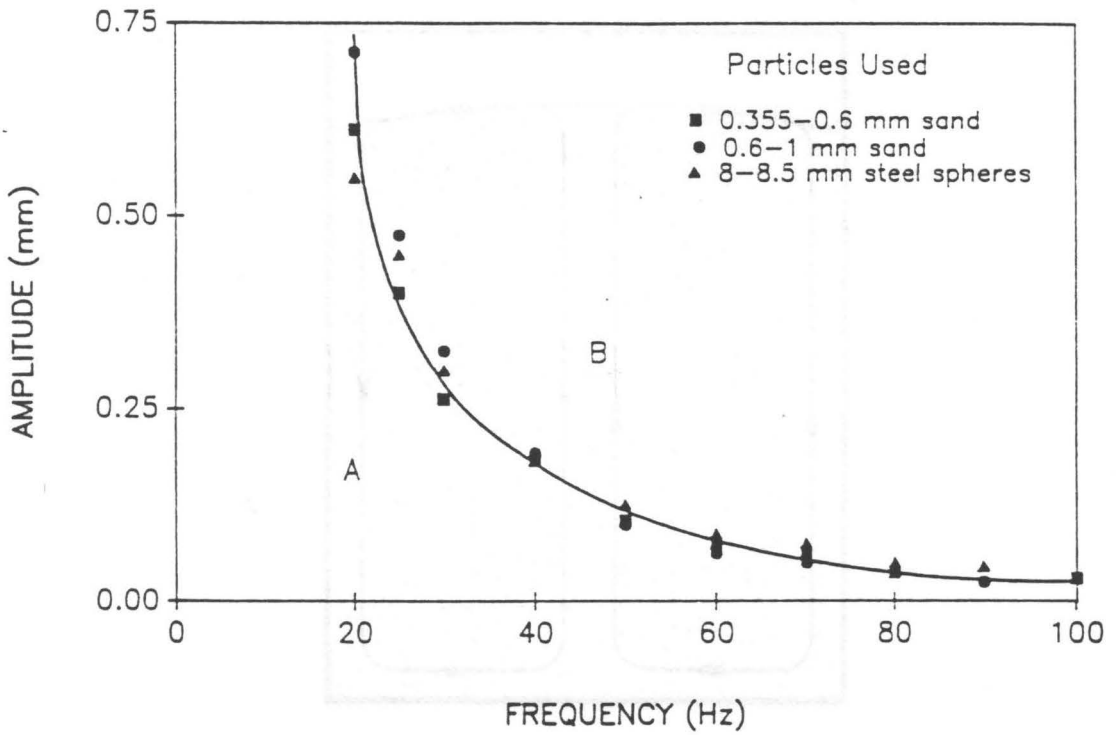

Figure 2.1. Transition from the vibropseudoliquid state to the vibrofluidized state: Curve shown is for K = 1. A represents the vibropseudoliquid region and B represents the vibrofluidized region. From Chlenov and Mikhailov [1964].

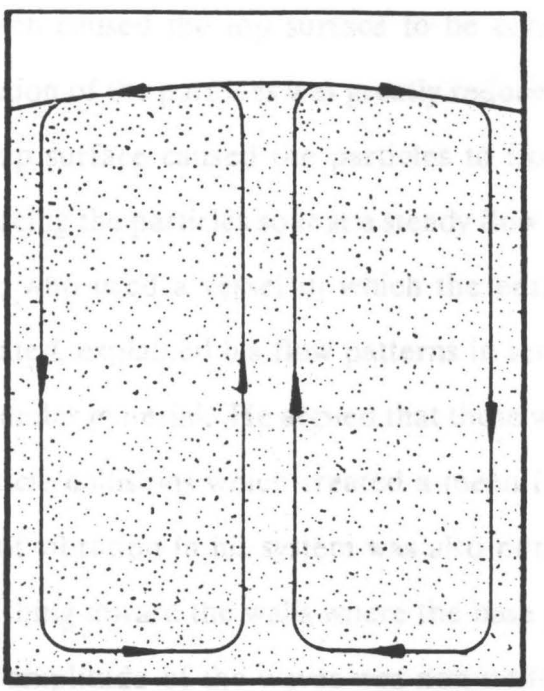

Figure 2.2. Solid circulation in a vibrated bed: Circulation reported for particles from 0.1 to 1 mm in diameter. From Kroll [1955].

Ratkai [1976] named his system, which consisted of a vibrated disc attached to a fixed cylinder by an elastic membrane, a "vibro-spouted" bed. He explained the observed flow in terms of the changing vibrational amplitude in the radial direction. The amplitude was greatest in the middle section of the bed directly above the vibrating plate, and gradually diminished to zero near the walls in a fashion which depended on the membrane characteristics. He reasoned that the larger amplitude in the center of the bed created a greater expansion in the powder above it, which caused the top surface to be convex (see Figure 2.2). Since the internal friction of the particles was greatly reduced by vibration, even a small angle on the top surface caused the particles to flow downhill, with the vibrating motion replacing the particles so that a steady flow was developed.

Savage [1988], who used a vessel in which the entire base plate, a thin metal sheet, was vibrated, explained his flow patterns in terms of propagation of waves through the granular material. He argued that these waves were attenuated by inelastic inter-particle collisions which created a mean force on the particles. Since the amplitude of vibration in his system was also non-uniform (greatest at the center and diminishing toward the walls where the base plate was fixed to the stationary walls), the amplitude of the waves was non-uniform, and this created the observed particle motion. He reasoned that these waves were similar to acoustic waves and proposed the term "acoustic streaming" for the motion in the granular medium.

Circulation in vibrated beds where the entire vessel is vibrated must, of course, be due to some other reason, since vibrational amplitude does not vary with radial position. Kapustin *et al.* [1980] found the same general circulation pattern of Figure 2.2 for particles larger than 100 μm, but reported random mixing for smaller particles. Muchowski [1980] also reported a turbulent, random

motion for glass spheres of 100 μm and a regular circulation pattern for 1-mm spheres. He argued that the circulation was due to friction forces at the walls. The particle layers nearest the walls were restricted in movement during the free-flight period of the cycle by this friction, which imparted a relative downward motion. Chlenov and Mikhailov [1972] explained the downward motion at the walls by gas movement. They measured a net negative pressure in the gaps beneath the bed and reasoned that the gas would preferentially flow down the walls since the porosity was greatest there. This gas flow, in their view, carried the particles nearest the wall with it. Their view is suspect; see Section 2.1.6 below.

Buevich *et al.* [1979] related particle movement in beds of small particles to differences in the average pressure beneath the bed at different locations. They found that the average floor pressure during the flight phase of the bed varied with bed depth as shown in Figure 2.3. As can be deduced from this figure, for certain bed depth combinations, fine particles tend to flow from shallower regions to deeper regions based on a difference in average pressure. They observed this predicted flow pattern to be the case. In fact, other investigators who worked with fine particles (d_p < 100 μm), reported that the top surface of the bed was not flat, but tended to "bunker." Thomas [1988] observed three stable bunker configurations for vibrated beds, and reported the circulation patterns associated with each, as shown in Figure 2.4. Note that in each case, the solids within the bulk of the bed tend to move from a shallower region toward a deeper region. The solids return to the shallower region in a flow occurring only at the bed surface. As the beds of Thomas [1988] were 30 mm in depth, this result agrees with the prediction of Buevich *et al.* [1979] from Figure 2.3.

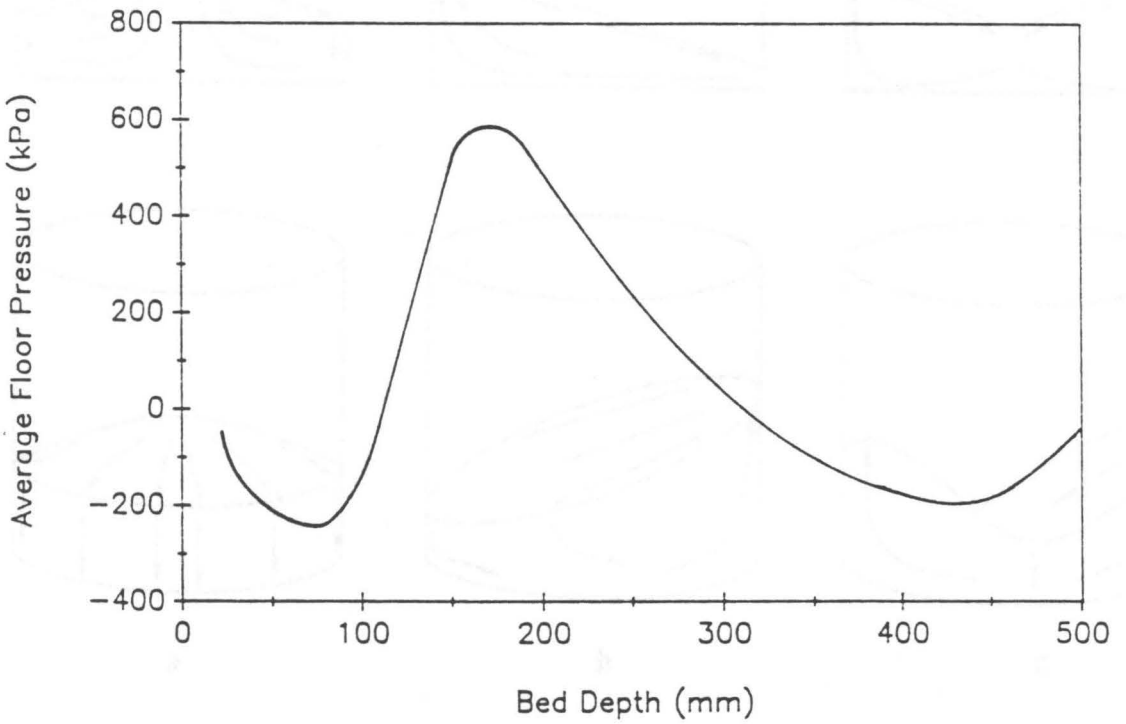

Figure 2.3. Average floor gauge-pressure during flight versus bed depth: Results for 80-μm corundum particles vibrated at 20 Hz with an amplitude of 2.7 mm. Adapted from Buevich *et al.* [1979].

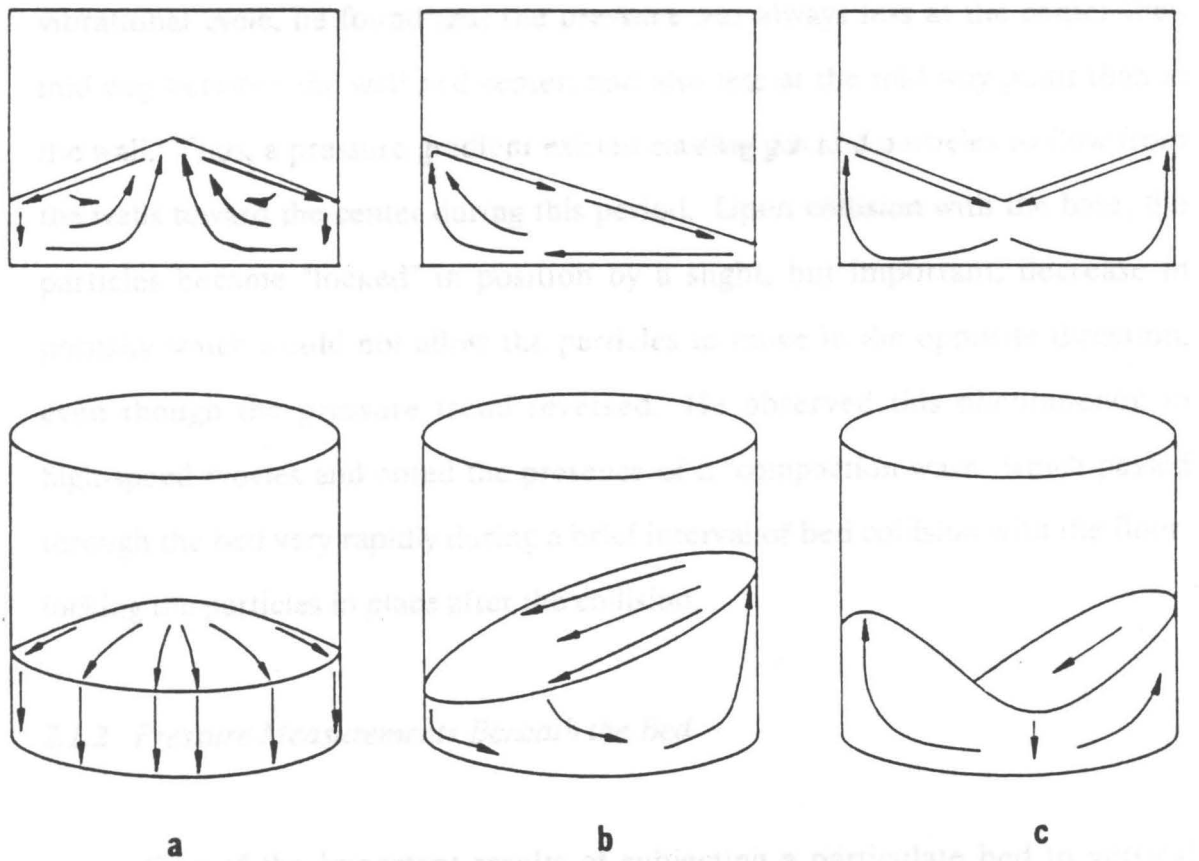

Figure 2.4. Stable configurations of bunkered beds. Particle circulation patterns observed to be stable for beds which bunker. Both rectangular (top) and cylindrical (bottom) vessel geometries are shown for: (a) center-high bunker; (b) wall-high bunker; and (c) center-low bunker. From Thomas [1988].

Thomas [1988] offered a different explanation for the observed circulation for his "center-high" configuration of Figure 2.4. He measured the instantaneous pressure beneath the bed at three points: at the center of the bed, half-way between the center and the wall, and at the wall. During the flight period of the vibrational cycle, he found that the pressure was always less at the center than mid-way between the wall and center, and also less at the mid-way point than at the wall. Thus, a pressure gradient existed causing gas and particles to flow from the walls toward the center during this period. Upon collision with the base, the particles became "locked" in position by a slight, but important, decrease in porosity which would not allow the particles to move in the opposite direction, even though the pressure trend reversed. He observed this phenomenon in high-speed movies and noted the presence of a "compaction wave" which passed through the bed very rapidly during a brief interval of bed collision with the floor, locking the particles in place after the collision.

2.1.2 Pressure Measurements Beneath the Bed

One of the important results of subjecting a particulate bed to vertical vibrations is the establishment of pressure fluctuations across and beneath the bed. Many investigators have measured the pressure beneath the bed with greatly varying findings--sometimes in direct contradiction. Some investigators have also modeled the pressure variations in a vibrated bed; their work will be covered in a later section on bed modeling (see Section 2.1.7).

Kroll [1954, 1955] first measured the pressure fluctuations beneath a vibrated bed of particles. He found that the pressure fluctuations were cyclic in nature and nearly sinusoidal in shape, and varied around atmospheric pressure,

but that the amplitude and phase angle of the oscillations were dependent upon the bed depth. For 130-μm glass beads, he found that for shallow bed depths, the amplitude of pressure fluctuations increased with increasing bed depth, reached a maximum for a depth of 60 mm, and then decreased as the bed depth was further increased up to 110 mm. The phase angles of the occurrence of the maximum and minimum values of gauge pressure were delayed as the bed depth was increased. The minimum pressure for a bed depth of 20 mm, for example, was found at about 130°, and this angle was observed to increase up to about 220° for a bed of 110 mm (here the angle was defined such that 0° corresponded to the point where the vibrated vessel's displacement crossed the rest position moving upward).

Chlenov and Mikhailov [1965b, 1972] found that the time-averaged gauge pressure beneath a vibrated bed of sand was negative, with a value of nearly -2 kPa under certain conditions (see Figure 2.5). They noted an effect they termed "pumping" across their porous grid plate which they attributed to this net negative pressure beneath the bed. Buevich and Kharisova [1978] reasoned that this non-zero average pressure was due to a voidage change during a vibrational cycle. They argued that the hydrodynamic force acting on the rising bed was greater than the force on the falling bed, which could expand. This difference in hydrodynamic forces during the two parts of the cycle created the net suction or pumping noted above. As shown previously in Figure 2.3, however, Buevich *et al.* [1979] found that the average pressure beneath the bed was not always negative. As can be seen in this figure, they found the average floor pressure to be a function of bed depth, and that it could assume both positive and negative values.

In direct opposition to the findings of Chlenov and Mikhailov of net negative gauge pressures beneath the bed, Gutman [1974] found that the

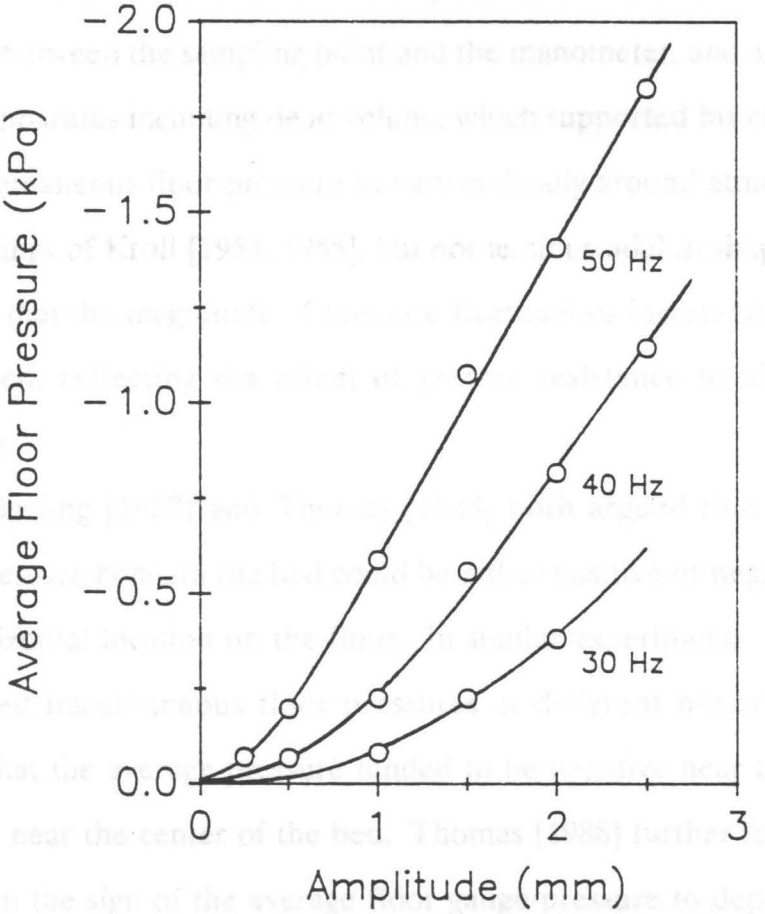

Figure 2.5. Average pressure beneath a vibrated bed of sand: Dependence of the time-averaged floor gauge-pressure on vibrational parameters. Adapted from Chlenov and Mikhailov [1965b].

time-averaged floor pressure was nearly zero and slightly positive, usually about three to four percent of the magnitude of the pressure fluctuations during the cycle. He explained the net negative pressure of Chlenov and Mikhailov in terms of their measuring apparatus, which consisted of a remote, U-tube manometer. He argued that the pressure which they measured reflected the effect of the dead volume between the sampling point and the manometer, and also ran experiments on his apparatus including dead volume which supported his claim. He too found the instantaneous floor pressure to vary cyclically around atmospheric (similar to the findings of Kroll [1954, 1955], but not as sinusoidal in shape). Gutman's data showed that the magnitude of pressure fluctuations increased as the particle size decreased, reflecting the effect of greater resistance to air flow for smaller particles.

Sprung [1987] and Thomas [1988] both argued that the time-averaged floor pressure beneath the bed could be either positive or negative, depending on the horizontal location on the floor. In similar experiments, they independently measured instantaneous floor pressures at different horizontal locations and found that the average pressure tended to be negative near the vessel walls and positive near the center of the bed. Thomas [1988] further found the magnitude and even the sign of the average floor gauge-pressure to depend on the particle size and K-value as shown in Figures 2.6 and 2.7.

As noted in Section 2.1.1, Thomas [1988] explained the particle circulation observed for small particles in terms of the instantaneous floor pressures found in different horizontal locations. He took instantaneous pressure data varying particle size, solid density, bed depth, and vibrational intensity. All data were taken with three pressure transducers placed directly in the floor of the vessel (in order to minimize dead volume), which measured the pressure at three horizontal

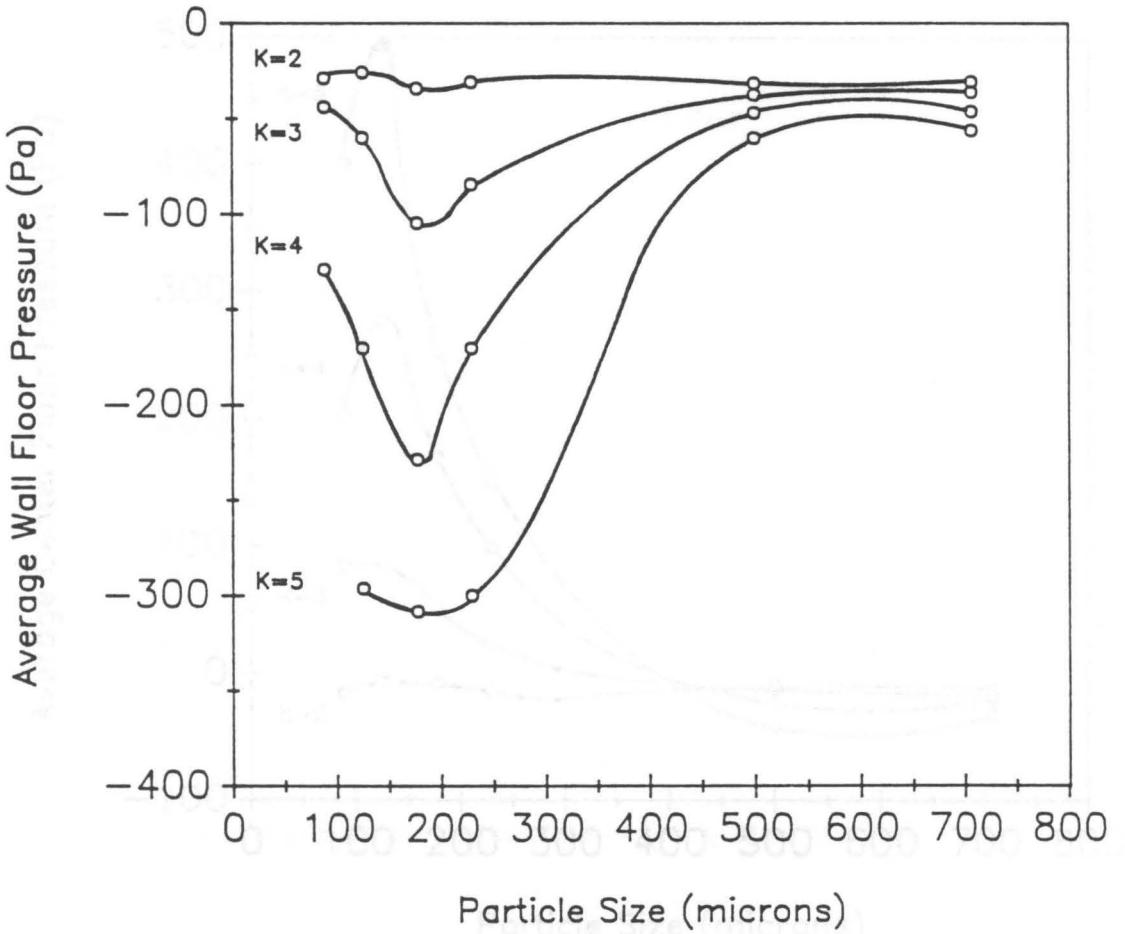

Figure 2.6. Average floor pressure at the wall: Time-averaged gauge pressures beneath a vibrated bed of Master Beads measured at the wall of the vessel as a function of particle size. From Thomas [1988].

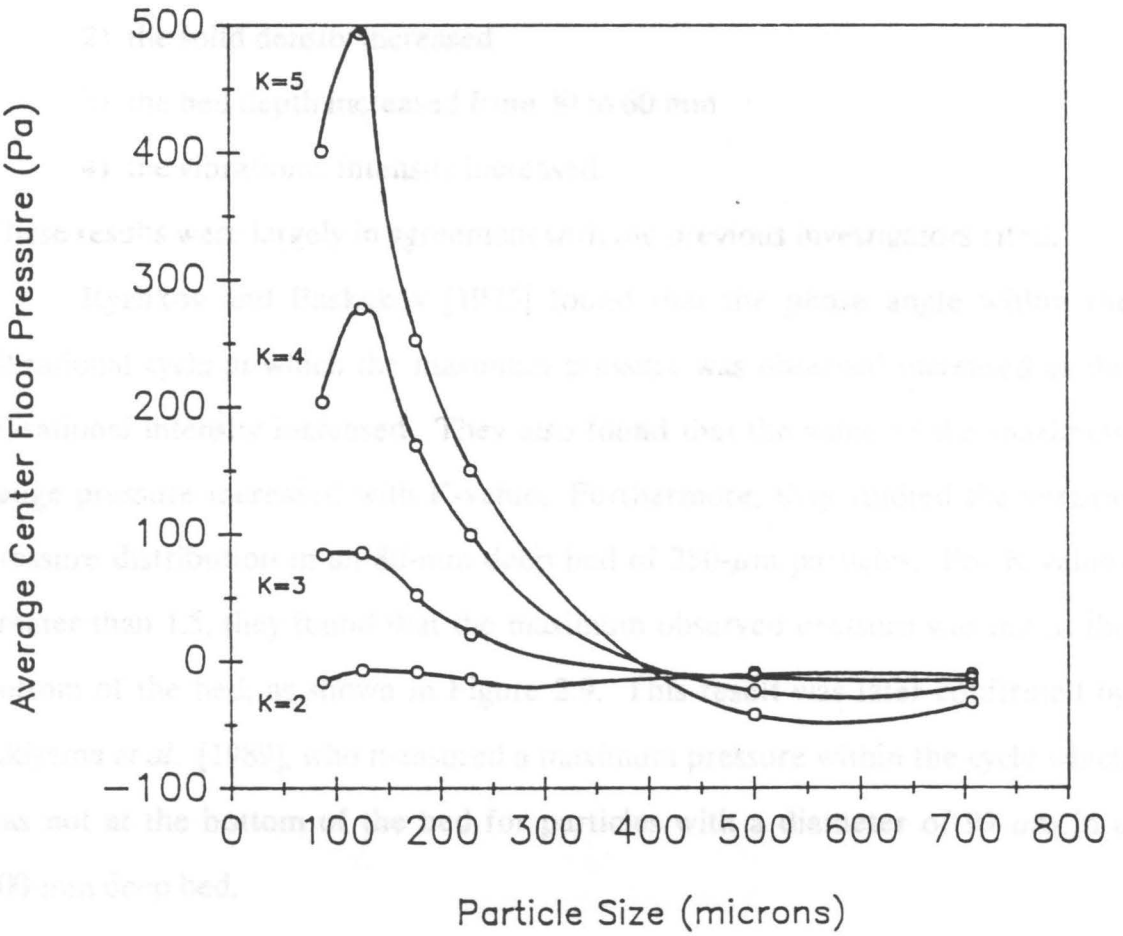

Figure 2.7. Average floor pressure at the center of the bed: Time-averaged gauge pressures beneath a vibrated bed of Master Beads measured beneath the center of the bed as a function of particle size. From Thomas [1988].

locations beneath the bed: at the center of the vessel; mid-way between the center and the wall; and at the wall. The results shown in Figure 2.8 were typical of his findings. In general, he found the magnitude of pressure fluctuations to increase as:

1) the particle diameter decreased
2) the solid density increased
3) the bed depth increased from 30 to 60 mm
4) the vibrational intensity increased.

These results were largely in agreement with the previous investigators cited.

Ryzhkov and Baskakov [1975] found that the phase angle within the vibrational cycle at which the maximum pressure was observed increased as the vibrational intensity increased. They also found that the value of the maximum gauge pressure increased with K-value. Furthermore, they studied the vertical pressure distribution in an 80-mm deep bed of 250-μm particles. For K-values greater than 1.5, they found that the maximum observed pressure was not at the bottom of the bed, as shown in Figure 2.9. This result was later confirmed by Akiyama *et al.* [1989], who measured a maximum pressure within the cycle which was not at the bottom of the bed for particles with a diameter of 99 μm in a 100-mm deep bed.

2.1.3 Effect of Wall Friction

The frictional force of vessel walls has been noted and used to explain observed phenomena in vibrated beds by several investigators. Wall friction can be important in the following situations:

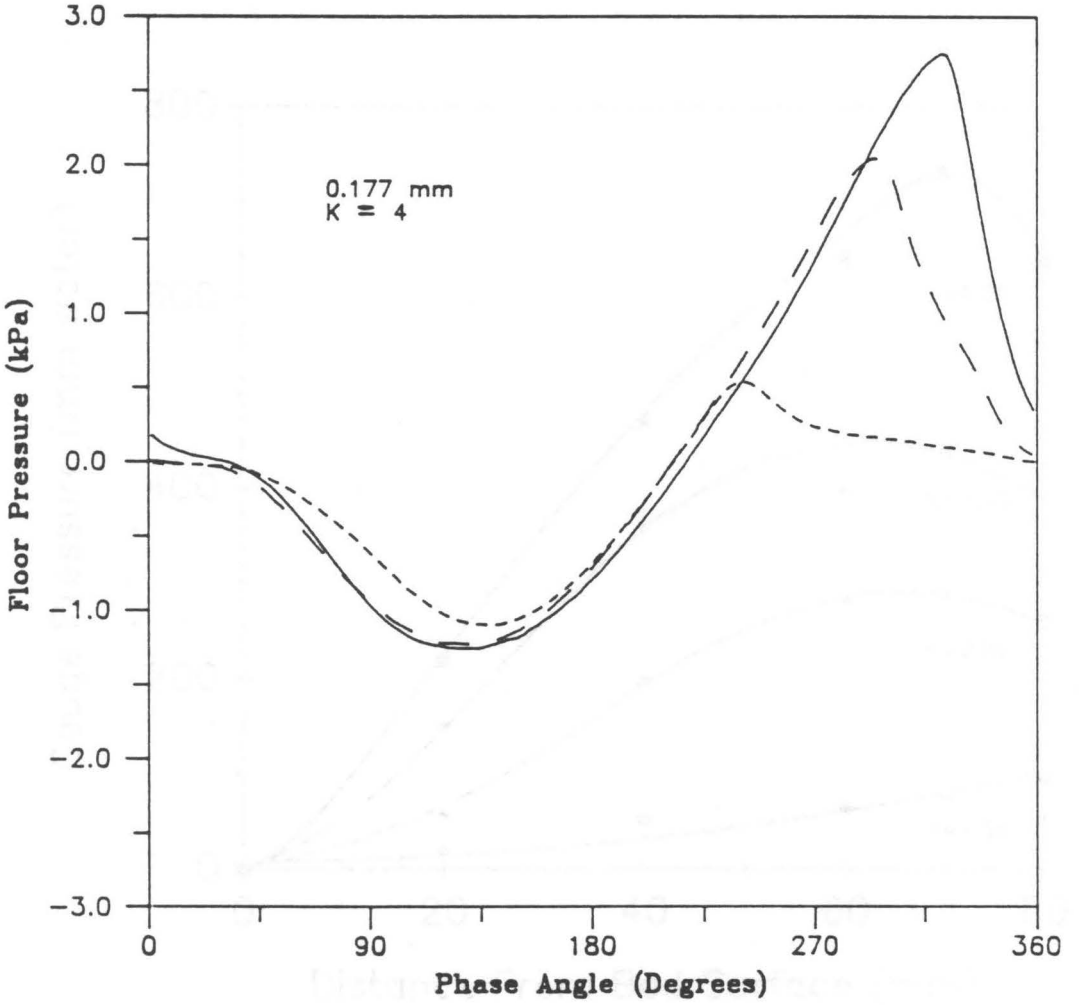

Figure 2.8. Cyclic floor pressures beneath a vibrated bed: Variation of floor pressures for 177-μm alumina at K = 4. Pressure is measured at three places beneath the bed: solid line - at the center of the bed; long-dashed line - midway between the center and wall; and short-dashed line - at the wall. From Thomas [1988].

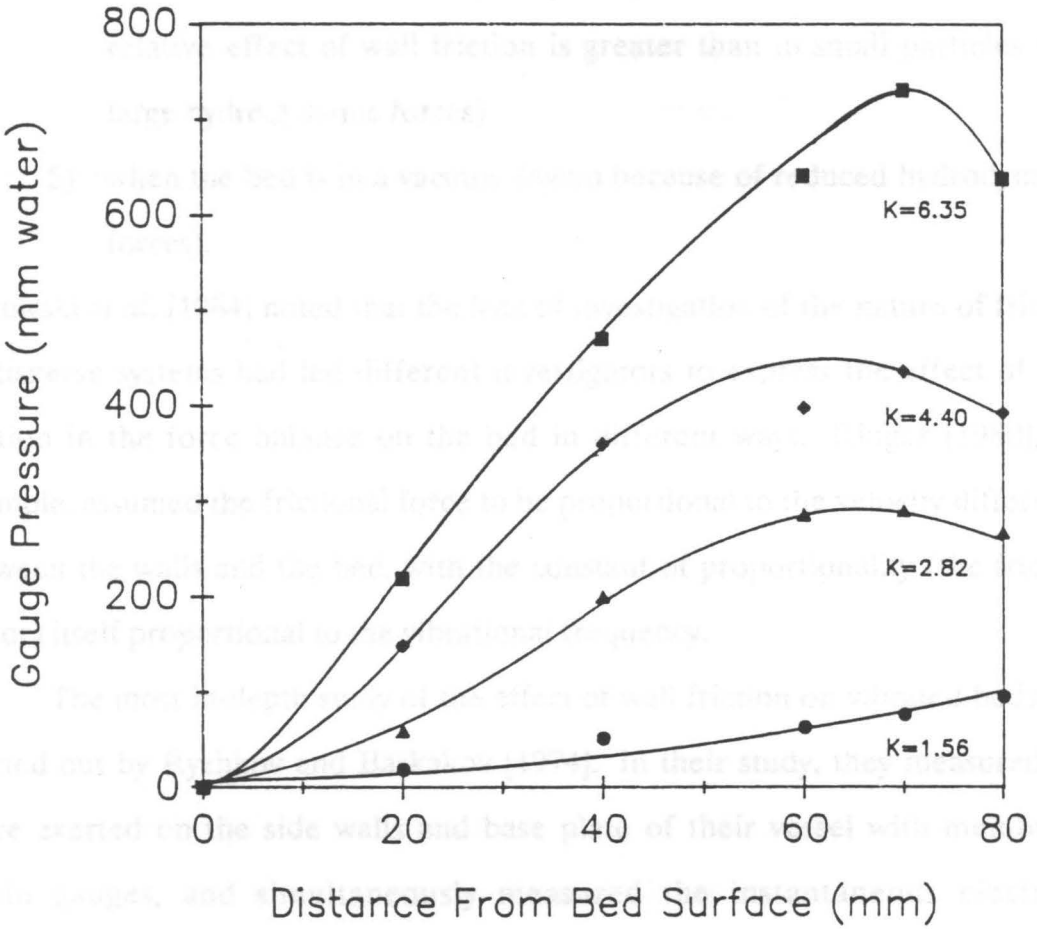

Figure 2.9. Maximum gauge pressure versus distance from the surface: Variation in the maximum pressure over the height of the bed for 250-μm corundum particles in a bed 80 mm deep. From Ryzhkov and Baskakov [1975].

1) when the bed of particles is deep
2) when the width of the bed is small
3) when the particles are sticky (as is often the case in drying)
4) when the particles are large (with large particles, the pressure drop across the bed is small so the hydrodynamic forces are small, and the relative effect of wall friction is greater than in small particles with large hydrodynamic forces)
5) when the bed is in a vacuum (again because of reduced hydrodynamic forces).

Pakowski *et al.* [1984] noted that the lack of investigation of the nature of friction in disperse systems had led different investigators to express the effect of wall friction in the force balance on the bed in different ways. Ringer [1980], for example, assumed the frictional force to be proportional to the velocity difference between the walls and the bed, with the constant of proportionality (the friction factor) itself proportional to the vibrational frequency.

The most in-depth study of the effect of wall friction on vibrated beds was carried out by Ryzhkov and Baskakov [1974]. In their study, they measured the force exerted on the side walls and base plate of their vessel with membrane strain gauges, and simultaneously measured the instantaneous electrical resistance between the walls of the vessel as well as between the particles and base (the particles for their study were graphite). For depths greater than 50-100 mm of graphite particles between 0.25 and 1 mm in diameter, they found that the separation of the bed from the floor was delayed due to wall friction. They deduced this because they observed a portion of the cycle in which the strain gauge at the vessel floor indicated a zero force, but the electrical resistance indicated that separation had not occurred. During this portion of the cycle, they

argued that the bed was held in place by the side walls even though there was no normal force at the vessel base, and that this condition persisted until the stresses at the wall decayed sufficiently to allow the bed to lift off of the vessel base.

Gutman [1974] investigated the importance of wall effects by measuring floor pressures as a function of bed depth and vessel diameter. He found that the vessel diameter had a large effect on the maximum negative gauge pressure for large (675-935 μm) particles, but that the effect on small (90-135 μm) particles was very much less. He concluded from his data that wall friction was important in beds of large particles and in beds with L/D (ratio of bed depth to vessel diameter) greater than one.

Thomas [1988] explained the circulation patterns he observed in large-particle beds in terms of wall friction. In a mechanism similar to the one put forward by Muchowski [1980], he argued that the layer closest to the wall was retarded in rising relative to the rest of the bed and thus had a net downward motion. He observed this downward flow to extend only two to three particle layers into the bed, with the rest of the bed moving upward at a much slower velocity, as shown in Figure 2.10. To substantiate his claim of wall friction being the dominant driving force for circulation in beds of large particles, he noted that his horizontal pressure measurements (discussed in the previous section) showed virtually no hydrodynamic driving force for circulation for these large particles. In a related observation, he extended his argument to all non-bunkered beds, since he observed the same characteristic circulation in any bed with very small hydrodynamic forces (a bed of any size particles in a vacuum, for example).

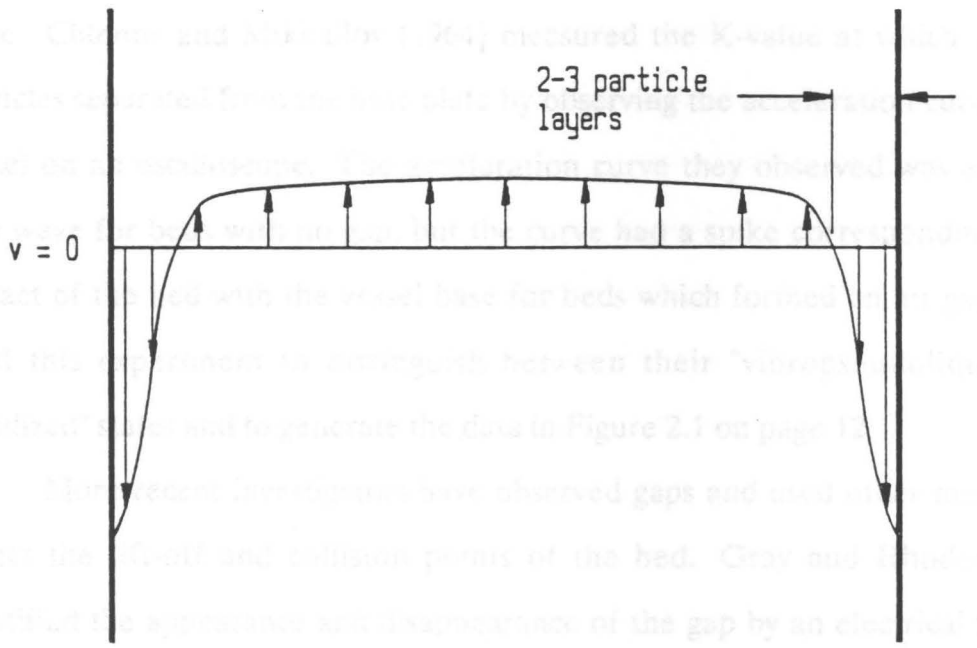

Figure 2.10. Schematic particle velocity gradient for large-particle beds: Downward particle movement occurs in only 2 or 3 layers at the two side walls (shown as dark lines). Notation: v is the particle velocity. From Thomas [1988].

2.1.4 Air-Gap Measurement

From the earliest work on vibrated beds, it was known that the bed of particles separated from the vessel floor during a portion of the vibrational cycle for a sufficiently high vibrational intensity. Bachmann [1940] observed a gap beneath a bed of large particles; Kroll [1954, 1955] also noted the appearance of a gap and developed a model which would predict the bed trajectory during the cycle. Chlenov and Mikhailov [1964] measured the K-value at which a bed of particles separated from the base plate by observing the acceleration curve of the vessel on an oscilloscope. The acceleration curve they observed was a smooth sine wave for beds with no gap, but the curve had a spike corresponding to the impact of the bed with the vessel base for beds which formed an air gap. They used this experiment to distinguish between their "vibropseudoliquid" and "fluidized" states and to generate the data in Figure 2.1 on page 12.

More recent investigators have observed gaps and used other methods to detect the lift-off and collision points of the bed. Gray and Rhodes [1972] identified the appearance and disappearance of the gap by an electrical method. They used phosphor bronze beads 3 mm in diameter, and created a circuit out of the base plate, the bed, and a metal probe inserted in the bed. During the portion of the cycle that a gap appeared, electrical contact was broken between the base plate and the metal probe, and this was monitored on an oscilloscope. They also concurrently monitored the deformation of the acceleration curve (similarly to Chlenov and Mikhailov [1964]), and found good agreement between the two methods. An attempt to use the electrical technique on fine (53 μm) phosphor bronze powder failed to give clear waveforms, however. In a conceptually similar manner, Rippie *et al.* [1978] monitored the gap by means of the voltage drop and

conduction of the bed. They used very large chrome steel spheres (2.38 - 5.56 mm in diameter) as particles. Their device, however, provided a means of precisely measuring the phase angle of the cycle so that the observed phenomena could be phase-correlated. This was done via a magnetic pickup coupled with a magnet which was mounted on and revolved with the vibrator's flywheel (they used a mechanical vibrator).

Ryzhkov and Baskakov [1974] detected the lift-off and collision points by concurrently monitoring base and wall-mounted strain gauges, electrical resistance between the bed and base and between the walls of the vessel, and the deformation of the acceleration signal. They worked with graphite particles of 0.25 - 1.0 mm and bed depths of 50 - 600 mm. As reported in the previous section on wall friction, for beds deeper than 50 - 100 mm, they noted a delay between the point in the cycle where the strain gauge indicated that the bed exerted no force on the base and the point where the resistance showed the formation of a gap, as shown in Figure 2.11.

Gutman [1974, 1976a] measured the gap by means of high-speed movies. Finding that method inadequate, he developed a capacitance method for gap detection, which consisted of measuring the change in capacitance of the bed by monitoring a parallel-plate capacitor (with the bed acting as dialectric between the plates). He not only measured the points at which the gap formed and collapsed, but also measured the size of the gap as it varied during the cycle, as shown in Figure 2.12. This instantaneous measurement of the bed trajectory allowed for comparison with trajectories predicted by his compressible-gas model (discussed in Section 2.1.7.3).

More recently, Thomas *et al.* [1987] developed a method which allowed for precise visual observation of air gaps. Their technique involved measuring the

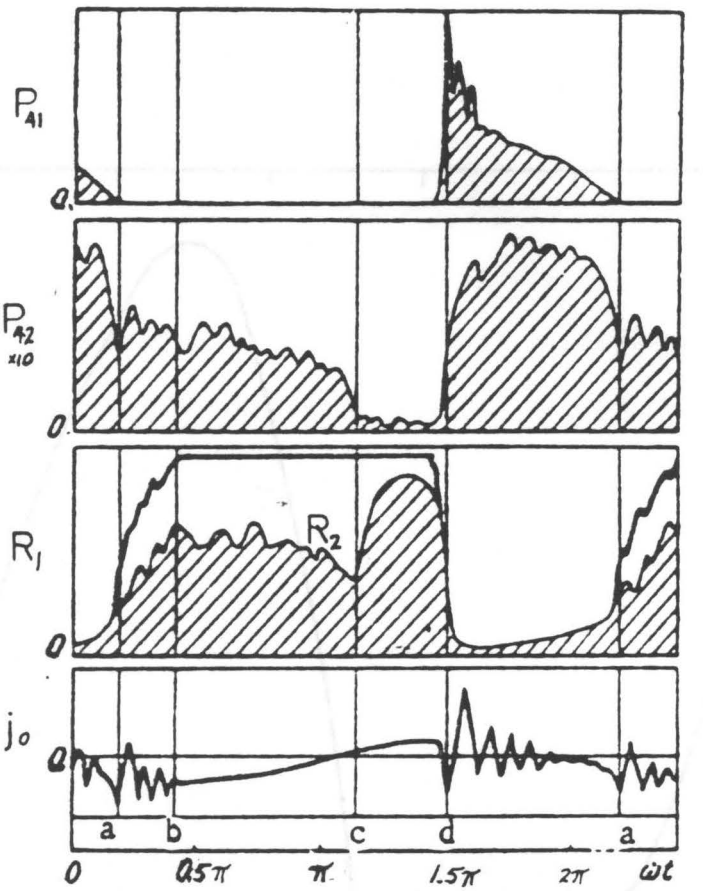

Figure 2.11. Delay in lift-off caused by wall friction: Particle pressure on the vessel floor (P_{41}) and on the vessel walls (P_{42}), electrical resistance between the floor and the graphite particles (R_1) and the two side walls (R_2), and the output from the accelerometer (j_o) versus vibrational phase angle. Floor pressure goes to 0 at point a, but R_1 indicates separation does not occur until point b. Point c represents minimum pressure at the walls and point d corresponds to collision. From Ryzhkov and Baskakov [1974].

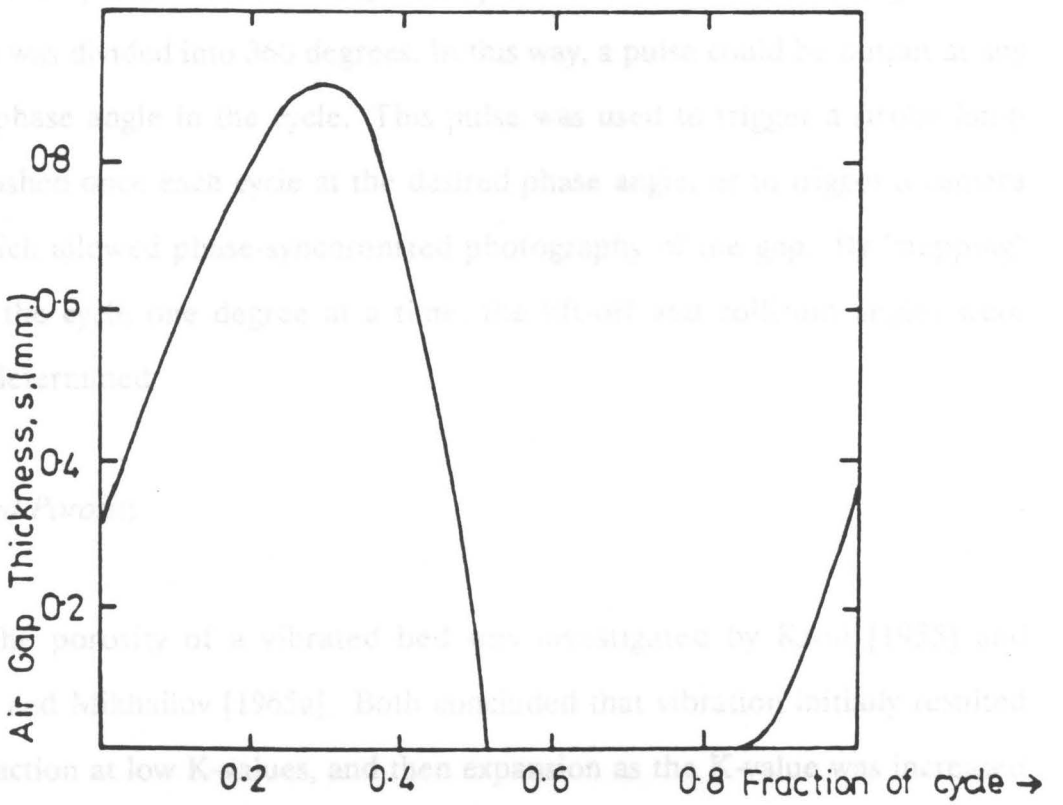

Figure 2.12. Measurement of air-gap thickness: Thickness of the air gap between a 40-mm deep bed of 250-599 μm glass spheres and the vessel floor vibrated at K = 5. From Gutman [1974].

position of the vessel very accurately with a linear-variable-differential-transformer (LVDT) displacement transducer. They built an electronic circuit which monitored the output from the LVDT transducer and determined the frequency of the input signal and the positive crossover point (the point at which the vessel passed through the rest position moving upward, which is the traditional 0° point in a sine wave). This point was defined as zero degrees and the cycle was divided into 360 degrees. In this way, a pulse could be output at any desired phase angle in the cycle. This pulse was used to trigger a strobe lamp which flashed once each cycle at the desired phase angle, or to trigger a camera flash which allowed phase-synchronized photography of the gap. By "stepping" through the cycle one degree at a time, the lift-off and collision angles were visually determined.

2.1.5 Bed Porosity

The porosity of a vibrated bed was investigated by Kroll [1955] and Chlenov and Mikhailov [1965a]. Both concluded that vibration initially resulted in compaction at low K-values, and then expansion as the K-value was increased past K = 1 with the extent of expansion levelling off at high K-values (see Figure 2.13). Little work was done to investigate the change in porosity during the cycle, however. In fact, most of the mathematical models [Kroll, 1954; Gutman, 1974; Ryzhkov and Baskakov, 1974; among others] of vibrated beds assumed constant voidage throughout the cycle. Observations have been made, however, which suggest that porosity must vary slightly during the cycle, and several measurements of the porosity change have been reported.

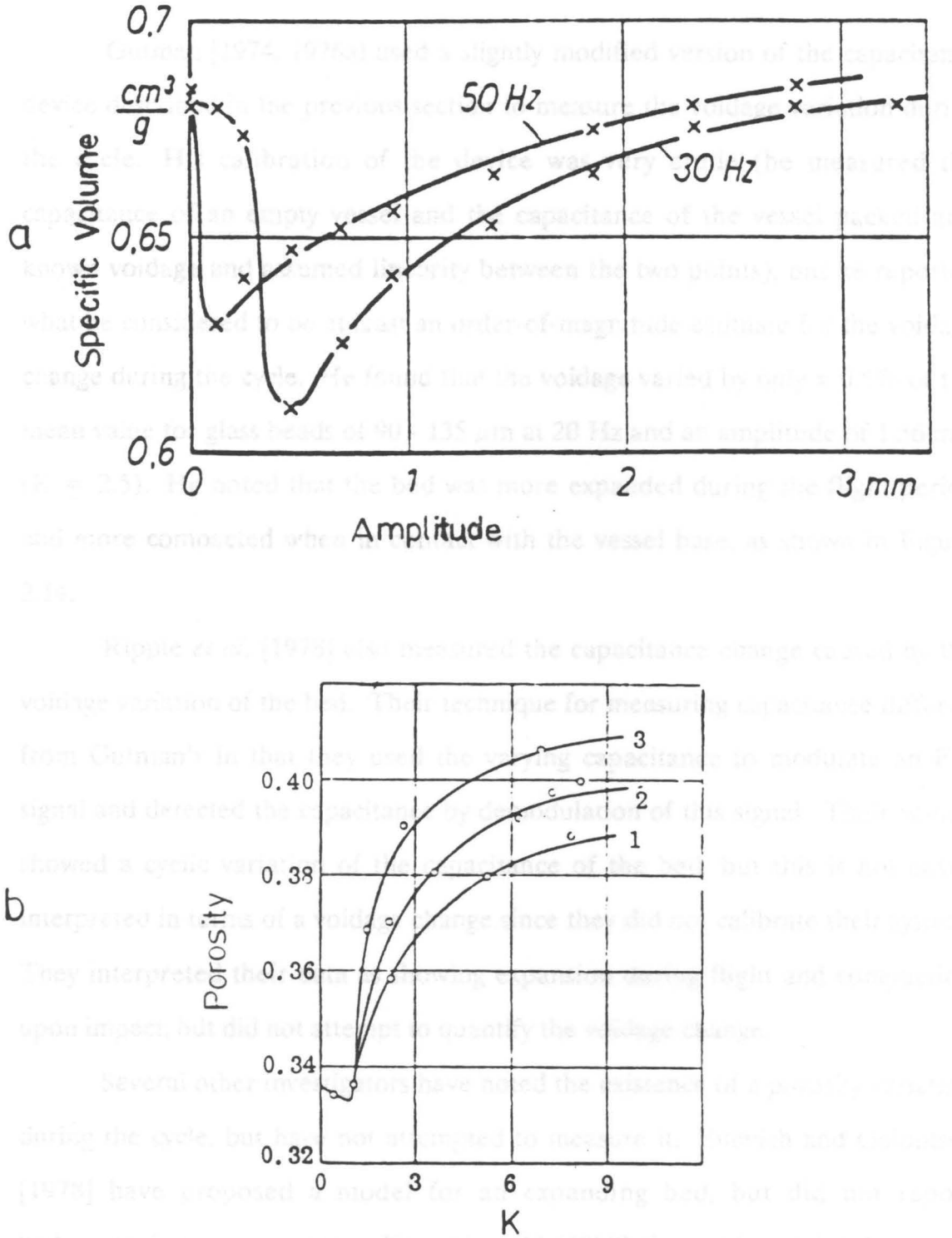

Figure 2.13. **Effect of vibrational intensity on bed porosity:** Dependence of: (a) specific volume on amplitude of vibration; and (b) bed porosity on K-value for beds of vibrated sand. Figure (a) from Kroll [1955], (b) from Chlenov and Mikhailov [1965a].

Gutman [1974, 1976a] used a slightly modified version of the capacitance device described in the previous section to measure the voidage variation during the cycle. His calibration of the device was very crude (he measured the capacitance of an empty vessel and the capacitance of the vessel packed at a known voidage and assumed linearity between the two points), but he reported what he considered to be at least an order-of-magnitude estimate for the voidage change during the cycle. He found that the voidage varied by only ± 0.5% of the mean value for glass beads of 90 - 135 μm at 20 Hz and an amplitude of 1.56 mm (K = 2.5). He noted that the bed was more expanded during the flight period and more compacted when in contact with the vessel base, as shown in Figure 2.14.

Rippie *et al.* [1978] also measured the capacitance change caused by the voidage variation of the bed. Their technique for measuring capacitance differed from Gutman's in that they used the varying capacitance to modulate an FM signal and detected the capacitance by demodulation of this signal. Their results showed a cyclic variation of the capacitance of the bed, but this is not easily interpreted in terms of a voidage change since they did not calibrate their system. They interpreted their data as showing expansion during flight and compaction upon impact, but did not attempt to quantify the voidage change.

Several other investigators have noted the existence of a porosity variation during the cycle, but have not attempted to measure it. Buevich and Galontsev [1978] have proposed a model for an expanding bed, but did not report bed-expansion measurements. Kapustin *et al.* [1980] observed porosity changes in a bed of millet grain via high-speed movies. Their movies showed that the bed sequentially expanded so that the top layer lifted off first with lower layers lifting in succession rather than lifting together. Akiyama *et al.* [1989] have made

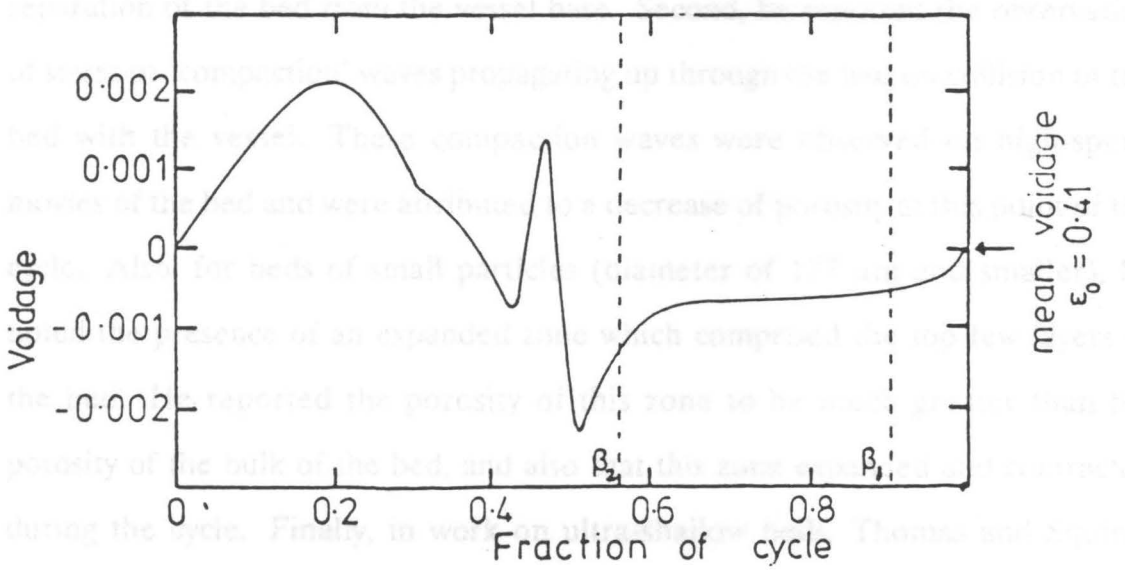

Figure 2.14. Variation in bed voidage during a vibrational cycle: Cyclic variation in the porosity of an 80-mm deep bed of 90-135 μm glass beads vibrated at K = 2.5. β_1 and β_2 are the measured lift-off and collision points. From Gutman [1974].

pressure measurements at different vertical locations in a vibrated bed which indicated that the local voidage change was not constant throughout the bed. They suggested from their data on small (99 μm) glass beads vibrated at K = 5 in a 100-mm deep bed that the voidage was changing more rapidly at a point 25 mm from the top surface than it was at the bottom of the bed.

Thomas [1988] noted several observations which indicated that the bed must change porosity during the cycle. First, he observed a delay in bed lift-off compared to the point in the cycle where the force balance predicted it and theorized that this delay was caused by an expansion of the particles prior to separation of the bed from the vessel base. Second, he reported the observation of stress or "compaction" waves propagating up through the bed on collision of the bed with the vessel. These compaction waves were observed on high-speed movies of the bed and were attributed to a decrease of porosity at this point of the cycle. Also, for beds of small particles (diameter of 177 μm and smaller), he noted the presence of an expanded zone which comprised the top few layers of the bed. He reported the porosity of this zone to be much greater than the porosity of the bulk of the bed, and also that this zone expanded and contracted during the cycle. Finally, in work on ultra-shallow beds, Thomas and Squires [1989] have reported that a bed with a static depth of 1 mm has been observed to display a cyclically varying depth, between 4 mm and 12 mm, at the same frequency as the vibration.

2.1.6 Effect of Vacuum

Several investigators have studied the effect of lowering the pressure on the particle circulation. Chlenov and Mikhailov [1965a], who explained their

observed particle circulation by motion of gas through the bed, found that the circulation was very much less when the particles were in vacuum. Under vacuum, they asserted that the primary motion of the particles was due merely to the vertical oscillation. Sapozhnikov and Syromyatnikov [1970] made similar observations, noting a decrease in mixing and an increase in vertical motion, presumably due to a decreased drag force. Thomas [1988] also conducted experiments with a vibrated bed under vacuum. He worked with particles of different sizes and concluded that all beds had the circulation pattern characteristic of large particles--downward in a very few layers at the walls and very slowly up everywhere else. He noted too that the main motion was due to the vertical oscillation of the vessel, and that this was increased because of reduced drag. The mixing or circulation velocity, however, was less than that at atmospheric pressure. Beds of particles which he had observed to bunker at atmospheric conditions had a level surface under vacuum.

2.1.7 Vibrated-Bed Models

The motion of a particulate bed subjected to vibration has been modeled by several investigators. Due to the complexity of the motion and the forces acting on the bed, different investigators have made simplifying assumptions about the bed behavior to aid in the development of dynamic models. All of the models assume that the bed can be treated as a single plastic mass, implying that the coefficient of restitution of the bed is zero (there is no rebound upon collision), and that the bed moves as a single unit, lifting and colliding instantaneously. All but the simplest model treat the bed as a porous piston. These models assume that the flow of gas through the bed follows Darcy's

Law, which Gutman and Davidson [1975] have shown experimentally to be valid for frequencies in the range of practical interest. Also, all of the models, except the one proposed by Thomas [1988], consider only the one-dimensional case. These models neglect motion except for in the vertical direction, and are thus unable to predict observed particle circulation patterns. Table 2.1 summarizes the models discussed in this section.

2.1.7.1 The Single-Particle Model

The simplest possible model for a vibrated bed attributed to Bachmann [1940], and also solved by Takahashi *et al.* [1968], treats the bed as a single plastic particle which travels with the vessel, lifts off when the acceleration of the vessel falls below gravitational acceleration, and collides (with no rebound) at some later point in the cycle. This model assumes that frictional as well as drag forces are negligible. In the notation of Figure 2.15, which shows a schematic general force balance on a single plastic mass, Newton's Second Law leads to

$$M_b \frac{d^2 (s + a)}{dt^2} = -F_G + F_N \qquad [2.1]$$

if only gravitational and normal forces are considered. At time t_s, the bed separates from the vessel base and $F_N = 0$. Since the gap s is still zero just at the instant of t_s, Equation [2.1] becomes

$$M_b \frac{d^2 a}{dt^2} = - F_G = -M_B g, \qquad t = t_s$$

Table 2.1 Vibrated-Bed Dynamics Models

Model	Forces Considered by the Model		Remarks
	Flight Period	Contact Period	
Single-particle	Gravity	Gravity Normal force due to vessel base	Simplest model Section 2.1.7.1
Kroll	Gravity Drag	Gravity Normal force due to vessel base	Incompressible gas Section 2.1.7.2
Gutman	Gravity Drag	Gravity Drag Normal force due to vessel base	Compressible gas Section 2.1.7.3
Expanding-bed	Gravity Drag (position dependent)	Gravity Normal force due to vessel base	Varying voidage Incompressible gas Section 2.1.7.4
Wall-friction	Gravity Wall friction	Gravity Normal force due to vessel base	Single-particle model with wall friction Section 2.1.7.5
Thomas	Gravity Drag (vertical and horizontal)	Gravity Drag Normal force due to vessel base	Two-dimensional Semi-empirical Section 2.1.7.6

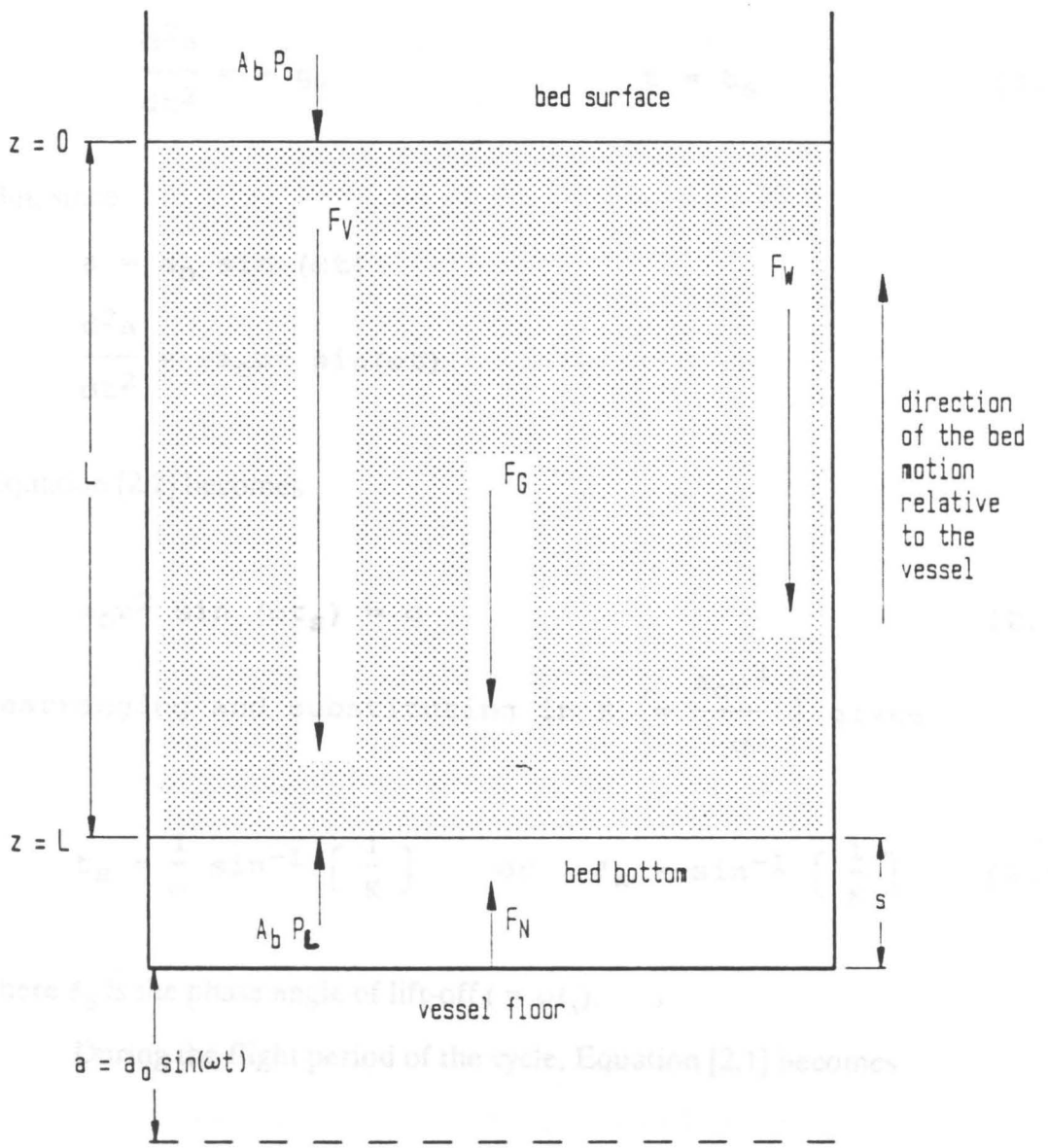

Figure 2.15. Force diagram for a vibrated plastic mass: Schematic of the forces acting on a vibrated bed modeled as a single, porous, plastic mass. Notation: L = bed depth; z = vertical ordinate; a = vessel displacement (= $a_0 \sin \omega t$); s = gap thickness; A_b = cross-sectional area of bed; P_o = atmospheric pressure; P_L = pressure in gap; F_V = viscous drag force due to air flow; F_G = gravitational force; F_W = wall-friction force; F_N = normal force due to vessel base (only during contact period). Adapted from Thomas [1988].

or

$$\frac{d^2a}{dt^2} = -g, \qquad t = t_s \qquad [2.2]$$

But, since

$$a = a_o \sin(\omega t)$$

$$\frac{d^2a}{dt^2} = -a_o\omega^2 \sin(\omega t)$$

Equation [2.2] becomes

$$a_o\omega^2 \sin(\omega t_s) = g \qquad [2.3]$$

Rearranging and substituting in $K \left[= \frac{a_o\omega^2}{g}\right]$ gives

$$t_s = \frac{1}{\omega} \sin^{-1}\left[\frac{1}{K}\right] \quad \text{or} \quad \theta_s = \sin^{-1}\left[\frac{1}{K}\right] \qquad [2.4]$$

where θ_s is the phase angle of lift-off ($= \omega t_s$).

During the flight period of the cycle, Equation [2.1] becomes

$$\frac{d^2(s + a)}{dt^2} = -g \qquad [2.5]$$

subject to the initial conditions

$$\text{at } t = t_s,\ (s + a) = a = a_o \sin(\omega t_s)$$

$$\text{and at } t = t_s,\ \frac{d(s + a)}{dt} = \dot{a} = a_o \cos(\omega t_s) \qquad [2.6]$$

Solution of this equation leads to an expression for the trajectory of the bed

$$(s+a) = -\frac{1}{2} g(t-t_s)^2 + a_o\omega \cos(\omega t_s)\ [t-t_s] + a_o \sin(\omega t_s) \qquad [2.7]$$

In dimensionless form, this trajectory is

$$X = \frac{1}{K}\left\{-\frac{1}{2}\left[\theta - \sin^{-1}\left(\frac{1}{K}\right)\right]^2 + \sqrt{K^2 - 1}\ \left[\theta - \sin^{-1}\left(\frac{1}{K}\right)\right] + 1\right\} \qquad [2.8]$$

where $X = \dfrac{s + a}{a_o}$, $\theta = \omega t$, and $K = \dfrac{a_o\omega^2}{g}$.

This crudest model has the least error for beds of large particles which are as shallow as possible, yet still meet the criteria of being coherent and plastic. Bachmann [1940] reported this type of behavior for beds deeper than about six particle diameters. Sprung [1987] found, however, that the assumption of no air drag on the bed in this model led to serious errors in calculated trajectories for even the largest particles (707 μm) he studied in 30-mm deep beds.

2.1.7.2 The Kroll Model

Kroll [1954, 1955] proposed a model for the vibrated bed assuming that the bed acted as a rigid, porous, plastic piston, but was affected by the drag force of the gas flowing through it. He also assumed that the air flowing through the bed could be treated as incompressible and was described by Darcy's Law for fluid flow through a porous medium:

$$u_o = \frac{-\kappa}{\mu} \frac{dP_z}{dz} \qquad [2.9]$$

where u_o is the superficial air velocity, P_z is the pressure of the air at depth z, μ is the viscosity of the air, and κ is the permeability of the medium. Carman [1937] amended the Kozeny equation to give an expression for κ:

$$\kappa = \frac{d_p^2 \, \varepsilon^3}{180(1-\varepsilon)^2} \qquad [2.10]$$

where d_p is the particle diameter and ε is the porosity of the bed.

Kroll's assumption of gas incompressibility means that the pressure drop through the bed must be linear, and his assumption of a rigid (no porosity change) piston implies that any gas flowing into the bed must accumulate in the gap beneath. Thus, the superficial gas velocity must equal the rate of gap growth (or diminution) so that

$$\frac{ds}{dt} = u_o = \frac{-\kappa}{\mu} \frac{P_L - P_o}{L} \qquad [2.11]$$

where P_L is the pressure at the bottom of the bed (or in the gap, when it exists), P_o is the pressure at the top (ambient pressure), and L is the bed depth.

The force balance for Kroll's model (which neglects friction) is

$$M_b \frac{d^2(s+a)}{dt^2} = A_b (P_L - P_o) - F_G + F_N \qquad [2.12]$$

in the notation of Figure 2.15. During the flight period, substitution of

$$\frac{d^2a}{dt^2} = -a_o \omega^2 \sin(\omega t) \qquad \text{and} \qquad F_G = M_b g$$

leads to

$$M_b \frac{d^2s}{dt^2} = A_b (P_L - P_o) - M_b g + M_b a_o \omega^2 \sin(\omega t) \qquad [2.13]$$

Since $M_b = \rho_b A_b L$, where ρ_b is the bulk density of the bed, Equation [2.13] becomes

$$\frac{d^2s}{dt^2} = \frac{(P_L - P_o)}{\rho_b L} - g + a_o \omega^2 \sin(\omega t) \qquad [2.14]$$

Differentiating Equation [2.11] and substituting into Equation [2.14] gives

$$\frac{\kappa}{\mu L} \frac{d}{dt} (P_L - P_o) + \frac{1}{\rho_b L} (P_L - P_o) = g - a_o \omega^2 \sin(\omega t) \qquad [2.15]$$

The instant of bed lift-off, t_s, can be calculated from the knowledge that

$$s = \frac{ds}{dt} = \frac{d^2s}{dt^2} = 0 \text{ at } t_s.$$

Equation [2.14] then becomes

$$\frac{P_L - P_o}{\rho_b L} - g + a_o\omega^2 \sin(\omega t_s) = 0 \qquad [2.16]$$

The assumption of gas incompressibility also implies that P_L is equal to P_o when the bed is in contact with the vessel, so that at t_s, $P_L - P_o = 0$. This makes Equation [2.16]

$$g = a_o\,\omega^2 \sin(\omega t_s) \qquad [2.17]$$

or, rearranging

$$t_s = \frac{1}{\omega} \sin^{-1}\left[\frac{1}{K}\right] \quad \text{or} \quad \theta_s = \sin^{-1}\left[\frac{1}{K}\right] \qquad [2.18]$$

which is the same result as in the single-particle model. Thomas [1988] examined the Kroll model and made it dimensionless by introducing the following variables:

$$\phi = \frac{(P_z - P_o)}{P_o} \; ; \; Z = \frac{z}{L} \; ; \; T = (\omega t)$$

Equation [2.15] may now be rewritten in dimensionless form as

$$\frac{P_o \kappa}{\mu L a_o \omega} \frac{d\phi_L}{dT} + \frac{P_o}{\rho_b L a_o \omega^2} \phi_L = \frac{1}{K} - \sin (T) \qquad [2.19]$$

Since Equation [2.15] (and thus Equation [2.19]) is valid only during the flight period of the cycle, it is convenient to shift the time axis so that T = 0 corresponds to the point of lift-off. Doing this, as well as introducing the following dimensionless groups

$$\Psi = \frac{P_o \kappa}{\mu L a_o \omega} \quad \text{and} \quad \Lambda = \frac{P_o}{\rho_b L a_o \omega^2}$$

leads to

$$\Psi \frac{d\phi_L}{dT} + \Lambda \phi_L = \frac{1}{K} - \sin (T + \theta_s). \qquad [2.20]$$

This is a first-order, ordinary differential equation subject to the initial condition

$$\phi_L = 0 \quad \text{at} \quad T = 0 \qquad [2.21]$$

which is merely a restatement that the assumption of gas incompressibility implies that the pressure throughout the bed is the same at the point of lift-off. The analytical solution to Equation [2.20] is

$$\phi_L = \frac{1}{\Lambda K} \left\{ 1 - \frac{R_h}{R_h^2 + 1} \left[\left[R_h \sqrt{K^2-1} + 1 \right] \sin T \right. \right. \qquad [2.22]$$

$$\left. \left. + \left[R_h - \sqrt{K^2-1} \right] \cos T + \frac{R_h \sqrt{K^2-1} + 1}{R_h} \exp \left[-R_h T \right] \right] \right\}$$

where $R_h = \frac{\Lambda}{\Psi}$

Equation [2.22] gives an expression for the pressure in the gap at any time during the flight period. During the period of contact between bed and vessel, the pressure beneath the bed is the same as at the top of the bed. The gap thickness may now be obtained from the dimensionless form of Equation [2.11] which is

$$\frac{dS}{dT} = -\Psi \phi_L \qquad [2.23]$$

where $S \left[= \frac{s}{a_o} \right]$ is the dimensionless gap thickness.

This equation may be solved using the initial condition

$$S = 0 \quad \text{at} \quad T = 0 \qquad [2.24]$$

Equation [2.23] is solved by integrating Equation [2.22] with respect to T and using Equation [2.24] to solve for the constant of integration. This leads to

$$S = -\frac{1}{R_h K}\left\{T - \frac{R_h}{R_h^2+1}\left[\left[R_h - \sqrt{K^2-1}\right]\sin T - \left[R_h\sqrt{K^2-1} + 1\right]\cos T - \frac{R_h\sqrt{K^2-1} + 1}{R_h^2}\exp\left[-R_h T\right]\right] - \frac{R_h\sqrt{K^2-1} + 1}{R_h}\right\} \qquad [2.25]$$

The Kroll incompressible-gas model, while still relatively simple, is a major improvement over the single-particle model. This model gives reasonable predictions for relatively shallow beds of fairly large particles, as demonstrated by Figure 2.16 from Thomas [1988]. As the particle size is decreased or the bed depth is increased, the assumption of gas incompressibility becomes worse and the predictions by the model are more inaccurate.

Yoshida and Kousaka [1966] also proposed a model which took air resistance on the bed into account. According to Gray and Rhodes [1972], this model was of the form

$$\frac{d^2(s + a)}{dt^2} = -C\frac{ds}{dt} - g \qquad [2.26]$$

where C is a "drag coefficient." According to Strumillo and Pakowski [1980], this drag coefficient was

$$C = \frac{180\ \mu}{(\phi_s\ d_p)^2\ \rho_s}\ \frac{(1 - \varepsilon)}{\varepsilon^3} \qquad [2.27]$$

where ϕ_s is a sphericity factor and ρ_s is the true solid density given by

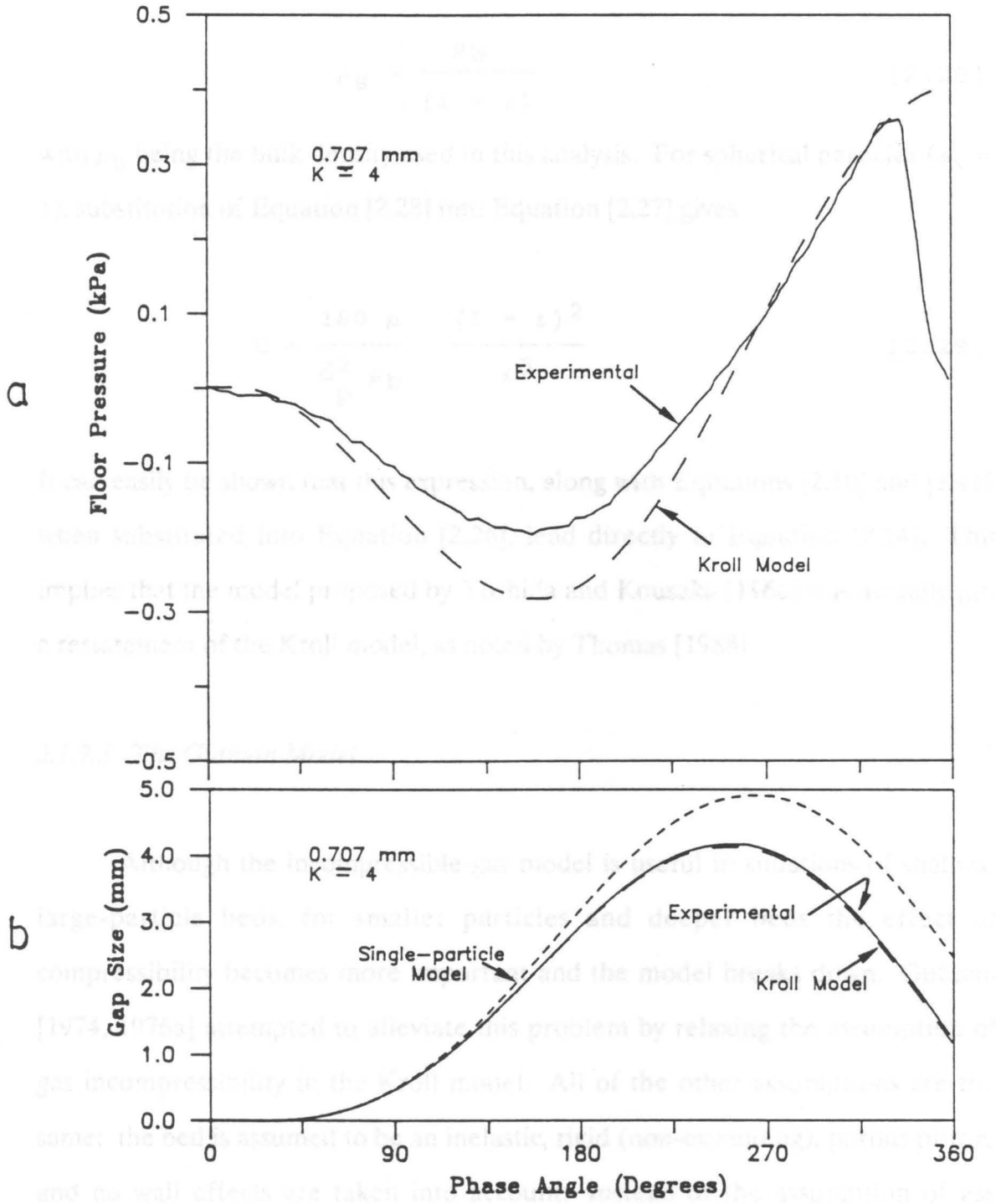

Figure 2.16. Comparison of Kroll model with experimental results: Floor pressure (a) and gap size (b) comparisons of the Kroll model with experimental values for 707-μm alumina particles vibrated at K = 4. Gap-size prediction for the single-particle model is also shown in (b). From Thomas [1988].

$$\rho_s = \frac{\rho_b}{(1 - \varepsilon)} \qquad [2.28]$$

with ρ_b being the bulk density used in this analysis. For spherical particles (ϕ_s = 1), substitution of Equation [2.28] into Equation [2.27] gives

$$C = \frac{180\ \mu}{d_p^2\ \rho_b} \quad \frac{(1 - \varepsilon)^2}{\varepsilon^3} \qquad [2.29]$$

It can easily be shown that this expression, along with Equations [2.10] and [2.11], when substituted into Equation [2.26], lead directly to Equation [2.14]. This implies that the model proposed by Yoshida and Kousaka [1966] was actually just a restatement of the Kroll model, as noted by Thomas [1988].

2.1.7.3 The Gutman Model

Although the incompressible-gas model is useful in situations of shallow, large-particle beds, for smaller particles and deeper beds the effect of compressibility becomes more important and the model breaks down. Gutman [1974, 1976a] attempted to alleviate this problem by relaxing the assumption of gas incompressibility in the Kroll model. All of the other assumptions are the same: the bed is assumed to be an inelastic, rigid (non-expanding), porous piston, and no wall effects are taken into account. Instead of the assumption of gas incompressibility, however, the Gutman model allows for isothermal compression of the gas.

Gutman [1974, 1976a] formulated the compressible-gas model so that the equation of motion (force balance) would be valid over the entire vibrational

cycle and solved the model semi-analytically. In practice, it is perhaps easier to split the cycle into a flight period and a period of contact with the base (similar to the approach presented for the formulation of the single-particle and Kroll models in the two previous sections). This approach has been taken by Thomas [1988] and Benge [1990], and is the method presented here. According to Bird *et al.* [1960], the one-dimensional equation of continuity, modified for a porous system, can be written as

$$\varepsilon \frac{\partial \rho}{\partial t} = \frac{-\partial}{\partial z} (\rho \ u_o) \qquad [2.30]$$

Substituting in Darcy's Law (Equation [2.9]) leads to

$$\frac{\mu\varepsilon}{\kappa} \frac{\partial \rho}{\partial t} = \frac{\partial}{\partial z} \left[\rho \frac{\partial P_z}{\partial z} \right] = \frac{\partial \rho}{\partial z} \frac{\partial P_z}{\partial z} + \rho \frac{\partial^2 P_z}{\partial z^2} \qquad [2.31]$$

For an isothermal, compressible gas

$$\rho = \rho_o \frac{P_z}{P_o} \qquad [2.32]$$

where ρ_o is the density at a reference pressure, P_o (taken here to be atmospheric).

Substituting this into Equation [2.31] gives

$$\frac{\mu\varepsilon}{\kappa} \frac{\partial P_z}{\partial t} = \left[\frac{\partial P_z}{\partial z} \right]^2 + P_z \frac{\partial^2 P_z}{\partial z^2}$$

or

$$\frac{\mu\varepsilon}{\kappa P_z}\frac{\partial P_z}{\partial t} = \frac{1}{P_z}\left[\frac{\partial P_z}{\partial z}\right]^2 + \frac{\partial^2 P_z}{\partial z^2} \qquad [2.33]$$

Assuming that the pressure variations are small in magnitude and vary about a mean (atmospheric) pressure, as Kroll [1954] found to be the case,

$$\frac{1}{P_o}\left[\frac{\partial P_z}{\partial z}\right]^2 << \frac{\partial^2 P_z}{dz^2}$$

and Equation [2.33] simplifies to

$$\frac{\partial P_z}{\partial t} = \frac{\kappa P_o}{\varepsilon\mu}\frac{\partial^2 P_z}{\partial z^2} \qquad [2.34]$$

which has the form of a diffusion equation in one dimension.

Using the same dimensionless variables from the previous section, this becomes

$$\frac{\partial \phi}{\partial T} = \Gamma\frac{\partial^2 \phi}{\partial Z^2} \qquad [2.35]$$

where Γ is a new dimensionless group proposed by Thomas [1988] so that

$$\Gamma = \frac{\kappa P_o}{\varepsilon\mu\omega L^2}$$

In dimensionless form, the initial condition is

$$\phi = 0 \text{ at } T = 0 \qquad [2.36]$$

Since the pressure at the top of the bed is always at P_o, the upper boundary condition is given by

$$\phi = 0 \quad \text{at} \quad Z = 0 \qquad [2.37]$$

The lower boundary condition, however, is more complicated due to the time-dependent nature of the pressure beneath the bed. The rate of accumulation of gas in the gap must equal the mass flow rate into the gap (across the lower boundary) for a bed of constant porosity. Combining this with Darcy's Law at the lower boundary yields

$$\frac{d(\rho s)}{dt} = \rho_o u_o = -\rho_o \frac{\kappa}{\mu} \frac{dP_z}{dz}\bigg|_{z=L} \qquad [2.38]$$

Assuming $S \dfrac{d\rho}{dt} << \rho \dfrac{ds}{dt}$ and $\rho \simeq \rho_o$ leads to

$$\frac{ds}{dt} = - \frac{\kappa}{\mu} \frac{dP_z}{dz}\bigg|_{z=L} \qquad [2.39]$$

In the dimensionless form (as defined in the previous section), this equation becomes

$$\frac{dS}{dT} = - \Psi \frac{d\phi}{dZ}\bigg|_{Z=1} \qquad [2.40]$$

The equation of motion for the flight period for this model is the same as that for the incompressible-gas model (Equation [2.14]), which, in dimensionless form is given, by

$$\frac{d^2S}{dT^2} = \Lambda\,\phi_L - \frac{1}{K} + \sin T \qquad [2.41]$$

Differentiating Equation [2.40] and substituting into this equation results in

$$\Lambda\,\phi_L - \frac{1}{K} + \sin T = -\Psi\,\frac{d}{dT}\left[\left.\frac{d\phi}{dZ}\right|_{Z=1}\right]$$

or

$$\phi_L = \frac{1}{\Lambda}\left[\frac{1}{K} - \sin T - \Psi\,\frac{d}{dT}\left[\left.\frac{d\phi}{dZ}\right|_{Z=1}\right]\right] \qquad [2.42]$$

which is the lower boundary condition during the period of flight. For the compressible-gas model, the pressure does not drop instantaneously to atmospheric as the bed collides with the vessel floor, but when the bed is in contact with the vessel the pressure gradient is zero (the base plate is impermeable). For the period of bed contact with the floor, then, the lower boundary condition is

$$\left.\frac{d\phi}{dZ}\right|_{Z=1} = 0 \qquad [2.43]$$

Gutman [1974, 1976a] solved this model by assuming that the pressure in the gap beneath the bed could be approximated by a Fourier series, and then solved the system iteratively for the Fourier coefficients. The problem has also

been solved numerically by Akiyama and Naito [1987], who used the method of orthogonal collocation. Akiyama and Kurimoto [1988] extended the numerical method to model situations of intense vibration in which the bed stays in flight longer than a vibrational cycle. This extended model has questionable physical significance, however, since beds undergoing such intense vibration tend to undergo porosity changes which violate the assumptions of the compressible-gas model.

For beds of large particles, the compressible-gas model gives only modest improvement over the incompressible model. As the particle size decreases, however, the compressible-gas model shows better agreement with experimental measurement. This is as expected, since the effect of gas compressibility is more important for smaller particles due to their higher resistance to air flow. Figure 2.17 and 2.18 show a comparison of both the Kroll and Gutman models with experimental measurements for large and small particle sizes, as reported by Gutman [1974]. Note that there is a large improvement in the latter part of the pressure curve in the Gutman model since the Kroll model predicts that the gauge pressure must fall to zero instantaneously upon contact. The Gutman model also predicts a larger gap width than the Kroll model, and, in the case of the large particles, overestimates the maximum gap width appreciably.

The compressible-gas model, while somewhat of an improvement over the Kroll model, still has its limitations. Since it is a one-dimensional model, it cannot predict the observed circulation patterns which have a horizontal component. The assumption of constant porosity also leads to error since the bed has been observed to expand and contract cyclically [Thomas, 1988]. An increase in voidage allows the bed to retain some gas that flows in, rather than having all of the gas which passes into the bed collect in the gap, as the model assumes. The

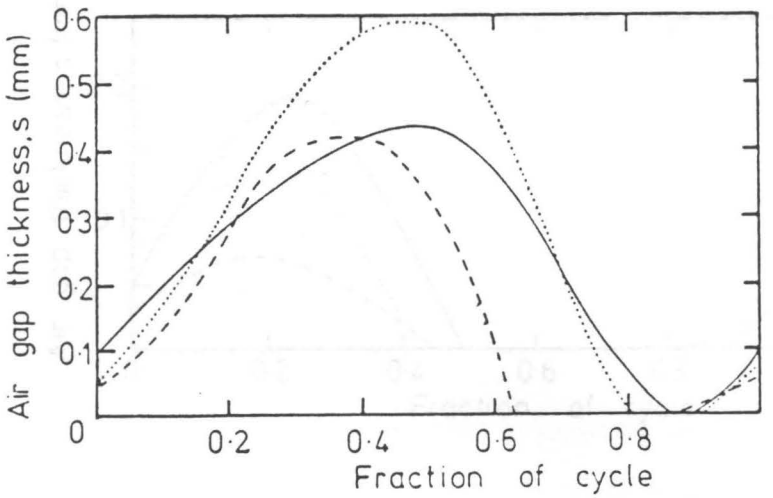

(a)

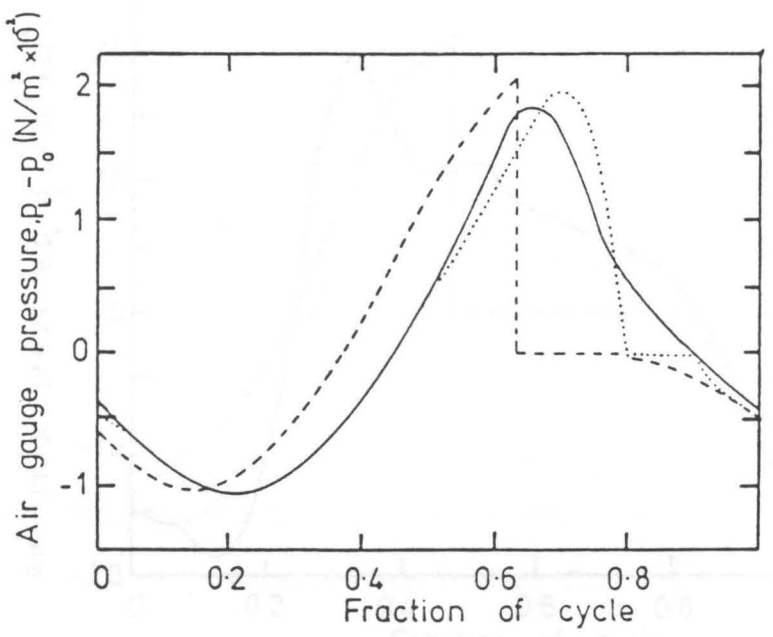

(b)

Figure 2.17. Comparison of Kroll and Gutman models with experiment for large particles: Air-gap thickness (a), and gauge pressure (b) for 710-850 μm glass beads vibrated at K = 2.8. Models based on 800-μm spherical particles. Solid line is experimental, dotted line is Gutman model, dashed line is Kroll model. Cycle starts at highest position of vibrated table (90° for a sine wave of displacement). From Gutman [1974].

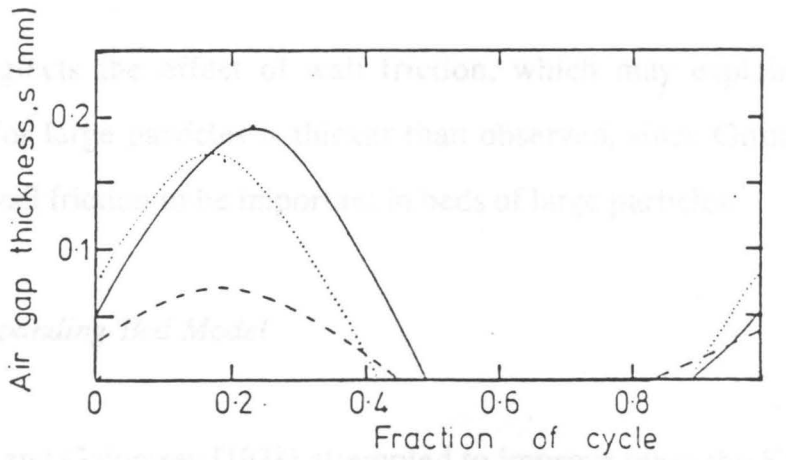

(a)

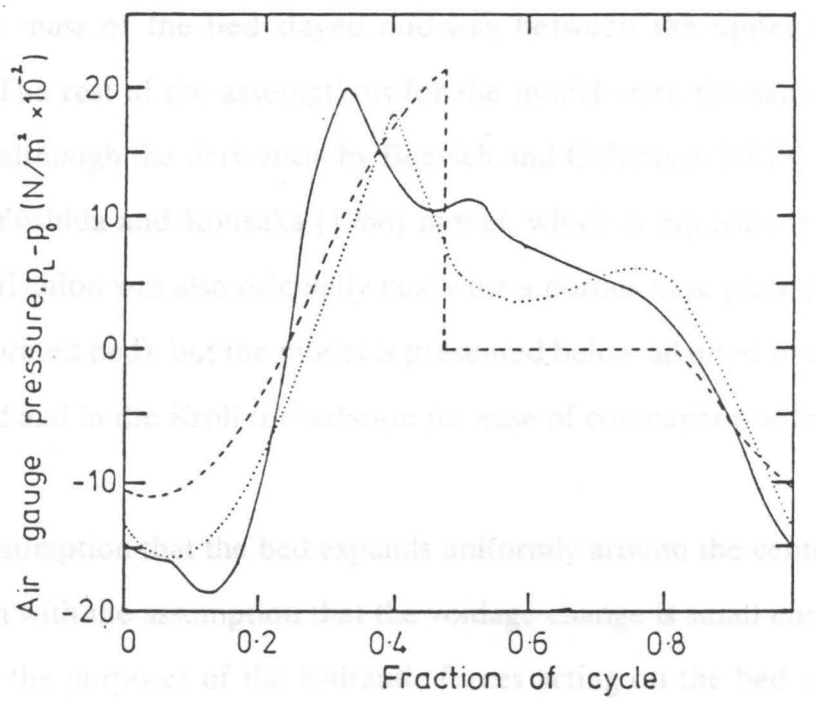

(b)

Figure 2.18. Comparison of Kroll and Gutman models with experiment for small particles: Air-gap thickness (a), and gauge pressure (b) for 89-124 μm glass beads vibrated at K = 2.8. Models based on 100-μm spherical particles. Solid line is experimental, dotted line is Gutman model, dashed line is Kroll model. Cycle starts at highest position of vibrated table (90° for a sine wave of displacement). From Gutman [1974].

model also neglects the effect of wall friction, which may explain why the predicted gap for large particles is thicker than observed, since Gutman [1974] himself found wall friction to be important in beds of large particles.

2.1.7.4 The Expanding-Bed Model

Buevich and Galontsev [1978] attempted to improve upon the Kroll model by relaxing the assumption of constant porosity. In their model, it was assumed that the extent of expansion at the top and bottom of the bed is the same, so that the center of mass of the bed stayed mid-way between the upper and lower boundaries. The rest of the assumptions for the model were the same as in the Kroll model, although the derivation by Buevich and Galontsev [1978] was in the form of the Yoshida and Kousaka [1966] model, which is equivalent (see page 50). Their derivation was also originally made for a porous base plate (as used in an aerated vibrated bed), but the model is presented below adapted to the case of a vibrated bed and in the Kroll formulation for ease of comparison with the other models.

The assumption that the bed expands uniformly around the center of mass in conjunction with the assumption that the voidage change is small enough to be negligible for the purposes of the hydraulic forces acting on the bed means that the equation of motion of the center of mass of the bed is identical to that used for the gap in the Kroll model. If z_c is the vertical position of the center of mass of the bed, the equation of motion during flight is given by

$$\frac{d^2 z_c}{dt^2} + \frac{\mu}{\rho_b \kappa} \frac{dz_c}{dt} = a_o \omega^2 \sin(\omega t) - g \qquad [2.44]$$

A comparison with Equation [2.14] (substituting in Equation [2.11] to eliminate the pressure gradient) shows that this equation is identical to the one in the Kroll model. If the time-dependent half-height of the bed is h (see Figure 2.19), then the equation of motion for the top surface, $z_c + h$, is given by

$$\frac{d^2(z_c+h)}{dt^2} + \frac{\sigma\mu}{\rho_b \kappa} \frac{d(z_c+h)}{dt} = a_o\omega^2 \sin(\omega t) - g \qquad [2.45]$$

where σ is the coefficient of drag reduction at the upper (or lower) boundary of the bed relative to the center of mass. Subtracting Equation [2.44] from [2.45] gives

$$\frac{d^2h}{dt^2} + \frac{\sigma\mu}{\rho_b \kappa} \frac{dh}{dt} = (1 - \sigma) \frac{\mu}{\rho_b \kappa} \frac{dz_c}{dt} \qquad [2.46]$$

The equation for the lower boundary, $z_c - h$, is derived identically and leads to

$$\frac{d^2h}{dt^2} + \frac{\sigma\mu}{\rho_b \kappa} \frac{dh}{dt} = - (1 - \sigma) \frac{\mu}{\rho_b \kappa} \frac{dz_c}{dt} \qquad [2.47]$$

A solution of the three equations of motion subject to the initial conditions

$$h = h_o, \; z_c = h_o, \; \frac{dh}{dt} = 0, \text{ and } \frac{dz_c}{dt} = 0 \quad \text{at } t = t_s \qquad [2.48]$$

leads to an expression for the expansion of the bed with time.

This model is not used frequently because of several problems. First, the coefficient of drag reduction at the boundary relative to the center of the bed, σ,

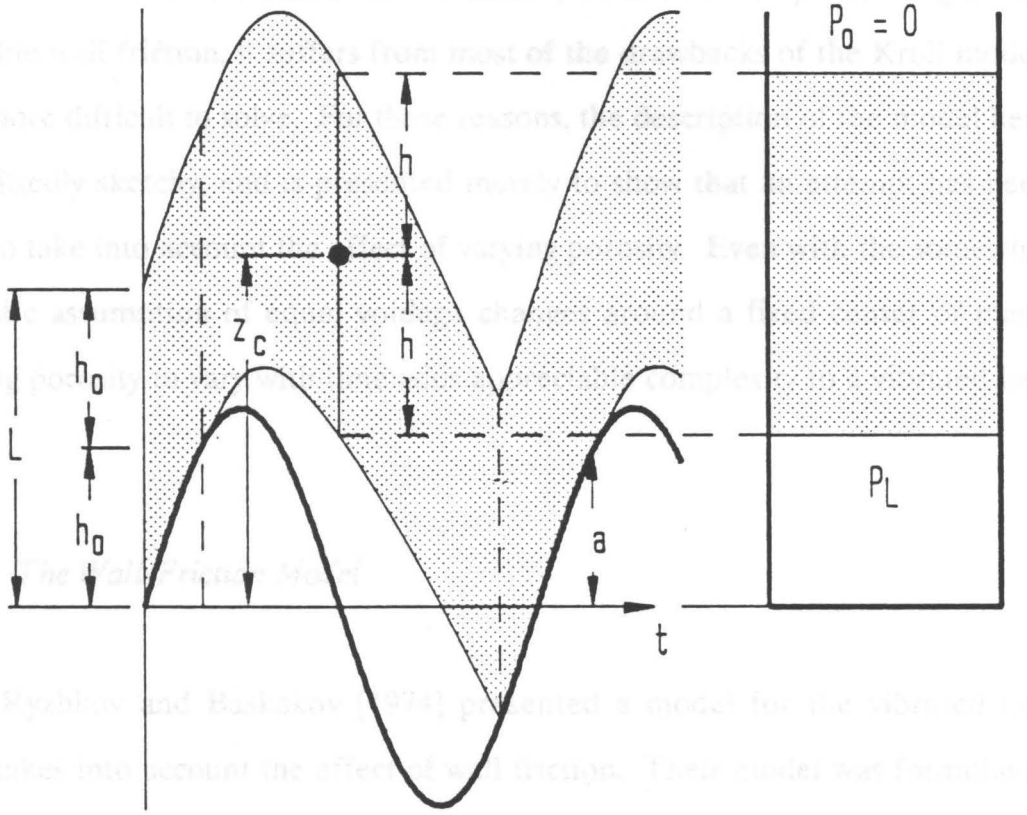

Figure 2.19. Schematic for the expanding-bed model: Representation of the bed behavior during the cycle. Notation: L = bed depth; h_o = half-bed height prior to lift-off; h = time-dependent half-bed height during flight; z_c = vertical coordinate of the bed center of gravity relative to the vessel floor; a = displacement of vessel; t = time; P_o = atmospheric pressure; P_L = pressure in the air gap. From Thomas [1988].

is not readily calculated, nor are values for it reported in the literature. Second, the assumption that the expansion occurs uniformly about the center of the bed is in opposition to observation (notably Kapustin *et al* [1980], who noted a sequential lift-off, with each layer lifting only after the one above had). Finally, since the model is still based on the assumptions of incompressible gas and negligible wall friction, it suffers from most of the drawbacks of the Kroll model, yet is more difficult to solve. For these reasons, the description of the model here is admittedly sketchy, and is presented merely to show that an attempt has been made to take into account the effect of varying porosity. Even with the somewhat simplistic assumption of equal voidage changes around a fixed center of mass, allowing porosity to vary with time adds appreciable complexity to a vibrated-bed model.

2.1.7.5 The Wall-Friction Model

Ryzhkov and Baskakov [1974] presented a model for the vibrated bed which takes into account the effect of wall friction. Their model was formulated for deep beds of large particles, and they assumed that porosity changes and hydraulic drag forces were negligible. Again, since the conditions of the formulation (deep beds of very large particles) are far removed from the primary conditions of interest in this study, the treatment of this model here will be brief. It is cited, however, since this model gives the most complete treatment of wall friction in the vibrated-bed modeling literature.

For a vibrated bed subjected only to the external forces of gravity and wall friction, the equation of motion of the flight period can be written as

$$\frac{d^2s}{dt^2} = a_o\omega^2 \sin(\omega t) - g - \text{sign}\left[\frac{ds}{dt}\right] f_T \qquad [2.49]$$

$$\text{where} \quad \text{sign}\left[\frac{ds}{dt}\right] = \begin{cases} +1 \text{ for } \frac{ds}{dt} > 0 \\ -1 \text{ for } \frac{ds}{dt} < 0 \end{cases}$$

and f_T is the wall-friction force per unit mass such that

$$f_T = \frac{4\alpha\,\lambda}{\rho_b\,L} \int_o^L \sigma_z\, dz \qquad [2.50]$$

Here, α and λ are the coefficients of dry friction and lateral pressure, respectively, and σ_z is the normal stress at a depth z averaged over the cross-section.

By assuming an exponential attenuation of the inertial acceleration of particles at a depth z, Ryzhkov and Baskakov [1974] defined an empirical coefficient of acceleration attenuation, η, with the equation

$$j = j_o \exp[-\eta(L - z)] \qquad [2.51]$$

with j being the inertial acceleration and j_o being the vibrational acceleration.

Following a rather laborious derivation of stresses within the material, a semi-empirical equation of motion was obtained:

$$\frac{d^2s}{dt^2} = a_o\omega^2 \sin(\omega t) - \begin{cases} g\psi_{(+)} & \text{for } \frac{ds}{dt} > 0 \\ g\psi_{(-)} & \text{for } \frac{ds}{dt} < 0 \end{cases} \qquad [2.52]$$

where $\psi_{(+)}$ and $\psi_{(-)}$ were defined as

$$\psi_{(+)} = \frac{D}{\chi L}\left[\exp\left(\frac{\chi L}{D}\right) - 1\right]$$

$$\left\{1 - \frac{\xi \exp(-\eta L)}{1 + \frac{D\eta}{\chi}}\left[1 - \frac{\chi\left[\exp(\eta L) - 1\right]}{D\eta\left[\exp\left(\frac{\chi L}{D}\right) - 1\right]}\right]\right\}$$

$$\psi_{(-)} = \frac{D}{\chi L}\left[1 - \exp\left(-\frac{\chi L}{D}\right)\right]$$

$$\left\{1 - \frac{\xi \exp(-\eta L)}{1 + \frac{D\eta}{\chi}}\left[1 - \frac{\chi\left[1 - \exp(-\eta L)\right]}{D\eta\left[1 - \exp\left(-\frac{\chi L}{D}\right)\right]}\right]\right\}$$

and $$\xi = \left[1 + \frac{\eta D}{\chi}\right]\left\{\frac{1 - \exp\left(\frac{-\chi L}{D}\right)}{1 - \exp\left[-L\left(\eta + \frac{\chi}{D}\right)\right]}\right\}$$

In these expressions, D is the diameter of the vessel and $\chi = 4\alpha\lambda$, which were defined previously. In practice, η and χ would have to be experimentally determined, η from Equation [2.51] and χ from the relation

$$\chi = \frac{\tau_z}{\sigma_z} \qquad [2.53]$$

where τ_z is the shear stress at the wall at depth z.

The authors noted that for shallow beds which meet the criteria

$$L << 1/\eta \quad \text{and} \quad L << D/\chi \ ,$$

the wall friction is slight, $\psi_{(+)}$ and $\psi_{(-)}$ approach unity, and Equation [2.52] reduces to the equation of motion of the single-particle model.

2.1.7.6 The Thomas Model

Thomas [1988] noted the vastly escalating degree of difficulty in removing the limitations of the Gutman model, and proposed that the best engineering approach to obtaining a better description of a vibrated bed would be a semi-empirical method. He was particularly interested in developing a model of more than one dimension. His work with pressure transducers mounted in three horizontal locations in the vessel base, as well as his observations of particle circulation of fine powders (which he observed to be radically altered in a vacuum) led him to believe that all the available models were inadequate for his conditions. Furthermore, he noted that the extension of a vibrated-bed model to two dimensions should allow for the calculation of horizontal particle velocities, which none of the one-dimensional models is capable of doing. He considered a two-dimensional version of the compressible-gas model. As shown in Figure 2.20 schematically, his model was formulated primarily around particle beds which bunker (since this is the case where horizontal effects are important), with

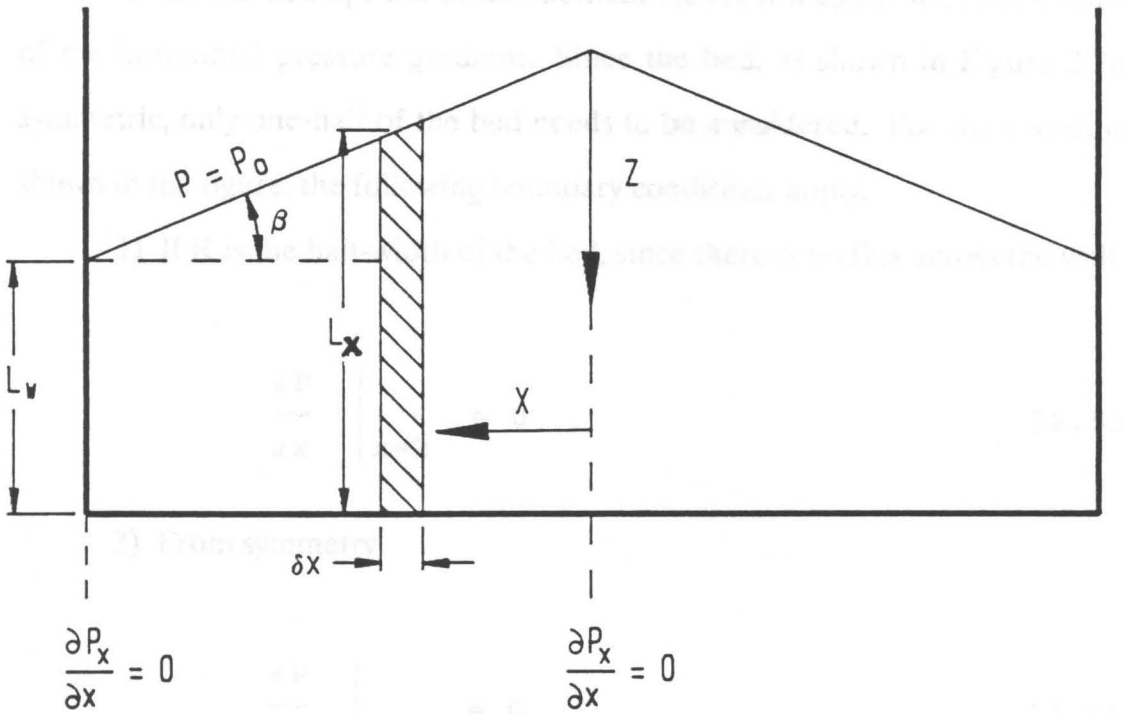

Figure 2.20. Schematic of bed for the Thomas model: Bed with center-high bunker. Notation: P = pressure; P_0 = atmospheric pressure; z = vertical coordinate; x = horizontal coordinate; L_w = bed height at the wall; β = angle of bunker from the horizontal; L_x = bed height at position x. From Thomas [1988].

symmetry around the horizontal mid-point. The governing equation for his model is merely a two-dimensional version of Equation [2.34]

$$\frac{\partial P}{\partial t} = \frac{\kappa P_o}{\varepsilon \mu} \left[\frac{\partial^2 P}{\partial x^2} + \frac{\partial^2 P}{\partial z^2} \right] \qquad [2.54]$$

Note that all the assumptions of the Gutman model still apply, with the exception of the horizontal pressure gradient. Since the bed, as shown in Figure 2.20, is symmetric, only one-half of the bed needs to be considered. For the coordinates shown in the figure, the following boundary conditions apply.

1) If R is the half-width of the bed, since there is no flux across the wall

$$\left. \frac{\partial P}{\partial x} \right|_{x=R} = 0 \qquad [2.55]$$

2) From symmetry

$$\left. \frac{\partial P}{\partial x} \right|_{x=0} = 0 \qquad [2.56]$$

3) Along the top surface

$$P = P_o \qquad [2.57]$$

As is the case with the one-dimensional compressible-gas model, the boundary condition beneath the bed is more complex. Note that for this case, the bed-depth, L, is not constant but is a function of horizontal position. It is given by

$$L(x) = L_w + (R - x) \tan \beta \qquad [2.58]$$

For the fourth boundary condition, Thomas [1988] suggested an empirical rather than analytic condition. He suggested measuring instantaneous floor pressures of at least three horizontal locations in one-half of the bed over a cycle. Since the instantaneous floor pressure at a point is periodic in nature, the pressure at each measured point can be expressed as a Fourier series of form

$$P(\theta) = \frac{c_o}{2} + \sum_{j=1}^{n} (c_j \cos j\theta + d_j \sin j\theta) \qquad [2.59]$$

where $\theta (= \omega t)$ is the dimensionless time (or phase angle).

The coefficients in this equation are evaluated using the pressure data. Once the pressure is known as a function of time at three points, the floor pressure can be interpolated as a function of horizontal position at any given instant using a cubic spline interpolating function. These two interpolating functions describe the pressure at any time in the cycle at the entire lower boundary, so Equation [2.54] can be solved.

The Thomas model, as proposed, makes an attempt to model a two-dimensional bed, and thus has an advantage over the other models for situations where horizontal effects are important. These effects are typically important in any vibrated bed which has a bunkered top surface, since bunkering is primarily due to horizontal pressure gradients [Sprung, 1987; Thomas, 1988]. This model is still limited by the assumption of constant porosity and the neglect of wall friction, however. An analysis by Thomas [1988] shows that any further relaxation of these assumptions is quite involved, either using an analytic or empirical method.

2.2 Heat Transfer in Vibrated Beds

Since the high heat-transfer rate of vibrofluidized beds is the major reason for their commercial interest, much of the reported work in the field of vibrofluidization is related to measurements of heat-transfer coefficients. This review treats only the work done on vibrated beds (without forced gas flow) with immersed contact heaters. Other sources [Strumillo and Pakowski, 1980; and Pakowski *et al.*, 1984, for example] have reviewed the entire range of vibrofluidized heat transfer including aerated vibrated beds and vibrated fluidized beds.

The rate of heat transfer in vibrated beds is intimately connected to the bed dynamics. Since there are so many factors which affect bed dynamics (as seen in the previous section), it is difficult to generalize on heat transfer in these beds. The reported values of heat-transfer coefficients vary from several times that of a stationary bed to twenty times greater or more. Values in excess of 1000 W/m^2-K have been reported by Zabrodskii *et al.* [1968] and Kal'tman and Tamarin [1969].

2.2.1 Effect of Varying Vibrating Parameters

All investigators agree that the heat-transfer coefficient increases dramatically as vibration imparts mobility to a static bed of particles. Whether the heat-transfer coefficient continues to increase, reaches a plateau, or goes through a maximum and begins to decrease as the vibrational intensity is further increased depends on other factors such as the particle size, heater geometry, and range of vibrational intensity studied. Several investigators have attempted to determine the effect of independently varying the two vibrational parameters,

amplitude and frequency. A comparison of different studies is difficult, however, since some studies correlate the results at constant vibrational velocity (frequency times amplitude) rather than at constant K-value.

Zabrodskii *et al.* [1968] found that the heat-transfer coefficient increased dramatically at a given "vibration rate" (they termed the product of frequency and amplitude the vibration rate). As shown in Figure 2.21, the value at which this increase occurred was dependent on the vibrational amplitude. From data presented in tabular form in the paper, one can conclude that they found higher heat-transfer coefficients for higher frequencies at the same K-value. The range of their vibrational parameters reported was 400-1600 rpm (6.7-26.7 Hz) and amplitudes of 1, 2, and 4 mm. Bukareva *et al.* [1969], who also plotted heat-transfer coefficients versus vibrational velocity, found the frequency of vibration to have a greater influence than the amplitude. Whether the influence had a positive or negative effect on the heat-transfer coefficient, however, depended on other factors. For example, for a bed of sand 280-355 μm in size and 70 mm deep, a vertical heater gave a higher heat-transfer coefficient at 60 Hz than 40 Hz (for constant $a_0 f$), while just the opposite was true of a horizontal bottom heater.

Kossenko *et al.* [1975], who worked in relatively deep (160 mm) beds with two rows of horizontal cylinders as heaters, also found the dependence of heat transfer on vibrational frequency not to be simple. In general, they found that the heat-transfer coefficient was highest at 40 Hz, intermediate at 20 Hz, and lowest at 60 Hz, all at constant K-value. For certain heater configurations, they found higher heat transfer at 20 Hz than 40 Hz at relatively low (K = 1.5-3) vibrational intensity, however. Furthermore, they found the shape of the heat-transfer coefficient versus K-value curves to be different for the different frequencies; the

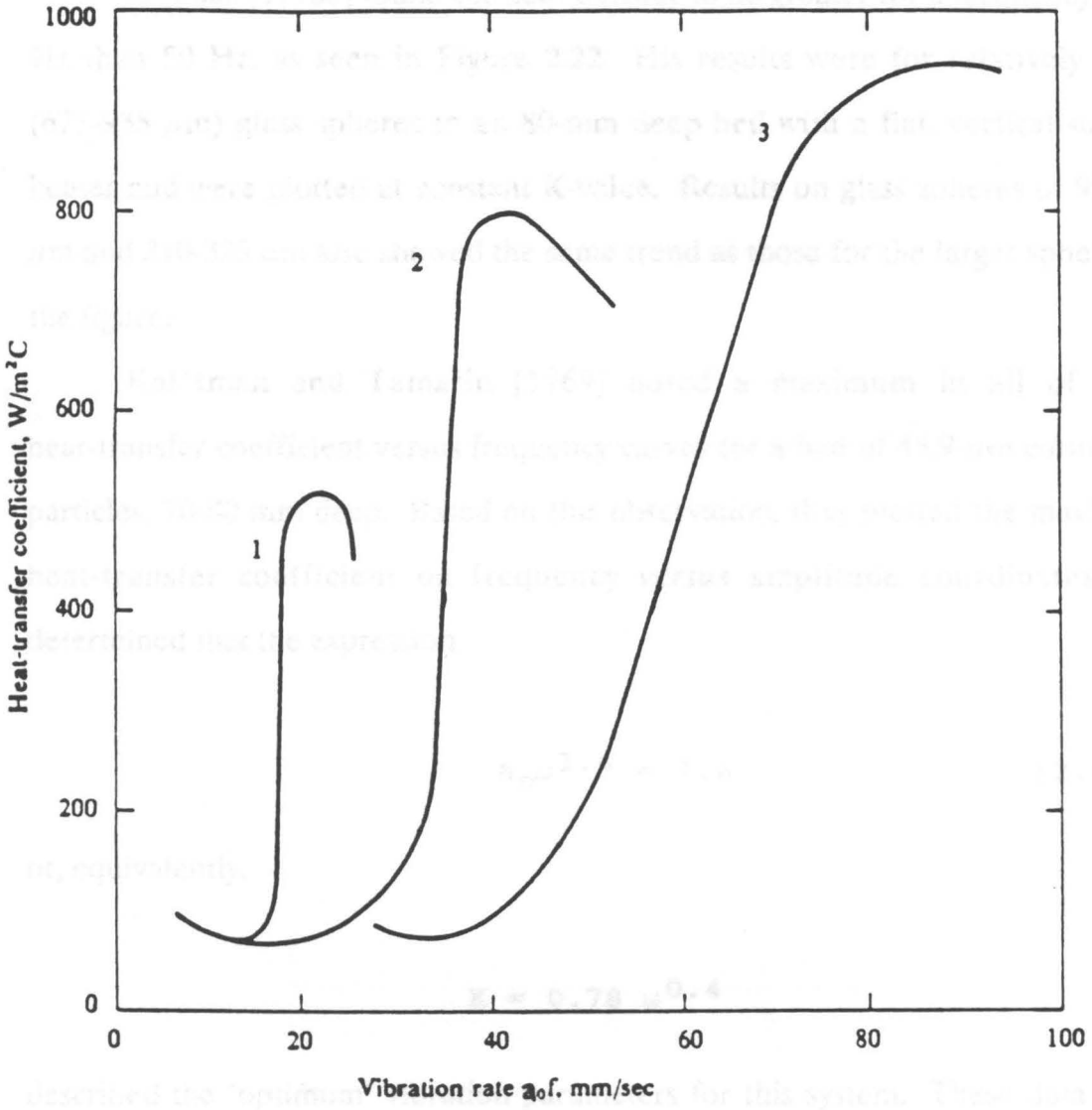

Figure 2.21. Effect of vibration rate on heat-transfer coefficients: Beds of 68-μm corundum particles. Curve (1) a_0 = 1 mm, (2) a_0 = 2 mm, (3) a_0 = 4 mm. From Zabrodskii *et al.* [1968].

curves at 20 and 40 Hz nearly always reached a maximum or plateau, while the curve at 60 Hz continued to increase throughout the range of K-values studied.

Gutman [1976b] found the heat transfer to be greater for a frequency of 20 Hz than 50 Hz, as seen in Figure 2.22. His results were for relatively large (675-935 μm) glass spheres in an 80-mm deep bed with a flat, vertical-surface heater and were plotted at constant K-value. Results on glass spheres of 90-135 μm and 210-325 μm also showed the same trend as those for the larger spheres in the figure.

Kal'tman and Tamarin [1969] noted a maximum in all of their heat-transfer coefficient versus frequency curves for a bed of 45.9-μm corundum particles, 70-80 mm deep. Based on this observation, they plotted the maximum heat-transfer coefficient on frequency *versus* amplitude coordinates and determined that the expression

$$a_o\omega^{1.6} = 7.6 \qquad [2.60]$$

or, equivalently,

$$K = 0.78\ \omega^{0.4}$$

described the "optimum" vibration parameters for this system. These data were taken in the range 13-36 Hz for frequency and 1.5-8 mm for amplitude with a spherical heater. Muchowski [1980] also made a plot of heat-transfer coefficient versus vibration frequency for 100-μm glass spheres. Using the vessel bottom as a heater, he found that the maximum heat-transfer occurred at a frequency of about 41 Hz for all vibrational amplitudes.

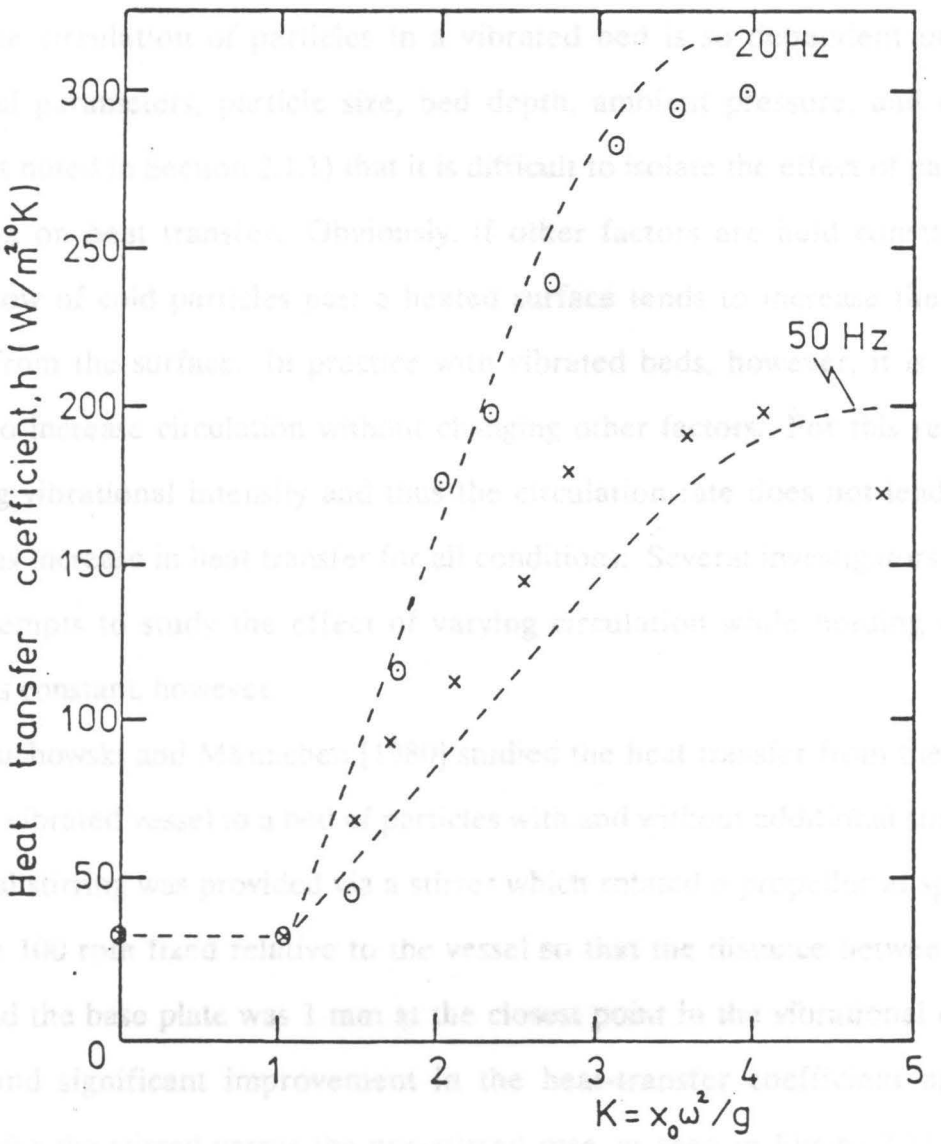

Figure 2.22. Comparison of heat-transfer coefficients at 20 Hz and 50 Hz: Heat transfer from a vertical, flat heater to an 80 mm layer of 675-935 μm glass spheres. From Gutman [1974].

2.2.2 *Effect of Particle Circulation*

The circulation of particles in a vibrated bed is so dependent on the vibrational parameters, particle size, bed depth, ambient pressure, and other factors (as noted in Section 2.1.1) that it is difficult to isolate the effect of particle circulation on heat transfer. Obviously, if other factors are held constant, a greater flow of cold particles past a heated surface tends to increase the heat transfer from the surface. In practice with vibrated beds, however, it is often difficult to increase circulation without changing other factors. For this reason, increasing vibrational intensity and thus the circulation rate does not lead to a continuous increase in heat transfer for all conditions. Several investigators have made attempts to study the effect of varying circulation while holding other conditions constant, however.

Muchowski and Männchen [1980] studied the heat transfer from the base plate of a vibrated vessel to a bed of particles with and without additional stirring. Additional stirring was provided via a stirrer which rotated a propellor at speeds from 0 to 100 rpm fixed relative to the vessel so that the distance between the blades and the base plate was 1 mm at the closest point in the vibrational cycle. They found significant improvement in the heat-transfer coefficient at low K-values for the stirred versus the non-stirred case, as seen in Figure 2.23. For both sizes of glass beads, the improvement decreased for all stirring rates as the vibrational intensity was increased, and in the case of the small particles, the heat-transfer coefficient was actually less for stirred than unstirred beds at high K. The authors explained this phenomenon by suggesting that at high K the propellor merely shifted the entire bed as a whole while the bed was in flight rather than causing mixing between particles.

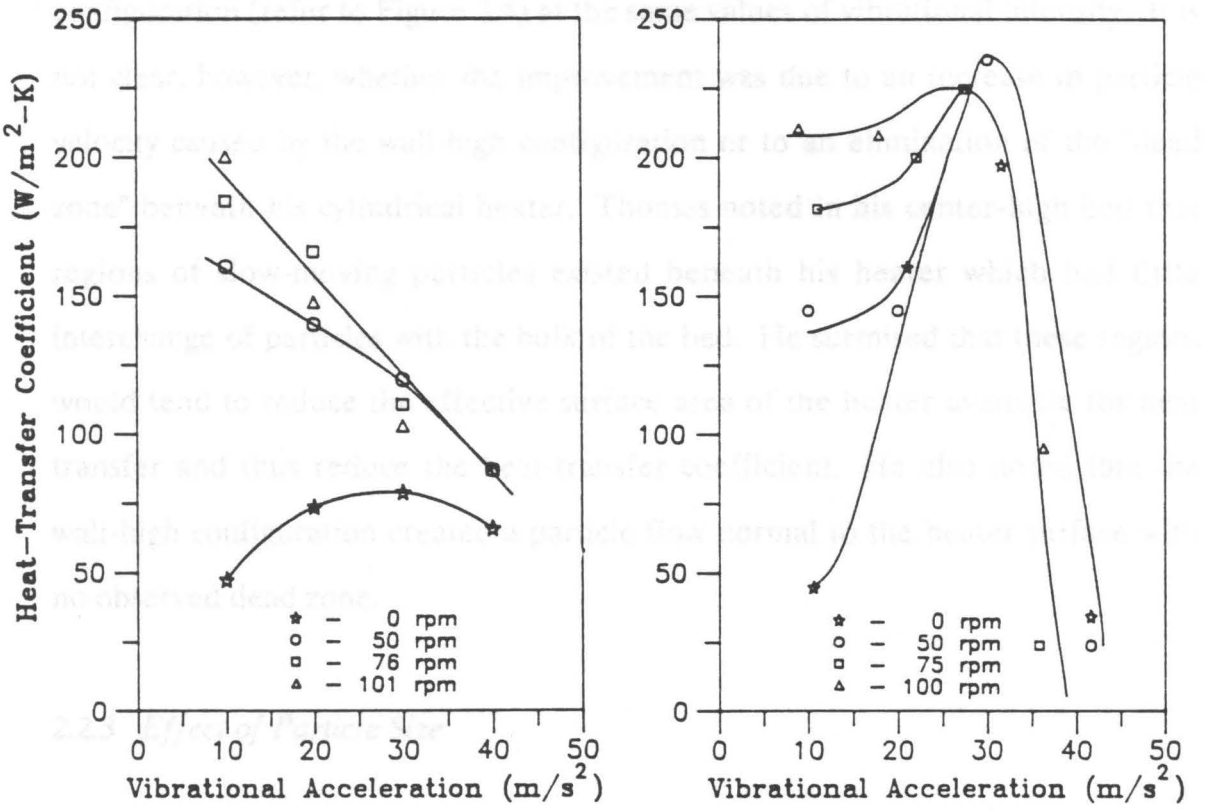

Figure 2.23. Effect of additional stirring on heat transfer in vibrated beds: Heat-transfer coefficients from the vessel floor to a vibrated bed with and without additional stirring for (a) 1 mm glass beads, and (b) 0.1 mm glass beads. From Muchowski and Mä nnchen [1980].

Thomas [1988] varied the circulation pattern while keeping other factors constant and measured the heat-transfer coefficient for 125-μm Master Beads at two different bunker configurations. He found the heat transfer to be significantly improved for the wall-high bunker configuration over the center-high configuration (refer to Figure 2.4) at the same values of vibrational intensity. It is not clear, however, whether the improvement was due to an increase in particle velocity caused by the wall-high configuration or to an elimination of the "dead zone" beneath his cylindrical heater. Thomas noted in his center-high bed that regions of slow-moving particles existed beneath his heater which had little interchange of particles with the bulk of the bed. He surmised that these regions would tend to reduce the effective surface area of the heater available for heat transfer and thus reduce the heat-transfer coefficient. He also noted that the wall-high configuration created a particle flow normal to the heater surface with no observed dead zone.

2.2.3 Effect of Particle Size

Although differences in operating conditions make generalizations difficult in vibrated-bed heat transfer, one of the most widely investigated and well-documented trends is the effect of particle size. Most investigators who have studied heat transfer in vibrated beds have varied particle size. Figure 2.24 shows a plot of measured heat-transfer coefficient *versus* particle size for various investigators at widely varying conditions. Table 2.2 gives a synopsis of the conditions under which the data were obtained. Clearly the trend is toward higher heat-transfer coefficients at smaller particle sizes. Individual investigations typically show the same trend when all conditions other than

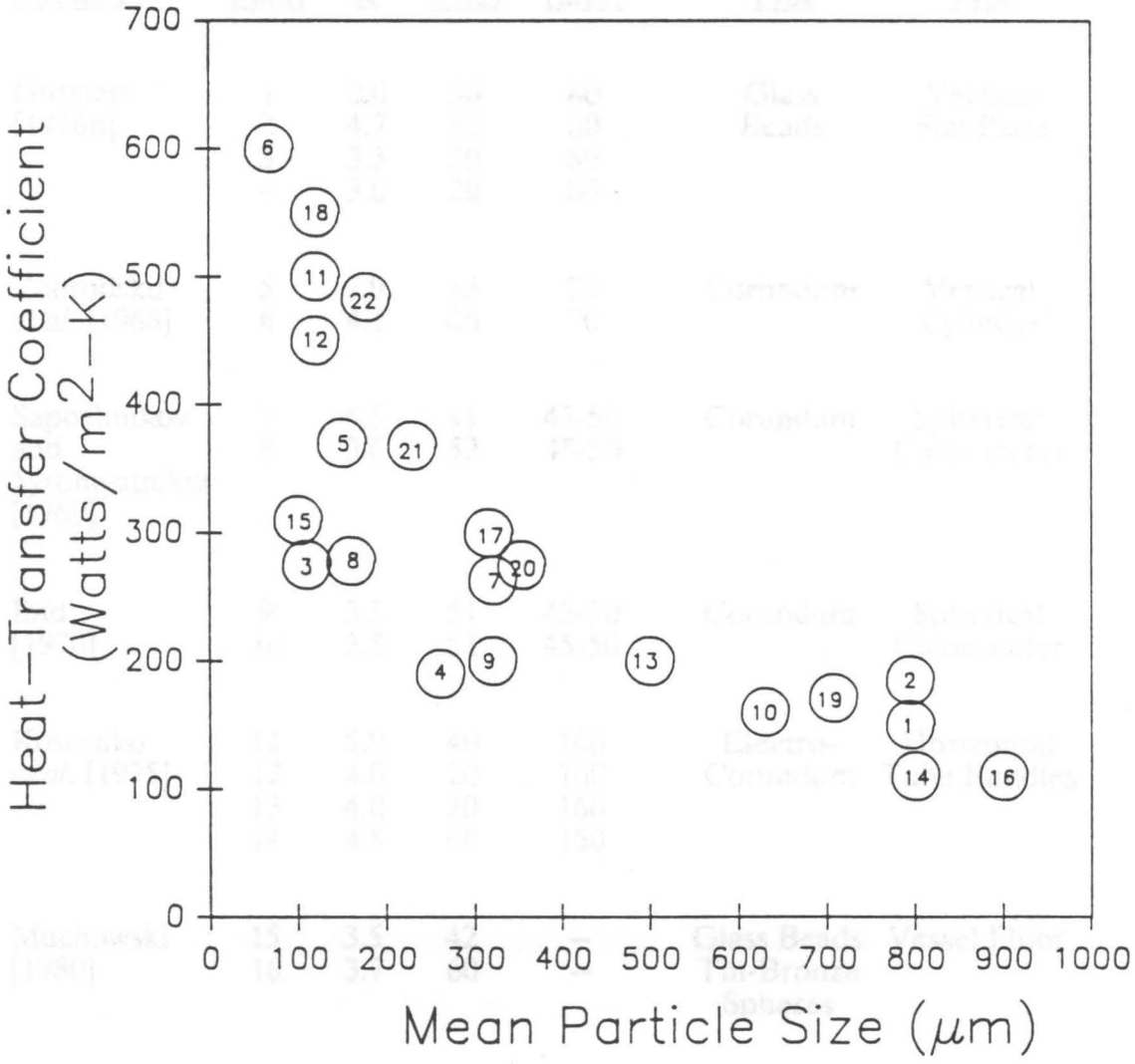

Figure 2.24. Heat-transfer coefficient versus particle size: Effect of particle size on heat-transfer coefficient from selected previous studies by different investigators under widely varying conditions. See Table 2.2 (next page) for a synopsis of conditions for the different data points.

Table 2.2 Synopsis of conditions used to measure heat-transfer coefficients reported in Figure 2.24.

Authors	Data Point	K	f(Hz)	Bed Depth (mm)	Particle Type	Heater Type
Gutman [1976b]	1	2.0	20	80	Glass Beads	Vertical Flat Plate
	2	4.7	50	80		
	3	3.3	20	80		
	4	3.0	20	80		
Zabrodskii *et al.* [1968]	5	2.9	13	70	Corundum	Vertical Cylinder
	6	4.1	16	70		
Sapozhnikov and Syromyatnikov [1969]	7	4.5	41	45-50	Corundum	Spherical Calorimeter
	8	3.6	52	45-50		
Ibid. [1970]	9	3.5	51	45-50	Corundum	Spherical Calorimeter
	10	3.5	51	45-50		
Kossenko *et al.* [1975]	11	5.0	40	160	Electro-Corundum	Horizontal Tube Bundles
	12	4.0	20	160		
	13	4.0	20	160		
	14	4.5	60	160		
Muchowski [1980]	15	3.5	42	--	Glass Beads	Vessel Floor
	16	3.7	60	--	Tin-Bronze Spheres	
Bukareva *et al.* [1969]	17	2.1	40	70	Quartz Sand	Vertical Heater
Ryzhkov *et al.* [1976]	18	4.4	20	150	Alumina	Vertical Heater
Thomas [1988]	19	4	25	30	Alumina	Horizontal Cylinder
	20	4	25	30		
	21	4	25	30		
	22	6	25	30		

particle size are held constant, although some indicate a maximum in heat transfer at small sizes, after which further reduction in particle size leads to a decrease in heat transfer.

Zabrodskii *et al.* [1968] noted a maximum in the heat-transfer coefficient at about 24 μm, below which the heat-transfer coefficient declined. In their study, they worked with corundum in narrow fractions with a mean size of 6, 10, 20, 24, 68, and 150 μm and with sand of 389 μm. They obtained remarkably high heat-transfer coefficients with some values in excess of 1000 W/m^2-K, as noted earlier. Their data were obtained using a vertical, cylindrical heater and a bed depth of 70 mm. Interestingly, they also measured heat-transfer coefficients in gas-fluidized beds and found the maximum obtainable coefficient to be greater in the vibrated bed compared to that obtainable in the gas-fluidized bed for all particle sizes.

Kossenko *et al.* [1975] noted a continuous increase in heat transfer as the particle diameter was decreased from 800 to 120 μm at K-values from 1.5 to 6. They also used corundum particles, but their heaters consisted of a single row of horizontal tubes immersed in a bed of 120-160 mm in depth. Muchowski [1980] also noted an increase in heat transfer with decreasing particle size for glass spheres of 1000, 500, and 100 μm. In his system, the vessel floor served as a heater, and K-value ranged from 0 to 5. Ryzhkov *et al.* [1976] further noted a continuously increasing heat-transfer coefficient as the size of alumina particles was decreased from 2000 to 60 μm. They worked with spherical, flat horizontal, and flat vertical heaters in deep beds of 150-500 mm.

Thomas [1988], on the other hand, found that heat transfer increased as particle size decreased from 707 to 177 μm, but that the heat transfer decreased again for smaller particles. He worked with shallow (30 mm) beds of Master

Beads using a horizontal, cylindrical heater. His data represented a constant frequency of 25 Hz and K-values up to 6.

The reason for the increase in heat-transfer coefficient with decreasing particle size has been given as an increase in circulation for the smaller size, a decrease in gas sub-layer between the heater and particle, and a decrease in the air gap which surrounds horizontal heaters during a portion of the cycle. The influence of the air gap around the heater on the heat-transfer coefficient is more closely investigated in the following sub-section.

2.2.4 *Effect of Heater Geometry*

Different heater geometries have been employed in the study of heat transfer from a surface to a vibrated bed of particles. Spherical calorimeters, vertical and horizontal cylinders, horizontal flat heaters (often the floor of the vibrated vessel), and vertical flat heaters are all reported in the literature. Several investigators have directly compared the effect of different heater geometries on heat transfer, and other investigators have made observations about certain geometries which explain observed trends in heat transfer.

Ryzhkov *et al.* [1976] conducted heat-transfer experiments with a spherical calorimeter and a flat heater which they oriented both vertically and horizontally. They found that the values of the heat-transfer coefficients for the sphere and the vertical surface were nearly the same, while those for the horizontal surface were somewhat lower. They explained these results by arguing that the particle velocity was greater across vertical and inclined surfaces than across horizontal ones. These conclusions were supported by Sapozhnikov *et al.* [1976], who made observations on the local heat-transfer coefficients on a horizontal, cylindrical

surface. Their data indicated that the heat transfer was greatest at the lateral surfaces and lower on the top and bottom. They, too, explained these results in terms of increased circulation at the lateral surfaces.

Bukareva *et al.* [1969] compared heat transfer from horizontal and vertical flat heaters and got results similar to Ryzhkov *et al.* [1976], but had a different explanation. As seen in Figure 2.25, heat-transfer coefficients for the vertical heater were greater than those observed for the horizontal heater. They explained the reduction in heat transfer from the horizontal surface not in terms of a reduction in particle velocity, however, but in terms of an air gap which formed during a portion of the cycle (see Section 2.1.4). The air in this gap acted as an additional resistance to heat transfer and thus caused the observed reduction in the heat-transfer coefficient. Other investigators have observed air-gap formation around horizontal surfaces. Pakowski and Mujumdar [1983] and Malhatra and Mujumdar [1985, 1987] have performed a series of experiments to measure the air gaps formed around horizontal cylinders to include in a model of heat transfer from an immersed tube to a vibrated bed. Sprung [1987] and Thomas *et al.* [1987] have also noted the presence of air gaps around horizontal cylinders and the importance of these gaps to heat transfer.

2.2.5 Effect of Ambient Gas Pressure

Sapozhnikov and Syromyatnikov [1969, 1970] investigated the effect of reducing the pressure of the air above the bed on the heat-transfer coefficient. Using corundum of 160, 320, and 630 μm in size at a depth of 45-50 mm, they studied the heat transfer from a spherical probe at pressures from atmospheric down to 30 Pa. Their results showed that the heat transfer decreased with

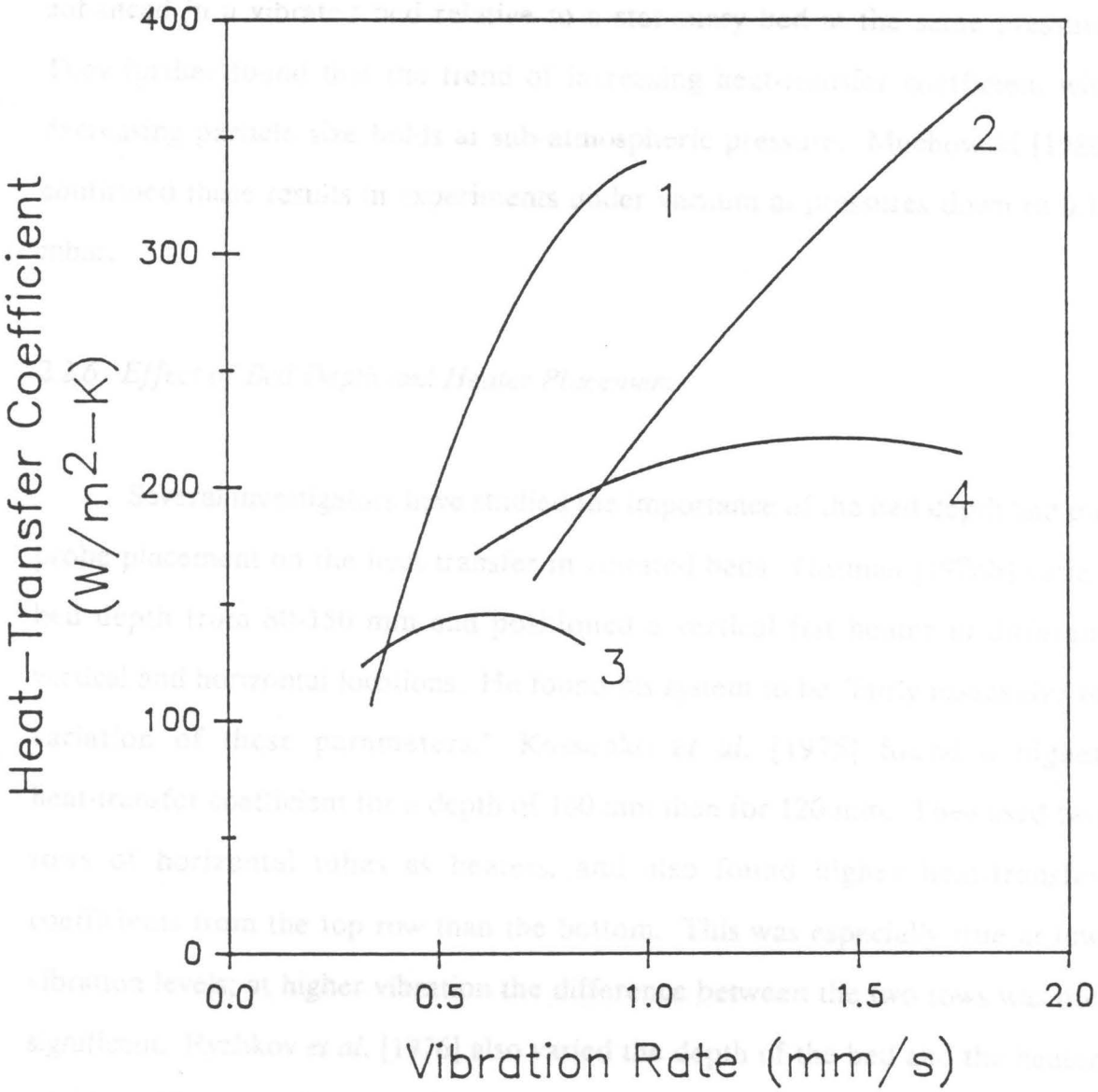

Figure 2.25. Vertical versus horizontal-surface heat transfer: Heat-transfer coefficients for 70-mm deep beds of 280-355 μm quartz sand. Curve (1) is for a vertical heater with vibrations at 60 Hz, (2) vertical and 40 Hz, (3) horizontal floor heater with vibrations at 60 Hz, (4) horizontal and 40 Hz. Adapted from Bukareva *et al.* [1969].

decreasing pressure, but they also noted that the heat-transfer rate was greatly enhanced in a vibrated bed relative to a stationary bed at the same pressure. They further found that the trend of increasing heat-transfer coefficient with decreasing particle size holds at sub-atmospheric pressure. Muchowski [1980] confirmed these results in experiments under vacuum at pressures down to 0.13 mbar.

2.2.6 Effect of Bed Depth and Heater Placement

Several investigators have studied the importance of the bed depth and the probe placement on the heat transfer in vibrated beds. Gutman [1976b] varied bed depth from 80-150 mm and positioned a vertical flat heater in different vertical and horizontal locations. He found his system to be "fairly insensitive to variation of these parameters." Kossenko *et al.* [1975] found a higher heat-transfer coefficient for a depth of 160 mm than for 120 mm. They used two rows of horizontal tubes as heaters, and also found higher heat-transfer coefficients from the top row than the bottom. This was especially true at low vibration levels; at higher vibration the difference between the two rows was not significant. Ryzhkov *et al.* [1976] also varied the depth of the bed and the heater position. They noted no significant decrease in heat-transfer coefficient in beds as deep as 500 mm in comparison with shallow beds. For very low K-values (1.2-1.4), they found that the bed was mobile only near the top for the deep beds. In this range, they found the heat-transfer to be much better at the top than near the bottom where the particles were essentially not moving. As vibrational intensity was increased, however, they found the values at the bottom approached those at the top of the bed.

2.2.7 *Proposed Heat-Transfer Mechanisms*

Several different controlling mechanisms have been advanced to explain observed trends in heat transfer in vibrated beds. One of the most common is based on the "packet" model, originally proposed by Mickley and Fairbanks [1955] for heat transfer between gas-fluidized beds and surfaces. In this model, the bed is represented as small, homogeneous groups of particles (packets) which move through the bed as individual units. The heat-transfer controlling mechanism is the contact time of the packets with the heater surface. The model predicts that a decreased contact time brought about by increased particle velocity increases the heat-transfer coefficient.

Kal'tman and Tamarin [1969] adapted this model for use in vibrated beds. They observed large-scale, slow circulation loops in the bulk of the bed as well as small-scale, fast loops in the vicinity of the immersed heater. The characteristic dimension of these small-scale loops was less than that for the heater, which led them to define an effective contact time based on the characteristic length and the average particle velocity of the small loop. Using this approach, they were able to correlate their data in terms of dimensionless numbers.

Gutman [1976b] argued against packet-type models for vibrated beds, however. Unlike Kal'tman and Tamarin [1969], the only circulation he observed was a slow movement of particles down the vessel walls. Based on the circulation velocities he observed, the contact time of the particles was much too long to produce the high heat-transfer rates he had measured when used in a packet model. He further reasoned that postulating a random motion at the frequency of vibration would lead to heat-transfer coefficients that were much too high. Therefore, he proposed a totally different mechanism. In his model, the main

resistance to heat transfer was in the conduction across the gas sub-layer between the nearest particles and the heater. (This gas sub-layer is not to be confused with the periodic air gap discussed in previous sections. The sub-layer is merely a consequence of spherical packing against a flat surface.) The large enhancement of heat transfer in vibrated versus static beds was therefore proposed to be due to the "scouring" of this thin gas film by particles as they moved back and forth across his vertical, flat heater due to vibration. He was able to fit his data very well using this model, but that was in large part due to an experimental fit of the parameters in the model. According to the scoured-film model, the particle circulation does not affect the heat transfer.

Sprung [1987] argued that the heat-transfer mechanism must be a two-step process involving both the gas layer and the transfer of the heat to the rest of the bed. In support of his argument for a two-step process he noted the effect of gas pressure on heat transfer [Sapozhnikov and Syromyatnikov, 1969, 1970; Muchowski, 1980], as well as the effect of solid circulation. He, therefore, modified another model which was originally proposed for gas-fluidized beds, the one-layer model of Zabrodsky [1966]. In this model, heat is conducted across the gas film to the closest layer of particles (heat transfer to particles further away is neglected, hence the name) which then leave the surface layer, carrying the acquired heat to the rest of the bed. Thus, in this model the effect of the gas sub-layer thickness as well as the circulation rate (which figures into the amount of time a particle spends in the closest layer, on the average), contribute to the heat transfer. Sprung [1987] modified the model to include the effect of air gaps which he had observed around his horizontal, cylindrical heater. This effect was incorporated by adding a constant to the sub-layer thickness to account for the extra gas layer.

2.3 Summary of Reviewed Literature

The preceding sections present a review of the current literature on vibrated-bed dynamics, modeling, and heat transfer. In light of the number of studies reviewed, a brief summary is included to clarify the major findings.

In the area of observed particle dynamics, it is well established that particles become mobile and circulate when vibrated above a threshold vibrational intensity. The circulation patterns vary, however, depending upon the particle size and vibrational conditions. Some researchers believe the particle motion to be driven primarily by wall friction, others state that pressure gradients and gas flows cause circulation. There is very little agreement on the average pressure beneath the bed, however. For sufficiently high vibrational intensities, a cyclic air gap forms between the bed and vessel base. The appearance and disappearance of this gap has been monitored in a variety of ways with varying degrees of success. The porosity of the bed throughout the vibrational cycle has been studied several times, but it is most often taken to be constant.

The models of vibrated-bed dynamics span a broad spectrum of complexity, but most are limited by simplifying assumptions. The simplest model, which assumes the bed to behave as a single particle, is insufficient for nearly all situations. The Kroll incompressible-gas model is perhaps the most widely used and represents a compromise between simplicity and applicability. It is usually adequate for relatively large particles in shallow beds. Gutman's compressible-gas model adds a fair amount of complexity to the solution, but gives improved results for smaller particles where compressibility is important. All of these models are hampered by the assumption of a fixed-porosity (non-expanding) bed. The expanding-bed model removes this restriction, but

only in an artificially simplistic way. It relies on several quantities which are not readily measured or calculated, and also suffers from the assumption of gas incompressibility. The wall-friction model assumes incompressibility as well as constant porosity and is probably adequate only for deep beds of very large particles. Finally, the Thomas semi-empirical model eliminates many of the drawbacks of the other models, including introducing two-dimensionality to account for observed horizontal motion, but is sufficiently complicated that it has not been solved.

Since the high heat transfer characteristic of vibrated beds is perhaps the main reason for interest, heat-transfer coefficients have been widely measured. The effect of increasing vibrational intensity is generally conceded to enhance the heat-transfer rate, although some researchers report a maximum after which further increase is detrimental. There is no consensus on which vibrational parameter, frequency or amplitude, is more important, however. Enhanced particle mixing increases heat transfer. In general, smaller particles result in higher heat-transfer coefficients, although very small particles (below 100 μm) do not follow this trend. Vertical heater surfaces are usually reported to have higher heat-transfer coefficients than horizontal ones, although the reasons given vary. The heat-transfer models for a vibrated bed are also greatly different. Packet-type models, similar to those employed for gas-fluidized beds, have been proposed. These models have the contact time of the packet with the heater as the controlling step. In the scoured-film model, the conduction across the gas sub-layer is the controlling step. Increased vibration causes an increase in "scouring" of this film by the particles which leads to a thinner film and increased heat transfer. Finally, the one-layer model has a two-step mechanism in which heat must be conducted across a gas film to the closest layer of particles. This

model predicts dependence of heat transfer on both the particle size, which determines the gas film thickness, and the circulation rate, which determines the amount of time a particle spends in the closest layer.

2.4 Scope of This Study

The foregoing literature review indicates several areas in vibrated-bed studies which are inadequately explored. As noted in the review, often the results of different investigations are in direct conflict or are ambiguous. This study, then, has been undertaken to clarify certain areas and to advance the current understanding of vibrated-bed dynamics and heat transfer.

In the area of bed dynamics, better equipment and techniques for measuring important cyclic phenomena such as lift-off and collision are needed. These phenomena have previously been studied, but often only for very large particles or with crude techniques. The nature of the lift-off is not well understood, for example. Thomas [1988] has observed a compaction of the bed upon collision and hypothesizes the existence of an expansion upon lift-off, but has not detected it. The collision point, while more easily detected, is also not well understood. The data on the duration of collision as well as the nature of the compaction wave cover only a narrow range of parameters. An investigation of these phenomena leading to a better understanding and explanation of observations is proposed.

The area of particle circulation has also not been fully explored. Many explanations of observed trends are found in the literature, but often they are in conflict or apply only to a narrow range of conditions. Since the circulation of the particles has such an effect on the heat transfer in the bed, a better understanding

of the factors which influence the velocity and direction of particle movement is vital. Therefore, a more complete explanation of particle circulation and the factors which affect it must be made based on experimental measurements and direct observations via high-speed movies.

As previously noted, heat transfer in vibrated beds is dependent on so many factors, many of which are interrelated, that generalizations based on comparisons between different studies is often not possible. With this in mind, a study is proposed which varies only one critical parameter, the heater geometry, from a thorough study conducted by Thomas [1988]. Thomas used a tubular heating surface; the present work uses a vertical surface. By keeping all other factors the same, a direct comparison between the two most important geometries for heat-transfer equipment design can be made. This comparison must extend over a range of different particle sizes and vibrational intensities. The trends in the heat-transfer coefficient can then be used to evaluate the different models proposed for vibrated-bed heat transfer and to explain the mechanism of heat transfer between a heated surface and a vibrated particulate bed.

Chapter 3 Equipment and Instrumentation

Chapter 3 describes the equipment and instrumentation used in this study. The three sections of the chapter provide descriptions of equipment used to generate the vibrations and its support structure, the vessels used to contain the particle beds in the experiments, and the instrumentation necessary to carry out the experiments.

3.1 Vibration System

The vibration system used is the one described in detail by Thomas [1988]. Its main components consist of a WAVETEK function generator which generates the sinusoidal waveform, a CROWN DC-300 power amplifier which amplifies the sine wave, and a Vibration Test Systems VG-100 electromagnetic vibrator.

As shown in Figure 3.1, vibrations are transmitted to a circular titanium plate via a drive shaft of 1/16-inch steel welding rod. Leaf springs suspend the titanium plate. From four to eight springs are used (depending on the weight of the bed under study) which are attached to a large outer support structure by adjustable mounting brackets. This special bracket can be seen in Figure 3.2. By correctly adjusting the positions of these mounting brackets and the tensions on the leaf springs, one can ensure that the titanium plate (and any vessel mounted on it) moves in a strictly vertical direction.

The power required to vibrate a given mass-spring system is greatly reduced if the system can be operated at its natural resonance frequency. This natural resonance frequency is

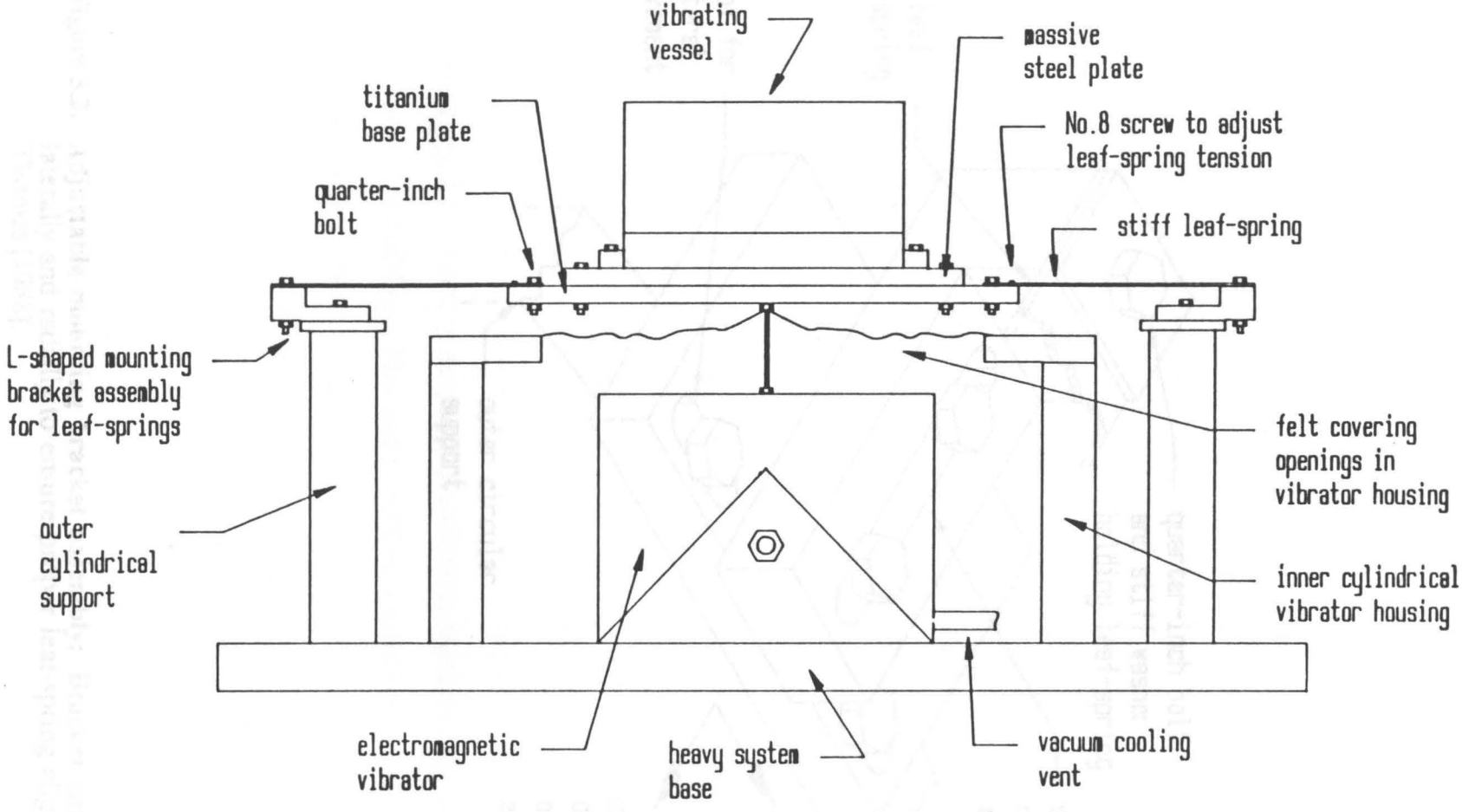

Figure 3.1. Schematic of vibration system: Drawing showing the details of the vibration system with the three-dimensional vessel in place. From Thomas [1988].

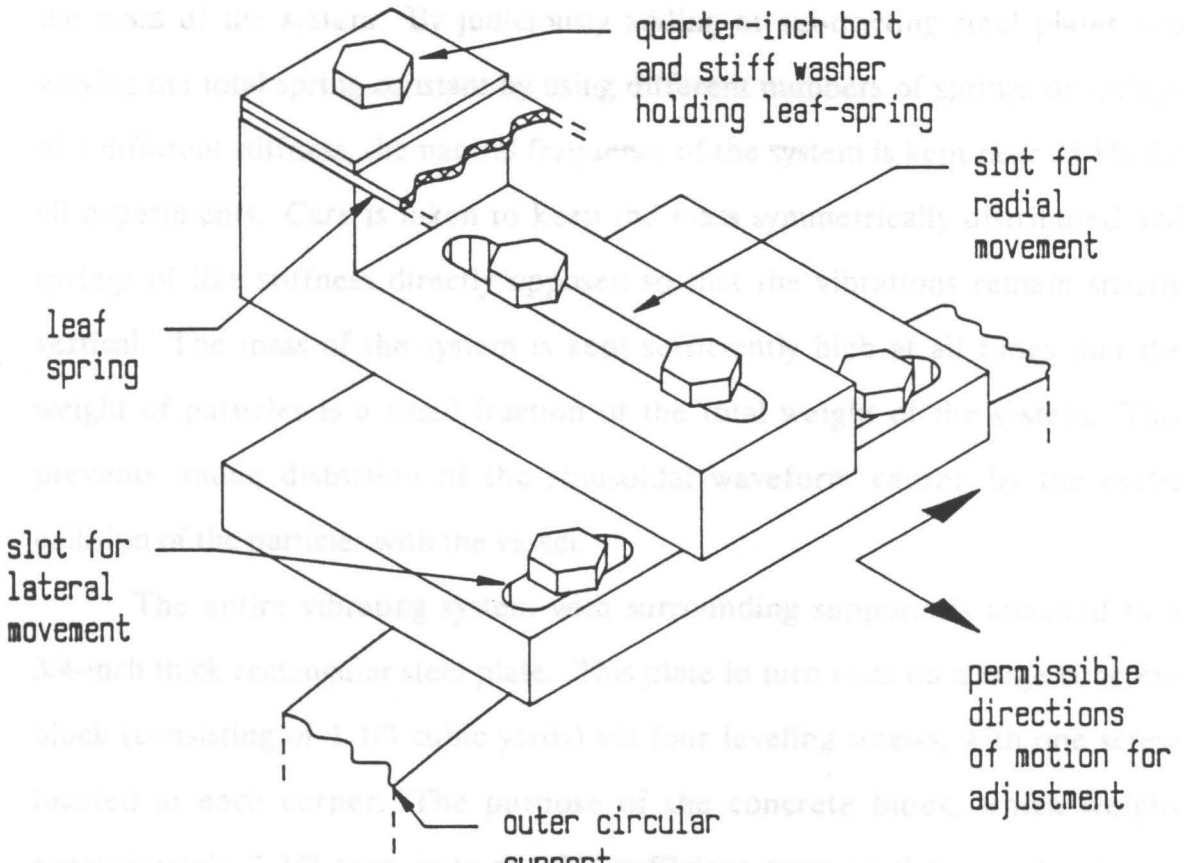

Figure 3.2. Adjustable mounting bracket assembly: Bracket can be adjusted laterally and radially to ensure proper leaf-spring alignment. From Thomas [1988].

$$\omega = 2\pi f = \sqrt{\frac{k}{m}} \qquad [3.1]$$

where ω is the angular frequency, f is the frequency, k the spring constant, and m the mass of the system. By judiciously adding or subtracting steel plates and varying the total spring constant by using different numbers of springs or springs of a different stiffness, the natural frequency of the system is kept near 25 Hz for all experiments. Care is taken to keep the mass symmetrically distributed and springs of like stiffness directly opposed so that the vibrations remain strictly vertical. The mass of the system is kept sufficiently high at all times that the weight of particles is a small fraction of the total weight of the system. This prevents undue distortion of the sinusoidal waveform caused by the cyclic collision of the particles with the vessel.

The entire vibrating system with surrounding supports is attached to a 3/4-inch thick rectangular steel plate. This plate in turn rests on a large concrete block (consisting of 1 1/3 cubic yards) via four leveling screws, with one screw located at each corner. The purpose of the concrete block, which weighs approximately 2 1/2 tons, is to provide sufficient mass so that no vibration is transmitted to the building. This end is further ensured by placing the concrete block on a wooden pallet. Even so, it is not possible to operate the vibrator between about 30 and 40 Hz without noticeably vibrating the building.

The electromagnetic coils must be kept cool, and this is achieved by drawing cooling air down through the vibrator housing. A venturi device is attached to the vacuum-cooling vent line of Figure 3.1 which provides the necessary air flow. All openings around the vibrator housing are covered in felt

to prevent small particles from being sucked into the coils along with the cooling air.

3.2 Vibrated Vessels

The study undertaken requires several different types of vessels for investigation of the phenomena of interest. The following sections describe the vessels used for the experimental work.

3.2.1 Heat-Transfer Vessel

The heat-transfer vessel is rectangular in shape, 6.75 in. x 6 in. and 4.25 in. deep. The longer walls are constructed of 1/4-in. aluminum, and the shorter walls of 3/16-in. Lexan. The heater-probe assembly runs lengthwise down the middle of the vessel and rests on the floor, which is a steel plate with a slightly raised surface inside the vessel and a thin lip outside the vessel. This lip contains a hole pattern which allows the vessel to be screwed down onto another steel plate, which in turn is bolted to the titanium plate as shown in Figure 3.1.

Vibration of the vessel in this configuration results in instabilities of the particles due to peculiar singularities at the corners, so the vessel has been modified as shown in Figure 3.3. The corners are rounded out with very thin (0.010 in.) brass shim formed into a radius of 2.5 in. The volume between the shim and the rectangular corners is loosely packed with glass wool to prevent excessive heat loss. All of the heat-transfer data have been taken with the bed in this modified configuration.

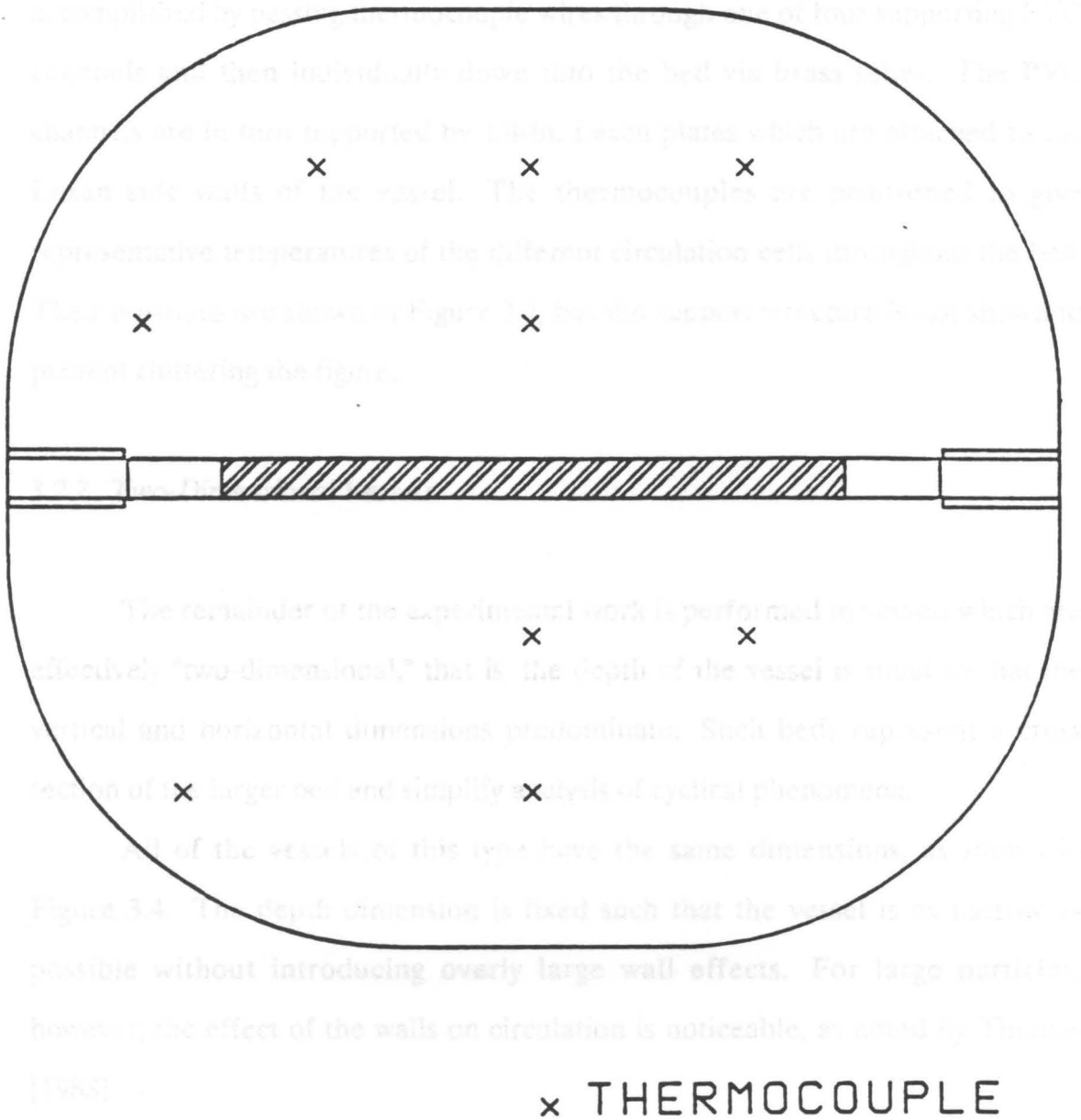

Figure 3.3. Top view of heat-transfer vessel: The heat-transfer vessel, as seen from above, showing the positions of the bed thermocouples and the heating probe assembly. Note that the structure which supports the thermocouples and passes them down into the bed is not shown to prevent cluttering of the figure.

Thermocouples are suspended in the bed from above. This is accomplished by passing thermocouple wires through one of four supporting PVC channels and then individually down into the bed via brass tubes. The PVC channels are in turn supported by 1/4-in. Lexan plates which are attached to the Lexan side walls of the vessel. The thermocouples are positioned to give representative temperatures of the different circulation cells throughout the bed. Their positions are shown in Figure 3.3, but the support structure is not shown to prevent cluttering the figure.

3.2.2 Two-Dimensional Vessels

The remainder of the experimental work is performed in vessels which are effectively "two-dimensional," that is, the depth of the vessel is small so that the vertical and horizontal dimensions predominate. Such beds represent a cross section of the larger bed and simplify analysis of cyclical phenomena.

All of the vessels of this type have the same dimensions, as shown in Figure 3.4. The depth dimension is fixed such that the vessel is as narrow as possible without introducing overly large wall effects. For large particles, however, the effect of the walls on circulation is noticeable, as noted by Thomas [1988].

The two-dimensional vessels are suspended from a "gallows" structure rather than directly bolted to the floor plate. This gallows consists of a hollow square steel frame to which the two-dimensional vessels are attached. This square frame is supported by four steel legs as shown in Figure 3.5, which are bolted to the titanium base and thus transmit the vibrations to the bed.

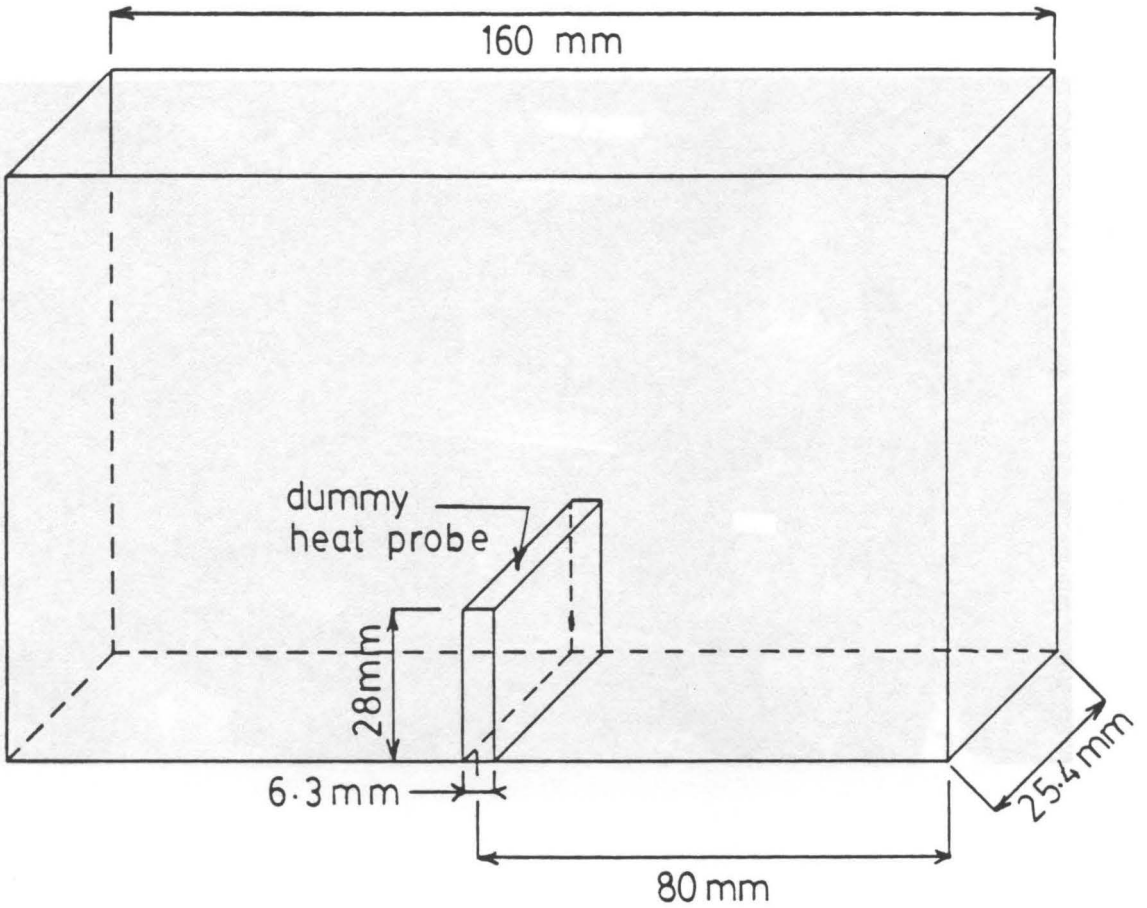

Figure 3.4. Generic two-dimensional vessel schematic: Drawing of a vibrated vessel which is effectively two-dimensional. Note that all experiments in this study are performed in a vessel of these dimensions except for the heat-transfer measurements. The dummy heat probe shown is removed for some experiments.

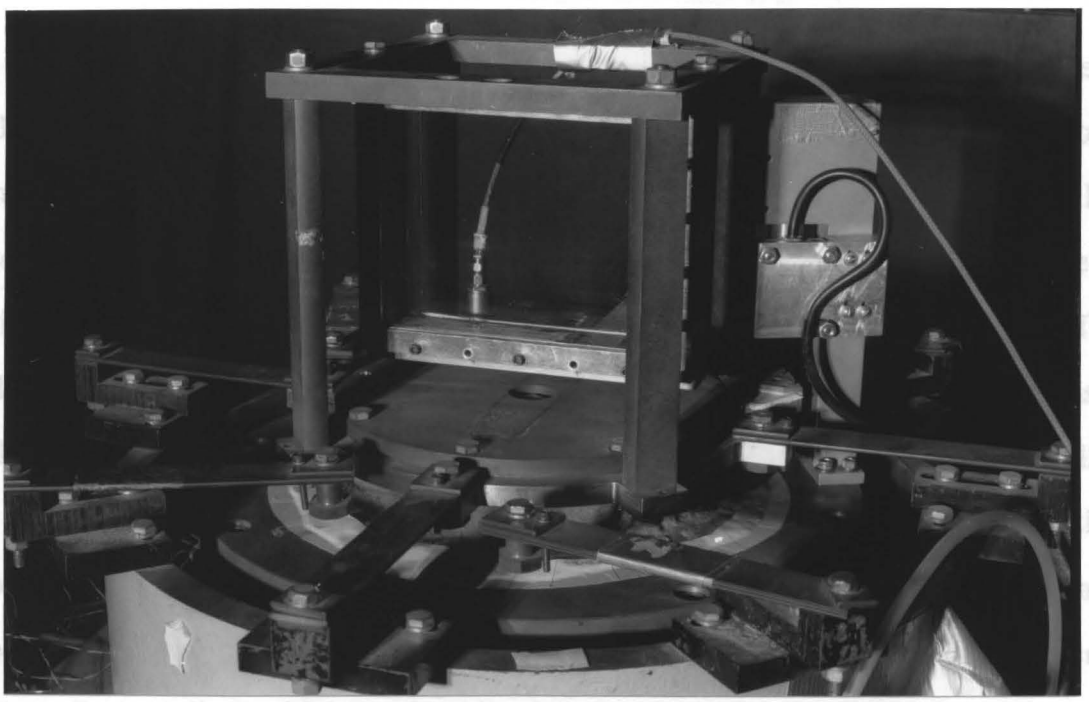

Figure 3.5. The gallows support structure: Photograph showing how the two-dimensional vessels are vibrated via the gallows structure.

Several two-dimensional vessels are used in this study: a glass-walled vessel, which is easily modified for many experiments; and a pressure-measurement bed. The following sections describe the different modifications in more detail.

3.2.2.1 The Glass-Walled Two-Dimensional Vessel

The glass-walled vessel, as shown in Figure 3.6, is basically the same as that used by Thomas [1988], but is modified to allow different experiments to be run. It is used as pictured for general observation of the bed and for filming. For some observations, a "dummy" heat probe is inserted in the middle of the vessel to simulate a cross section of the heat-transfer vessel with heat probe in place. This dummy probe consists of a 1/4-in. piece of Lexan, 1 1/8 in. high (the dimensions of the heat-transfer probe), and extends the full depth of the bed from wall to wall.

For determination of the onset and duration of gaps between the particle bed and vessel floor, this vessel must be modified. This is done by adding a false bottom of 1/2-in. Lexan machined to allow placement of electronic components. Two vibrated discs, which are described in the instrumentation section, are placed in the false bottom as shown in Figure 3.7. The false bottom has the same dimension as the vessel bottom, and is affixed to it with "Super Glue" which holds the false bottom securely, but also allows for relatively easy removal. This vessel is further fitted with a special glass wall which has had a 1/8-in. hole drilled in it to accommodate a capacitance probe as shown in the figure. This capacitance probe is described in the instrumentation section.

A second modification to this vessel is necessary to determine the passage of the compaction wave through the bed using piezoelectric films. The subtle

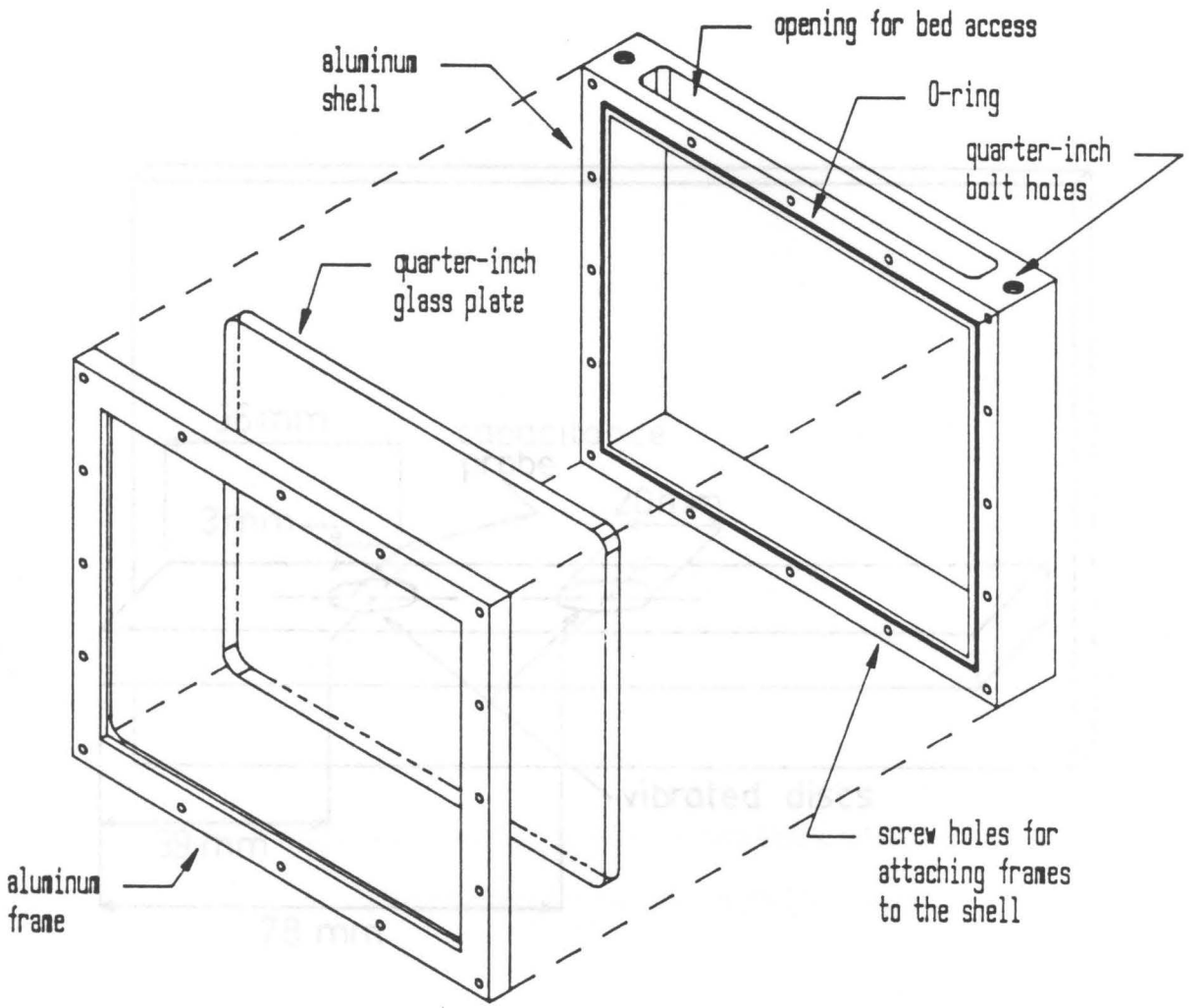

Figure 3.6. Drawing of glass-walled two-dimensional vessel: Exploded view of the glass-walled vessel showing its composition. The rear wall (not pictured) is identical to the front. Note that this is the vessel shown suspended from the gallows in Figure 3.5. From Thomas [1988].

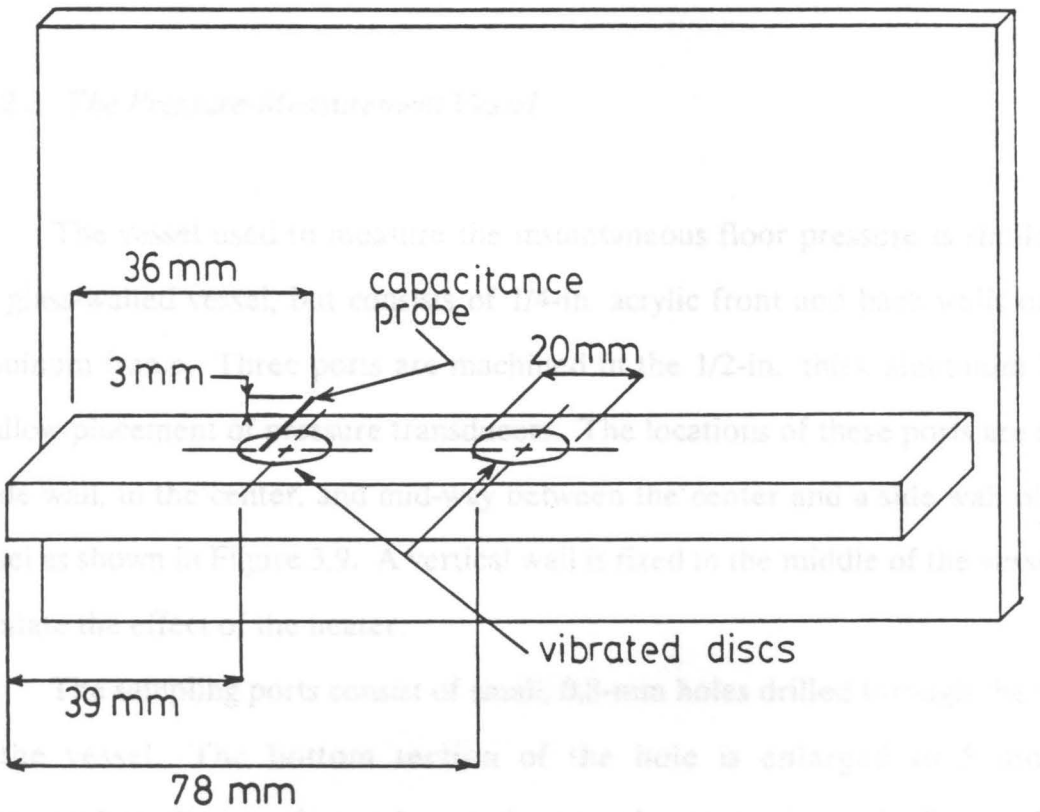

Figure 3.7. Schematic of false bottom and adapted back wall for two-dimensional vessel: Positioning of the two vibrated discs and the capacitance probe in the two-dimensional vessel is shown. The false bottom and adapted glass wall are fitted into the glass-walled vessel shown in Figure 3.6.

effect of the vertical propagation of the compaction wave requires a very rigid wall for mounting of the piezoelectric detector. Therefore, one of the glass walls is replaced by a 3/4-in. thick aluminum one which has 1/8-in. diameter piezoelectric dots affixed to it as shown in Figure 3.8. Further piezoelectric dots mounted on the base as shown in the figure allow determination of the horizontal propagation of the wave as well.

3.2.2.2 The Pressure-Measurement Vessel

The vessel used to measure the instantaneous floor pressure is similar to the glass-walled vessel, but consists of 1/4-in. acrylic front and back walls on an aluminum frame. Three ports are machined in the 1/2-in. thick aluminum base to allow placement of pressure transducers. The locations of these ports are near a side wall, in the center, and mid-way between the center and a side wall of the vessel as shown in Figure 3.9. A vertical wall is fixed in the middle of the vessel to simulate the effect of the heater.

The sampling ports consist of small, 0.8-mm holes drilled through the base of the vessel. The bottom section of the hole is enlarged to 5 mm to accommodate the sampling tube on the transducer, as shown in Figure 3.10. Pressure transducers are mounted directly in the base of the vessel to keep the dead volume between the bed floor and the measuring device to a minimum. The space between the bed floor and the pressure transducer is packed with steel wool to prevent particles from falling into the transducer. Steel wool is chosen because it creates a tortuous path which keeps out particles, yet the steel wool imposes little pressure drop, so its presence introduces little phase lag in the pressure

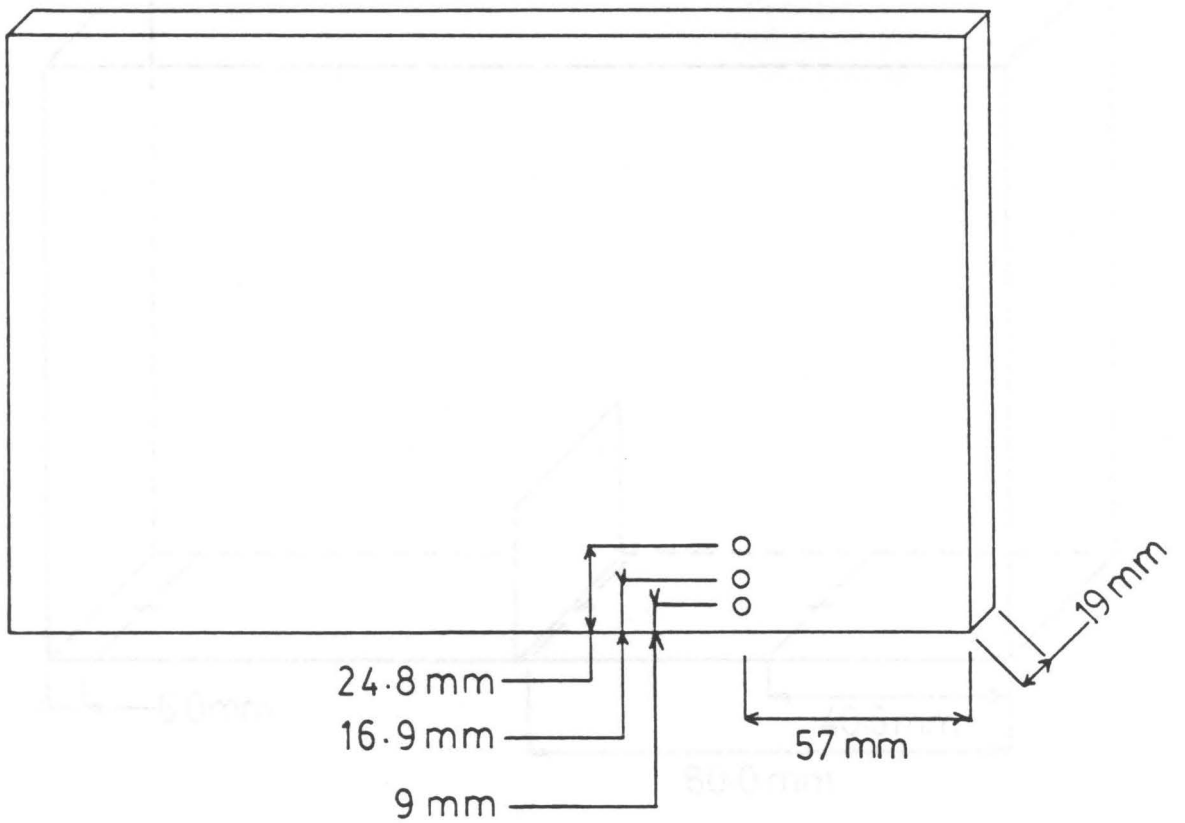

Figure 3.8. Adaptation for the vertical compaction-wave experiment: Schematic showing placement of piezoelectric dots on a rigid aluminum wall for the measurement of vertical propagation of the compaction wave.

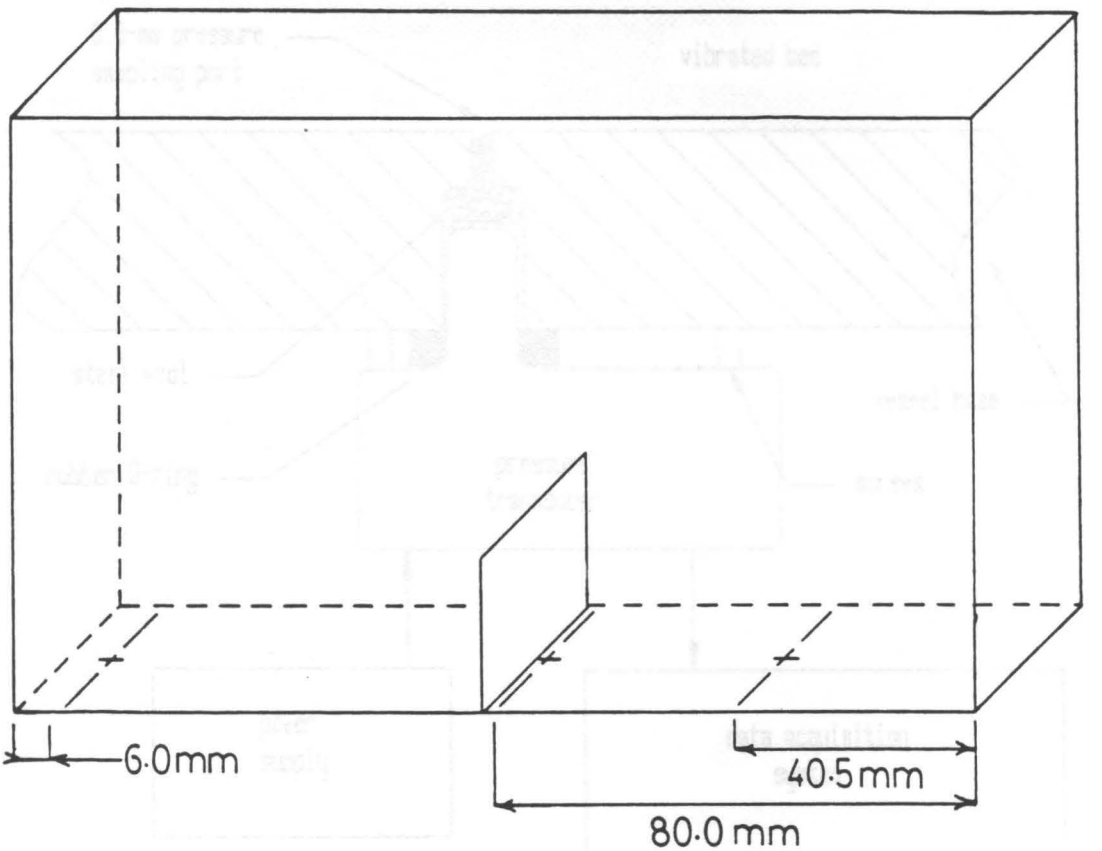

Figure 3.9. Location of floor-pressure measuring ports: Drawing showing the location of the pressure ports (indicated by "+") and the thin, vertical wall used to simulate the vertical-surface heater.

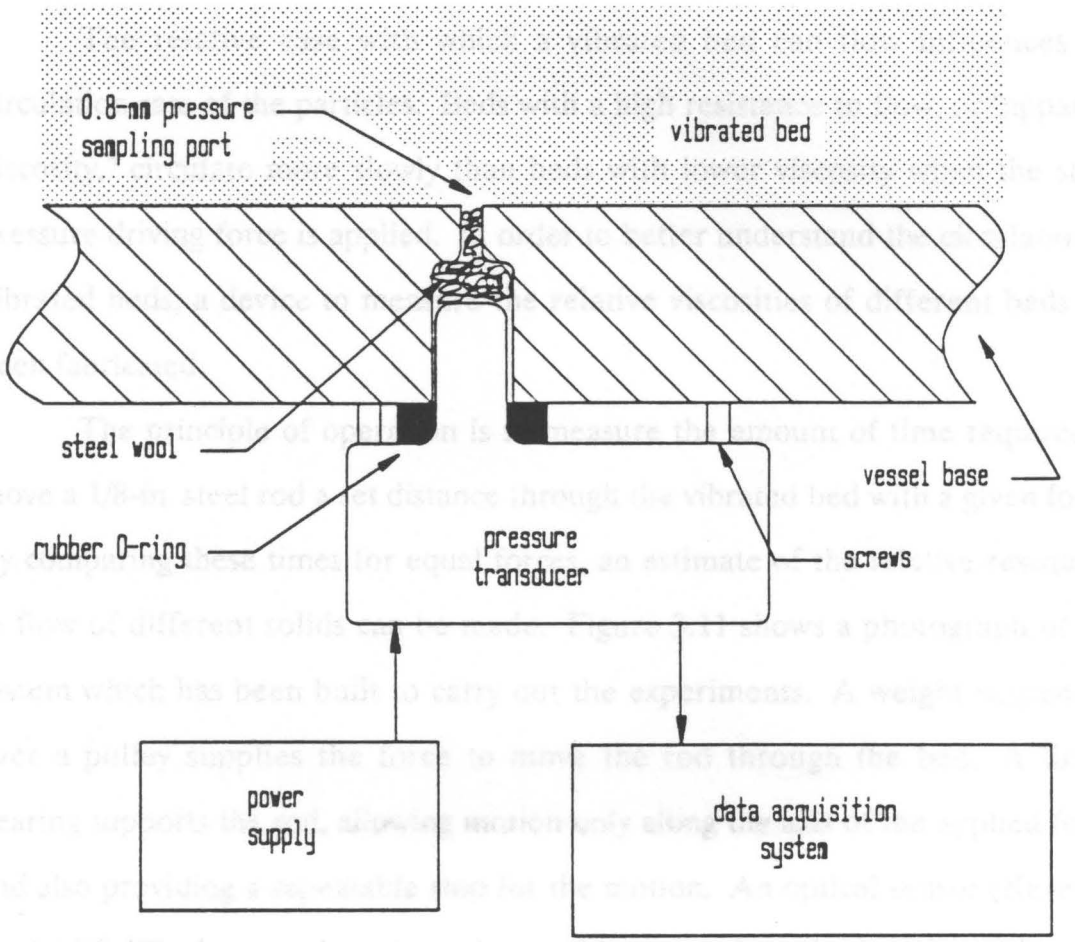

Figure 3.10. Schematic showing the mounting of a pressure transducer: Pressure transducer is fixed to the vessel base by two screws; steel wool prevents particles from entering the transducer. From Thomas [1988].

reading. That is, the pressure which the transducer reads is the pressure beneath the bed at that instant.

3.2.2.3 Apparatus for Measuring Particle Resistance to Flow

The relative ease with which a vibrated bed can flow influences the circulation rate of the particles. Beds with a high resistance to flow, or "apparent viscosity," circulate more slowly than beds with lower viscosity when the same pressure driving force is applied. In order to better understand the circulation in vibrated beds, a device to measure the relative viscosities of different beds has been fabricated.

The principle of operation is to measure the amount of time required to move a 1/8-in. steel rod a set distance through the vibrated bed with a given force. By comparing these times for equal forces, an estimate of the relative resistance to flow of different solids can be made. Figure 3.11 shows a photograph of the system which has been built to carry out the experiments. A weight suspended over a pulley supplies the force to move the rod through the bed. A linear bearing supports the rod, allowing motion only along the axis of the applied force and also providing a repeatable stop for the motion. An optical sensor (Keyence model FS-17), detects when the rod assembly moves from its initial position and triggers the A/D board to begin collecting data. The output from a LVDT transducer (TRANS-TEK model 0243-0000), mounted horizontally to measure the distance traveled by the rod, is collected and stored using a personal computer.

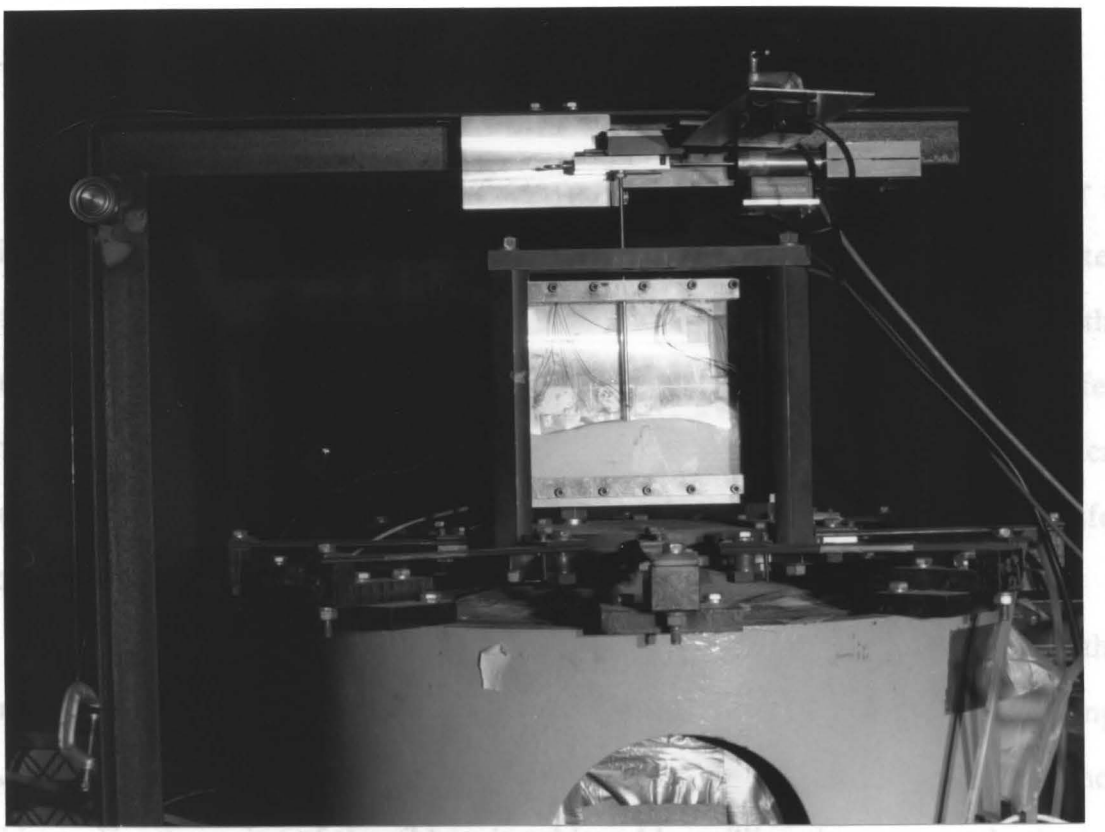

Figure 3.11. Photograph of the resistance-to-flow measurement system: A mass suspended over a pulley draws the rod through the bed at a known force. Resistance is determined by measuring the time it takes for the rod to move one inch.

3.3 Instrumentation

The following sections describe the instruments needed to carry out this investigation.

3.3.1 Heat-Transfer Probe

Thomas [1988] and Sprung [1987] conducted studies of heat transfer in vibrated beds using horizontal, cylindrical heaters. Both of these studies noted the cyclic formation of air gaps around the heating surface above and below the heater, and both found the effect of these gaps to be detrimental to heat transfer. In light of their findings, a heat-transfer probe was designed with a vertical heating surface to reduce the effect of air gaps and thus improve the heat-transfer coefficient.

The design of the probe is shown in Figure 3.12. The internals of the probe consist of a fiberglass core 1/16-in. thick, 3/8-in. wide, and 4.5-in. long. Around the middle 4 in. of this core is wrapped 1/16-in. nichrome resistance ribbon. Exact spacing of the ribbon is achieved by milling tiny grooves in the top and bottom of the core to serve as guides for the nichrome. This type of heater assembly is preferable to commercially available heaters because this arrangement allows for a very uniform heat flux.

The outer shell of the heat probe consists of two copper halves as shown in Figure 3.12. Each half is 4 in. long, 1/2 in. wide, and 3/32 in. thick with a lip of 1/32 in. both top and bottom so that when the two halves are placed together, the core assembly fits slightly loosely inside. Each copper half has three tiny holes in it, one in the middle and one 3/8 in. from each end, to allow for the placement of

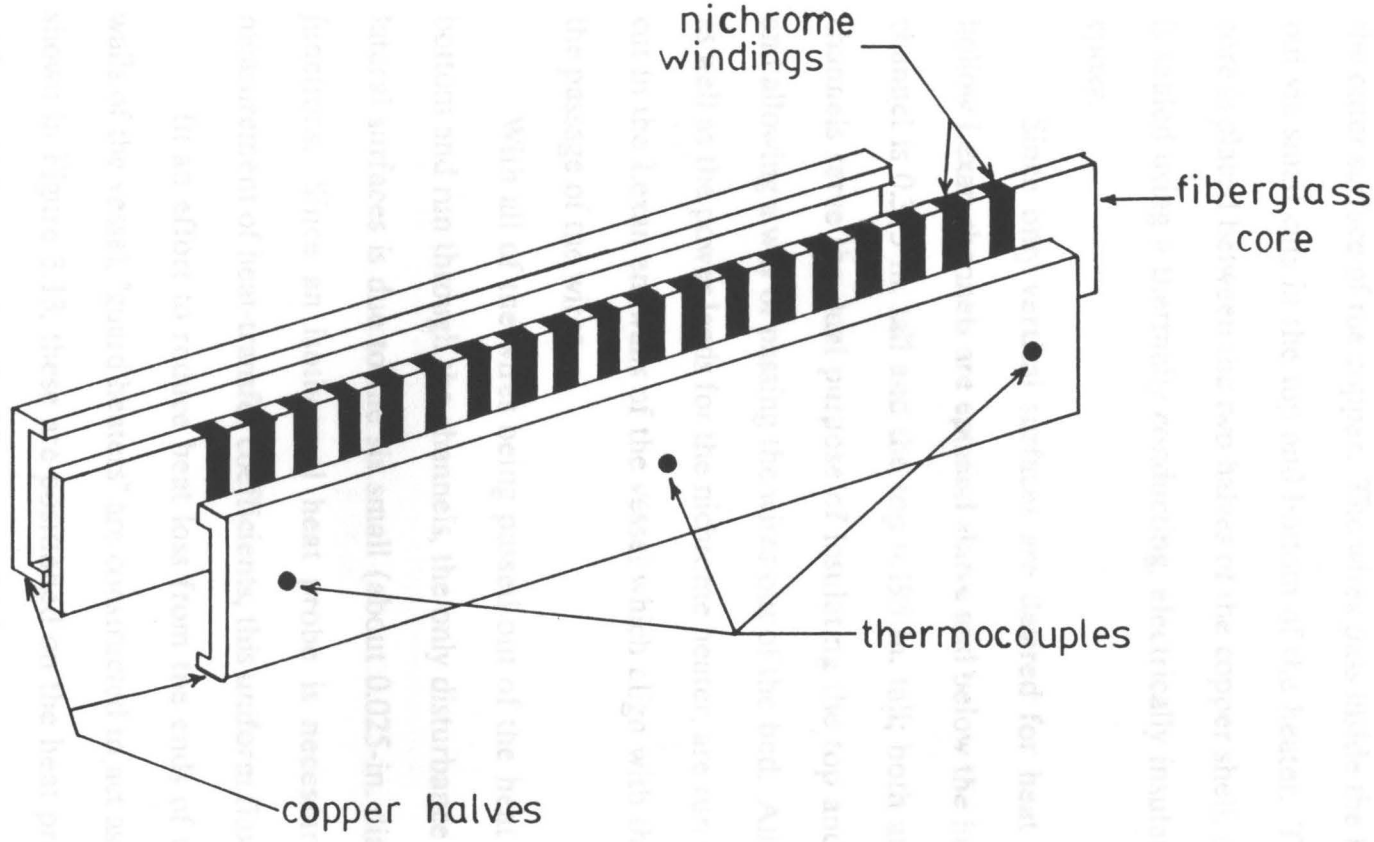

Figure 3.12. Schematic of heat-probe design: Exploded view of the vertical-surface heat probe showing the outer copper halves with thermocouple locations and the inner core with nichrome wrapping.

thermocouples. The thermocouples are set so that the junctions are flush with the outer surface of the copper. The wires pass inside the heater, and are brought out via small cuts in the top and bottom of the heater. The nichrome/fiberglass core is placed between the two halves of the copper shell, and the entire assembly is sealed using a thermally conducting, electrically insulating, high-temperature epoxy.

Since only vertical surfaces are desired for heat transfer in this study, hollow Lexan channels are epoxied above and below the heat probe. The bottom channel is 0.395 in. tall and the top 0.195 in. tall; both are 1/4 in. wide. These channels serve the dual purpose of insulating the top and bottom of the heater and allowing a way of passing the wires out of the bed. All of the thermocouples, as well as the power leads for the nichrome heater, are run in this way; small holes cut in the Lexan endwalls of the vessel which align with these channels allow for the passage of the wires.

With all of the wires being passed out of the heat probe via the top and bottom and run through the channels, the only disturbance in the heat flux on the lateral surfaces is due to the six small (about 0.025-in. diameter) thermocouple junctions. Since an isothermal heat probe is necessary to ensure accurate measurement of heat-transfer coefficients, this uniform flux is desirable.

In an effort to reduce heat loss from the ends of the probe through the walls of the vessel, "guard heaters" are constructed to act as heat flux barriers. As shown in Figure 3.13, these are positioned on the heat probe apparatus at each end next to the vessel walls. These guard heaters are crude heaters consisting of a W-shaped nichrome wire coil epoxied between a thin (.020 in.) copper sheet and a 1/4-in. thick piece of copper. The dimensions of the guard heaters are 3/4 in. by 1/2 in. Each guard heater has a thermocouple affixed to it, and these

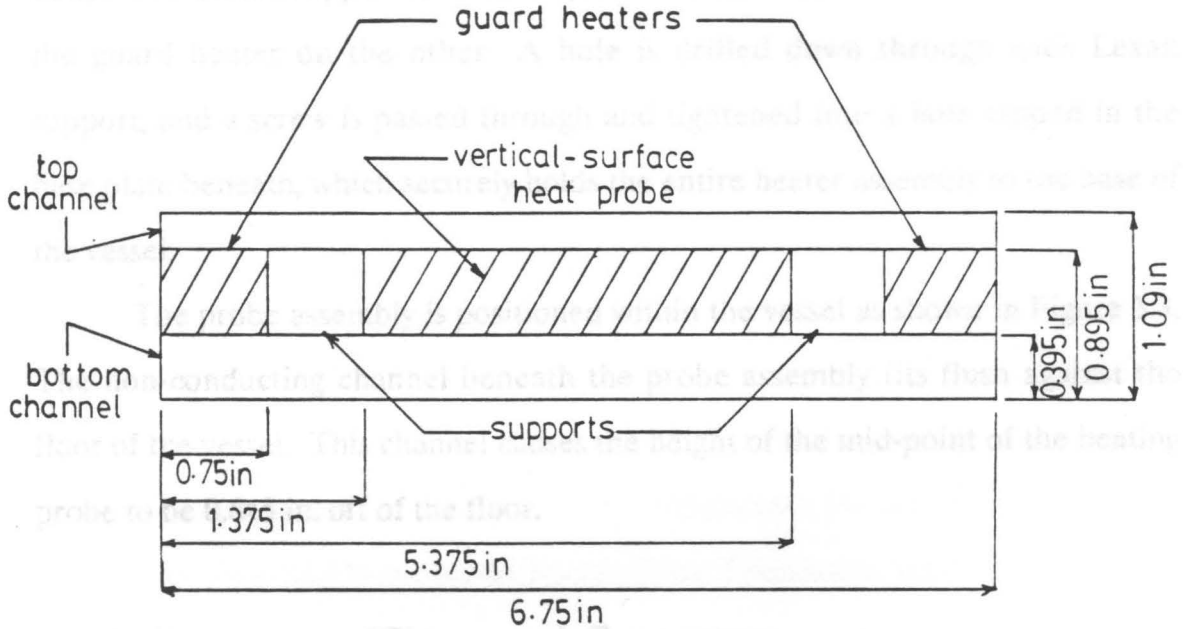

Figure 3.13. Vertical-surface heat-probe assembly: Side view of the heat-probe assembly showing the top and bottom insulating channels and guard heaters, separated from the main heater by Lexan supports.

thermocouples are compared with thermocouples from the main heater by a PID controller which holds the temperature of the guard heaters at the temperature of the main heater.

The guard heaters are separated from the main heat probe by a 5/8-in. piece of 1/4-in. Lexan which is machined in two halves so that the end of the fiberglass core from the heater fits securely into it. The two halves of the Lexan support are glued together using methylene chloride, which provides a very strong bond. The Lexan supports are then epoxied to the main heater on one side and the guard heater on the other. A hole is drilled down through each Lexan support, and a screw is passed through and tightened into a hole tapped in the base plate beneath, which securely holds the entire heater assembly to the base of the vessel.

The probe assembly is positioned within the vessel as shown in Figure 3.3. The non-conducting channel beneath the probe assembly fits flush against the floor of the vessel. This channel causes the height of the mid-point of the heating probe to be 0.645 in. off of the floor.

3.3.1.1 Measurement of Thermocouple Temperatures

The thermocouple switching circuit of Thomas [1988] is employed to sample the thermocouples readings both in the heat probe and immersed in the bed. The main features of this circuit are a high-accuracy amplifier (Doric Model 410 A) which gives a temperature reading of the T-type thermocouples with an error of about ± 0.5° C, and a series of sixteen dual-pole reed relays. When a particular relay is closed, the amplifier reads the temperature of the thermocouple attached to that relay.

3.3.2 Instruments for Measuring Vibrational Parameters

Two vibrational parameters, acceleration and displacement, need to be measured accurately for the purposes of this study. Since many of the phenomena of interest change quickly in short time periods, the instrument used to quantify these parameters must have relatively fast response. Separate instruments are used to measure the vessel displacement and acceleration as described below.

3.3.2.1 Vessel Acceleration

Vessel acceleration is measured by a Scientific Atlanta DYMAC M90 accelerometer. This model has internal amplification of the voltage output which reduces the problem of noise. It also has a nominal sensitivity of 100 mV/g (actual calibration value of 105 mV/g), and a linear response between 2 and 5000 Hz. It is powered by an 18-volt DC source which further reduces noise of the output, which is normally monitored on an oscilloscope, but can be sampled on an analog-to-digital (A/D) converter board (Data Translation model 2801 A) and read by an IBM personal computer.

The accelerometer contains a mass with a pre-loaded force on a piezoelectric crystal. When the device is subjected to an upward force, the net force on the crystal due to the mass is reduced and the crystal emits a positive voltage proportional to the upward force (and thus proportional to the acceleration). Conversely, a negative voltage is obtained for a downward force. Since the accelerometer is attached directly to the vibrating table, the output signal exhibits small deformations due to particle-vessel collisions. This property

has been used in past studies to determine cyclic lift-off and collision, as well as critical K-values, as described in Section 2.1.4.

3.3.2.2 Vessel Displacement

An optical system, the Keyence PA-1801 U photoelectric proximity sensor, is used to monitor the displacement of the vibrating table. In this device, a light-emitting-diode (LED) beam is focused through a lens on a piece of white paper on the vibrating table. The spot is reflected from the paper to a light reception lens which refocuses the spot on a photo-detector. The distance between the transmission lens and the vibrating table determines the location of the image on the photo-detector. The position of the image on the photo-detector, in turn, determines the electrical output signal, and thus the distance between the transmission lens and vibrating table is measured.

This device must be zeroed with the vibrating table in the null position (before vibration is applied). Since the proximity sensor is held stationary, knowing the distance between the sensor and the vibrating table as a function of time is analogous to knowing the displacement of the table from its null position as a function of time. The optical sensor is capable of resolving the distance between the table and the lens to 10 microns. Its response is linear up to about 250 Hz. The output signal of this device is also internally amplified. It does not display the distortion upon bed impact that the accelerometer output does, which implies that the deformations of the accelerometer signal are caused by impulse forces and not a disturbance in the sinusoidal movement of the vibrating plate.

3.3.3 Vibrational Phase-Angle Measurement

Since many of the phenomena of interest take place within a single cycle, it is necessary to determine the phase angle at which important events occur. For this purpose, the phase-delayed trigger system of Thomas *et al.* [1987] has been employed, with the improvements made as described in Thomas [1988]. As the details are thoroughly described in these two references, only the principles of operation are related here.

The displacement sine wave of the proximity sensor is electronically converted to a square wave which is exactly in phase. The frequency of this square wave is then multiplied by 360 (to provide 1° resolution) and this higher-frequency square wave is passed to a down counter. The phase angle of the desired trigger (0 to 359 degrees) is preset into the counter. When a zero-crossover point is detected in the vibrational cycle, the counter starts counting down from the preset angle the number of (multiplied) square waves it receives. When the counter reaches zero, an electronic trigger pulse is produced which is delayed after the zero-crossover point by the desired phase angle and the cycle repeats.

Since this device can be operated in either a single pulse or continuous mode, it is quite useful for phase correlation of many different types of experiments in a vibrated bed. It is used in the continuous mode to run a strobe light which allows observation of the bed at any phase angle. In this mode, the strobe flashes once each cycle at the desired phase angle so the bed appears to be "frozen" at that angle. With this technique, a visual measurement of the lift-off and collision angles of the bed has been reported by Thomas [1988]. In the single-pulse mode, the trigger can be used to fire a flash for a camera or to initiate

phase-correlated data acquisition. This method has been used to obtain the pressure, bed separation, and collision data in this study.

Due to the resolution limit of the proximity sensor, the accuracy of the phase-delayed trigger is only about 2° even though the resolution is 1°. More important to the accuracy of the phase angle correlation, however, is a knowledge of the phase lags inherent in the system. The strobe light used, a General Radio Strobatac model 1531-A, has been calibrated by Thomas [1988] and found to have a delay of 0.2 ms, which corresponds to about 2 degrees at 25 Hz. The method used to determine the phase lag was a comparison of the trigger pulse sent to the strobe with the output as measured by a photo-diode. The delay caused by the phase-delay trigger circuitry itself, as measured by comparing an input signal with the output pulse was found to be less than 0.05 degrees at 25 Hz, and is therefore neglected.

Since the response frequency of the accelerometer is so high relative to the vibrational frequency (5000 Hz *vs.* 25 Hz), one expects very little phase lag in the output from this instrument. This has been shown to be the case by Thomas [1988] who measured the phase lag at less than 1° at 25 Hz. Since this phase lag is so small, the accelerometer output is taken as the standard and the phase lags of other instruments are measured by comparing outputs on an oscilloscope. Using this technique, the phase lag of the optical transducer is found to be about 12°.

Since the actual triggered output pulse from the phase-delay system is the sum of the input angle and all of the phase lags inherent in the system, care is needed in selecting the angle to be input. For example, if one wishes to observe the bed at 90° with the strobe lamp, one must set the phase-delay trigger for 76° to allow for the phase lags of the strobe lamp and the optical transducer.

3.3.4 Vibrated-Disc System

The vibrated discs in the false bottom of the glass-walled vessel (as shown in Figure 3.7, page 102) are used to determine the point in the vibrational cycle when the particle bed separates from the vessel floor and also the point of collision between bed and vessel. These angles of separation and collision have been previously reported by Thomas [1988] using a visual technique, and by Ryzhkov and Baskakov [1974] using strain gauges, but there are possible problems with these data. Thomas himself suggested that the visual technique may be flawed due to wall effects which would cause a few particles near the glass walls to obstruct the line of sight after the bulk of the bed has separated. This would lead to a measurement of the angle of separation later in the cycle than the true angle of separation. In fact, his reported angles are significantly later than those he calculated using his semi-empirical model. The results of Ryzhkov and Baskakov [1974] are for deep beds, and therefore may or may not be significant for the shallow beds of interest in this study.

The vibrated discs are piezoelectric buzzers manufactured by Archer which have been removed from their plastic housing and edge mounted above the holes machined in the Lexan false bottom so that they fit flush. They are driven using a second WAVETEK function generator (adapted with an extra potentiometer to allow fine tuning) at their resonance frequency (about 4.5 kHz). The amplitude of the output from the discs is processed, sampled on the A/D board, and read on the IBM PC. When the particles are in contact with the disc, the amplitude of the output is very small, but when the bed has separated from the vessel, the discs resonate and the amplitude is much greater.

The signal processing involves amplification, rectification, and filtering. First, the signal is amplified three times. Next, the signal is precision-rectified to give only a positive output and filtered to give an envelope of these rectified peaks. The circuit which performs this processing has been developed in-house and is illustrated in Figure 3.14.

The phase lag due to the vibrated disc itself is in the microsecond range and can therefore be neglected. The phase lag due to the signal processing has been measured on an oscilloscope by comparing the output with a square wave input, and it also is negligible.

3.3.5 The Capacitance Probe

A second device has been developed to measure the appearance and disappearance of the gap beneath the bed of particles. This device measures the differences in capacitance caused by the presence or absence of solids near the vessel floor. Since the solid has a much higher dielectric constant than air, the capacitance is higher when the solids are in the field of the capacitor than when an air gap is present.

A schematic of the capacitance probe circuit appears in Figure 3.15. A high-frequency (about 200 kHz) sine wave is passed through a diode to a small wire which acts as the charged "plate" of the capacitor sensor assembly. The aluminum vessel itself acts as ground. As shown in the figure, the charge transferred to the charged wire by the diode is drained off by the large resistor, producing a voltage across the measuring capacitor which is proportional to the current flow. A change in the capacitance in the sensor assembly causes a proportionate change in the current flow and thus a proportionate change in the

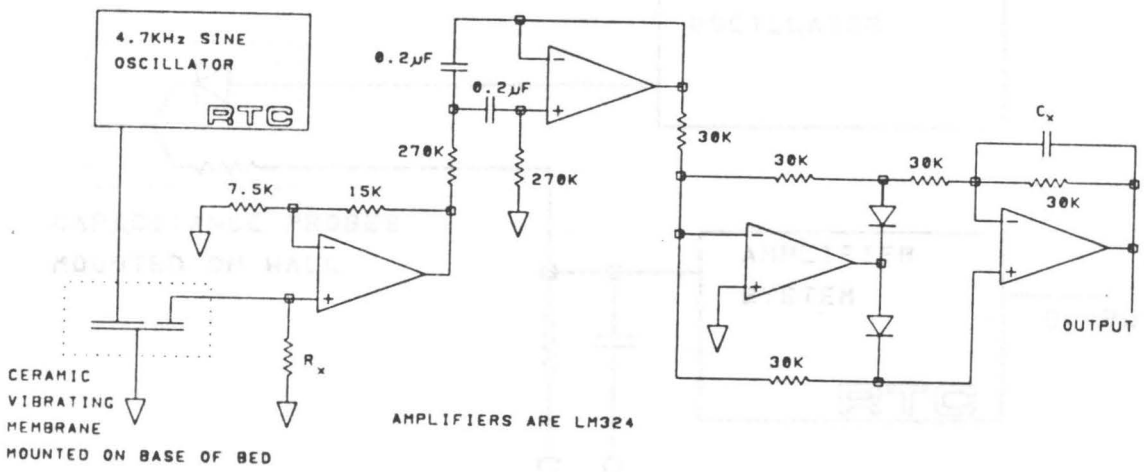

Figure 3.14. Circuit for processing the raw output from the vibrated discs.

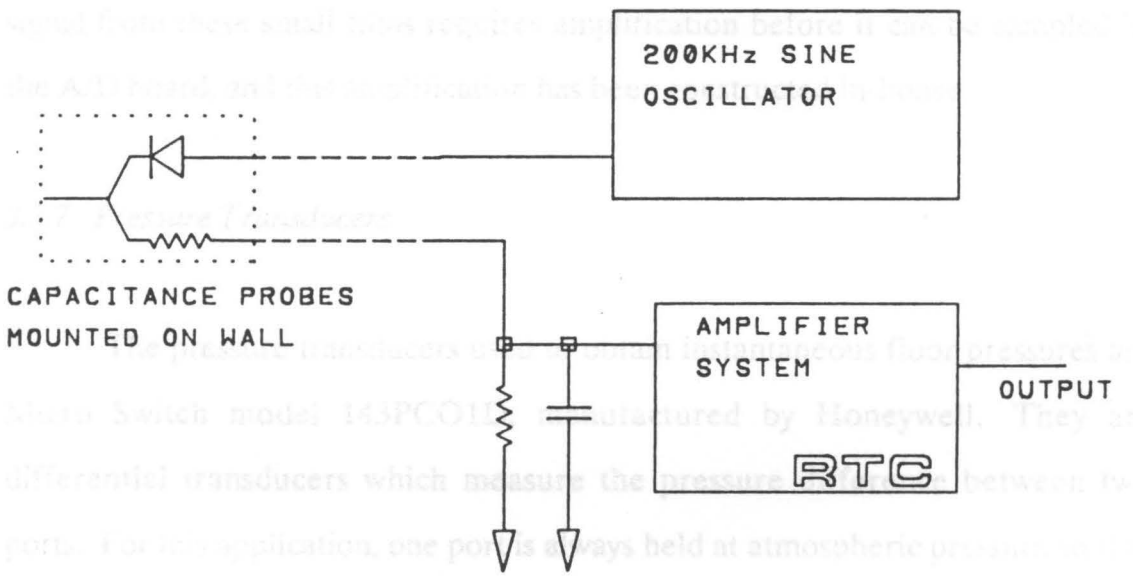

Figure 3.15. Schematic of the capacitance probe circuit.

voltage across the measuring capacitor. This voltage is then amplified and measured on the A/D board and read by the IBM PC. The phase lag of this circuit, as measured by comparing input and output signals, is about 7° .

3.3.6 Piezoelectric Collision Detectors

The piezoelectric films used to determine passage of the compaction wave are manufactured by the Pennwalt Corporation under the name Kynar Piezo Film, code KH-110 K. They have a sensitive area 1/8 in. in diameter. The output signal from these small films requires amplification before it can be sampled by the A/D board, and this amplification has been constructed in-house.

3.3.7 Pressure Transducers

The pressure transducers used to obtain instantaneous floor pressures are Micro Switch model 143PCO1D, manufactured by Honeywell. They are differential transducers which measure the pressure difference between two ports. For this application, one port is always held at atmospheric pressure so that the output from the transducer is the gauge pressure sampled by the other port (*i.e.*, the gauge pressure beneath the particle bed). These transducers have a range of ± 1 psi. full scale and a flat response up to 1000 Hz. Their response is very nearly linear over the full range, and the three transducers have been individually calibrated using a Wallace and Tiernan pressure gauge calibrated by the National Bureau of Standards.

The phase lag of this model pressure transducer has been measured by Thomas [1988]. This experiment consisted of placing a piece of stiff, nylon tube

beneath the vibrating table such that the tube was partially compressed with the table in the equilibrium position. A pressure transducer was placed in each end of the tube, with one end having a 0.8-mm hole loosely packed with steel wool, as shown in Figure 3.16. This exactly simulates the situation in the pressure measurement vessel. The table was then vibrated and the output from both transducers compared with the accelerometer output. Since a downward movement of the table (corresponding to a positive acceleration) creates an increase in pressure in the tube and *vice versa*, the pressure and accelerometer outputs should be in phase. Thomas [1988] detected no phase lag in the output of the pressure transducers, even with the constriction and steel wool packing, at frequencies up to 60 Hz.

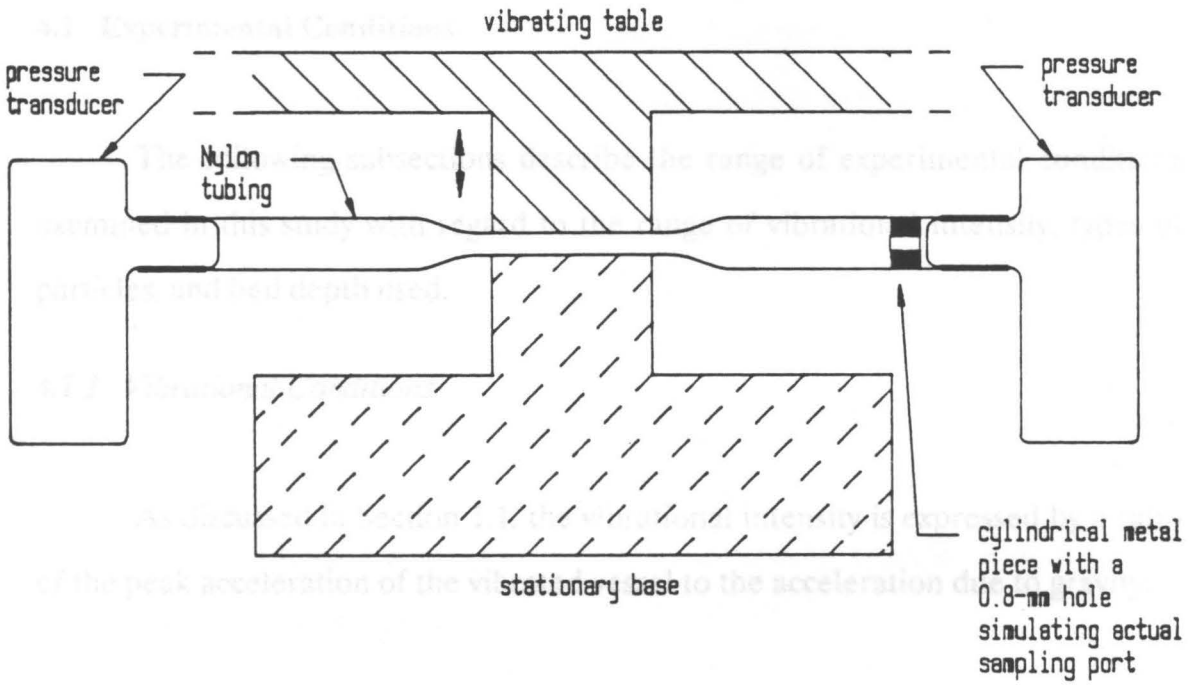

Figure 3.16. Apparatus for measurement of phase lags in pressure measurements: Device used to simulate floor-pressure measurements in a vibrated bed to check for phase lags in the system. From Thomas [1988].

Chapter 4 Experimental Conditions and Techniques

Chapter 4 describes the conditions and procedures used to carry out the experimental study proposed. Section 4.1 covers the conditions, and Section 4.2 deals with procedures.

4.1 Experimental Conditions

The following subsections describe the range of experimental conditions examined in this study with regard to the range of vibrational intensity, types of particles, and bed depth used.

4.1.1 Vibrational Conditions

As discussed in Section 1.1, the vibrational intensity is expressed by a ratio of the peak acceleration of the vibrated vessel to the acceleration due to gravity:

$$K = \frac{a_o \omega^2}{g} \qquad [4.1]$$

where K is the vibrational intensity parameter, a_0 the amplitude of vibration, ω the angular frequency, and g the acceleration due to gravity. For this study, the vibrational frequency is held constant at 25 Hz, so that the angular frequency (ω) is also constant.

There are several reasons for not varying the frequency in this study. First, as can be seen in Equation 4.1, the dependence of the K-value on ω, and thus

frequency, is squared. Therefore, a reduction in frequency from 25 Hz to, for example, 15 Hz results in an increase of 2.8 times in amplitude to maintain the same K-value. Since the amplitude is limited on the vibrator by stops, this would unduly limit the K-value. Secondly, vibrated beds become "dead" at higher frequencies. Chlenov and Mikhailov [1972] note a reduction in the degree of bed expansion above 40 Hz. Furthermore, as noted in Section 3.1, despite the design features intended to suppress transmission of vibrations, the building shakes perceptibly at frequencies near 35 Hz. Lastly, since the system is operating at the natural resonance frequency, it is convenient not to vary frequency since this would necessitate many combinations of mass and spring stiffness to achieve the desired resonant frequencies.

Since frequency is held constant, the only variable left for altering the vibrational intensity is the amplitude. Table 4.1 shows the amplitude necessary for a given K-value. The equipment used in this study has a practical upper limit at 25 Hz of K = 7. Operation of the equipment above this has resulted in a broken driveshaft, and thereafter K = 7, and usually even K = 6, has been taken as the maximum value.

4.1.2 Particle Types and Sizes

The particles used in this study consist mainly of three types: 1) Master Beads manufactured by Norton-Alcoa; 2) low-density glass beads manufactured by Potters' Industries (their P-series); and 3) high-density glass beads, also made by Potters' Industries (their H-series).

Master Beads are nearly spherical particles composed primarily of alumina (86%), with the remainder being silica (2-4%), iron oxide (6-8%), and titania

Table 4.1 Amplitude of vibration for K-values from one to seven at a frequency of 25 Hz.

K	Amplitude (mm)
1	0.40
2	0.79
3	1.19
4	1.59
5	1.99
6	2.38
7	2.78

(4-5%). The density of the solid is about 3650 kg/m^3, and the manufacturer gives its thermal conductivity and heat capacity as about 36 W/m-K and 765 J/kg-K, respectively. The color is nearly black, due to the presence of the impurities, which lends itself well to front-lit photography.

Low-density glass beads are quite spherical and are made of a soda-lime silicate glass with a solid density of 2500 kg/m^3. The heat capacity and thermal conductivity are 750 J/kg-K and 1.4 W/m-K, respectively [Incropera and DeWitt, 1981]. The high-density glass beads are also spherical and have a solid density of 4490 kg/m^3. They are composed of a barium-titanate glass, and values for thermal conductivity and heat capacity are not readily available, although Thomas [1988] gives a ballpark figure of 1 W/m-K for the thermal conductivity.

The particles are sized using U.S. Standard Mesh screens into eight ranges for Master Beads, and nine for both types of glass beads as shown in Table 4.2. The size range listed in column 2 of the table is the size of the opening of the two screens used, and the mean diameter listed is the geometric mean particle diameter ($\overline{d}p$) obtained from

$$\overline{d}_p = (d_{p1}\ d_{p2})^{\frac{1}{2}} \qquad [4.2]$$

where d_{p1} is the opening of the smaller screen and d_{p2} is the opening of the larger screen.

All of these particles behave as Geldart group B particles, although the smallest low-density glass beads are in the group A range according to his chart [Geldart, 1973]. The two smallest glass bead sizes fall into the group A range according to the Grace [1986] modification of the Geldart classification. Experiments with these particles, however, show that they exhibit fluid-like behavior while being vibrated, but that this fluid-like behavior stops immediately

Table 4.2 Size ranges of particles used in this study and the equivalent geometric mean diameter

U.S. Standard Mesh Designation	Size Range (microns)	Geometric Mean Diameter (microns)
-20 +30	595 - 841	707
-30 +40	420 - 595	500
-40 +50	297 - 420	353
-50 +60	250 - 297	272
-60 +70	210 - 250	229
-70 +100	149 - 210	177
-100 +140	105 - 149	125
-140 +200	74 - 105	88
-200 +270	53 - 74	63

upon cessation of vibration. This type behavior is characteristic of group B solids rather than group A, which tend to lose fluidity slowly due to imbibed air.

4.1.3. Bed Depth

As discussed in the literature review section, the behavior of vibrated beds is dependent on the bed depth, or more accurately, the ratio of bed depth to vessel diameter, L/D. In all experiments in this study, the depth of the bed is 30 mm. This figure is an average, static, gravity-packed depth. In practice, the depth is achieved by using the volume of particles necessary for the given vessel's cross-sectional area rather than by a direct measurement of the depth. The widths of the vessels used in this study range from 152 mm to 170 mm, which give L/D values of from 0.20 to 0.18, which fall into the category of "shallow beds." (Shallow beds are loosely defined to be those with an L/D < 1.)

4.2 Experimental Procedures

The following subsections briefly describe the methods used to obtain the data for this study.

4.2.1 Measurement of Surface-to-Bed Heat-Transfer Coefficients

The steady-state heat-transfer coefficient between the heating probe described in Section 3.3.1 and vibrated beds of solids is measured. Power is supplied to the heating probe via a DC power supply, since a very stable source is needed. The circuit of Figure 4.1 is employed to determine accurately the power

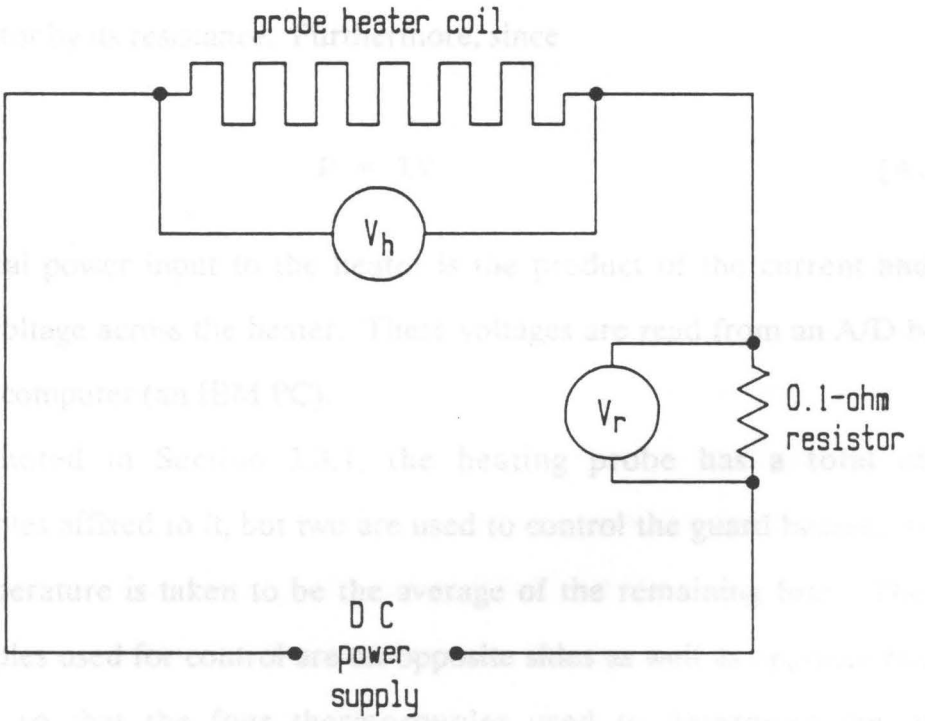

Figure 4.1. Circuit for measuring the heating probe power input: Voltage V_h and V_r are measured across the heating probe and the 0.1 Ω power resistor, respectively. From Thomas [1988].

input to the heater. The voltage across the power resistor of known resistance (0.1 Ω) is measured, as well as the voltage across the heating probe.

Since, from Ohm's Law,

$$I = \frac{V}{R} \qquad [4.3]$$

the current in the circuit is calculated by dividing the measured voltage across the power resistor by its resistance. Furthermore, since

$$P = IV \qquad [4.4]$$

the electrical power input to the heater is the product of the current and the measured voltage across the heater. These voltages are read from an A/D board by a digital computer (an IBM PC).

As noted in Section 3.3.1, the heating probe has a total of six thermocouples affixed to it, but two are used to control the guard heaters, so the probe temperature is taken to be the average of the remaining four. The two thermocouples used for control are on opposite sides as well as opposite ends of the probe, so that the four thermocouples used to determine the probe temperature reflect the most representative profile possible.

The temperature of the bed is determined by an average of nine thermocouples readings within the bed as shown in Figure 3.3. There are fourteen thermocouples suspended in the bed, but since the thermocouple switching circuit can monitor only sixteen temperatures, only nine from the bed are used. Preliminary experiments are therefore necessary to determine which thermocouples to use. Since the heat probe apparatus essentially forms a barrier

down the center of the vessel, circulation patterns in the two halves (and thus temperatures) tend to be symmetric with respect to it. Thermocouples nearest to the heating probe tend to be slightly warmer, and those farther away, particularly those near the corners, tend to be cooler. With this knowledge, the thermocouples are placed to provide the most representative temperature profile of the bed.

The remaining three temperatures in the sixteen-channel thermocouple circuit are used to monitor the temperature in the Lexan support between the guard heater and main heating probe, in the non-conducting channel beneath the heating probe, and in one of the guard heaters. These temperatures are not used in the calculation of the heat-transfer coefficient, but are used to estimate the heat loss from the heating probe in the cases of the channel and support thermocouples, and as a check on the controller in the case of the guard heater.

As mentioned previously, the heat-transfer coefficient is only measured at steady-state. The power input to the heating probe is set by the digital computer, which controls this power to ± 0.5%. Steady-state is reached by slowly increasing the power set-point until the probe temperature stabilizes between 80 and 90 degrees Celsius. When the bed temperature reaches a steady value (usually between 1-2 hrs.), data collection begins. The computer samples each thermocouple approximately every 45 seconds, so this is the period in which the value of heat-transfer coefficient is updated. In order to obtain more representative data, however, a value of the heat-transfer coefficient is taken only every 6 or 7 cycles, so that the values used are gathered somewhat over 5 minutes apart. Each data point reported represents the average of 6 or 7 of these values, and thus the heat-transfer coefficient is an average over about half an hour.

4.2.2 *Determination of Onset and Duration of the Air Gap*

Two different sets of experiments are used to determine the onset and duration of the cyclic air gap which is formed beneath the bed of particles. In the first, the vibrated disc system, as described in Section 3.3.4, is used. The second employs the capacitance probe of Section 3.3.5. The experimental procedure for both techniques is similar.

For the vibrated discs, the first step is to "tune" the disc to its resonance frequency. To do this, the output voltage is monitored on an oscilloscope and the frequency of the function generator is carefully adjusted until a maximum amplitude is found. For the center disc, the resonance frequency is about 4.18 kHz, while the edge disc resonates at 4.36 kHz. Since the resonance frequencies are slightly different, only one disc is monitored at a time, and then the frequency is adjusted and the other disc is monitored.

After the frequency of the signal sent to the vibrated disc is set, solid particles are added to an equivalent depth of 3 cm. The baseline voltages of the accelerometer and vibrated disc are sampled via the A/D board and the computer. The vibrational acceleration is set on an oscilloscope to the desired K-value, and the phase-delayed trigger is set to 348° (to allow for the 12 degrees of lag in the optical sensor). Upon triggering, the phase-delay device sends a pulse which is synchronized to 0 degrees to the A/D board that begins data collection. Each channel is sampled at a rate of 128 points per cycle for ten cycles. The results are then corrected for the baselines and plotted on the computer monitor and checked for consistency between cycles. If all cycles are consistent, the results are stored on a diskette.

The technique for the capacitance probe is the same, except that the signal input to it is 200 kHz. This is set on the function generator as measured on the oscilloscope, and then the data collection proceeds as described above.

4.2.3 Determination of the Point of Collision

The collision of the particle bed with the vessel base can be determined by three experimental systems: the vibrated-disc system; the capacitance-probe system; and the piezoelectric film system. The collision data for the first two systems are collected as described in the previous section. The piezoelectric films are not driven by an input signal, but rather generate an output voltage when an applied stress (such as the passing of the compaction wave upon collision) creates a strain.

Data collection with this system, described in Section 3.2.2.1, is similar to that for the vibrated-disc and capacitance-probe systems. An equivalent depth of 3 cm (130 ml) of the desired solid is put into the piezoelectric vessel. The vibrations are adjusted to the desired K-value and the phase-delayed trigger is set to 348° (to allow for the 12° of lag in the optical sensor). The phase-delayed trigger thus initiates data collection at 0°, and the output from all six piezoelectric films are sampled on the A/D board at a rate of 128 points per film per vibrational cycle. Four cycles are sampled and checked for consistency. If they are consistent, two cycles are stored to diskette.

4.2.4 *Observation of the Compaction Wave*

In addition to measuring the movement of the compaction wave via the piezoelectric films, the vibrated beds have been filmed using a high-speed movie camera to allow for direct observation of the passage of the compaction wave. The films are shot using 400 ASA color film at 2500 frames per second using tungsten lamps. For the vibrational frequency of 25 Hz, this film speed gives 100 frames per cycle which allows observation of the intra-cyclic behavior of the bed.

The two-dimensional glass-walled vessel described in Section 3.2.2.1 is used for this filming. The particles used are medium-to-large-sized Master Beads, since they photograph well with front lighting and have more easily discernible compaction waves than the smallest sizes. The procedure for filming consists of charging the desired amount of particles to the vessel, setting the desired K-value, turning on the tungsten lamps, and then starting the camera. At this rate of filming, a 400-foot roll of film (the largest that the camera can hold) takes about 7 seconds to shoot.

4.2.5 *Measurement of Instantaneous Floor Pressures*

The vessel shown in Figure 3.9 is used to measure the pressure beneath the bed of solids during the vibrational cycle. First, an equivalent depth of 3 cm. of the particles to be used for the experiment is placed in the vessel. Next, the baseline voltages of the pressure transducers and the accelerometer are read. The acceleration is then set to the desired vibrational intensity by measuring the output on an oscilloscope. The phase-delayed trigger angle is set to 348° (to

allow for the 12° of phase lag inherent in the optical displacement sensor--see Section 3.3.3), and the system is triggered.

At the equivalent angle of 0° (348° plus the 12° phase lag), the phase-delayed trigger sends a pulse to the A/D board which initiates data collection. Ten complete, consecutive cycles are simultaneously sampled for each of the three pressure transducers and the accelerometer. The sampling rate is 128 points per cycle per transducer. The results, corrected for the baseline voltages and converted to pressures and accelerations using calibration curves, are plotted on the PC screen and checked for consistency. If the data are consistent in all the cycles sampled, the results are stored on a diskette.

4.2.6 Measurement of Particle Motion

For the study of circulation rates and patterns with a vertical heat probe in place, the vessel described in Section 3.2.2.1 is used with the dummy heat probe, a Lexan barrier with the same cross section as the actual heat probe. In these studies, glass beads (both high and low density) are used.

A few milliliters of glass beads of each size and type to be studied are dyed with fluorescent ink, either A-946 blue ultra-violet ink manufactured by the Volk Corporation, or yellow or orange permanent fluorescent ink from markers manufactured by Sakura Color Products Corporation. The dyeing procedure consists of wetting the beads with acetone, adding a few drops of the dye, stirring in a Petri dish to distribute the dye, and adding a few drops of clear fingernail polish to fix the dye on the beads. After more stirring, the beads are allowed to air dry, are gently ground in a mortar and pestle to break up the clumps that form, and are re-sized in sieves.

Once the beads are dyed, the circulation can be studied. For this, 129 ml of the desired undyed beads are put into the vessel, the vibrator is turned on and set to K = 2, and the bed is vibrated until the center-high bunker forms. At this point, the vibrations are stopped and 0.5 ml of one color of dyed beads (of the same size and density as the bulk of the particles) is added next to one side wall. The same amount of a second color of the dyed beads is added at the opposite wall. The bed is illuminated by an ultra-violet lamp (Ultra-Violet Products, Incorporated model B-100 A), the white lights are turned off, a video camera is turned on, and the vibrations are restarted at K = 2. Under these conditions, the dyed beads act as tracer particles which allow the circulation patterns to be mapped. Also, since the video camera has a clock which is superimposed on the tape, and a centimeter scale is drawn on the vessel with UV ink, the motion of individual particles can be timed to allow estimation of particle velocities. The particles are taped for about 15-20 minutes, and then the K-value is increased to 4. After another 15 or 20 minutes, the K-value is set to 6. Following this, a different size or type of particle is used and the procedure is repeated.

4.2.7 Measurement of Resistance to Flow

The apparatus described in Section 3.2.2.3 is used to measure the relative resistance to flow, or relative "apparent viscosity," of different types and sizes of particles. As mentioned in that section, the principle of the experiment is to measure the time taken to pull a steel rod through the vibrated bed over a set distance with a given force. Comparison of the times for different particles then gives the relative viscosities of the different particles.

The experiment is run in the two-dimensional vessel with 130 ml (3 cm equivalent depth) of the desired solid. Vibrations are set to the desired K-value, and the bunker (if there is one) is allowed to form. The apparatus holding the rod (see Figure 3.11) is slowly moved to the right by the length of travel of the linear bearing (1 inch). This lifts the weight by that amount and also moves the rod assembly just into the beam of the optical sensor. As soon as the rod assembly is released, it moves out of the sensor beam which sends a trigger to the A/D board and begins data collection. The A/D board then samples the output from the LVDT transducer which provides position of the rod assembly versus time. These data are then stored to diskette by an IBM PC. The time at which the curve of rod position *versus* time becomes horizontal, which occurs when the linear bearing hits its stop, is taken as the time of travel.

Chapter 5 Vibrated-Bed Dynamics: Results and Discussion

This chapter presents the work undertaken in this study on particle dynamics in shallow vibrated beds. The first section reports experiments on the nature of the bed-vessel separation, including predictions from two porous-piston models. The second section reports work on bed-vessel collision with comparisons to the same two models. Following this, observations on propagation of stress waves caused by bed compaction on collision are reported, and the vertical and horizontal components of propagation of the waves are estimated from experiment.

Particle circulation patterns, as observed in a two-dimensional vessel with a "dummy" heating probe, are presented for 707, 177, and 88-μm particles of both high and low-density glass at K-values of 2, 4, and 6. An estimate of particle velocities for the two smaller sizes of low-density glass is made. The instantaneous floor pressures are measured at three horizontal locations beneath a vibrated bed of solids to identify horizontal pressure gradients. Resistance of a vibrated bed to a rod pulled through it is used as a measure of "apparent viscosity" of the bed. The results from the experiments and observations are used to formulate explanations for both bunkered and non-bunkered circulation. Finally, the most significant results from this particle dynamics study are summarized.

5.1 Bed-Vessel Separation

Separation of the particle bed with the vessel floor occurs cyclically for most particle sizes at sufficiently high vibrational intensity. As noted in Section

2.1.4, many previous investigators have studied this phenomenon with different techniques. Most of the models in Section 2.1.7 can be solved to predict the point of separation. This section examines the predictions made by two of the models for specific particles, presents the measurements from this study, and compares the predictions with observed results.

5.1.1 Separation Calculated from the Kroll and Thomas Models

Two models of the vibrated bed are used to predict the point of separation of the bed with the vessel floor: the Kroll model discussed in Section 2.1.7.2 and the Thomas model discussed in Section 2.1.7.6.

The Kroll model is based on the rigid, porous, plastic piston assumption. Furthermore, the gas passing through the bed and accumulating in the gap beneath is assumed to be incompressible in this model. A result of this latter assumption is that the bed-vessel separation is not a function of particle size, but merely of vibrational intensity.

The Thomas model cited in this section is a one-dimensional version of the one described in Section 2.1.7.6. This model uses directly-measured gas pressures in the gap rather than theoretically calculated ones. For this reason, Thomas [1988] termed his model "semi-empirical."

Table 5.1 presents the calculated vibrational phase angles of separation based on these models for three size ranges of Master Beads: 707, 177 and 88 μm. The solutions to the Kroll model are obtained from equation [2.18] and the solutions to the Thomas model are from Thomas [1988] who used a numerical method to solve his model.

Table 5.1. Phase angles of bed-vessel separation predicted by the Kroll and Thomas models.

K-value	Kroll Model	Thomas Model
707-μm Master Beads		
2	30.0°	31.2°
3	19.5°	20.2°
4	14.5°	14.3°
5	11.5°	--
177-μm Master Beads		
2	30.0°	31.4°
3	19.5°	20.5°
4	14.5°	15.1°
5	11.5°	12.1°
88-μm Master Beads		
2	30.0°	30.7°
3	19.5°	19.8°
4	14.5°	14.3°
5	11.5°	--

Note that the separation angle of a given particle size at a fixed K-value does not vary by more than two degrees for the two models. The angles calculated by the Thomas semi-empirical model based on measured pressures tend to be slightly larger than those from the Kroll model.

5.1.2 Results of the Vibrated-Disc Experiments

The apparatus described in Section 3.3.4 has been used to measure the separation of the particle bed with the vessel floor as described in Section 4.2.2. The principle of operation is that the sine wave imposed on the disc at its resonance frequency creates a relatively large vibrational amplitude. Since the disc is piezoelectric, it generates an output voltage proportional to the displacement of the disc from its rest position. When displayed on an oscilloscope, this output voltage also appears sinusoidal with the same frequency as the input signal. The addition of relatively few particles onto the vibrating disc causes the mass of the system (now the disc and the particles) to change. This change in mass means that the system is no longer at resonance, and the amplitude of the disc displacement (and thus the output voltage amplitude) is greatly reduced. Monitoring the output voltage, therefore, constitutes one method of determining when the particles separate from the vessel floor.

Figures 5.1-5.15 show plots of the output from the vibrated-disc experiment. Note that the data for the two discs (the two plots which appear in the same figure) were not gathered in the same run, but sequentially due to the slight difference in resonance frequency of the discs. For this reason, the output voltage for the two plots cannot be compared meaningfully. It is the abrupt increase in voltage within a single plot which is of interest, however. This point is

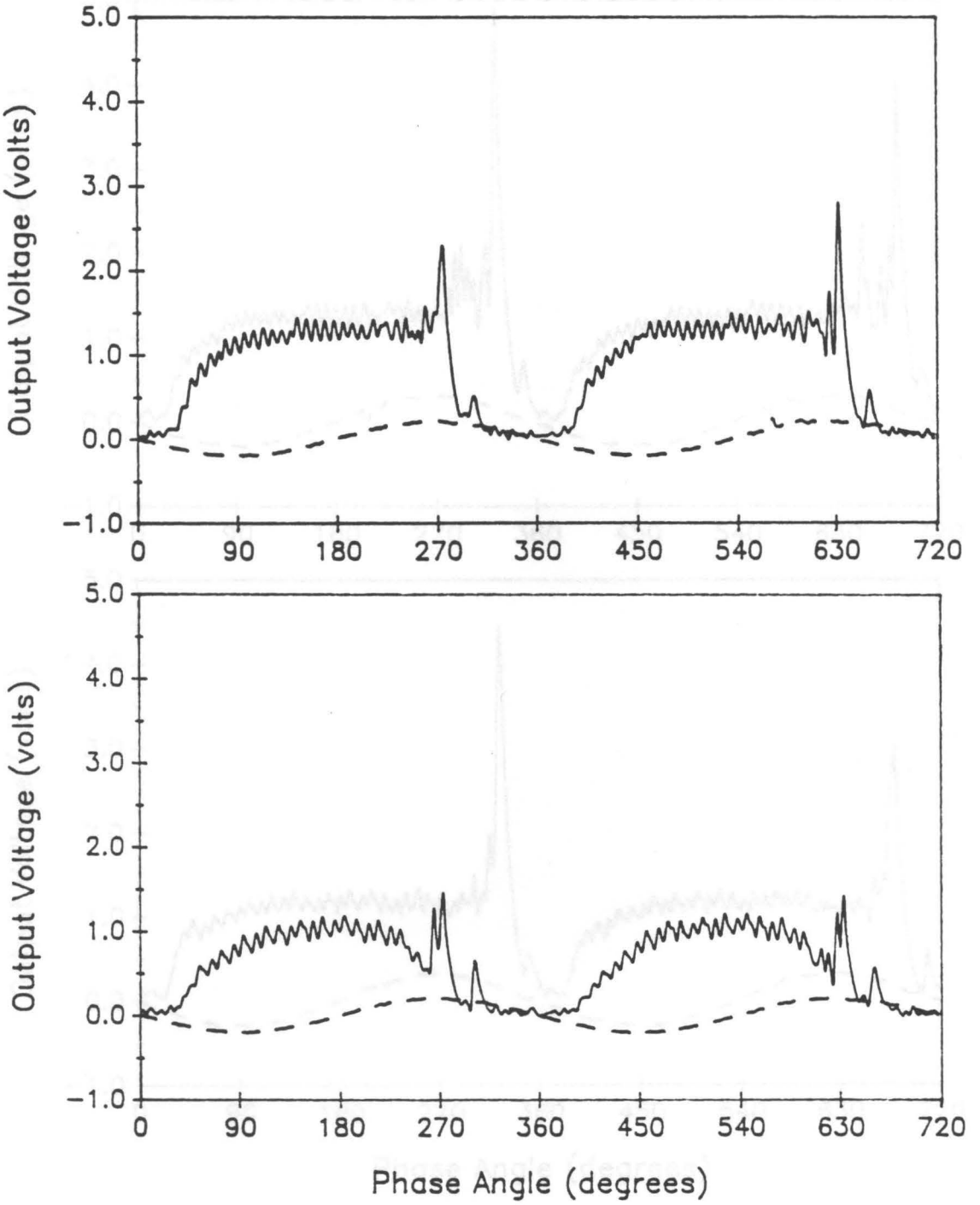

Figure 5.1. Output from the vibrated-disc experiment for 707-μm Master Beads at K = 2: Output voltage *versus* phase angle for output from disc (solid line) and accelerometer (dashed line) over two vibrational cycles. Top plot is for the edge disc; bottom plot is for the center disc.

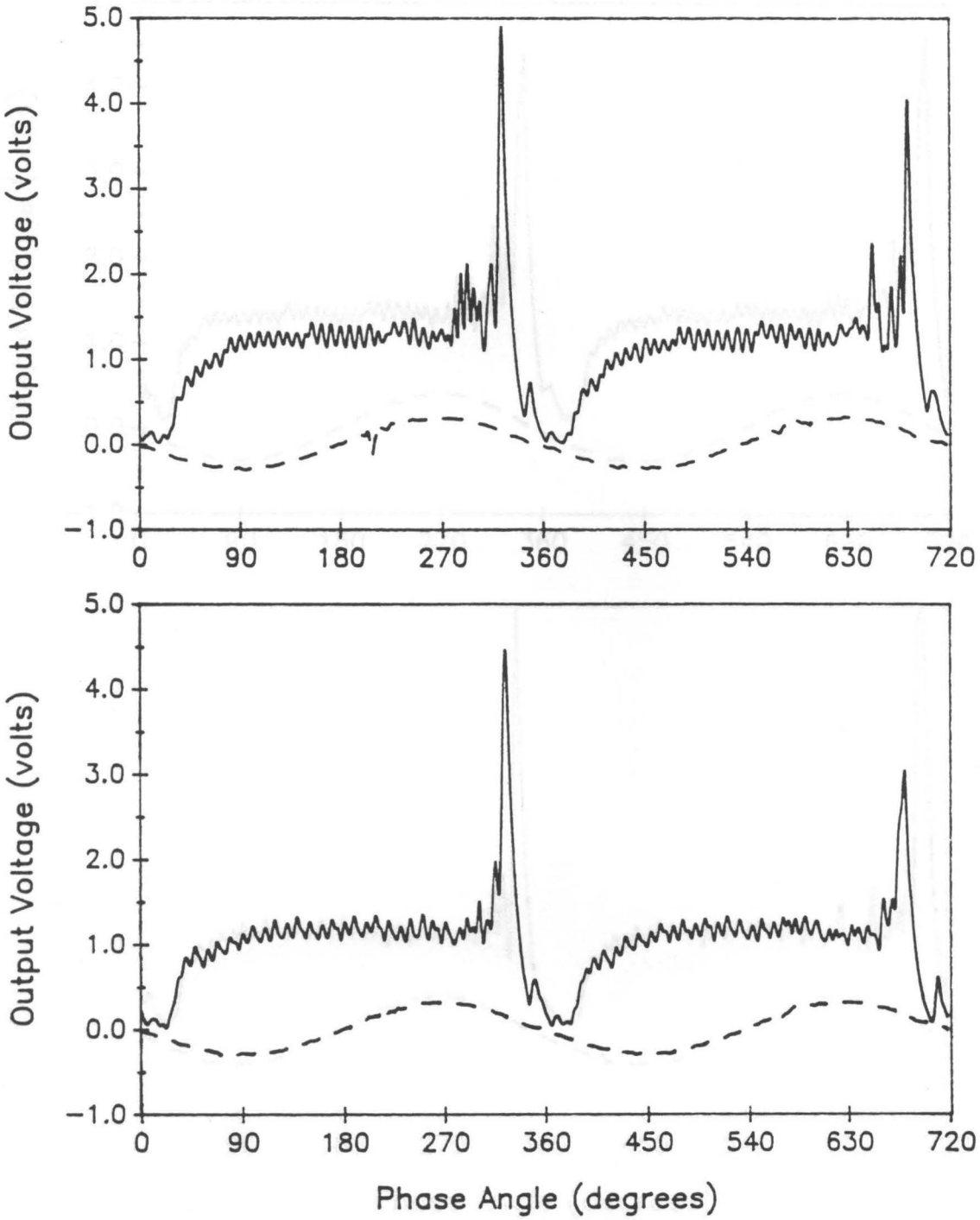

Figure 5.2. Output from the vibrated-disc experiment for 707-μm Master Beads at K = 3: Output voltage *versus* phase angle for output from disc (solid line) and accelerometer (dashed line) over two vibrational cycles. Top plot is for the edge disc; bottom plot is for the center disc.

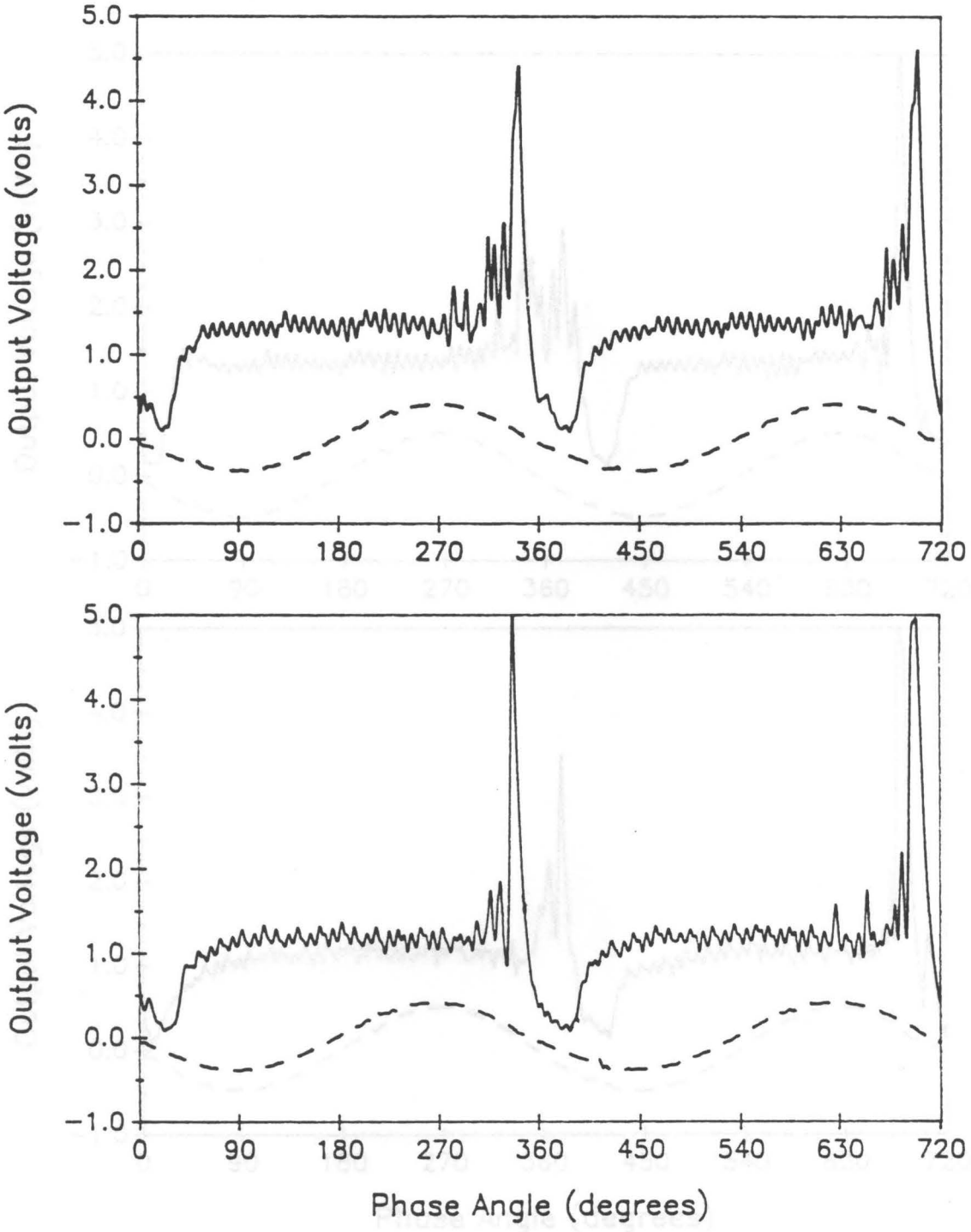

Figure 5.3. Output from the vibrated-disc experiment for 707-μm Master Beads at K = 4: Output voltage *versus* phase angle for output from disc (solid line) and accelerometer (dashed line) over two vibrational cycles. Top plot is for the edge disc; bottom plot is for the center disc.

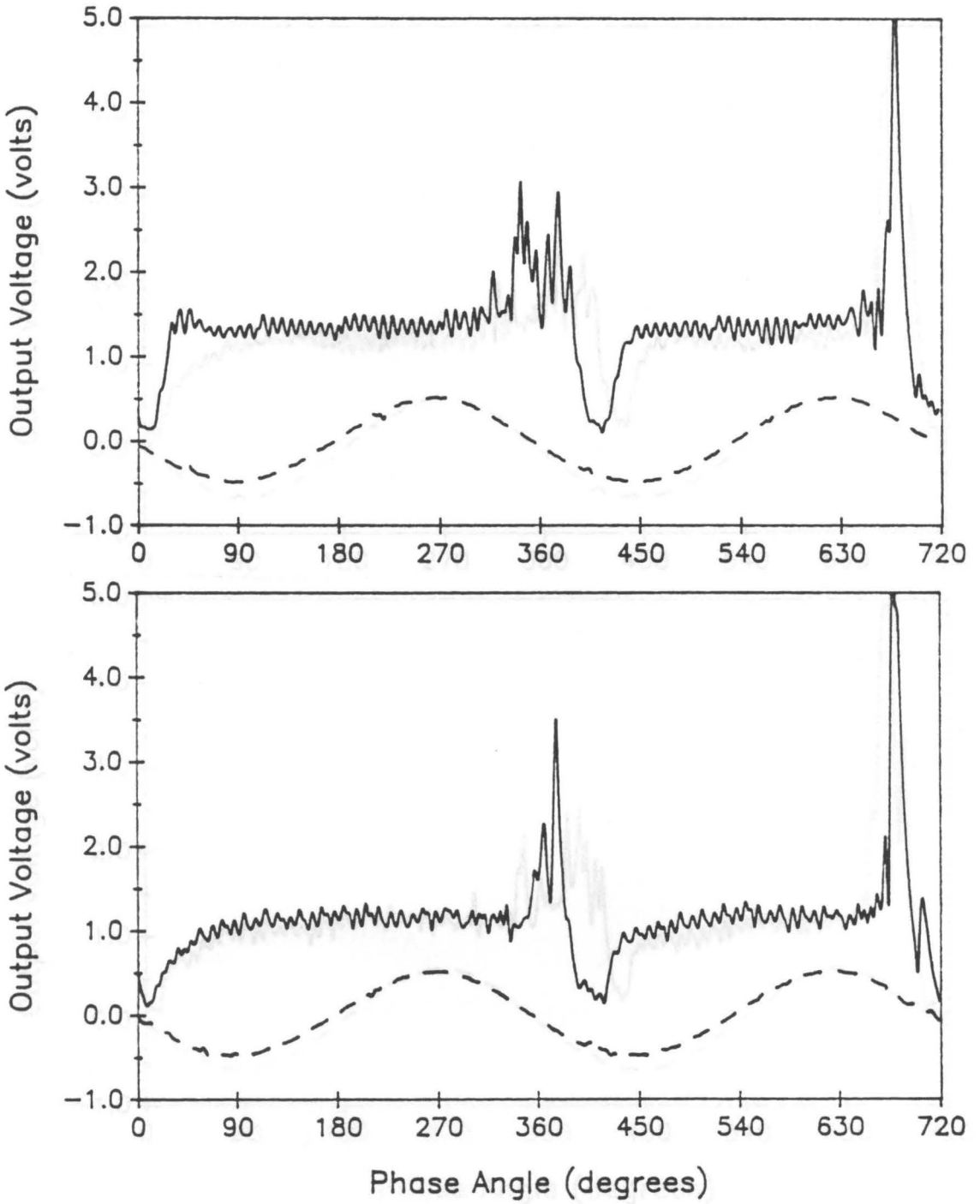

Figure 5.4. Output from the vibrated-disc experiment for 707-μm Master Beads at K = 5: Output voltage *versus* phase angle for output from disc (solid line) and accelerometer (dashed line) over two vibrational cycles. Top plot is for the edge disc; bottom plot is for the center disc.

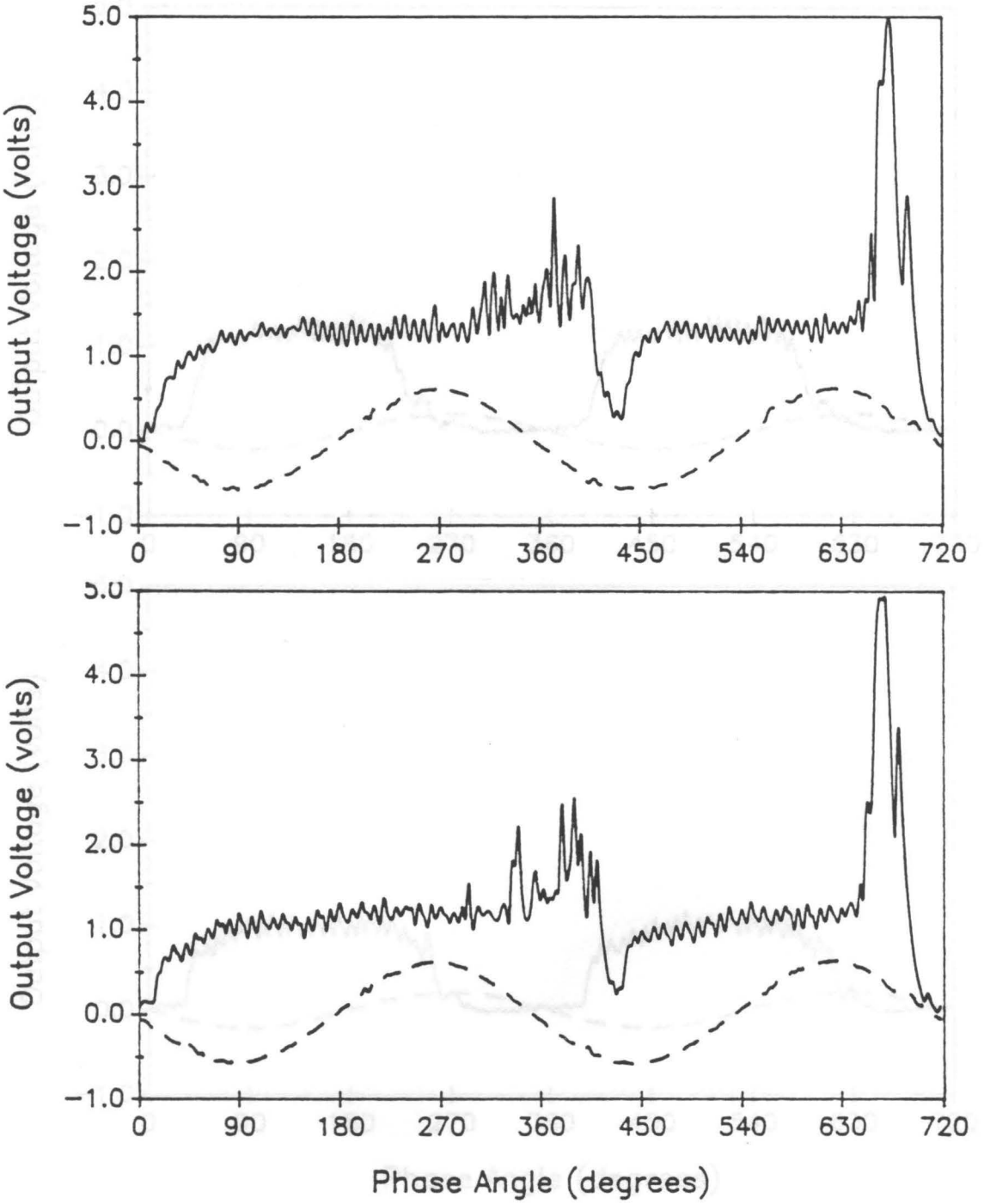

Figure 5.5. Output from the vibrated-disc experiment for 707-μm Master Beads at K = 6: Output voltage *versus* phase angle for output from disc (solid line) and accelerometer (dashed line) over two vibrational cycles. Top plot is for the edge disc; bottom plot is for the center disc.

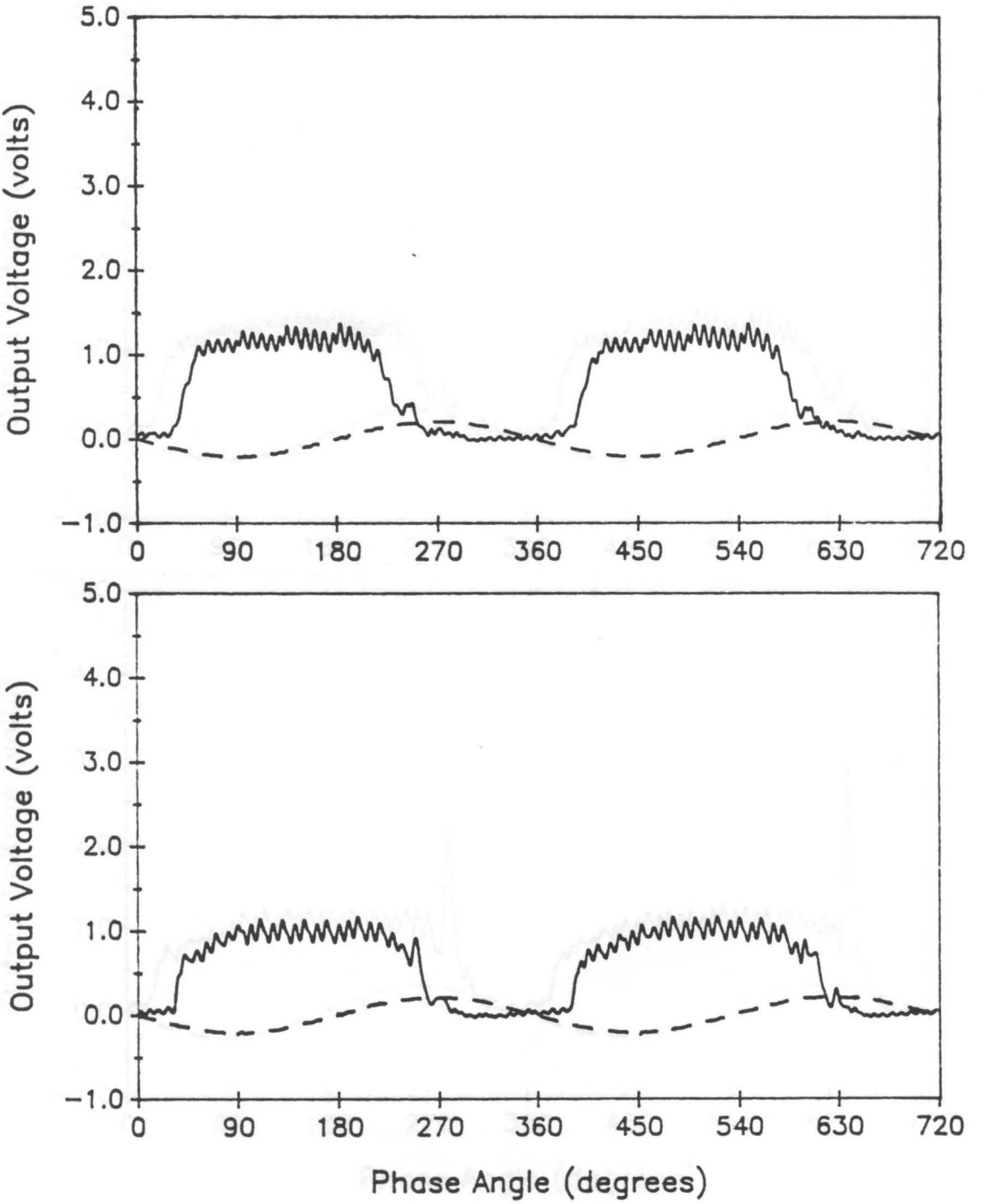

Figure 5.6. Output from the vibrated-disc experiment for 177-μm Master Beads at K = 2: Output voltage *versus* phase angle for output from disc (solid line) and accelerometer (dashed line) over two vibrational cycles. Top plot is for the edge disc; bottom plot is for the center disc.

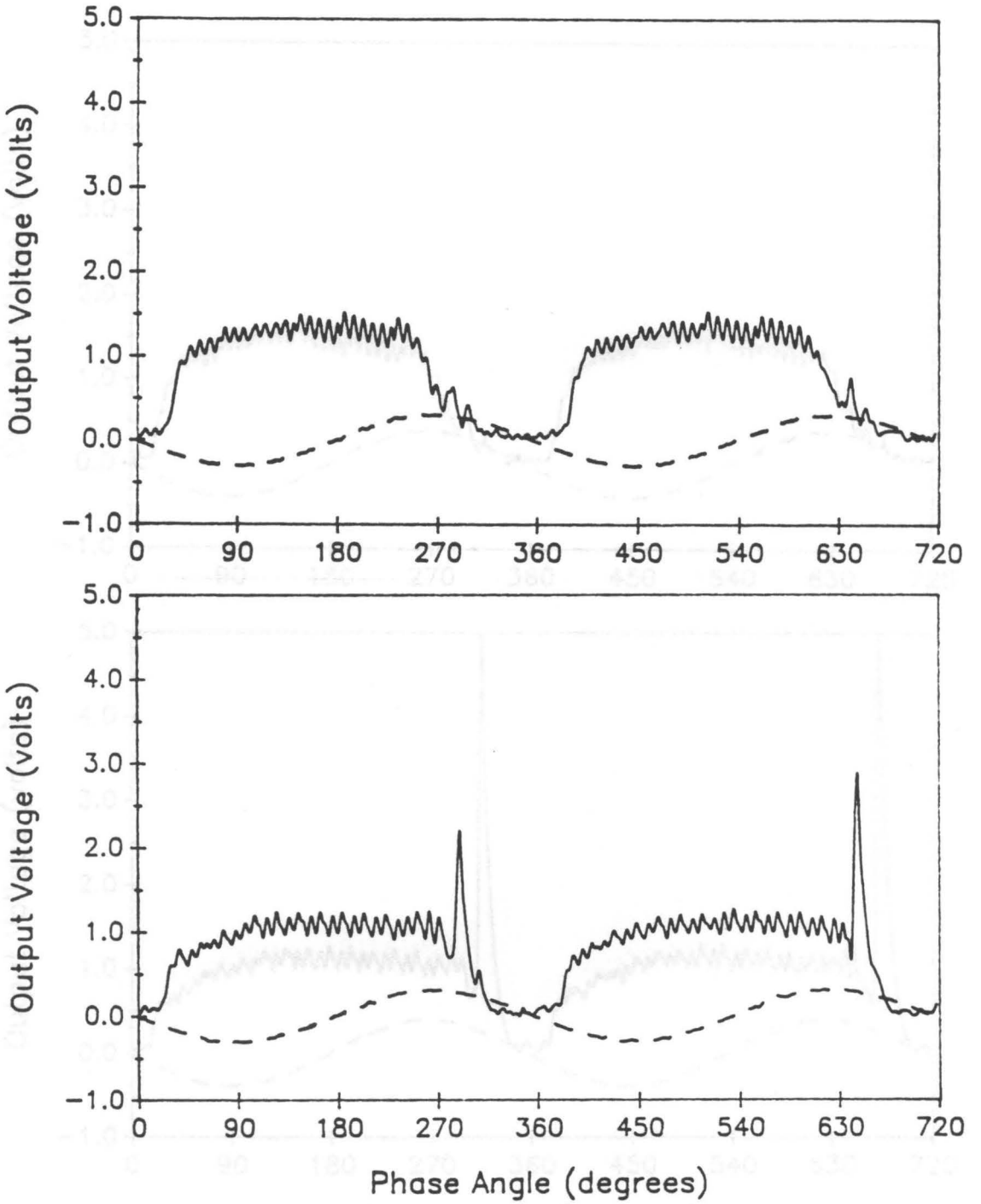

Figure 5.7. Output from the vibrated-disc experiment for 177-μm Master Beads at K = 3: Output voltage *versus* phase angle for output from disc (solid line) and accelerometer (dashed line) over two vibrational cycles. Top plot is for the edge disc; bottom plot is for the center disc.

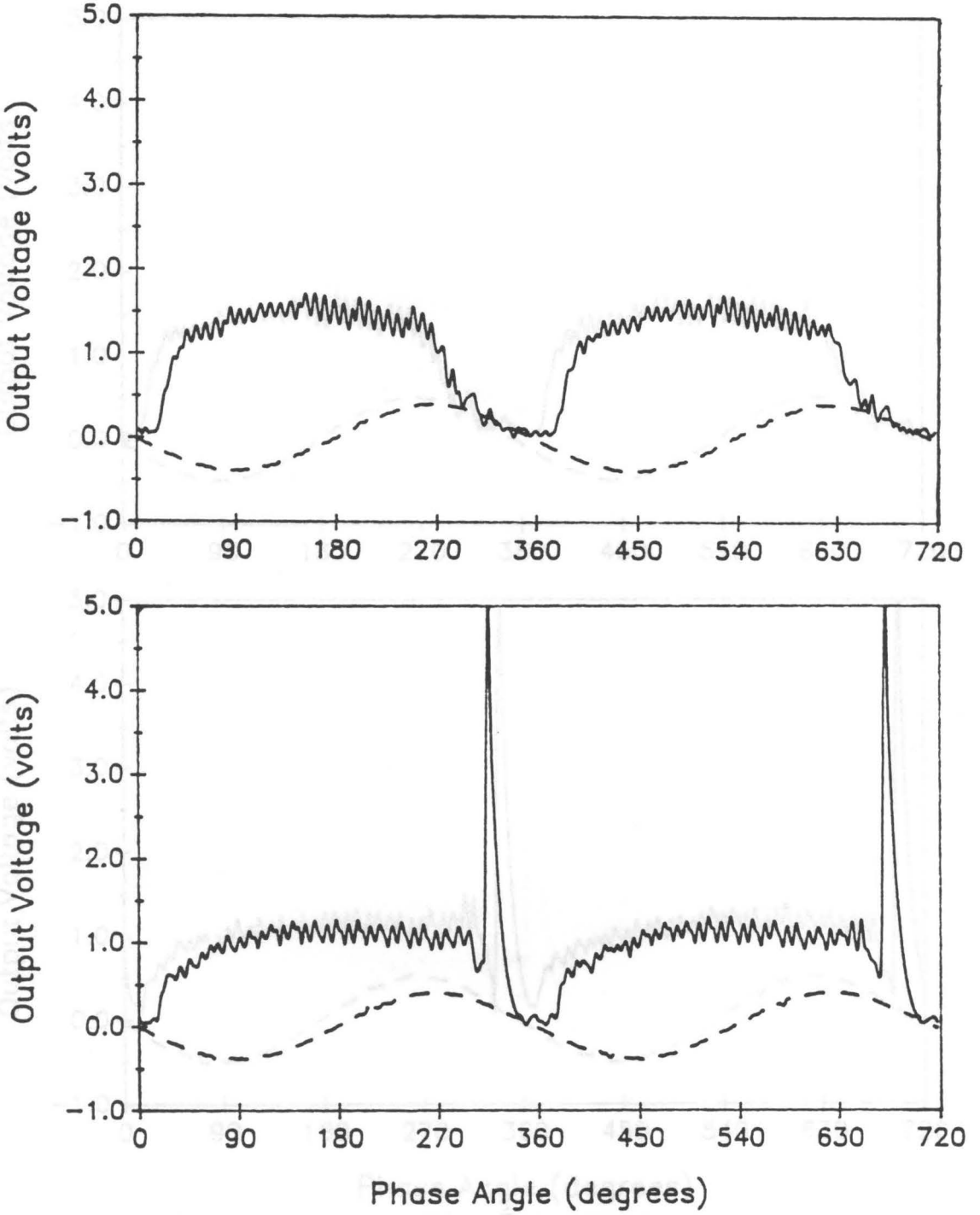

Figure 5.8. Output from the vibrated-disc experiment for 177-μm Master Beads at K = 4: Output voltage *versus* phase angle for output from disc (solid line) and accelerometer (dashed line) over two vibrational cycles. Top plot is for the edge disc; bottom plot is for the center disc.

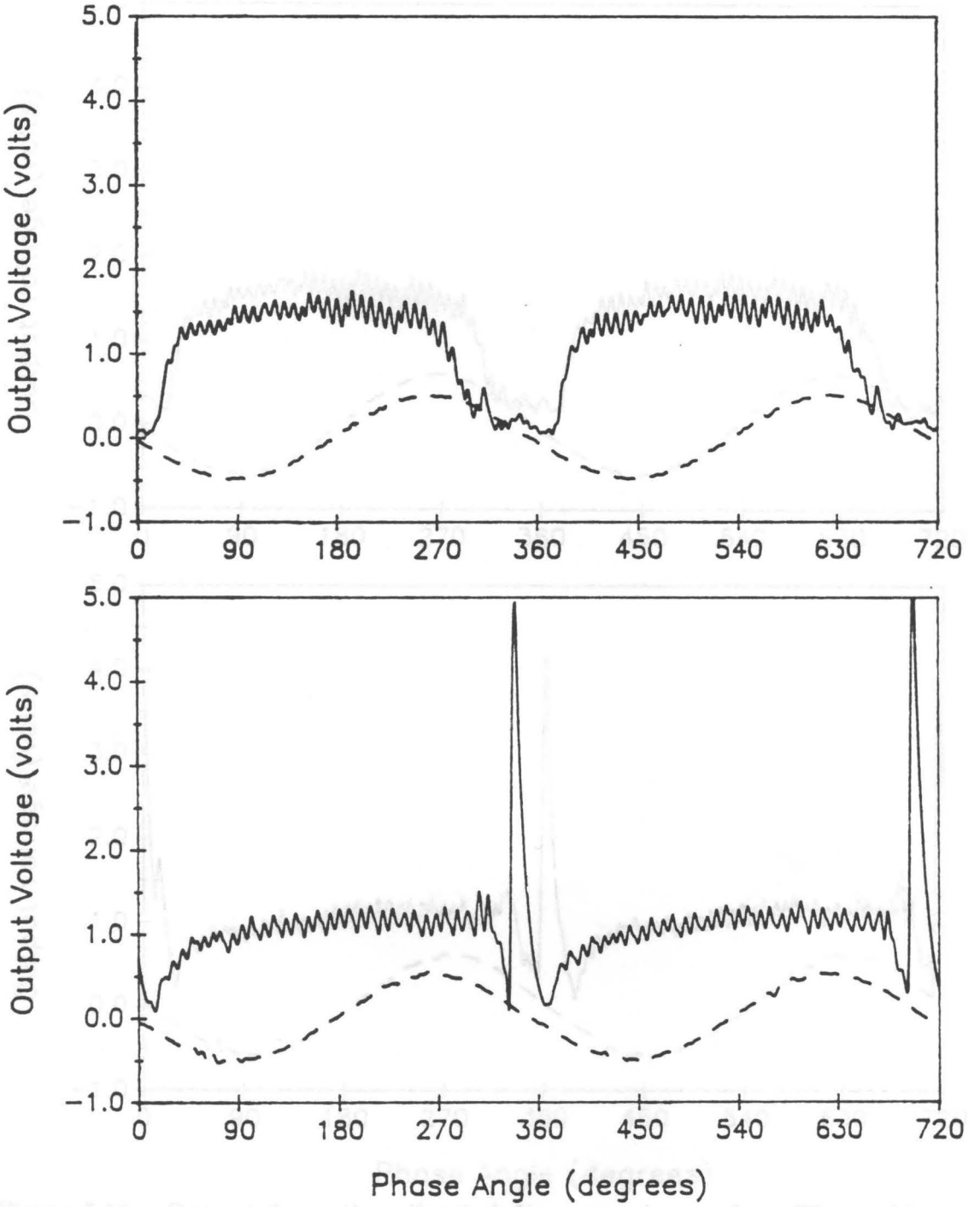

Figure 5.9. Output from the vibrated-disc experiment for 177-μm Master Beads at K = 5: Output voltage *versus* phase angle for output from disc (solid line) and accelerometer (dashed line) over two vibrational cycles. Top plot is for the edge disc; bottom plot is for the center disc.

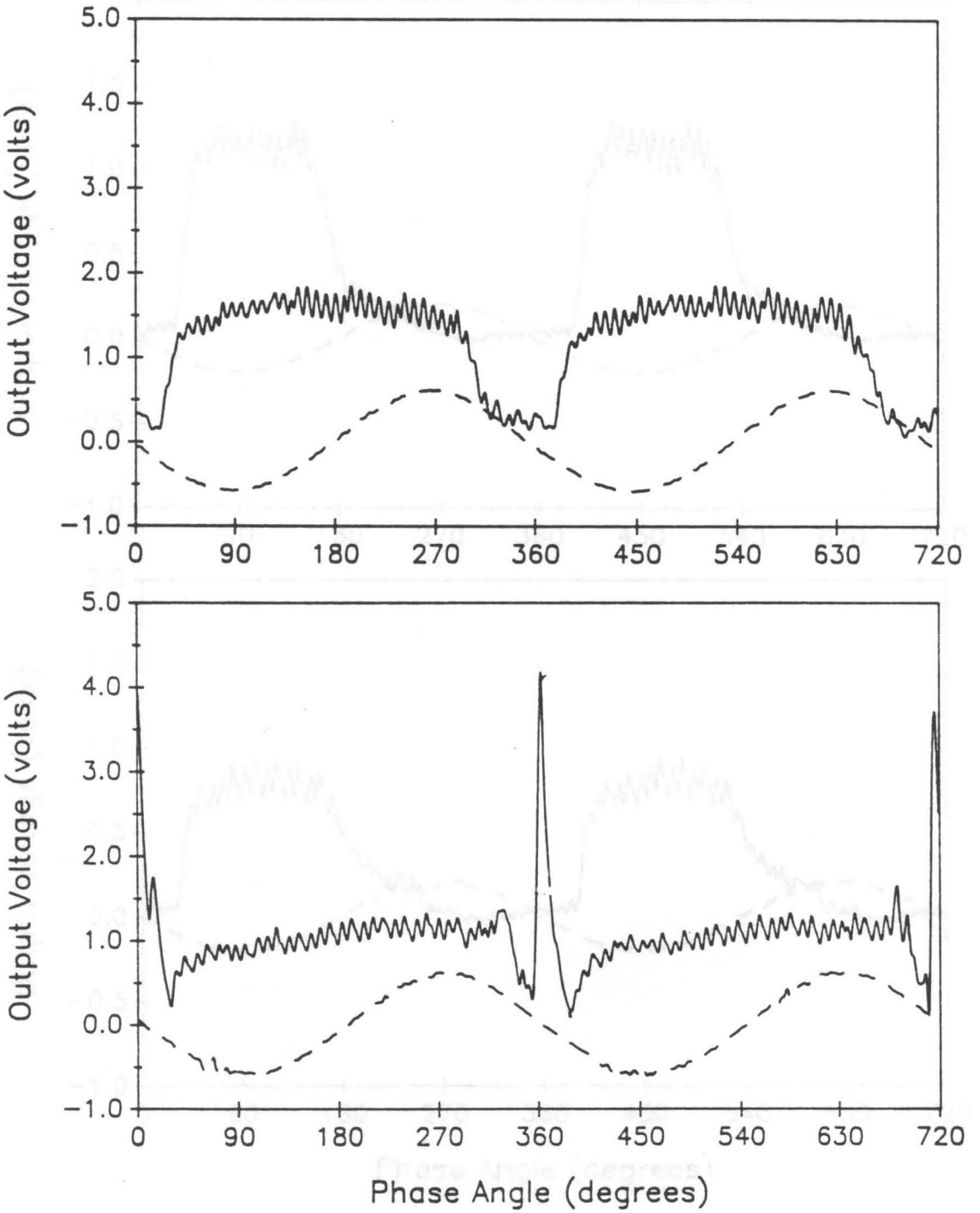

Figure 5.10. Output from the vibrated-disc experiment for 177-μm Master Beads at K = 6: Output voltage *versus* phase angle for output from disc (solid line) and accelerometer (dashed line) over two vibrational cycles. Top plot is for the edge disc; bottom plot is for the center disc.

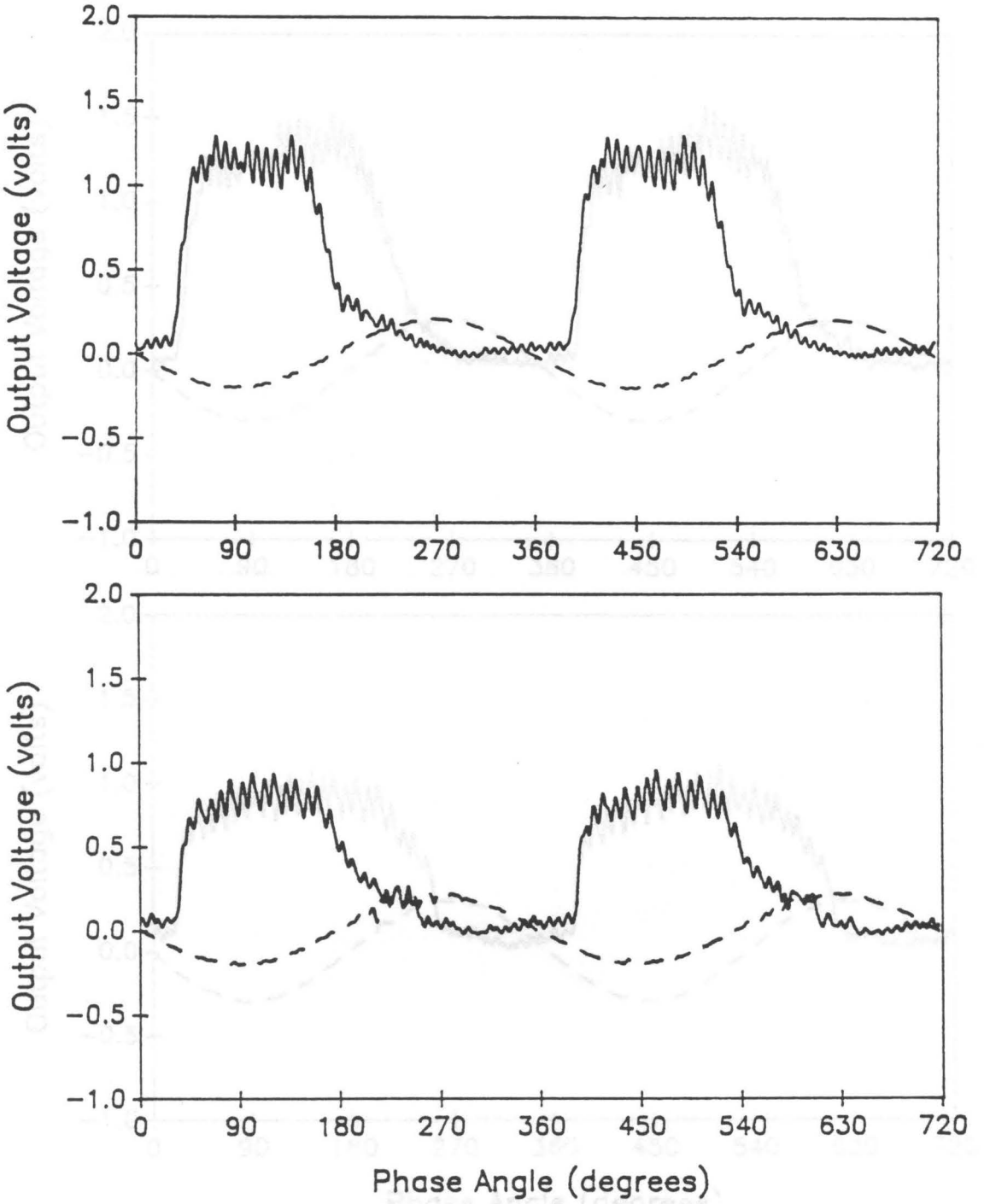

Figure 5.11. Output from the vibrated-disc experiment for 88-μm Master Beads at K = 2: Output voltage *versus* phase angle for output from disc (solid line) and accelerometer (dashed line) over two vibrational cycles. Top plot is for the edge disc; bottom plot is for the center disc.

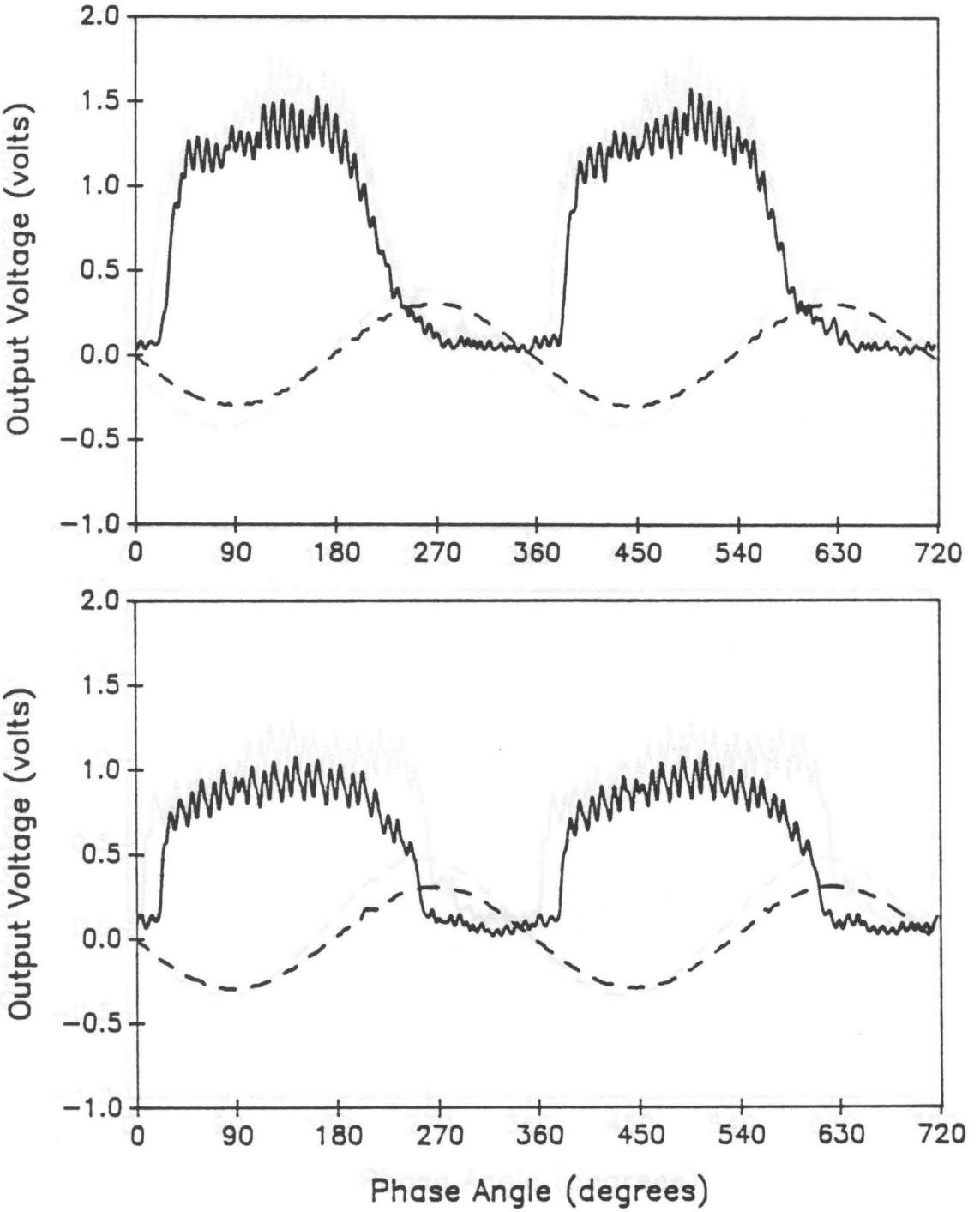

Figure 5.12. Output from the vibrated-disc experiment for 88-μm Master Beads at K = 3: Output voltage *versus* phase angle for output from disc (solid line) and accelerometer (dashed line) over two vibrational cycles. Top plot is for the edge disc; bottom plot is for the center disc.

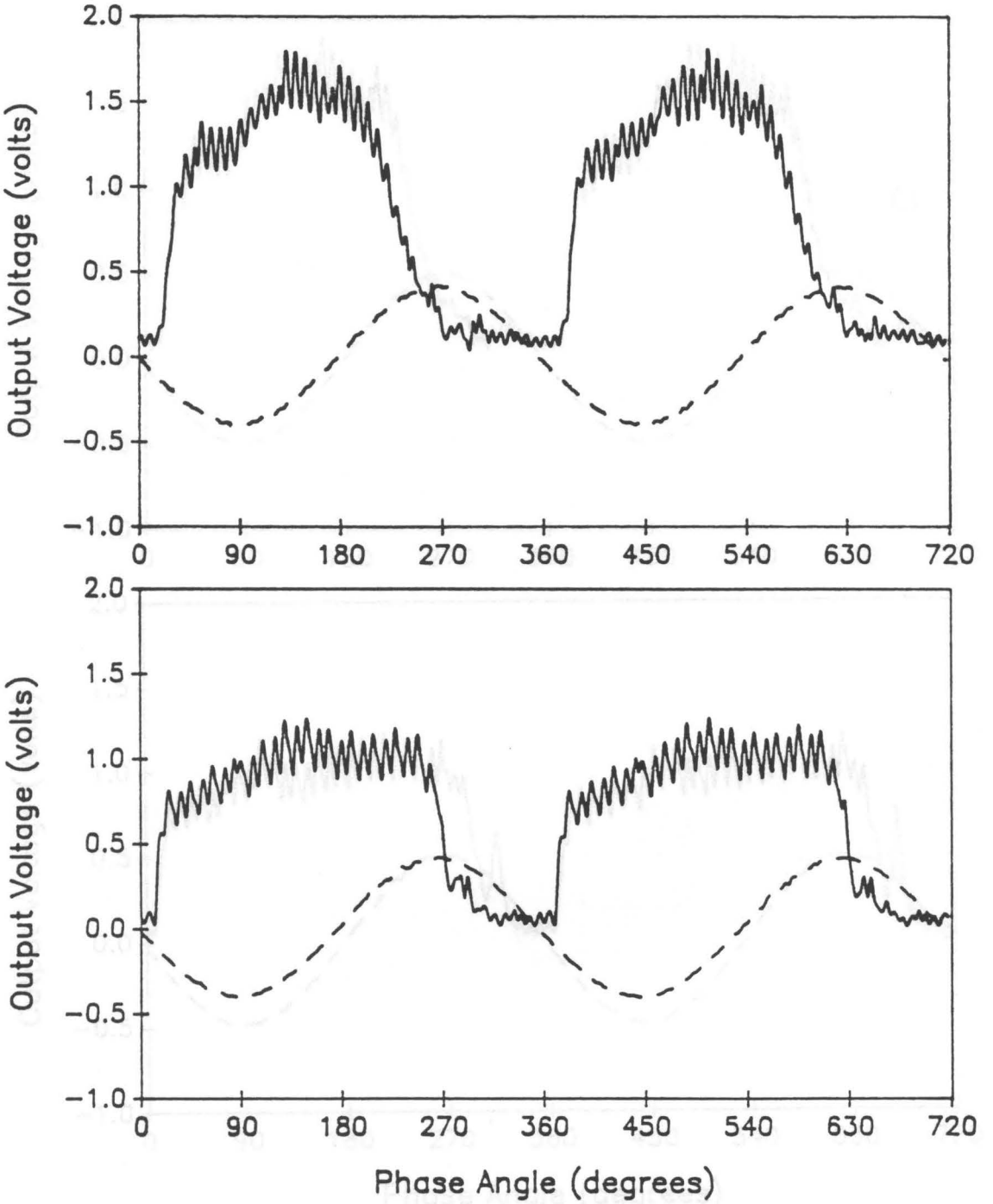

Figure 5.13. Output from the vibrated-disc experiment for 88-μm Master Beads at K = 4: Output voltage *versus* phase angle for output from disc (solid line) and accelerometer (dashed line) over two vibrational cycles. Top plot is for the edge disc; bottom plot is for the center disc.

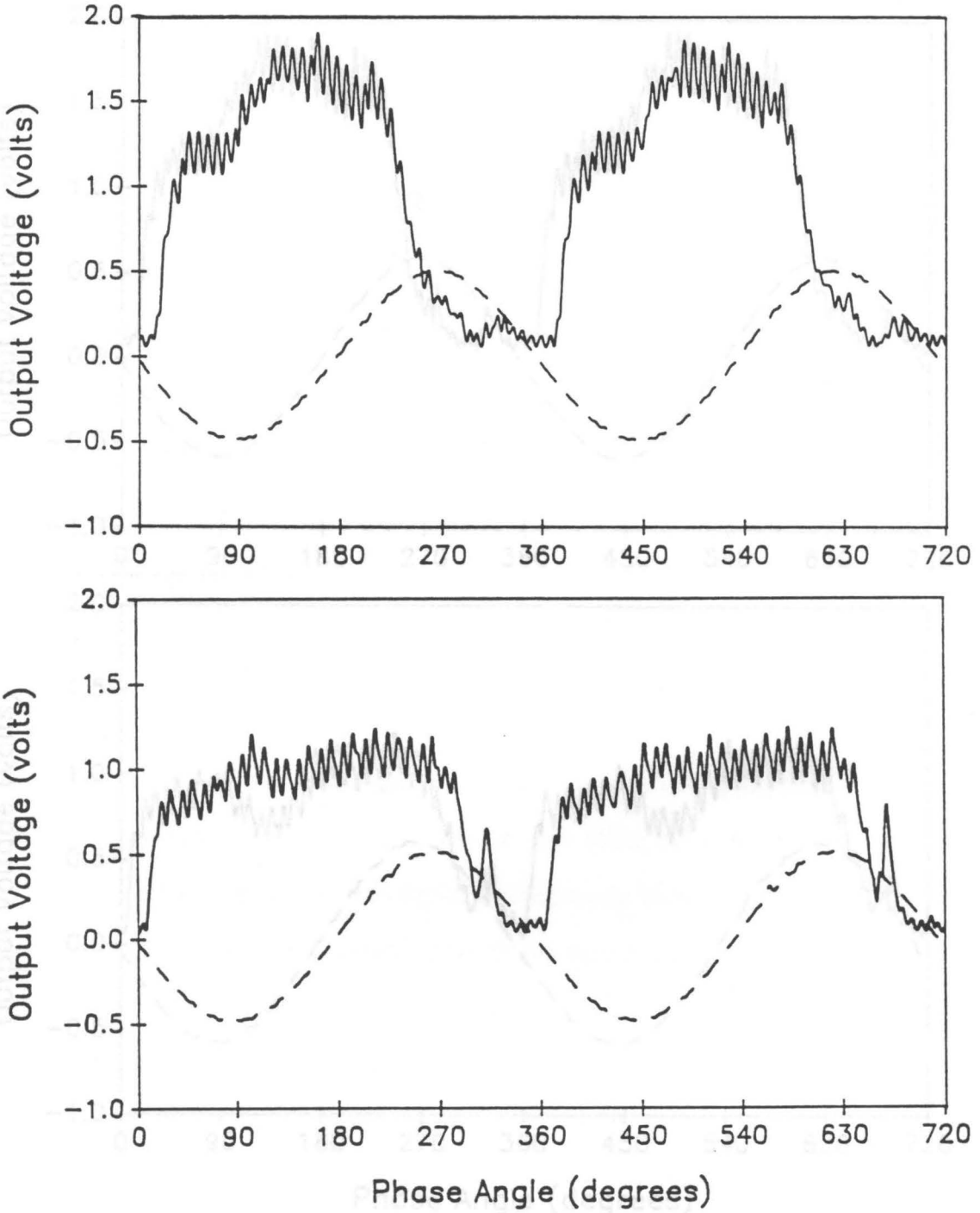

Figure 5.14. Output from the vibrated-disc experiment for 88-μm Master Beads at K = 5: Output voltage *versus* phase angle for output from disc (solid line) and accelerometer (dashed line) over two vibrational cycles. Top plot is for the edge disc; bottom plot is for the center disc.

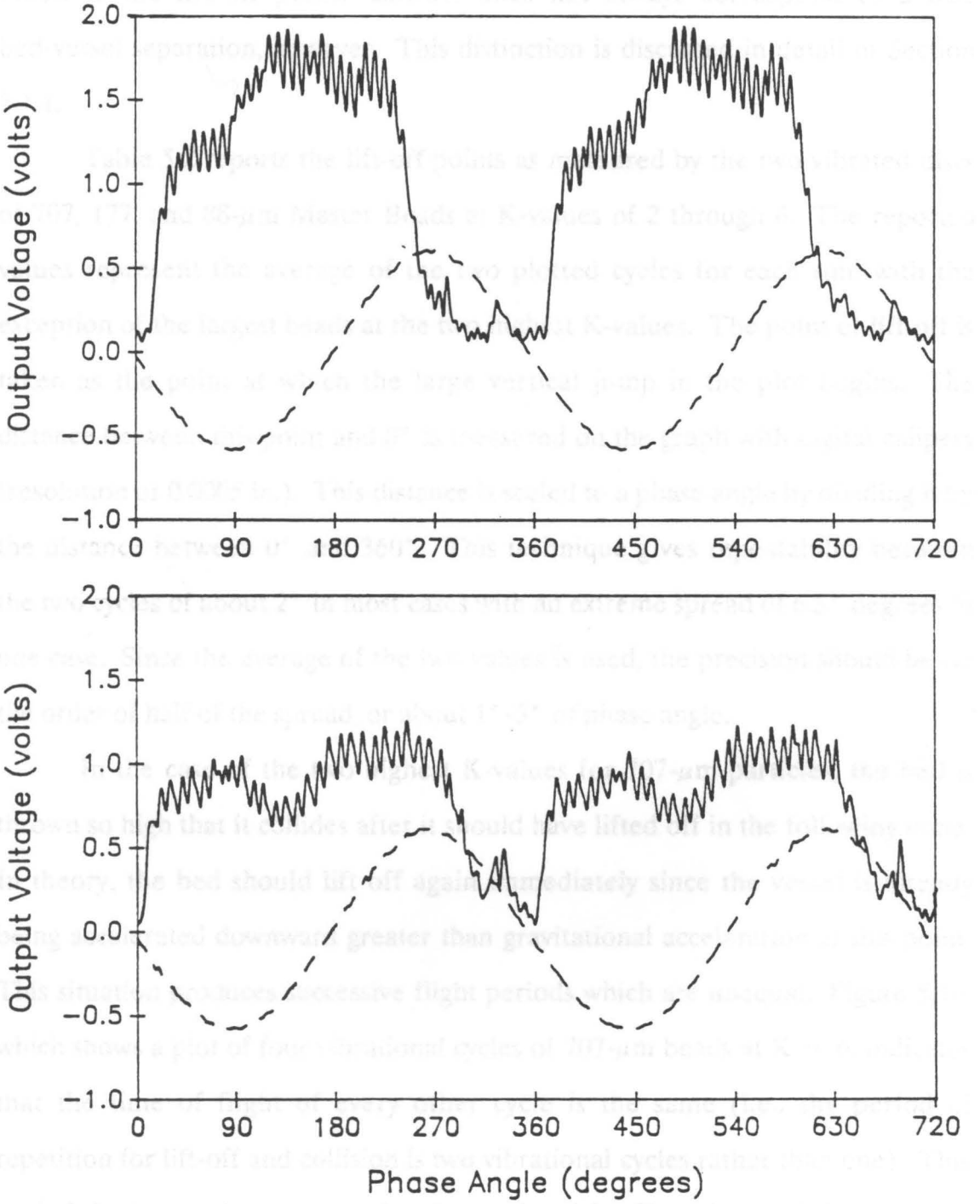

Figure 5.15. Output from the vibrated-disc experiment for 88-μm Master Beads at K = 6: Output voltage *versus* phase angle for output from disc (solid line) and accelerometer (dashed line) over two vibrational cycles. Top plot is for the edge disc; bottom plot is for the center disc.

taken as the lift-off point. Lift-off does not always correspond to a true bed-vessel separation, however. This distinction is discussed in detail in Section 5.1.4.

Table 5.2 reports the lift-off points as measured by the two vibrated discs of 707, 177, and 88-μm Master Beads at K-values of 2 through 6. The reported values represent the average of the two plotted cycles for each run, with the exception of the largest beads at the two highest K-values. The point of lift-off is taken as the point at which the large vertical jump in the plot begins. The distance between this point and 0° is measured on the graph with digital calipers (resolution of 0.0005 in.). This distance is scaled to a phase angle by dividing it by the distance between 0° and 360°. This technique gives repeatability between the two cycles of about 2° in most cases with an extreme spread of 6.5° degrees in one case. Since the average of the two values is used, the precision should be on the order of half of the spread, or about 1°-3° of phase angle.

In the case of the two highest K-values for 707-μm particles, the bed is thrown so high that it collides after it should have lifted off in the following cycle. In theory, the bed should lift off again immediately since the vessel is already being accelerated downward greater than gravitational acceleration at this point. This situation produces successive flight periods which are unequal. Figure 5.16, which shows a plot of four vibrational cycles of 707-μm beads at K = 6, indicates that the time of flight of every other cycle is the same (i.e., the period of repetition for lift-off and collision is two vibrational cycles rather than one). This period-doubling phenomenon has been noted by Douady *et al.* [1989], who observed it in relatively large-diameter (in the range of 630-800 μm) glass spheres above a critical threshold vibrational intensity. Since there are essentially two values of lift-off for these period-doubled cases (one for the long flight time and a

Table 5.2. Lift-off points measured by the vibrated discs.

All data are for Master Beads

K-value	Center Disc	Edge Disc
	707 μm	
2	35°	36°
3	23°	25°
4	24°	23°
5*	11° 58°	13° 55°
6*	11° 67°	11° 74°
	177 μm	
2	31°	34°
3	18°	18°
4	15°	17°
5	12°	13°
6	29°	19°
	88 μm	
2	38°	30°
3	18°	19°
4	11°	14°
5	6°	12°
6	0°	11°

*Bed is in a period-doubling state

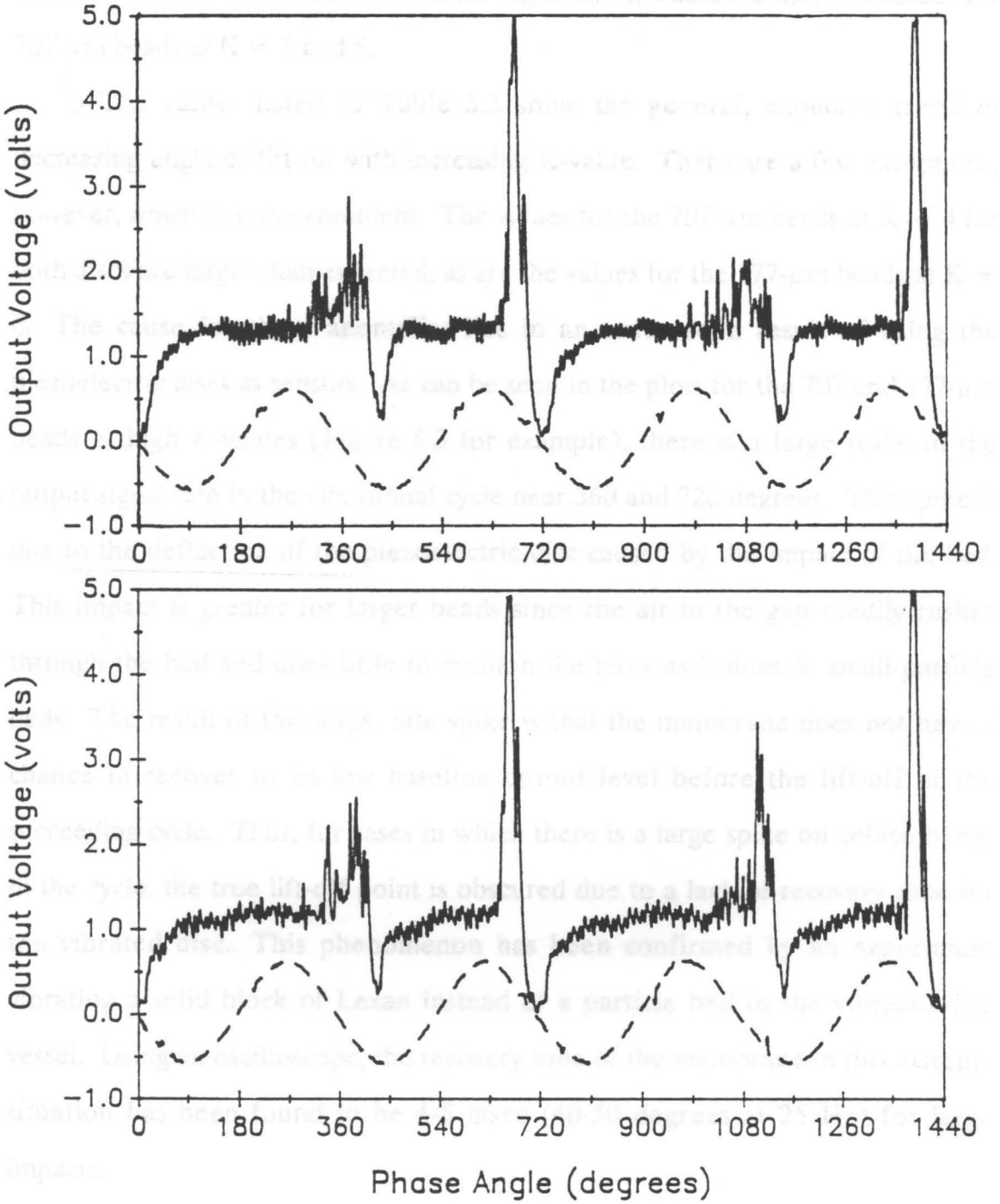

Figure 5.16. Output from vibrated discs over four cycles for 707-μm Master Beads at K = 6: Note that cycles 1 and 3 are the same, as are 2 and 4.

different one for the successive shorter flight time), Table 5.2 lists two values for 707-μm beads at K = 5 and 6.

The values listed in Table 5.2 show the general, expected trend of decreasing angle of lift-off with increasing K-value. There are a few exceptions, however, which deserve comment. The values for the 707-μm beads at K = 4 for both discs are larger than expected, as are the values for the 177-μm beads at K = 6. The cause for these anomalies lies in an unforeseen result of using the piezoelectric discs as sensors. As can be seen in the plots for the 707 and 177-μm beads at high K-values (Figure 5.3 for example), there is a large spike in the output signal late in the vibrational cycle near 360 and 720 degrees. This spike is due to the deflection of the piezoelectric disc caused by the impact of the bed. This impact is greater for larger beads since the air in the gap readily rushes through the bed and does little to cushion the blow as it does in small-particle beds. The result of this large, late spike is that the membrane does not have a chance to recover to its low baseline output level before the lift-off of the succeeding cycle. Thus, for cases in which there is a large spike on collision late in the cycle, the true lift-off point is obscured due to a lack of recovery time for the vibrated disc. This phenomenon has been confirmed by an experiment vibrating a solid block of Lexan instead of a particle bed in the vibrated-disc vessel. Using an oscilloscope, the recovery time of the membrane in this extreme situation has been found to be 4-5 msec (40-50 degrees at 25 Hz) for large impacts.

Comparison of the lift-off times for the center and edge discs at the same K-values shows little significant difference for the 707-μm beads. For the two smaller sizes, where the beads exhibit bunkered behavior, the center lifts marginally earlier (with the exception of the spurious K = 6 case for the 177-μm

beads mentioned above). This effect is most clearly seen for the smallest (88 μm) beads at the higher K-values. A probable cause for this is the residual pressure beneath the bed. Since the bed is deepest in the center for bunkered beds, the pressure beneath the center of the bed is greater than at the edge upon collision. Since the gas is compressible, the pressure does not decay instantaneously and is still greater than atmospheric at the start of the next cycle. This positive pressure acts as an upward force on the bed which causes an earlier lift-off.

5.1.3 Results of the Capacitance-Probe Experiments

The capacitance-probe device described in Section 3.3.5 has been used to measure lift-off as described in Section 4.2.2 for the same solids as used in the vibrated-disc experiment. The principle behind this experiment is to measure the onset and growth of the gap by monitoring the change in capacitance. The capacitance change is brought about by the difference in dielectric constant between the particle bed and the gap (air).

Figures 5.17-5.31 show plots of the output obtained from the capacitance probe experiments. The interpretation of this data is more difficult than in the case of the vibrated-disc experiments because the changes are less dramatic. The point in the cycle at which the curve departs from the horizontal is taken as the point of lift-off. As before, the values for the two cycles plotted are averaged. Due to greater uncertainty in the measurements, the repeatablity is only about 10° for the 707-μm particle, but still about 3° for 177-μm particles. Period-doubling is again observed in the 707-μm beads at K = 5 and 6.

Table 5.3 reports apparent lift-offs of 707 and 177-μm Master Beads. Although data have been plotted for 88-μm beads in Figures 5.27-5.31, no lift-off

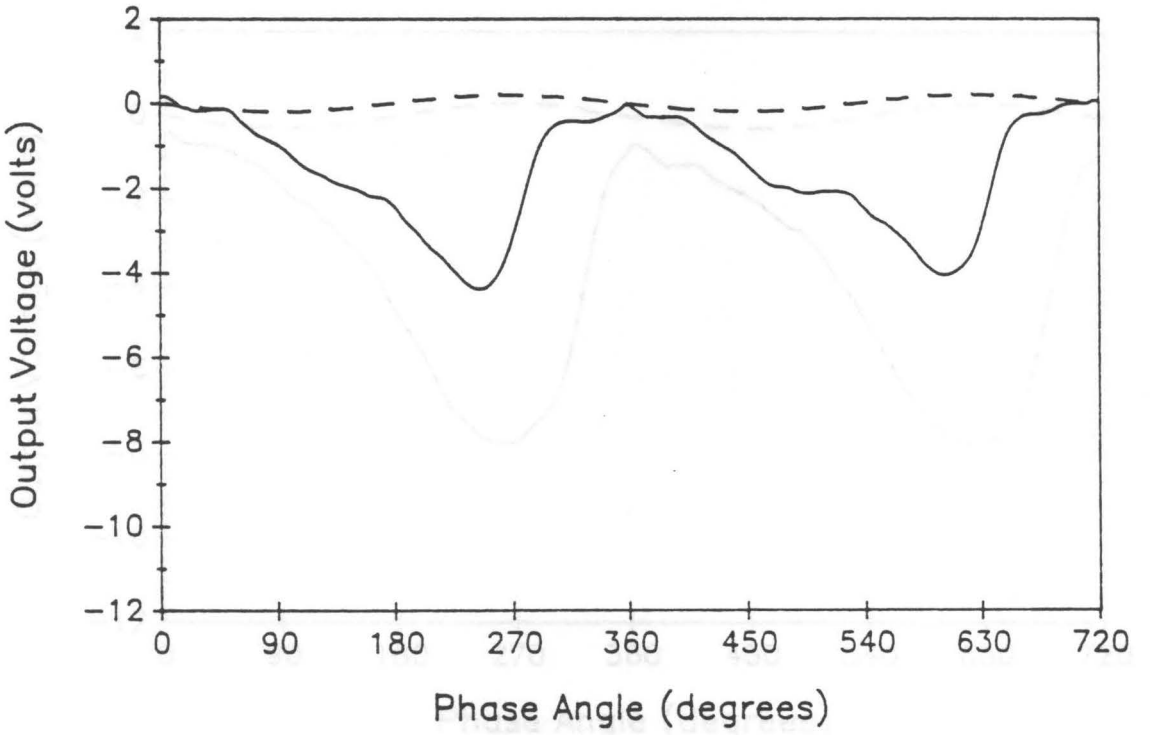

Figure 5.17. Output from the capacitance-probe experiment for 707-μm Master Beads at K = 2: Output voltage *versus* phase angle for output from capacitance probe (solid line) and accelerometer (dashed line) over two vibrational cycles.

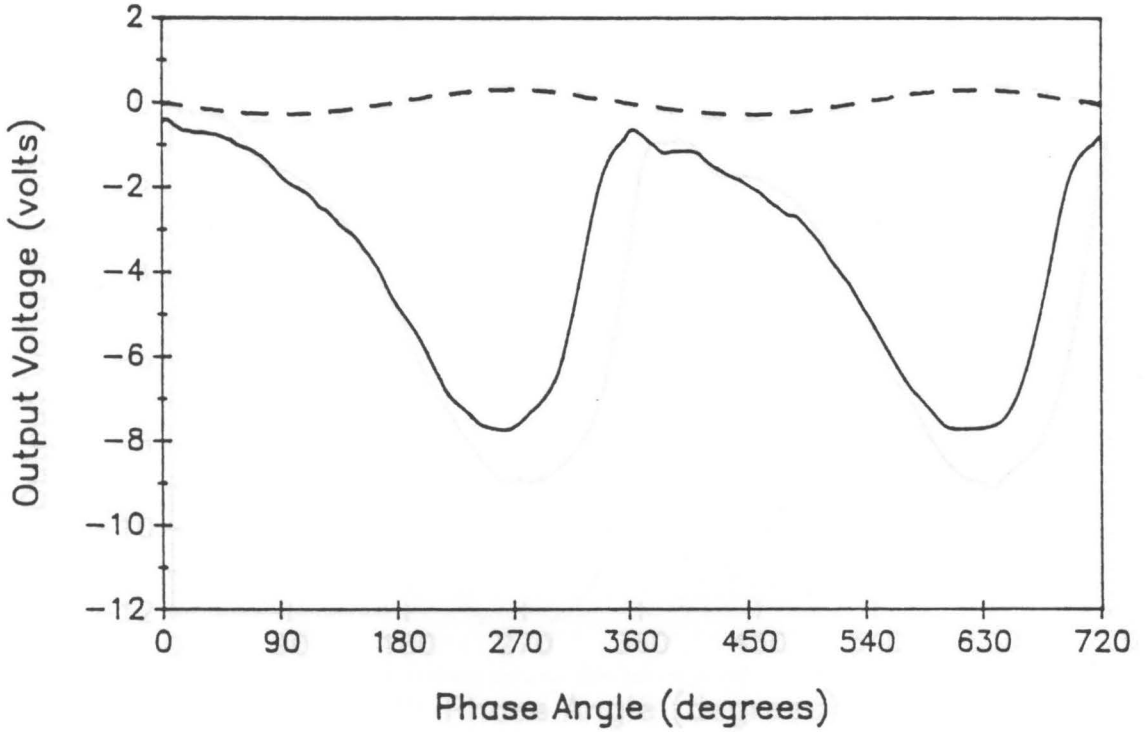

Figure 5.18. Output from the capacitance-probe experiment for 707-μm Master Beads at K = 3: Output voltage *versus* phase angle for output from capacitance probe (solid line) and accelerometer (dashed line) over two vibrational cycles.

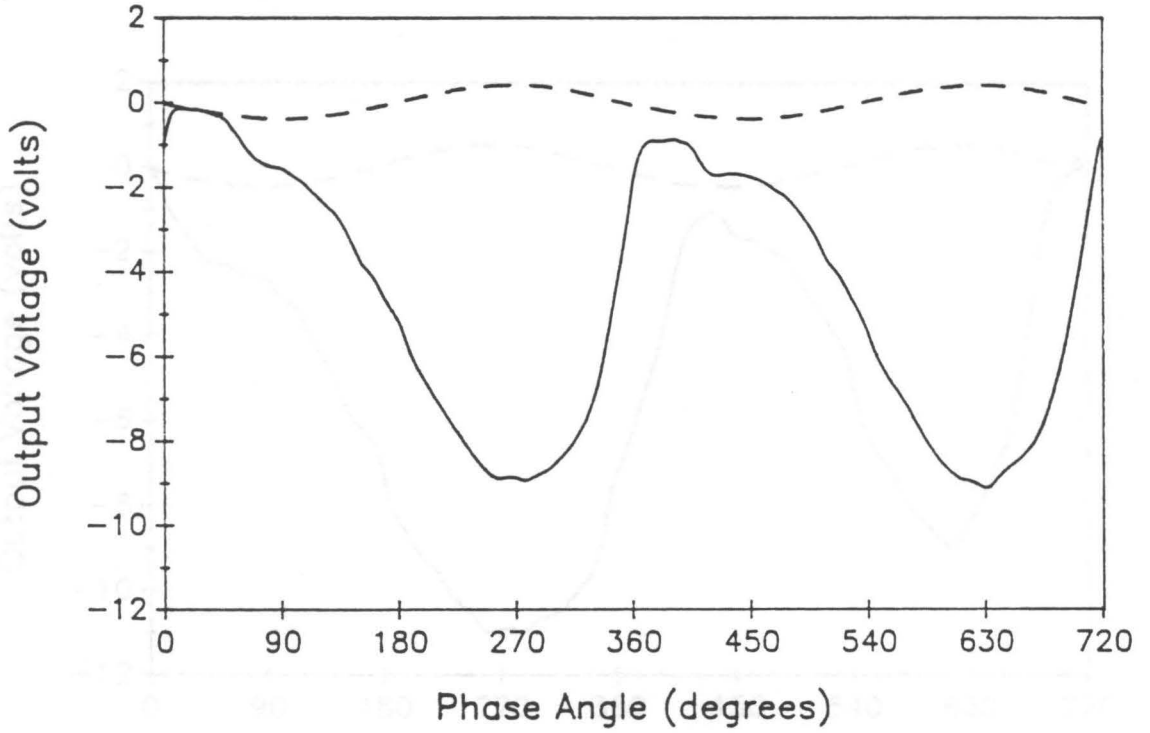

Figure 5.19. Output from the capacitance-probe experiment for 707-μm Master Beads at K = 4: Output voltage *versus* phase angle for output from capacitance probe (solid line) and accelerometer (dashed line) over two vibrational cycles.

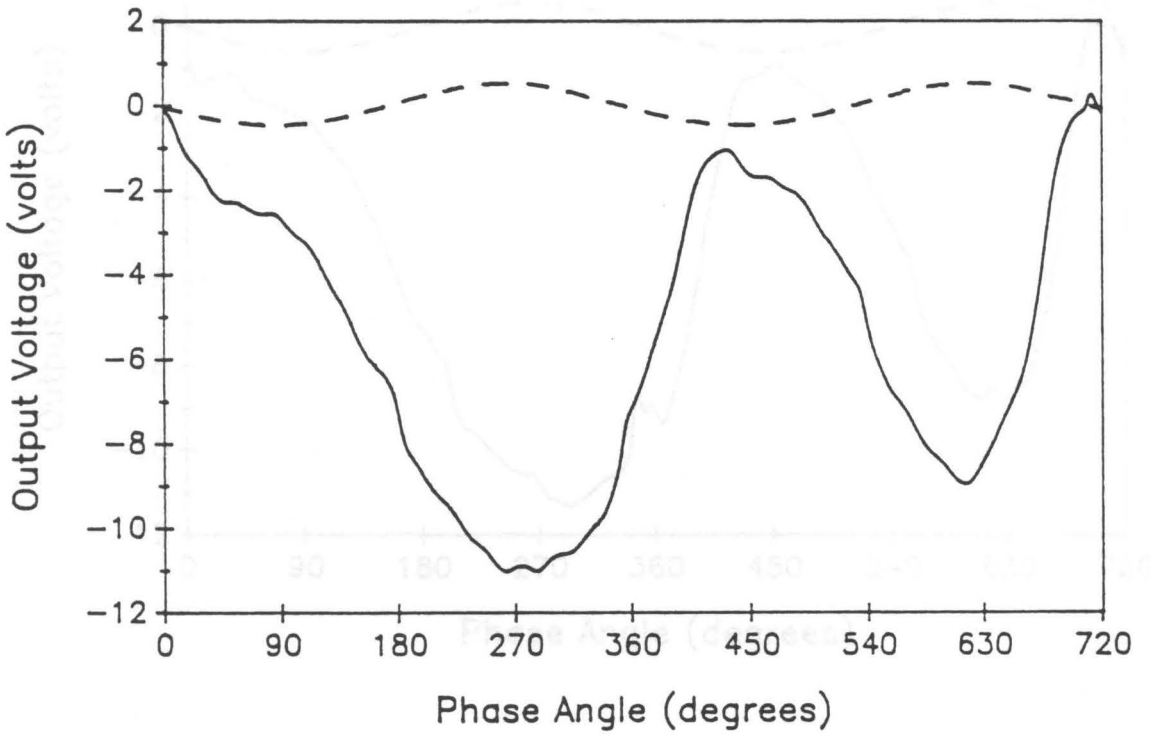

Figure 5.20. Output from the capacitance-probe experiment for 707-μm Master Beads at K = 5: Output voltage *versus* phase angle for output from capacitance probe (solid line) and accelerometer (dashed line) over two vibrational cycles.

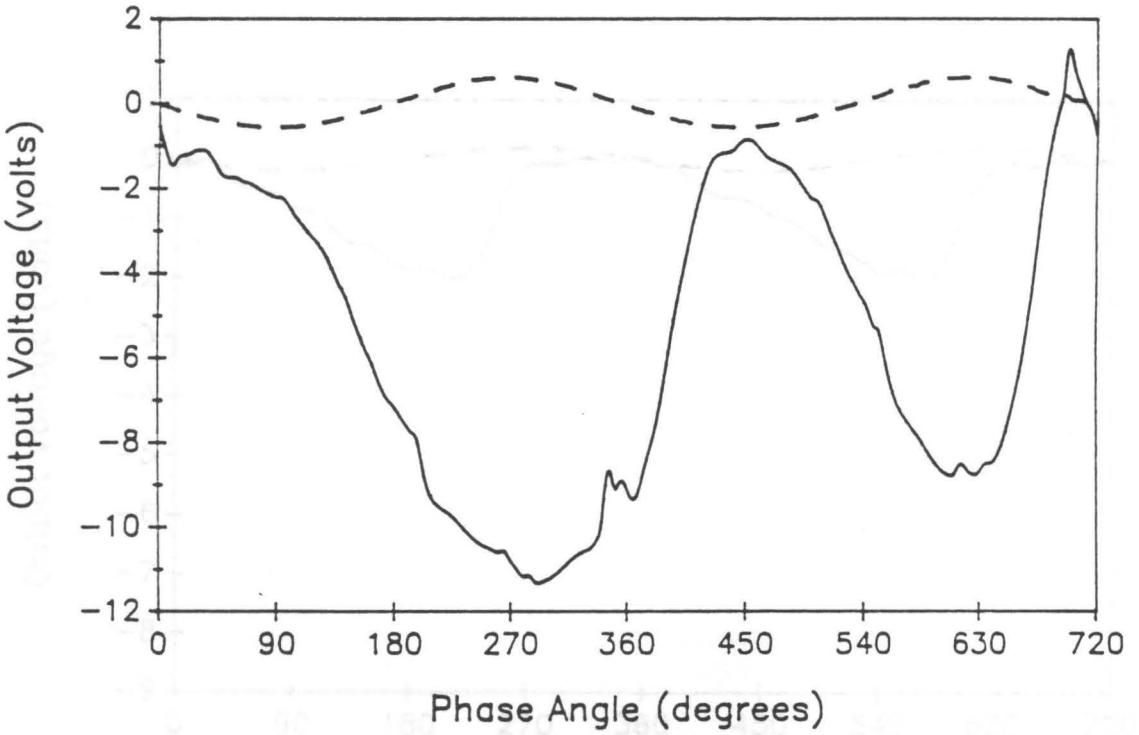

Figure 5.21. Output from the capacitance-probe experiment for 707-μm Master Beads at K = 6: Output voltage *versus* phase angle for output from capacitance probe (solid line) and accelerometer (dashed line) over two vibrational cycles.

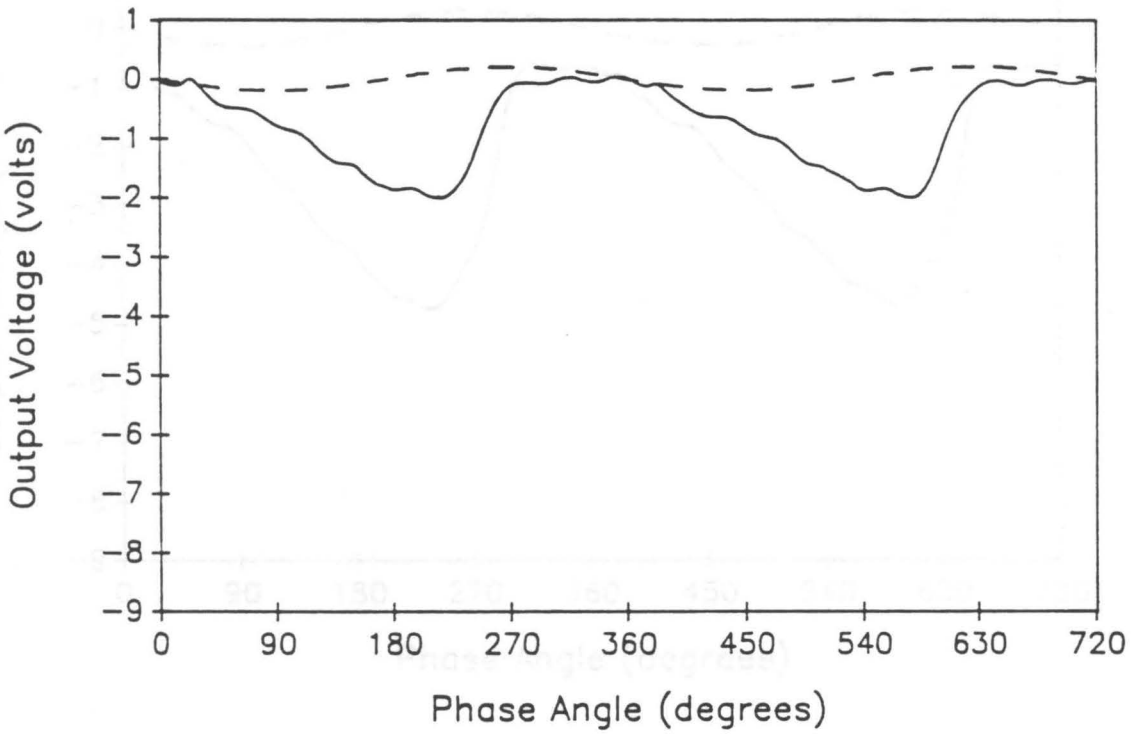

Figure 5.22. Output from the capacitance-probe experiment for 177-μm Master Beads at K = 2: Output voltage *versus* phase angle for output from capacitance probe (solid line) and accelerometer (dashed line) over two vibrational cycles.

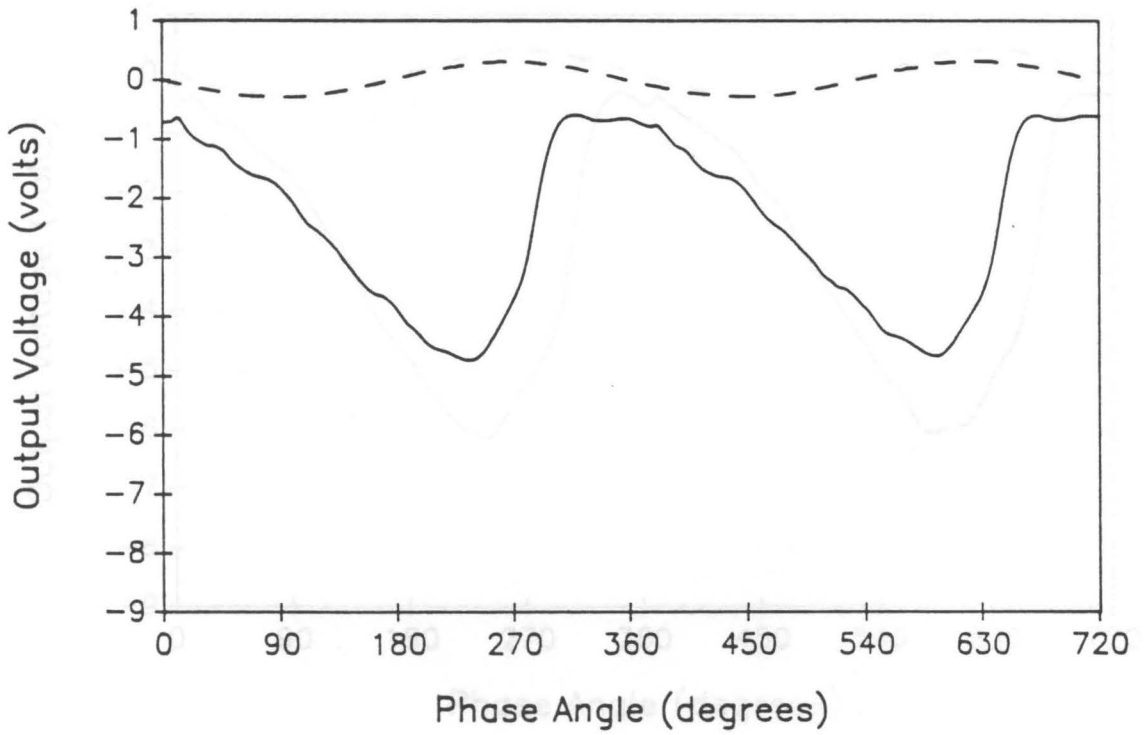

Figure 5.23. Output from the capacitance-probe experiment for 177-μm Master Beads at K = 3: Output voltage *versus* phase angle for output from capacitance probe (solid line) and accelerometer (dashed line) over two vibrational cycles.

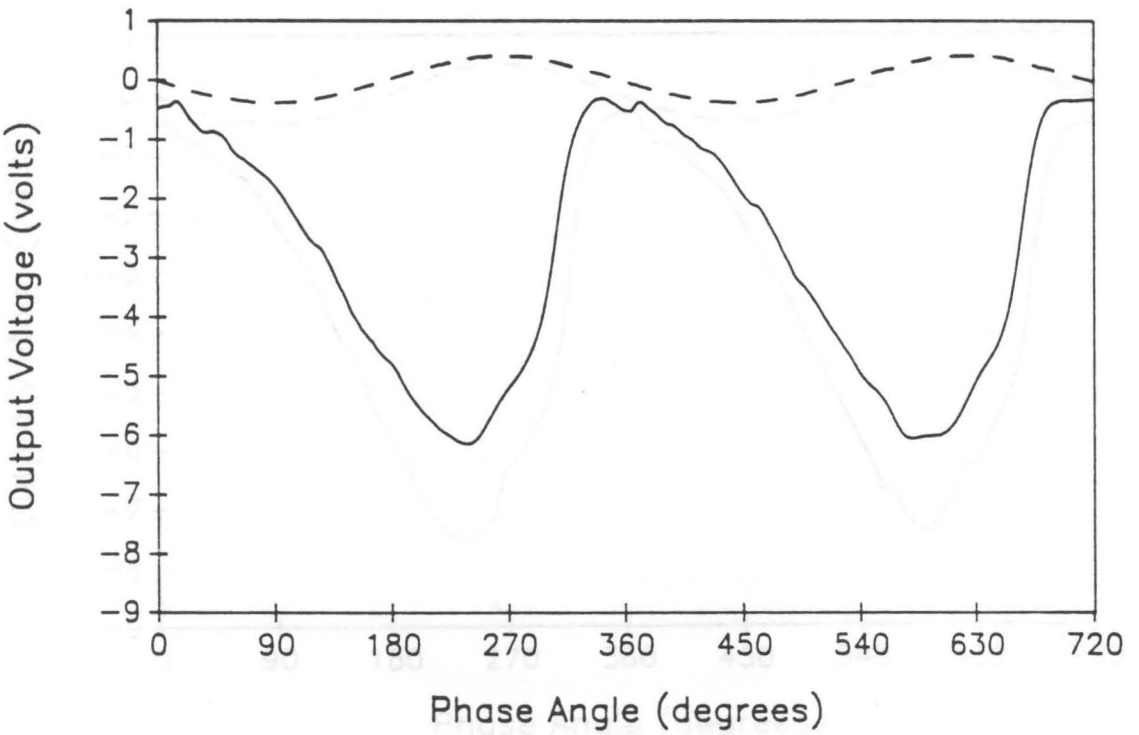

Figure 5.24. Output from the capacitance-probe experiment for 177-μm Master Beads at K = 4: Output voltage *versus* phase angle for output from capacitance probe (solid line) and accelerometer (dashed line) over two vibrational cycles.

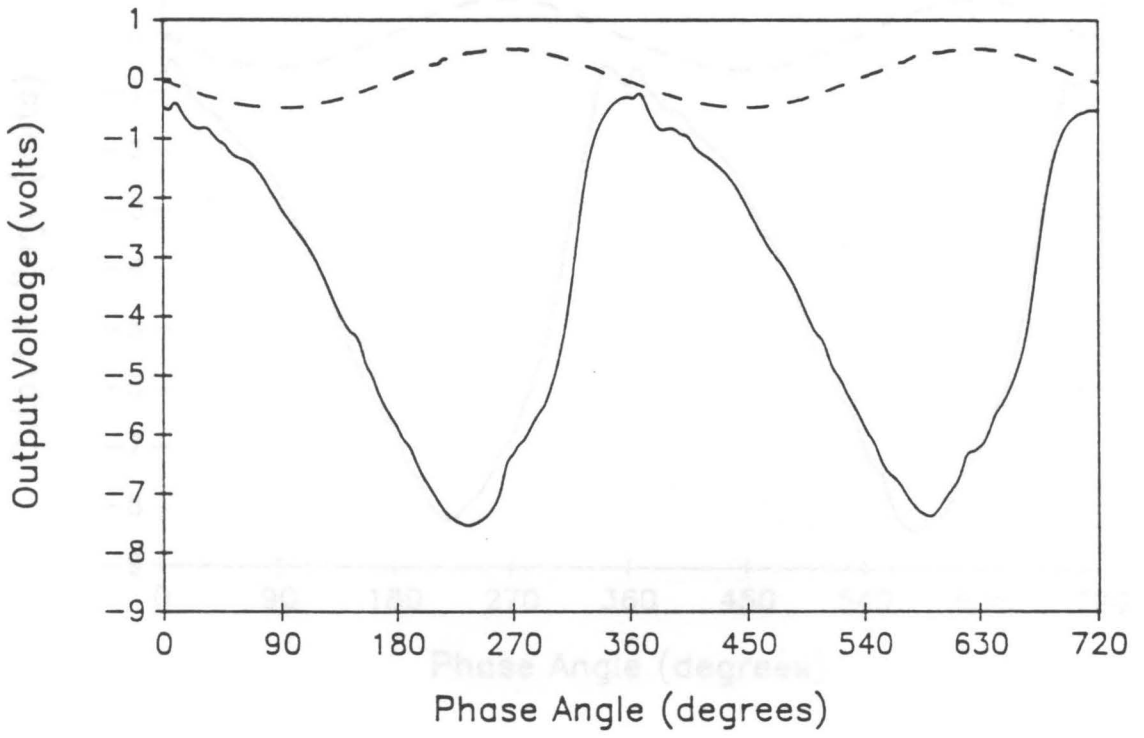

Figure 5.25. Output from the capacitance-probe experiment for 177-μm Master Beads at K = 5: Output voltage *versus* phase angle for output from capacitance probe (solid line) and accelerometer (dashed line) over two vibrational cycles.

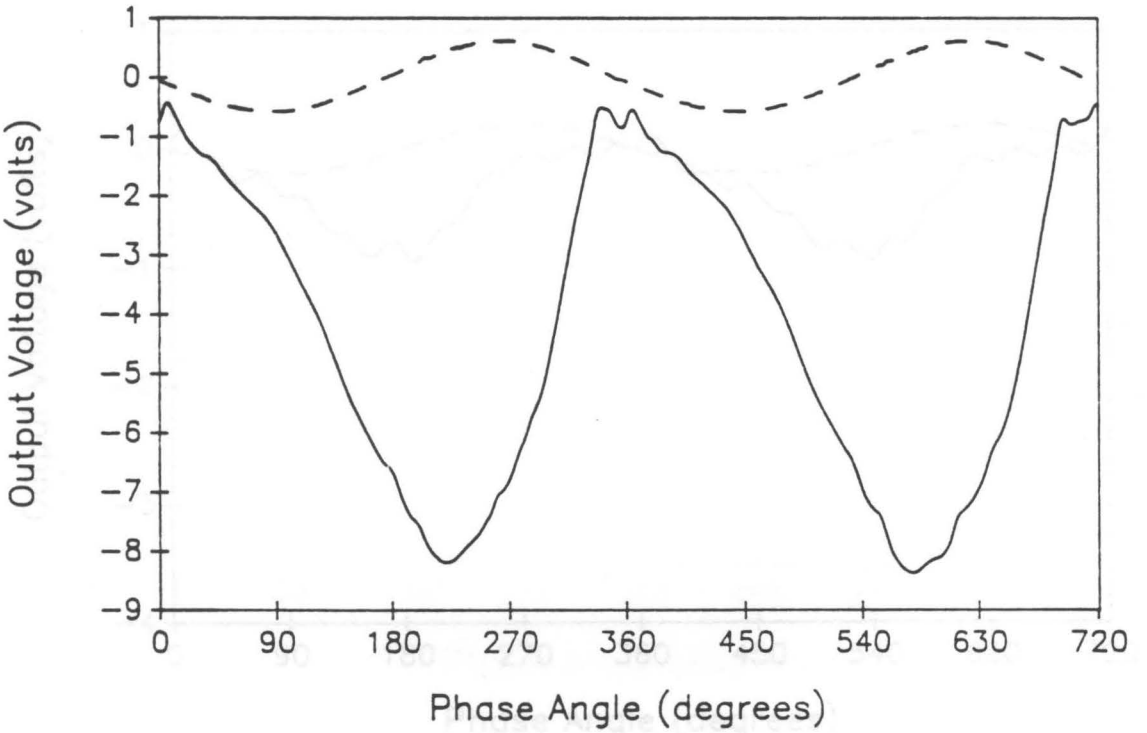

Figure 5.26. Output from the capacitance-probe experiment for 177-μm Master Beads at K = 6: Output voltage *versus* phase angle for output from capacitance probe (solid line) and accelerometer (dashed line) over two vibrational cycles.

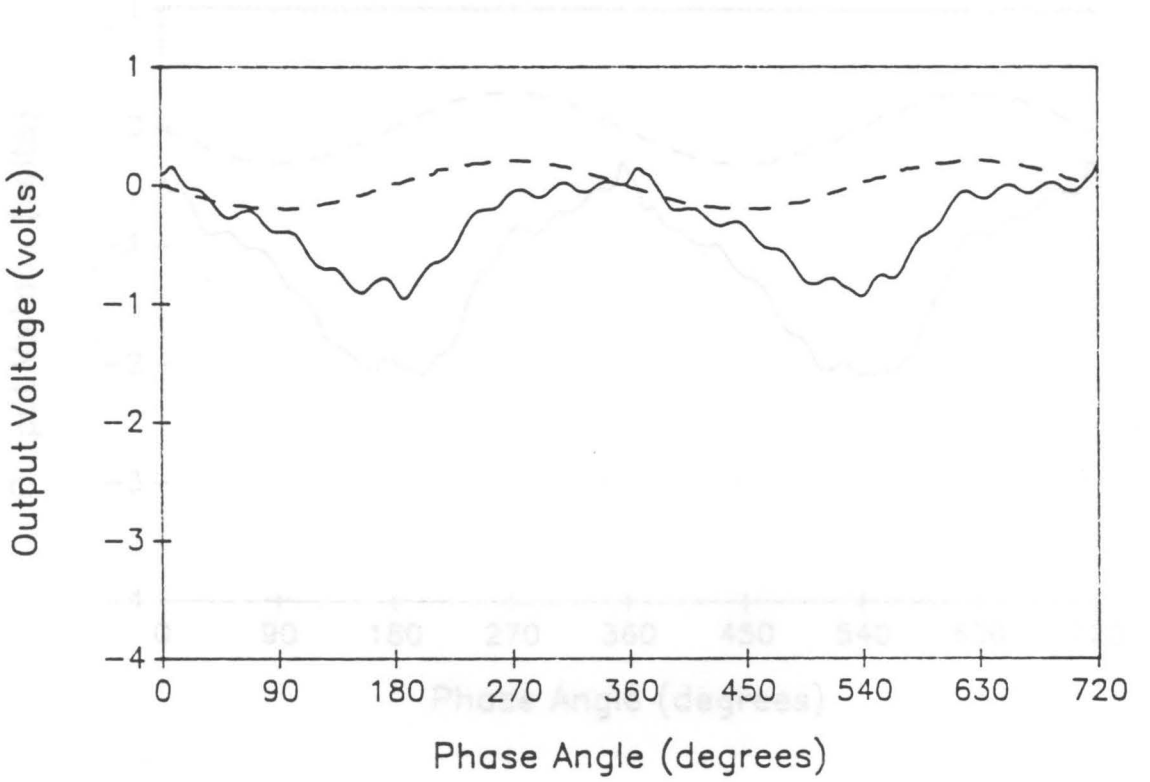

Figure 5.27. Output from the capacitance-probe experiment for 88-μm Master Beads at K = 2: Output voltage *versus* phase angle for output from capacitance probe (solid line) and accelerometer (dashed line) over two vibrational cycles.

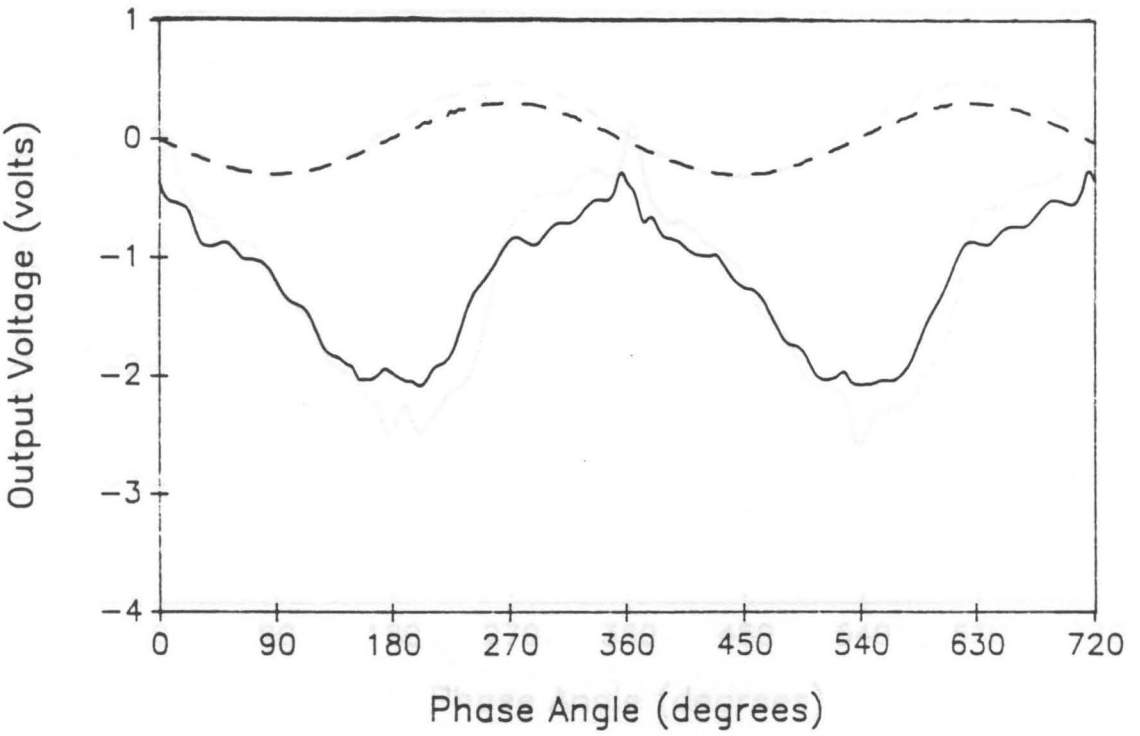

Figure 5.28. Output from the capacitance-probe experiment for 88-μm Master Beads at K = 3: Output voltage *versus* phase angle for output from capacitance probe (solid line) and accelerometer (dashed line) over two vibrational cycles.

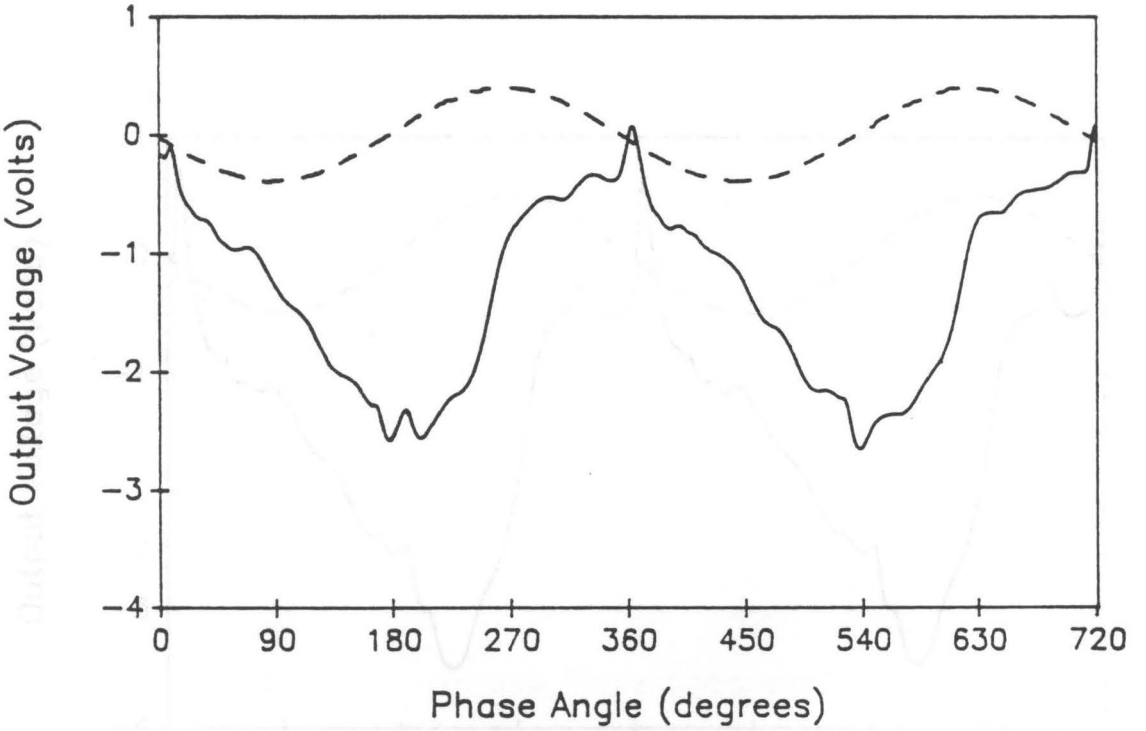

Figure 5.29. Output from the capacitance-probe experiment for 88-μm Master Beads at K = 4: Output voltage *versus* phase angle for output from capacitance probe (solid line) and accelerometer (dashed line) over two vibrational cycles.

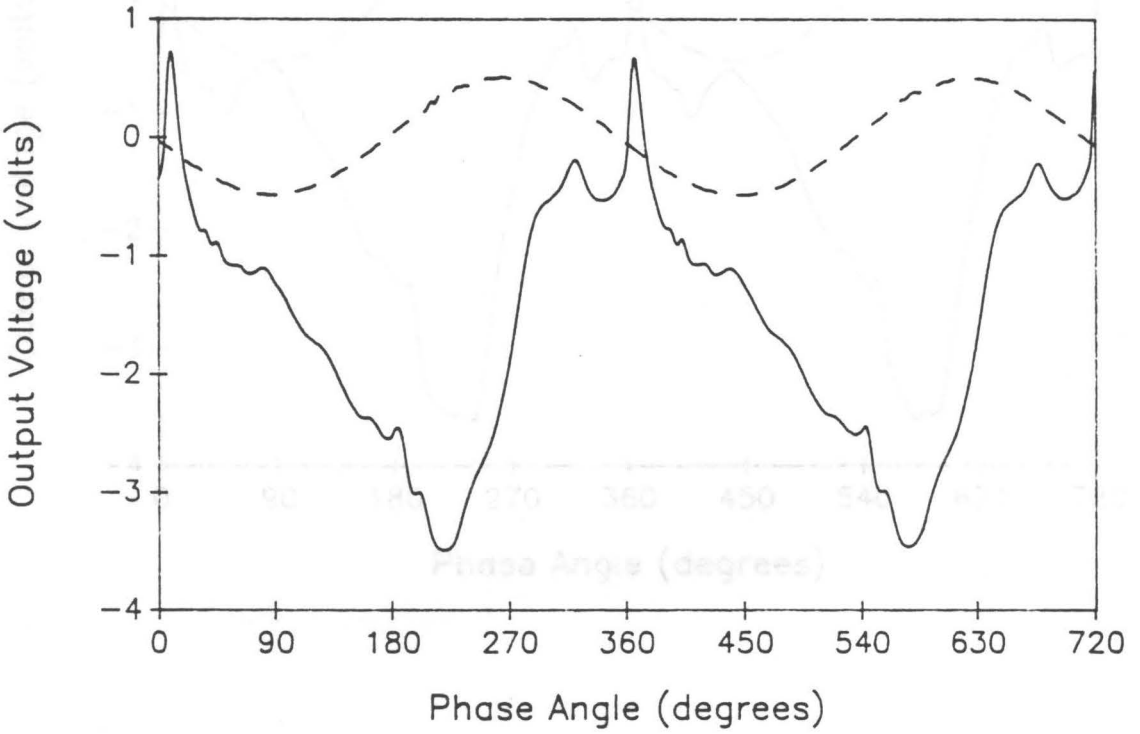

Figure 5.30. Output from the capacitance-probe experiment for 88-μm Master Beads at K = 5: Output voltage *versus* phase angle for output from capacitance probe (solid line) and accelerometer (dashed line) over two vibrational cycles.

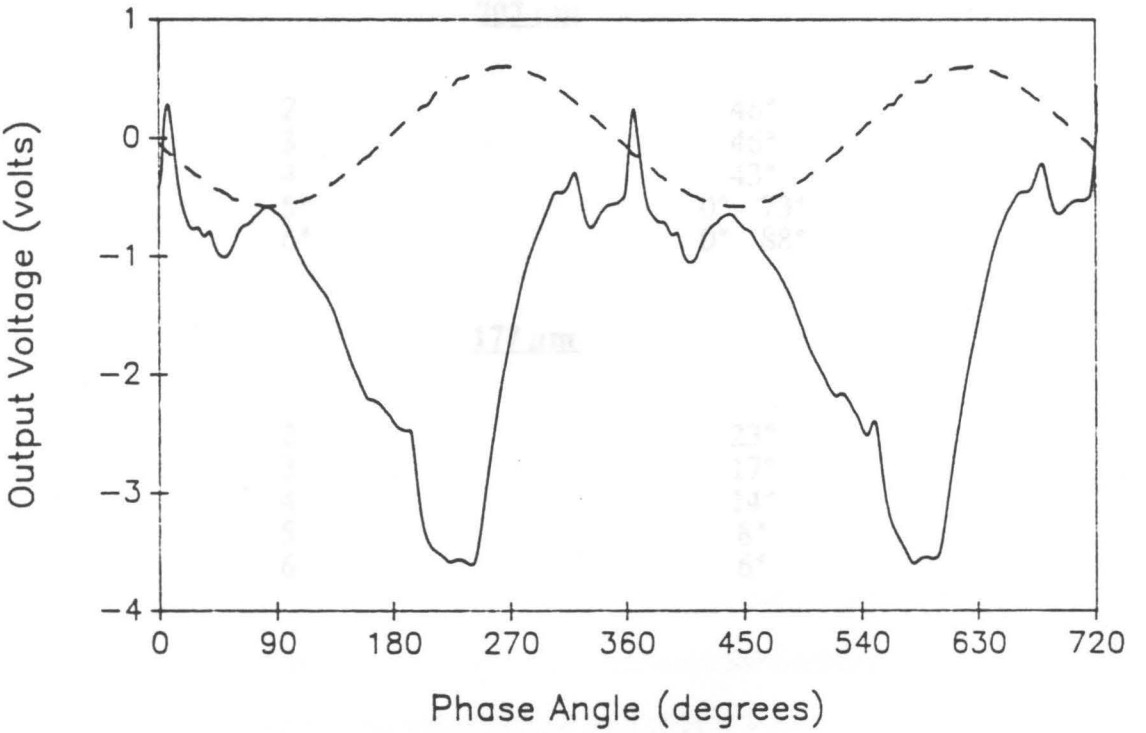

Figure 5.31. Output from the capacitance-probe experiment for 88-μm Master Beads at K = 6: Output voltage *versus* phase angle for output from capacitance probe (solid line) and accelerometer (dashed line) over two vibrational cycles.

Table 5.3. Lift-off points measured by the capacitance probe.

All data are for Master Beads

K-value	Lift-off
707 μm	
2	46°
3	46°
4	43°
5*	0° 73°
6*	0° 88°
177 μm	
2	23°
3	17°
4	14°
5	8°
6	6°

*Bed is in a period-doubling state

values are reported. This is because no lift-off is apparent based on the plots. Rather, the plots seem to show a cyclic increase and decrease in capacitance corresponding to a change in bed voidage rather than a sharp lift-off and collision. This point is discussed further in Section 5.1.4.

The values reported in Table 5.3 are much more anomalous than those from the vibrated-disc experiment. This is partially due to the more subtle data obtained in this experiment. The change in slope is not nearly as abrupt and there is more scatter in interpreting the data. Also, it appears as though the probe is detecting not necessarily the onset of the gap, but possibly the onset of an increase in bed voidage. This effect was not expected to appear since previous measurements of variation in bed voidage throughout the cycle have quoted a figure of ± 0.002 around a mean voidage of 0.41 [Gutman, 1974]. Voidage changes of this magnitude were not thought to affect the relatively large capacitance changes caused by the onset of the gap, but this may not be the case. Finally, as shown in Figure 5.32, the capacitance probe device is susceptible to the vibrations themselves at high K-values, unlike the vibrated discs. This effect adds spurious peaks to the plots which further complicate the analysis.

For these reasons, the values given in Table 5.3 are suspect and should be taken *cum grano salis*. Instead, it is best to use the plots in Figures 5.17-5.31 in a qualitative way as an aid for understanding the intracyclic bed dynamics.

5.1.4 Discussion of Discrepancies in Bed-Vessel Separation

Since both of the theoretical models discussed in Section 5.1.1 predict such similar phase angles of separation and the results obtained from the vibrated-disc experiments agree well (no angle is off by more than 6 degrees from any of the

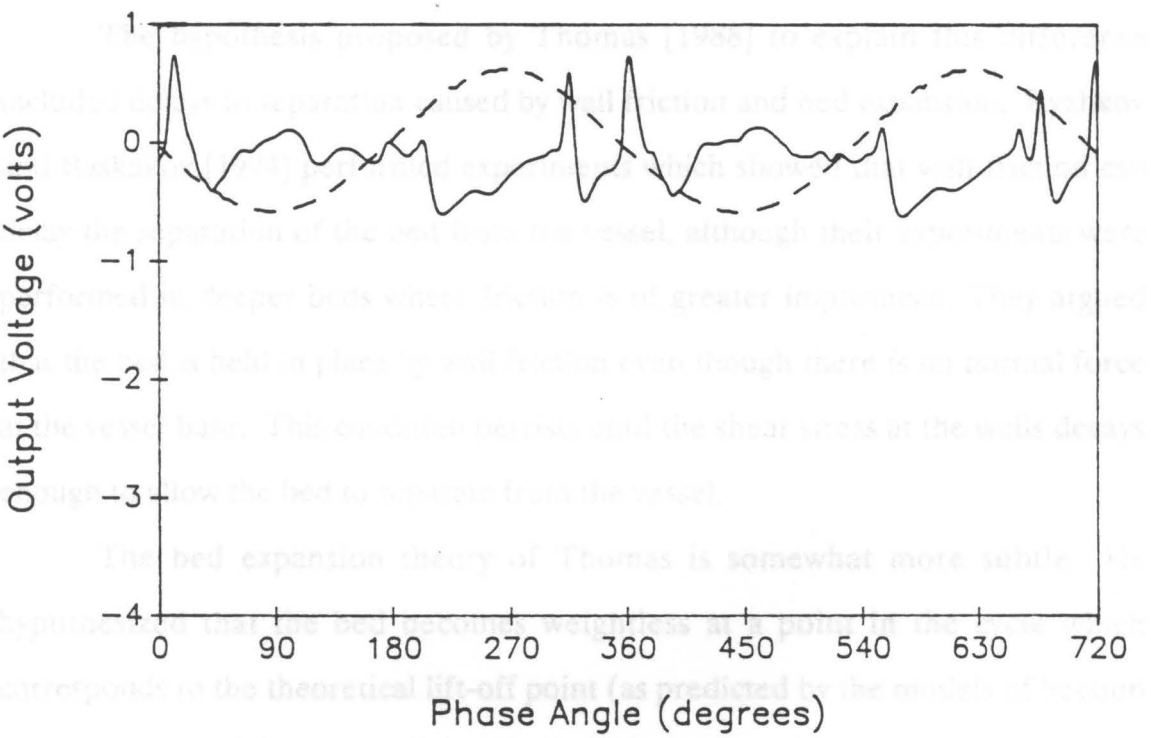

Figure 5.32. Output of the capacitance probe at K = 6 with an empty vessel: Output voltage from the capacitance probe (solid line) and accelerometer (dashed line) *versus* phase angle for two cycles.

models with the exception of the spurious values discussed earlier, and most agree to within 2-3 degrees), at first glance the phenomenon of bed-vessel separation appears to be well understood. Closer study shows that things are not necessarily so simple, however. The visual experiments of Thomas [1988], for example, found that the separation of the bed and vessel occurred much later in the cycle than predicted by the models for 707 and 177-μm Master Beads (see Table 5.4), and that no separation occurred at all for 88-μm particles for K-values as high as 5.

The hypothesis proposed by Thomas [1988] to explain this difference included delays in separation caused by wall friction and bed expansion. Ryzhkov and Baskakov [1974] performed experiments which showed that wall friction can delay the separation of the bed from the vessel, although their experiments were performed in deeper beds where friction is of greater importance. They argued that the bed is held in place by wall friction even though there is no normal force at the vessel base. This condition persists until the shear stress at the walls decays enough to allow the bed to separate from the vessel.

The bed expansion theory of Thomas is somewhat more subtle. He hypothesized that the bed becomes weightless at a point in the cycle which corresponds to the theoretical lift-off point (as predicted by the models of Section 5.1.1). He termed this the "null-force point." Instead of physically separating from the vessel at this point, however, the bed merely undergoes an expansion which results in a porosity increase. His calculations showed that an expansion of as little as 0.33% for 707-μm beads, of 1.9% for 177-μm beads, and of 5% for 88-μm beads would reconcile his observed separations with those calculated from his model. Bagnold [1954, 1966] has shown that the degree of bed expansion (porosity) and amount of dispersive pressure caused by shearing of the bed

Table 5.4. Bed-vessel separation measured visually.

Data are for Master Beads. From Thomas [1988]

K-value	Observed Separation
707 μm	
3	36° -52°
4	36° -52°
177 μm	
3	112°
4	93°
5	68°
6	58°
7	47°

(which generates shear forces at the walls) are closely inter-related. This obviously suggests that the two parts of Thomas' hypothesis are not separate phenomena, but rather are closely connected: the bed expansion and decay of wall friction, which cause a delay in separation in his view, are one phenomenon. Since both of the models of Section 5.1.1 assume no wall friction and no bed expansion, they are not valid if this hypothesis is correct.

Vibrated beds are known to undergo compaction during collision (see Section 5.3; also Thomas [1988] observed this in high-speed movies), so an equivalent expansion during some part of the cycle is necessary. The expansion is more subtle and not as easily observed in high-speed movies, but the occurrence of such an expansion at the point when the bed becomes weightless is a logical assumption. Kapustin *et al.* [1980], in fact, have reported observing a sequential, layer-by-layer lift-off of the bed from the top toward the bottom for millet grains. This represents one type of expansion which could cause the delay.

The plots of the vibrated-disc experiments in Figures 5.1-5.15 may actually be showing the point at which the particles cease to impose a force on the vibrated disc rather than the point of actual separation of the bed with the vessel base. In light of this argument, then, the values of "lift-off" reported in Table 5.2, and in fact the term lift-off as used throughout this chapter (as opposed to the term separation), refers to the hypothetical null-force point of Thomas [1988].

A closer examination of Figure 5.7 for 177-μm particles at K = 3 for the center disc lends more credence to this theory. Note that after the initial jump in voltage, reported as the lift-off point, the voltage increases slowly until approximately 110° into the cycle where it levels off. If the initial jump corresponds to the sudden loss of force of the particles on the disc, the slow increase might represent the gradual expansion of the bed until the particles

physically separate from the vessel base. At this point, the disc is totally free to vibrate and maintains the same level of output voltage until the point of collision. This value of about 110° is also quite close to the visually measured angle of separation of Thomas [1988] (see Table 5.4). The same feature appears in all of the plots of the vibrated-disc experiments of this particle size for the center disc.

An alternative explanation of this slow ramp in voltage after the initial jump is possible, however. The vibrated disc may require a "relaxation time" after the bed is separated from it before it achieves its full-amplitude vibration. This possibility has been investigated via the solid Lexan block experiment described in Section 5.1.2. Since the solid piece of Lexan cannot expand upon lift-off as a particle bed can, if the same sort of ramp is observed for it, then the ramp must be due to a relaxation of the disc and not a bed expansion. Observations on an oscilloscope show that there is, in fact, a relaxation in this case, but that it is only on the order of 3-4 msec (30-40 degrees at 25 Hz) which is much shorter than that observed for the particles.

Evidence for expansion also exists in the 88-μm beads. As noted in the capacitance-probe section (Section 5.1.3), values of lift-off for this particle size are not even reported due to a lack of sharp change. Figures 5.27-5.31 all appear to show a rather sinusoidal increase and decrease in voidage with a sharp compaction only becoming apparent at high K-values. It should also be noted that the voltage scale has been changed for these figures so that a capacitance change of less than half of that for the 177-μm beads and less than a third of that for the 707-μm beads is observed. For the vibrated-disc experiments, the amplitude of vibration of the discs is not held constant for different particle sizes so that output voltages cannot be compared from one particle size to another as is the case with the capacitance probe.

A separate experiment has been run, however, holding the same amplitude on the vibrated discs for 88 and 177-μm particles. At K = 4, it is observed by monitoring the output voltage on an oscilloscope that the 88-μm beads only produce half of the output voltage that the 177-μm beads do at the same vibrated-disc amplitude. In light of this observation, perhaps the 88-μm beads do not truly separate from the vessel floor, which would agree with visual evidence.

While the experiments admittedly cannot conclusively prove or disprove the theory of Thomas [1988], the weight of evidence does suggest that the bed-vessel separation is a two-step process involving the calculated point of lift-off (or point at which the bed becomes weightless due to the vessel's acceleration) and a subsequent expansion. After this expansion, the bed may truly separate from the vessel base as is the case for the two larger particle sizes studied. On the other hand, the particles may remain in contact with the vessel throughout the cycle merely undergoing expansion and compaction, as appears to be the case for the smallest size of particles studied.

5.2 Bed-Vessel Collision

Particle beds which separate from the vessel base must collide at some later point. As mentioned in Section 5.1.2, for large particles at high K-values, the collision may not occur in the same vibrational cycle as the separation. If collision occurs after separation should have occurred in the succeeding cycle, the previously mentioned period-doubling phenomenon is observed.

The same models which were used to predict separation in the previous section are again used to predict collision. Also, the same experimental techniques are used to measure the point of collision. Since the collision point is

more easily measured, however, the additional method of passive piezoelectric films is employed. As before, an analysis and discussion of the discrepancies between prediction and observation follows the presentation of results.

5.2.1 Collision Calculated from the Kroll and Thomas Models

Table 5.5 presents calculated collision points obtained from the same models for the same particles as the separation points reported in Section 5.1.1. In order to obtain the collision point from the Kroll model, Equation [2.25] must be solved to determine when S (the gap width) is zero. This has been done by Benge [1990]. The solution to the Thomas model is as cited in Section 5.1.1.

Unlike the situation found in bed-vessel separation, the models predict appreciably different collision times--especially for the 177 and 88-μm particles. They agree fairly well for the 707-μm particles, although the agreement is not as close as it is for separation (see Section 5.1.1). For the 177-μm beads, however, the difference becomes apparent. The Kroll model predicts an earlier collision than the Thomas model with the disparity increasing as the K-value increases. This difference can be attributed to the way in which the pressure in the gap is obtained for the two models. The Kroll model calculates the pressure based on the assumption of gas incompressibility, whereas the Thomas model employs experimentally measured values. This trend becomes even more exaggerated for the 88-μm particles.

Table 5.5. Phase angles of bed-vessel collision predicted by the Kroll and Thomas models.

K-value	Kroll Model	Thomas Model
	707-μm Master Beads	
2	289.6°	284.5°
3	345.3°	340.3°
4	386.4°	374.1°
	177-μm Master Beads	
2	246.4°	247.4°
3	278.0°	295.6°
4	295.6°	313.5°
5	307.5°	337.6°
	88-μm Master Beads	
2	227.3°	245.3°
3	256.4°	285.2°
4	272.2°	305.9°
5	283.0°	--

5.2.2 *Results of the Vibrated-Disc Experiments*

The same battery of vibrated-disc experiments used to determine bed lift-off also gives bed-vessel collision information. Table 5.6 reports the bed-vessel collisions as measured from Figures 5.1-5.15. As before, the period-doubling phenomenon shows up in the 707-μm beads at K-values of 5 and 6, and the two values reported in the table reflect the two uneven cycles for these cases. As in the case of lift-off with this experiment, precision is on the order of 3° of phase angle.

The two values reported for the 177-μm beads reflect a different phenomenon. Unlike the large particles which have been observed to hit flat [Thomas, 1988] and relatively hard, the smaller beads tend to land at the wall first with the gap closing toward the center. Figures 5.1 through 5.5 show a relatively constant voltage output with a sudden voltage spike (or series of spikes) indicating a sudden, violent collision for the large beads. For the 177-μm beads, however, the vibrated-disc voltage drops and then shows a spike (see Figures 5.6-5.10). This output is theorized to represent a two-part collision process for the smaller beads. The decrease in voltage is taken to be due to the first few particles of the expanded bed settling on the disc, which is sufficient to dampen its amplitude of vibration. The later spike is due to the full force of the bed impacting on the disc and corresponds to the passage of the compaction wave over the disc (see Section 5.3 for a further discussion of compaction waves). This spike is much more prominent for the center disc (where the bed is deepest) and for the higher K-values, both of which are expected trends. The two values of Table 5.6 for 177-μm beads thus represent the first contact of beads with vessel base and the time of full compaction, successively.

Table 5.6. Bed-vessel collision measured by the vibrated discs.

All data are for Master Beads

K-value	Center Disc	Edge Disc
	707 μm	
2	272°	273°
3	321°	323°
4	338°	341°
5*	377° 345°	388° 318°
6*	411° 320°	403° 329°
	177 μm	
2	245° 249°	237° 241°
3	280° 289°	274° 283°
4	309° 316°	293° 302°
5	334° 341°	303° 311°
6	352° 360°	318° 323°
	88 μm	
2	--	--
3	259°	--
4	277°	--
5	303°	--
6	314°	--

*Bed is in a period-doubling state

The smallest beads, as mentioned in Section 5.1.4, do not totally separate from the vessel base and thus cannot truly collide with it. At K = 2 and for all of the edge disc experiments, the output does not show any sharp drop but rather a gradual tailing in voltage. This corresponds to the decreasing porosity and increasing force of the bed on the disc. Since no sharp feature is observed in these cases, no values for them are reported in Table 5.6. For the center disc at K-values of 3 and higher, the deeper bed and increase in vibrational intensity combine to cause a more sudden compaction of the bed. This results in a sharper drop in output voltage, which is reported in Table 5.6.

The data for the vibrated-disc experiments show several trends. First, the 707-μm beads land very close to the same time at the center and edge disc positions for the K-values where period-doubling does not occur. This agrees with the observations of Thomas [1988], who noted that the gap closes nearly simultaneously for these large beads. The 177-μm beads, however, which exhibit bunkered behavior, collide from the wall toward the center. The amount of delay between the collision at the edge disc and collision at the center generally increases with increasing vibrational intensity. Finally, the collision occurs earlier in the cycle as the particle size decreases for the same K-value (note that in this comparison, the first value in Table 5.6 for the 707-μm beads at K = 5 and 6 should be used). This trend holds true even for the "apparent" collisions of the 88-μm beads. Again, this is an expected result which is predicted by both theoretical models.

5.2.3 Results of the Capacitance-Probe Experiments

As mentioned in Section 5.1.3, the results of the capacitance-probe experiment are somewhat disappointing in that they are influenced by voidage changes and thus do not show lift-off and collision. Values in Table 5.7 should thus be taken as the point at which the maximum compaction (minimum voidage) of the bed occurs and not as a true collision. As in Section 5.1.3, only values for 707 and 177-μm particles are reported because the curves for 88-μm particles are inconclusive. Unlike lift-off measured with this experiment, however, the precision of reported values is about 3° of phase angle. All of the plots of the data appear in Figures 5.17-5.31.

The data for these experiments again show the period-doubling phenomenon for the 707-μm beads at the two highest K-values. The trends followed are the same as in the vibrated-disc experiments: the point of maximum compaction occurs earlier for the smaller size at the same K-value; and for the same solid the point of maximum compaction occurs later in the cycle as vibrational intensity is increased. The value at K = 6 for 177-μm particles violates this second trend and is unexpectedly low. This anomaly is not easily explained since no similar behavior is observed for the vibrated-disc experiment under the same conditions. Perhaps the problem lies with the susceptibility of the capacitance-probe system to high acceleration forces, as previously noted (see Section 5.1.3 and Figure 5.32).

Table 5.7. Bed-vessel collision measured by the capacitance probe.
Data are for Master Beads

K-value	Collision
707 μm	
2	304°
3	354°
4	369°
5*	433° 357°
6*	448° 339°
177 μm	
2	274°
3	309°
4	335°
5	351°
6	337°

*Bed is in a period-doubling state

5.2.4 Results of Floor-Mounted Piezo-Film Experiments

In an effort to explore the way in which the gap closes, an experiment has been run employing passive piezoelectric sensors at three locations on the vessel floor: at the center, 29 mm from the center, and 58 mm from the center. Observations have shown [Thomas, 1988] that the gap closes nearly simultaneously for large-particle, unbunkered beds, but that the gap closes from the sides toward the center for bunkered beds in which a gap appears (*i.e.*, 177-μm particles). The vessel described in Section 3.2.2.1 modified for the piezoelectric films is employed, and the procedure outlined in Section 4.2.3 is followed. Figures 5.33 through 5.42 present the results of these experiments for particles of 707 and 177-μm Master Beads. These plots represent the output from the piezo-films over two vibrational cycles. Note that the voltage scale has been varied from one figure to another in order to optimize the output peaks, but that the scale is the same for all three plots of each figure.

Even a cursory examination of these plots shows that the output voltage from each piezo-film is non-zero for a relatively broad range of phase angles. Usually this range is 60-80 degrees wide, and it is over 100 degrees in some instances. Such a broad response band is unfortunate since it introduces a large degree of uncertainty in the angle of collision obtained from these plots and limits the conclusions which can be drawn from them. Several explanations for this output response are possible. First, the spread may indicate the duration of collision at each horizontal point on the vessel floor. The first, small-amplitude signals may correspond to the first few expanded layers of particles making contact. The large spike or spikes near the center of the response band would then correspond to the center of mass of the bed colliding, with the signal

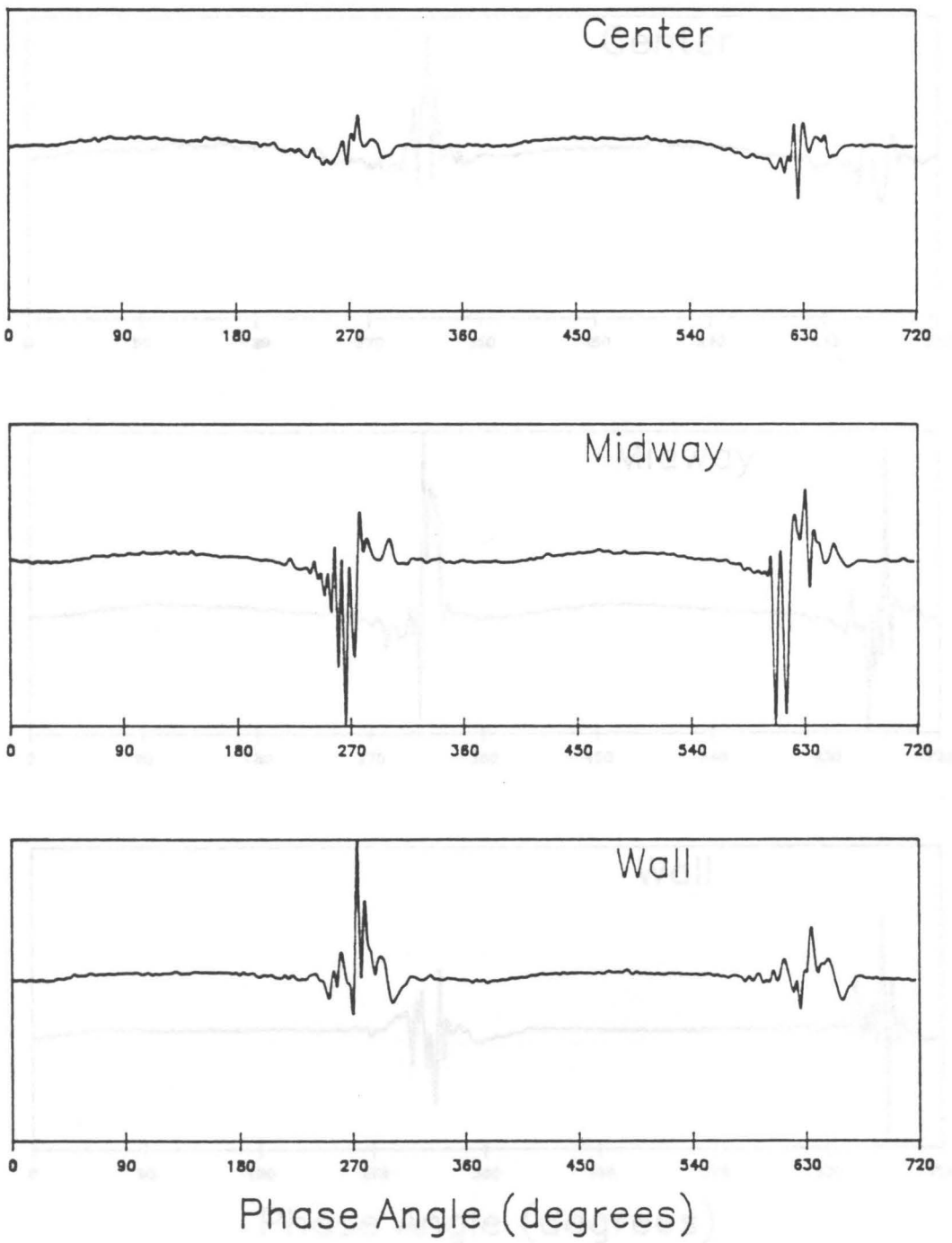

Figure 5.33. Output from the floor-mounted piezo-films for 707-μm Master Beads at K = 2: Output *versus* phase angle over two cycles. Top plot is for the center dot, center plot is for the dot 29 mm from the center, and bottom plot is for the dot 58 mm from the center.

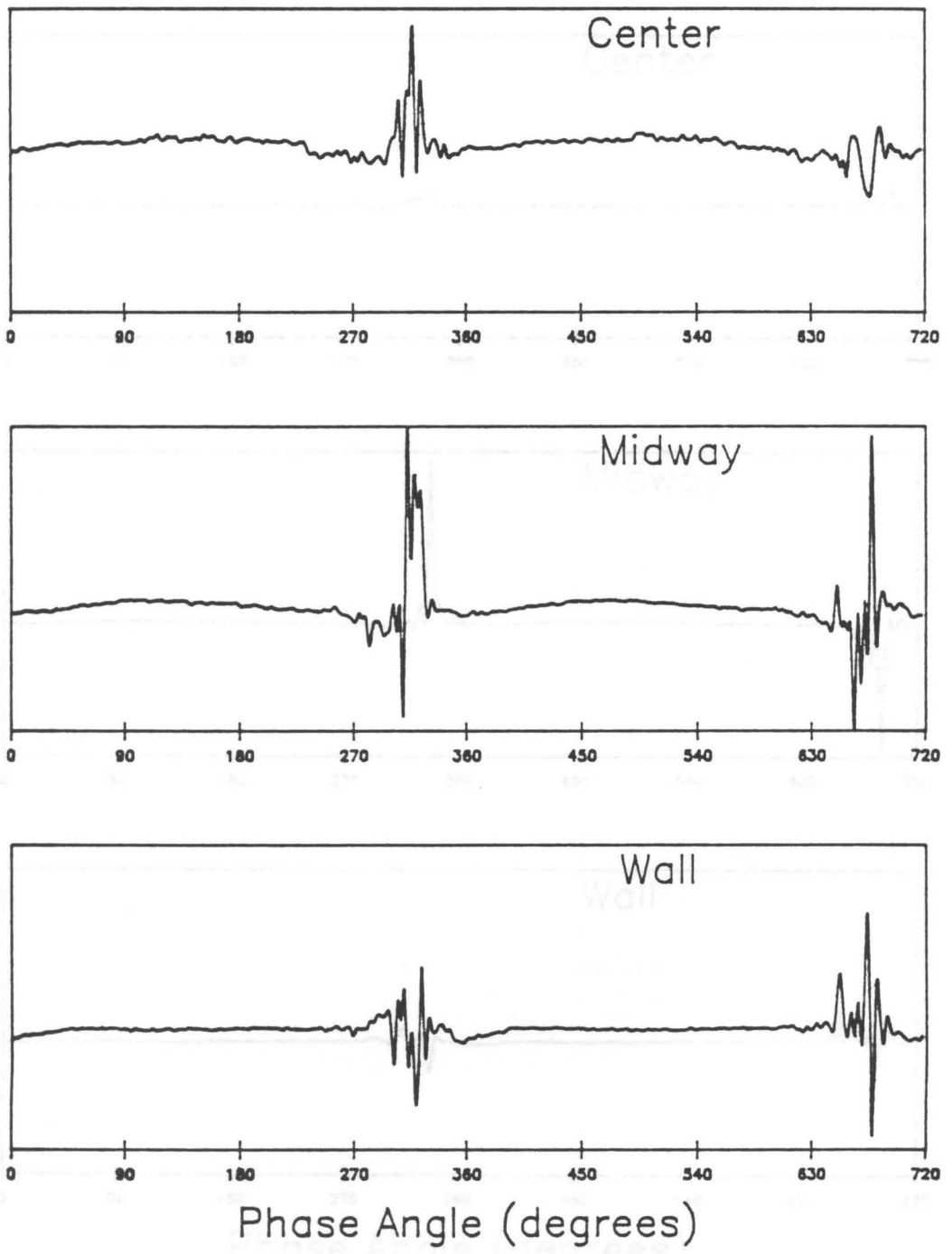

Figure 5.34. Output from the floor-mounted piezo-films for 707-μm Master Beads at K = 3: Output *versus* phase angle over two cycles. Top plot is for the center dot, center plot is for the dot 29 mm from the center, and bottom plot is for the dot 58 mm from the center.

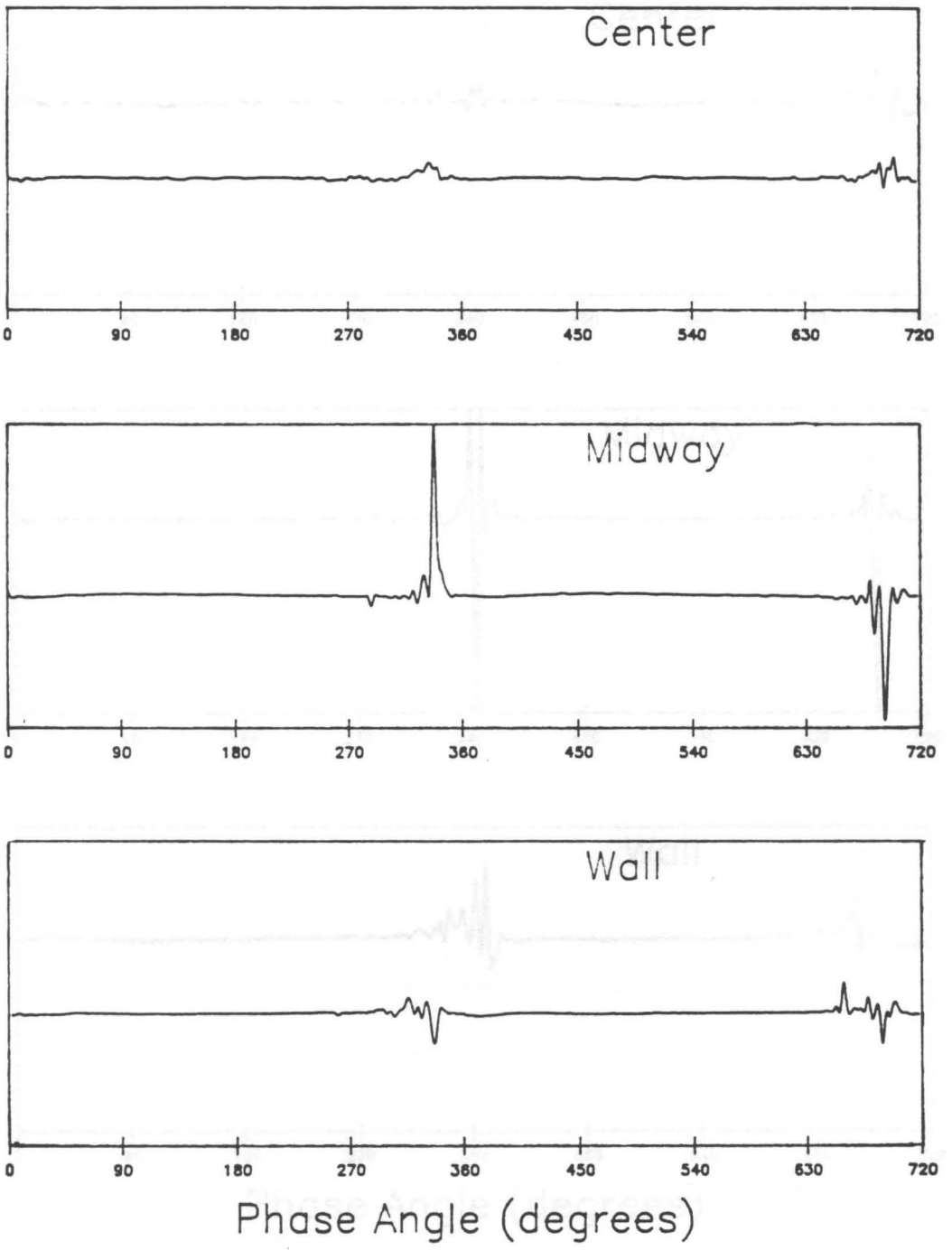

Figure 5.35. Output from the floor-mounted piezo-films for 707-μm Master Beads at K = 4: Output *versus* phase angle over two cycles. Top plot is for the center dot, center plot is for the dot 29 mm from the center, and bottom plot is for the dot 58 mm from the center.

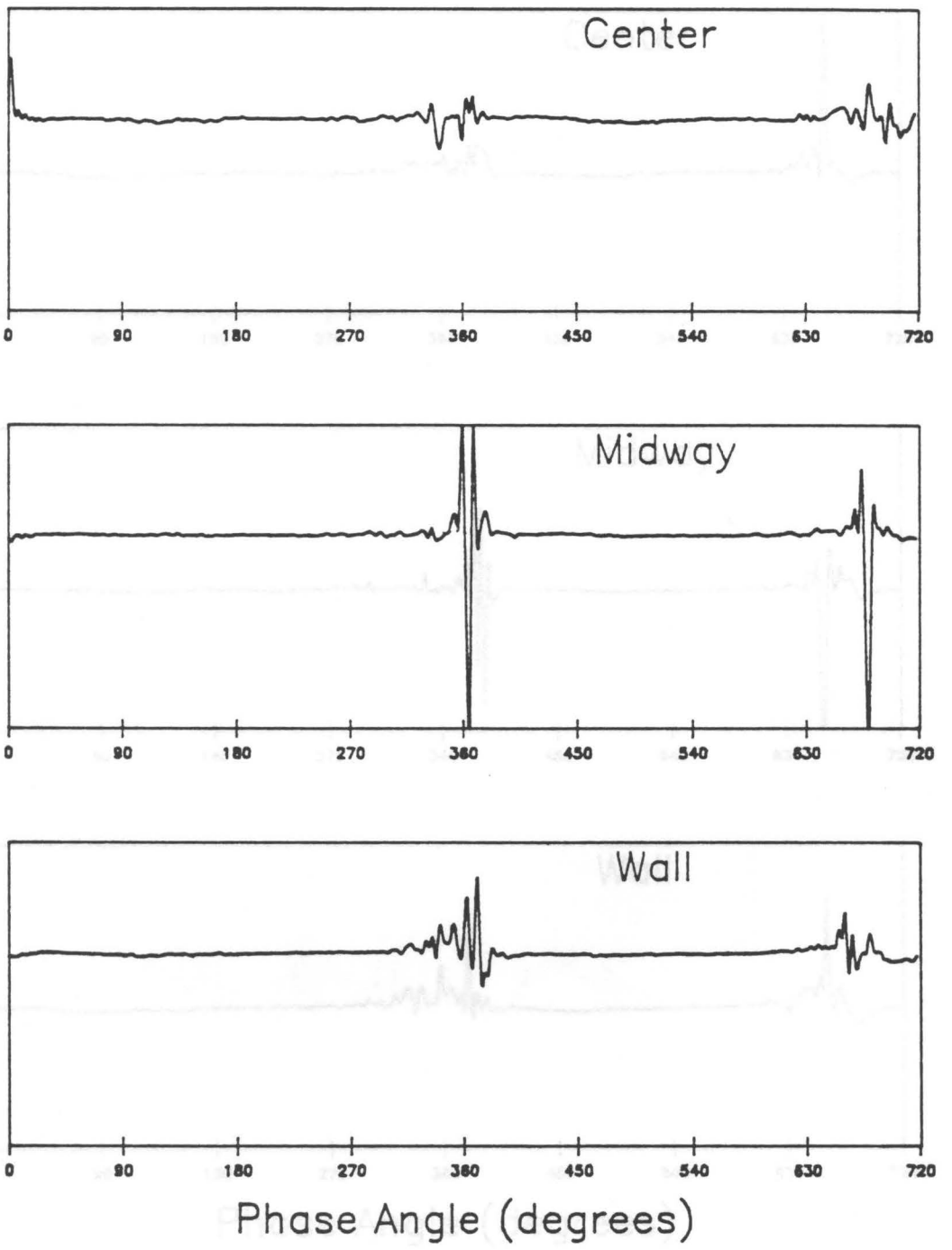

Figure 5.36. Output from the floor-mounted piezo-films for 707-μm Master Beads at K = 5: Output *versus* phase angle over two cycles. Top plot is for the center dot, center plot is for the dot 29 mm from the center, and bottom plot is for the dot 58 mm from the center.

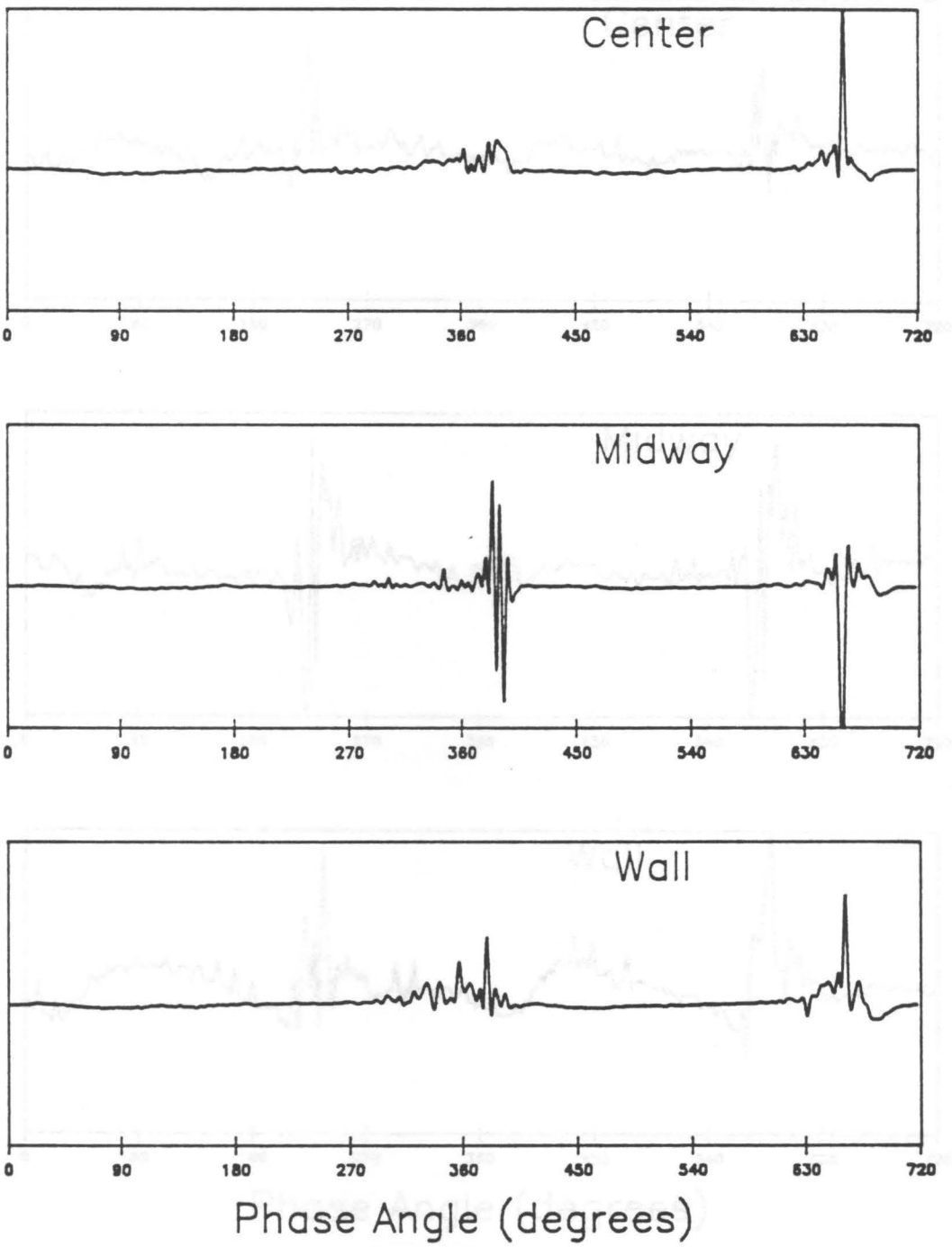

Figure 5.37. Output from the floor-mounted piezo-films for 707-μm Master Beads at K = 6: Output *versus* phase angle over two cycles. Top plot is for the center dot, center plot is for the dot 29 mm from the center, and bottom plot is for the dot 58 mm from the center.

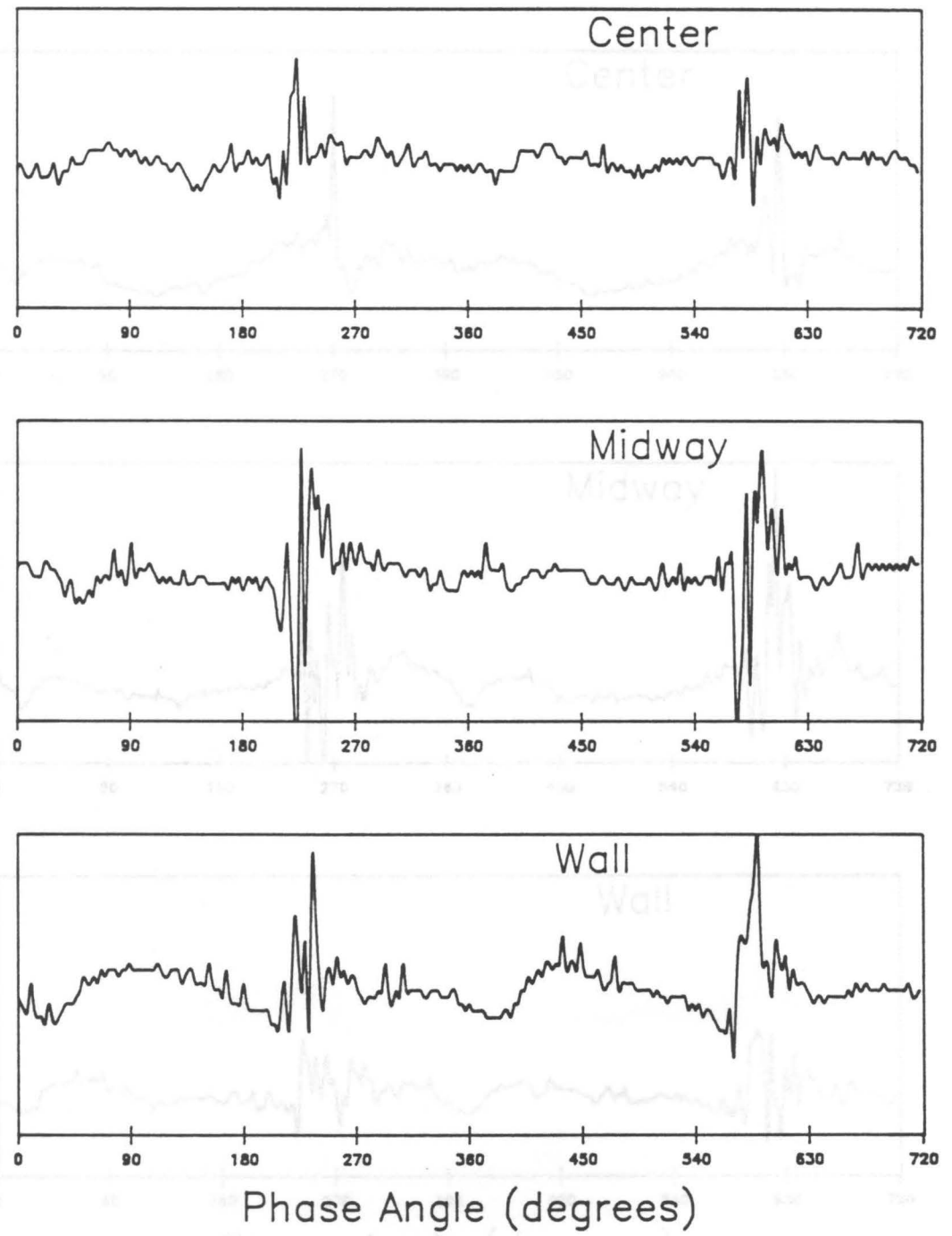

Figure 5.38. Output from the floor-mounted piezo-films for 177-μm Master Beads at K = 2: Output *versus* phase angle over two cycles. Top plot is for the center dot, center plot is for the dot 29 mm from the center, and bottom plot is for the dot 58 mm from the center.

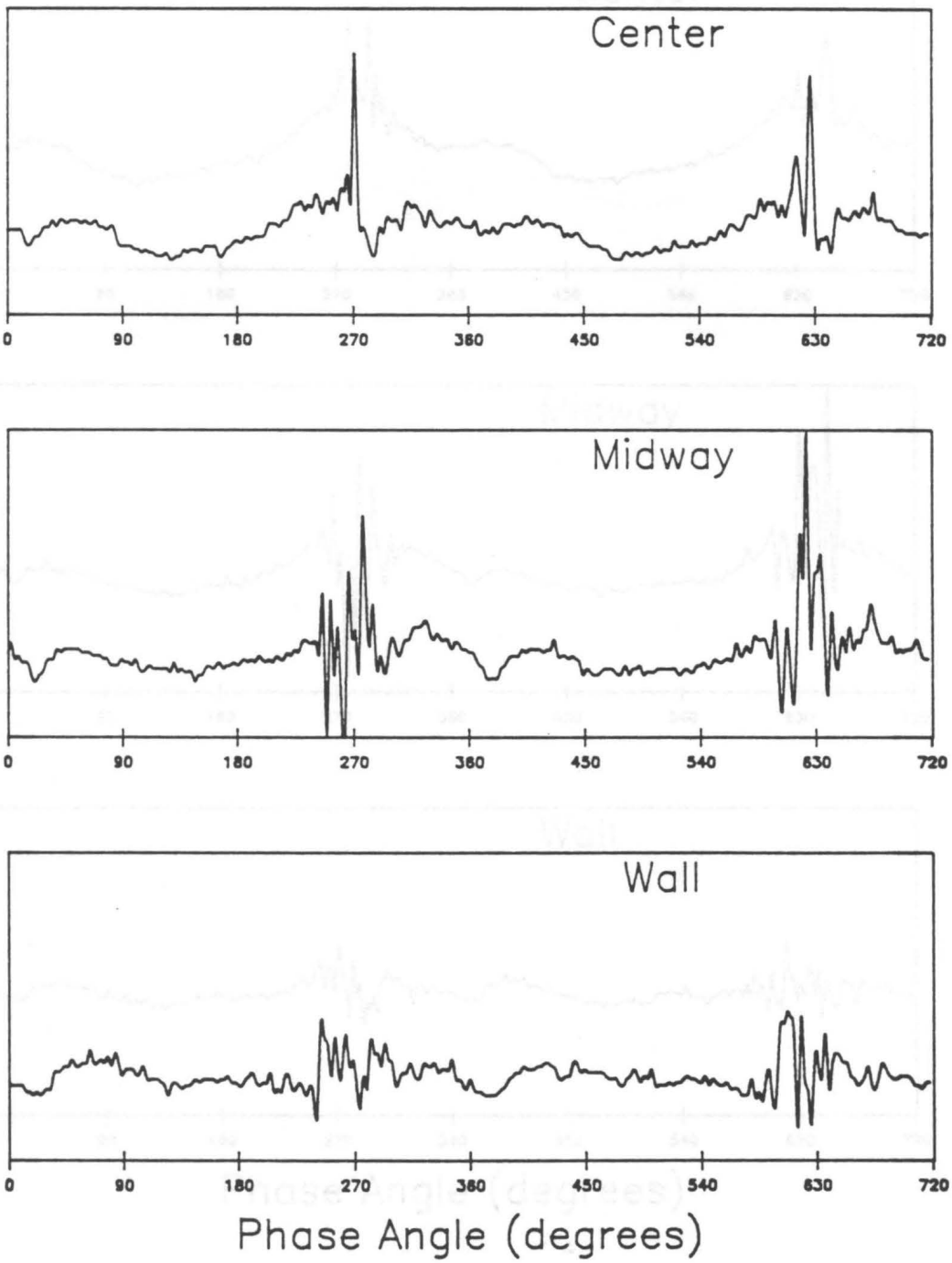

Figure 5.39. Output from the floor-mounted piezo-films for 177-μm Master Beads at K = 3: Output *versus* phase angle over two cycles. Top plot is for the center dot, center plot is for the dot 29 mm from the center, and bottom plot is for the dot 58 mm from the center.

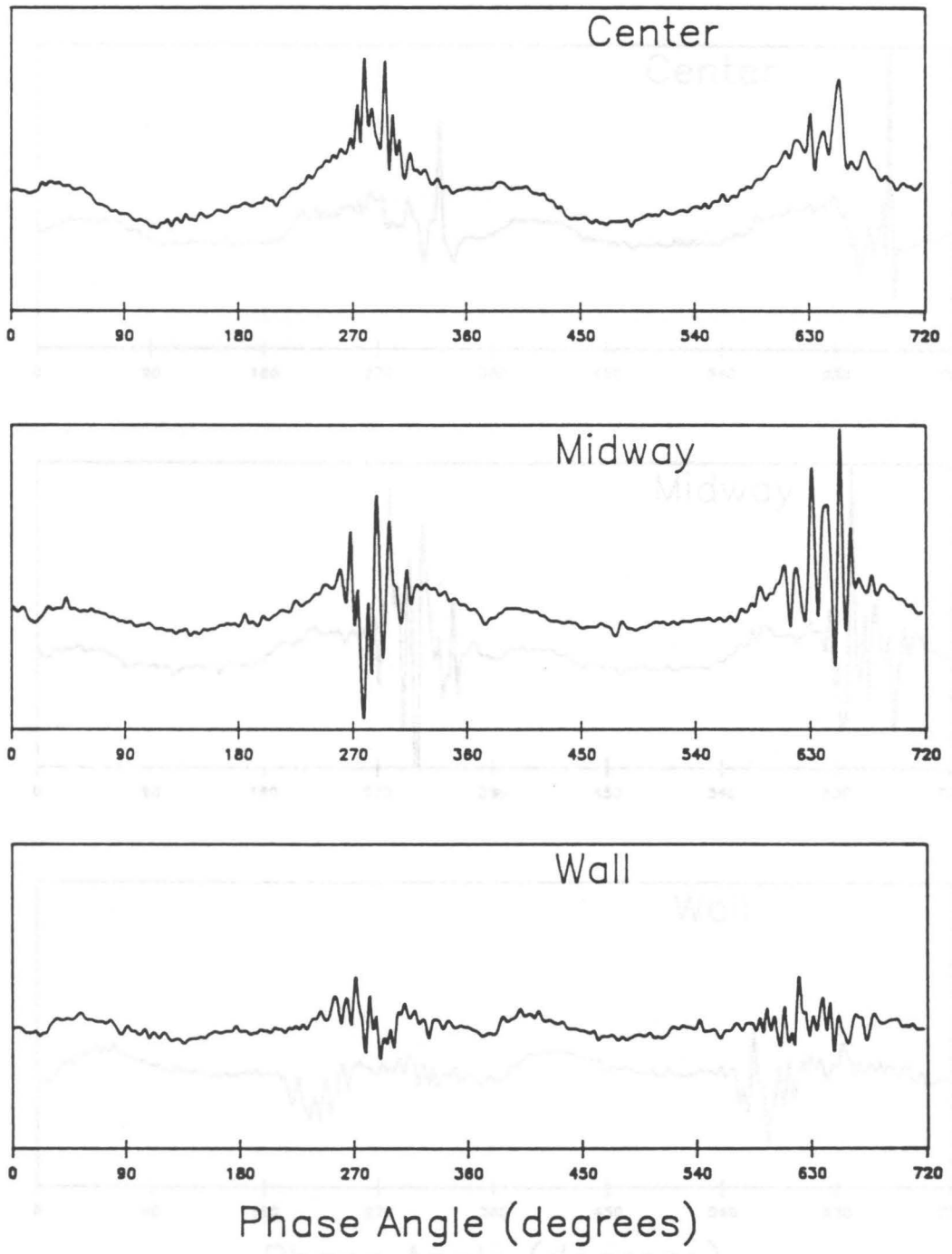

Figure 5.40. Output from the floor-mounted piezo-films for 177-μm Master Beads at K = 4: Output *versus* phase angle over two cycles. Top plot is for the center dot, center plot is for the dot 29 mm from the center, and bottom plot is for the dot 58 mm from the center.

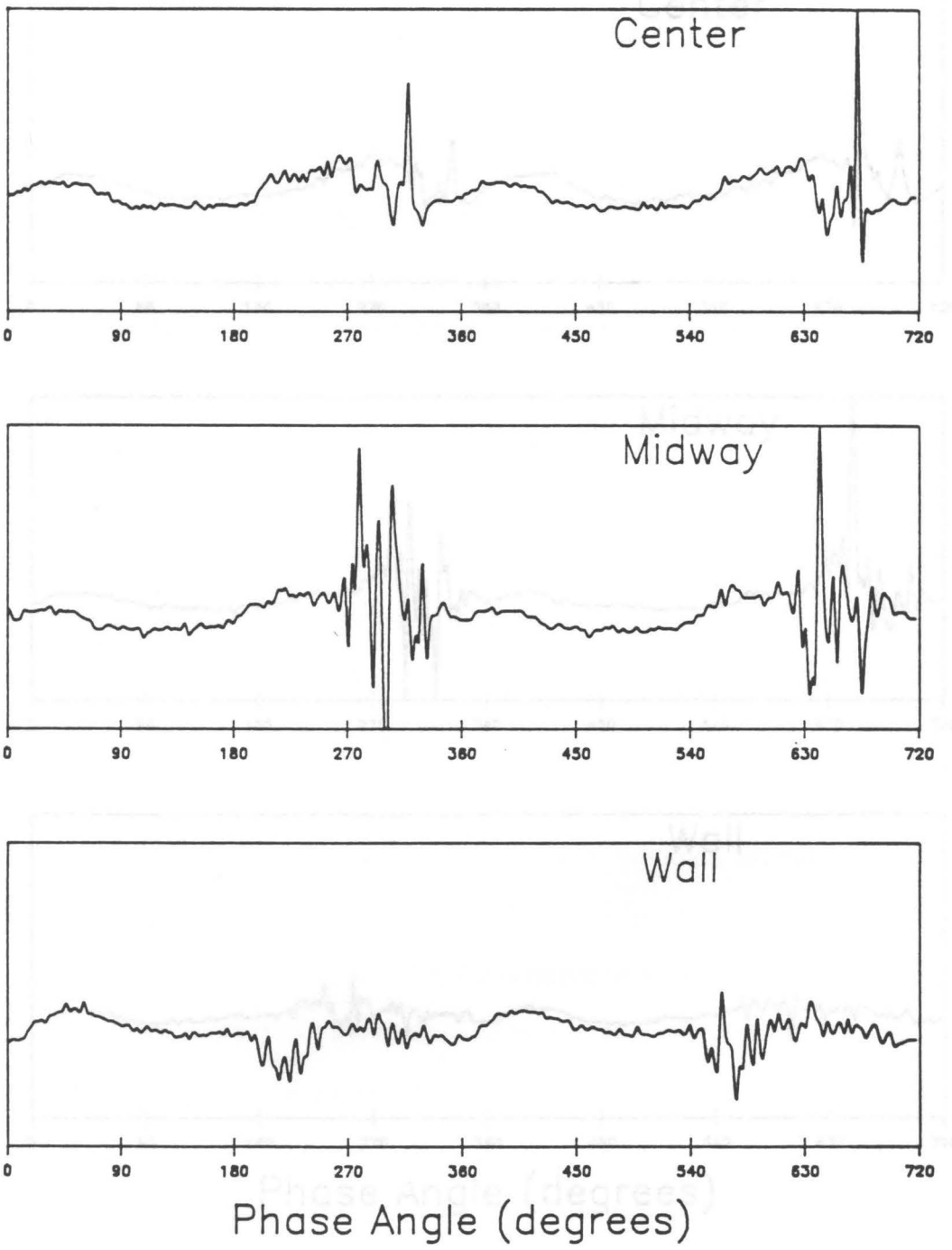

Figure 5.41. Output from the floor-mounted piezo-films for 177-μm Master Beads at K = 5: Output *versus* phase angle over two cycles. Top plot is for the center dot, center plot is for the dot 29 mm from the center, and bottom plot is for the dot 58 mm from the center.

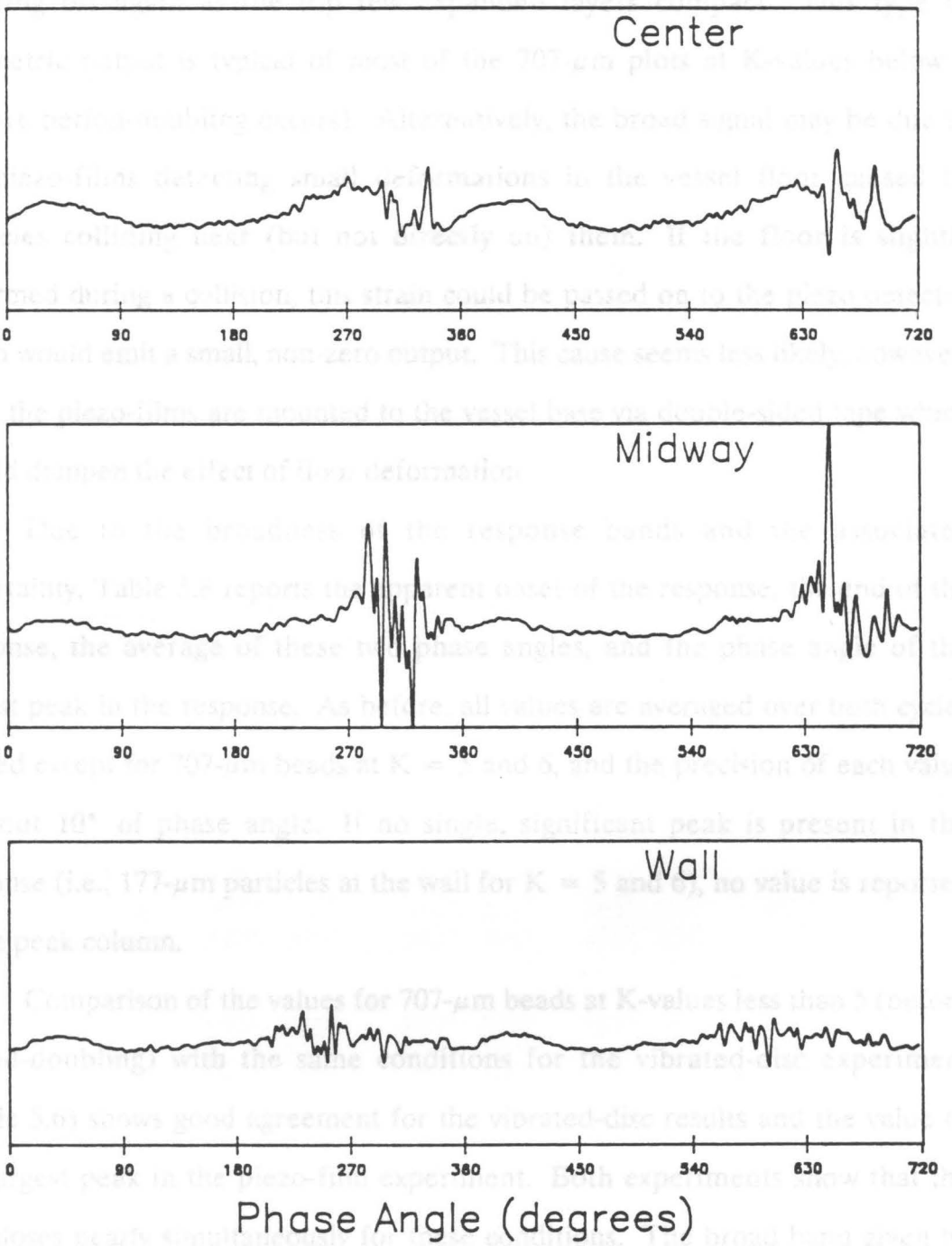

Figure 5.42. Output from the floor-mounted piezo-films for 177-μm Master Beads at K = 6: Output *versus* phase angle over two cycles. Top plot is for the center dot, center plot is for the dot 29 mm from the center, and bottom plot is for the dot 58 mm from the center.

tapering off again as the top few expanded layers compact. This type of symmetric output is typical of most of the 707-μm plots at K-values below 5 (before period-doubling occurs). Alternatively, the broad signal may be due to the piezo-films detecting small deformations in the vessel floor caused by particles colliding near (but not directly on) them. If the floor is slightly deformed during a collision, this strain could be passed on to the piezo detector which would emit a small, non-zero output. This cause seems less likely, however, since the piezo-films are mounted to the vessel base via double-sided tape which should dampen the effect of floor deformation.

Due to the broadness of the response bands and the associated uncertainty, Table 5.8 reports the apparent onset of the response, the end of the response, the average of these two phase angles, and the phase angle of the largest peak in the response. As before, all values are averaged over both cycles plotted except for 707-μm beads at K = 5 and 6, and the precision of each value is about 10° of phase angle. If no single, significant peak is present in the response (i.e., 177-μm particles at the wall for K = 5 and 6), no value is reported in the peak column.

Comparison of the values for 707-μm beads at K-values less than 5 (before period-doubling) with the same conditions for the vibrated-disc experiment (Table 5.6) shows good agreement for the vibrated-disc results and the value of the largest peak in the piezo-film experiment. Both experiments show that the gap closes nearly simultaneously for these conditions. The broad band given by the piezo-film indicates that the collision is not instantaneous, however, and that the compaction takes 35-70 degrees of phase angle (about 3-7 msec) for these particles. Above K = 5, the agreement between the two experiments is not good. Under these conditions of period-doubling, the output signal from the piezo-films

Table 5.8. Response of floor-mounted piezo-films

All data are for Master Beads

K-value	Piezo-Dot	Onset of Response	End of Response	Average	Largest Peak
			707 μm		
2	wall	250°	316°	283°	277°
	midway	246°	309°	278°	276°
	center	247°	308°	278°	276°
3	wall	286°	350°	318°	322°
	midway	285°	356°	321°	318°
	center	292°	349°	320°	324°
4	wall	296°	351°	324°	337°
	midway	314°	355°	335°	337°
	center	315°	347°	331°	339°
5*	wall	327° 296°	395° 337°	361° 317°	373° 308°
	midway	342° 302°	387° 352°	365° 327°	367° 326°
	center	323° 286°	382° 366°	353° 326°	364° 326°
6*	wall	297° 258°	407° 347°	352° 303°	381° 307°
	midway	301° 272°	409° 348°	355° 310°	387° 306°
	center	325° 265°	404° 333°	365° 299°	390° 306°

*Bed is in period-doubling state

(table continued on following page)

Table 5.8 (continued)

K-value	Piezo-Dot	Onset of Response	End of Response	Average	Largest Peak
			177 μm		
2	wall	204°	278°	241°	235°
	midway	200°	258°	229°	233°
	center	200°	264°	232°	225°
3	wall	234°	327°	281°	247°
	midway	236°	320°	278°	272°
	center	248°	301°	275°	271°
4	wall	232°	332°	282°	267°
	midway	241°	324°	283°	294°
	center	252°	325°	289°	297°
5	wall	193°	342°	268°	--
	midway	242°	344°	293°	284°
	center	257°	343°	300°	318°
6	wall	204°	346°	275°	--
	midway	255°	347°	301°	297°
	center	289°	346°	318°	332°

is not symmetric around the major peak; instead the peak tends to occur later in the output band. This is further demonstrated by the poorer agreement between the phase angle of the largest peak and the average of the onset and end of response for these high K-values.

A comparison of the piezo-film collision values for 177-μm beads with those from the vibrated-disc experiment shows much poorer agreement. In nearly all cases the value of the largest peak for the piezo-films occurs at a significantly smaller phase angle than the collision observed by the vibrated-disc technique. Also, the shape of the output response from the piezo-films is less consistent than that for the 707-μm beads. For 177-μm particles, the major peak appears sometimes early, sometimes near the center, and sometimes late in the response band in an apparently random fashion. Unfortunately, this inconsistency in response band makes analysis of the data more difficult. Furthermore, since the voltage scales for these plots are smaller, the background signal in the output voltage is relatively larger than for the 707-μm beads which makes the selection of the onset and end of the output response somewhat arbitrary, particularly for the lower K-values. At K-values below 4, therefore, little can be said about the rate of gap closure. At K-values of 5 and 6 (Figures 5.41 and 5.42), the plots suggest qualitatively that the collision occurs from the wall toward the center as expected. The values given in Table 5.8 are considered too unreliable to warrant a calculation of the rate of closure, however.

Figures 5.43 to 5.47 represent plots of the output from floor-mounted piezoelectric detectors for 88-μm Master Beads. These plots are interesting because they show cyclically varying outputs without the sharp peaks associated with collision. Note that the signals, particularly for K-values above 2, are nearly sinusoidal and of the same phase as the vessel acceleration (*c.f.* the accelerometer

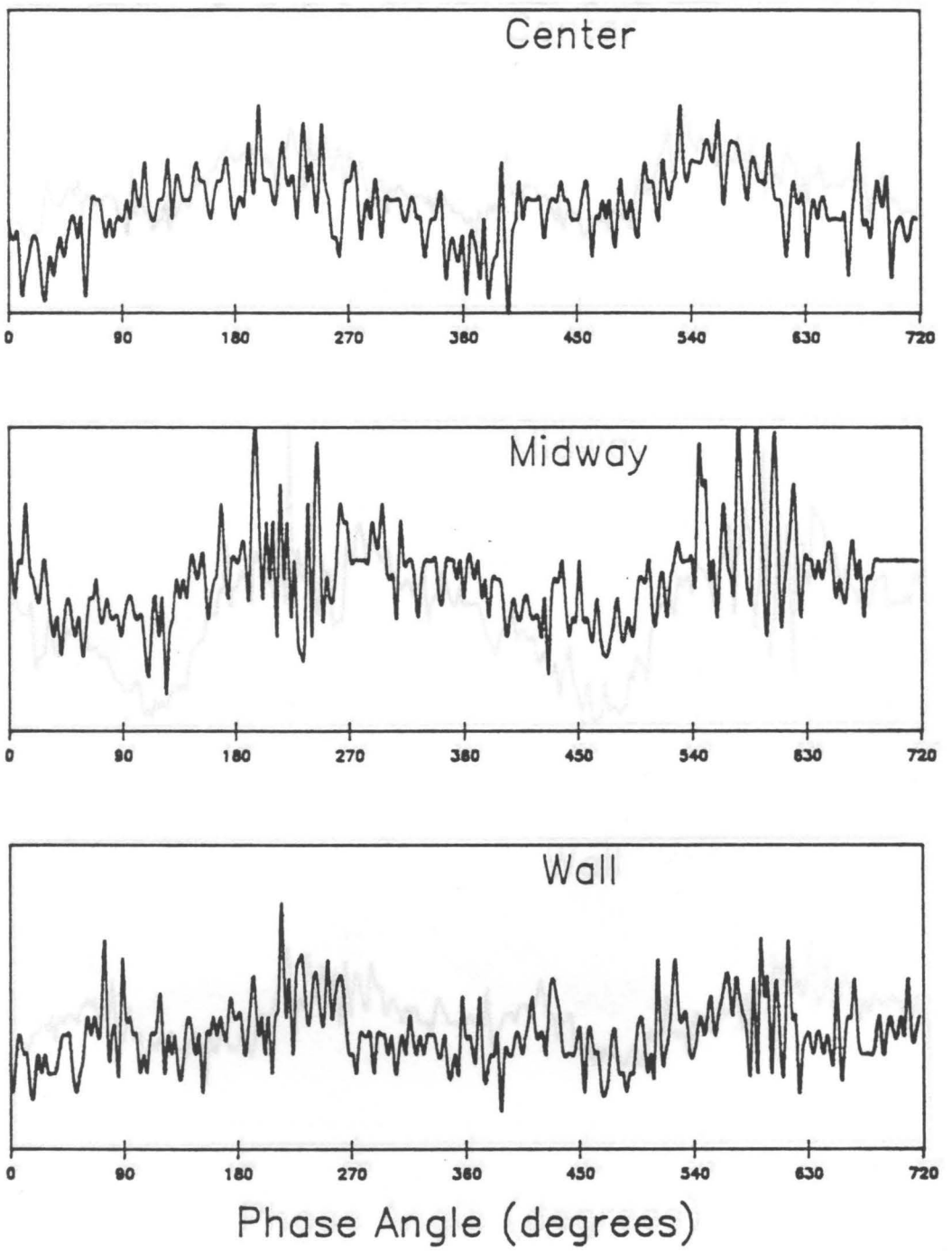

Figure 5.43. Output from the floor-mounted piezo-films for 88-μm Master Beads at K = 2: Output *versus* phase angle over two cycles. Top plot is for the center dot, center plot is for the dot 29 mm from the center, and bottom plot is for the dot 58 mm from the center.

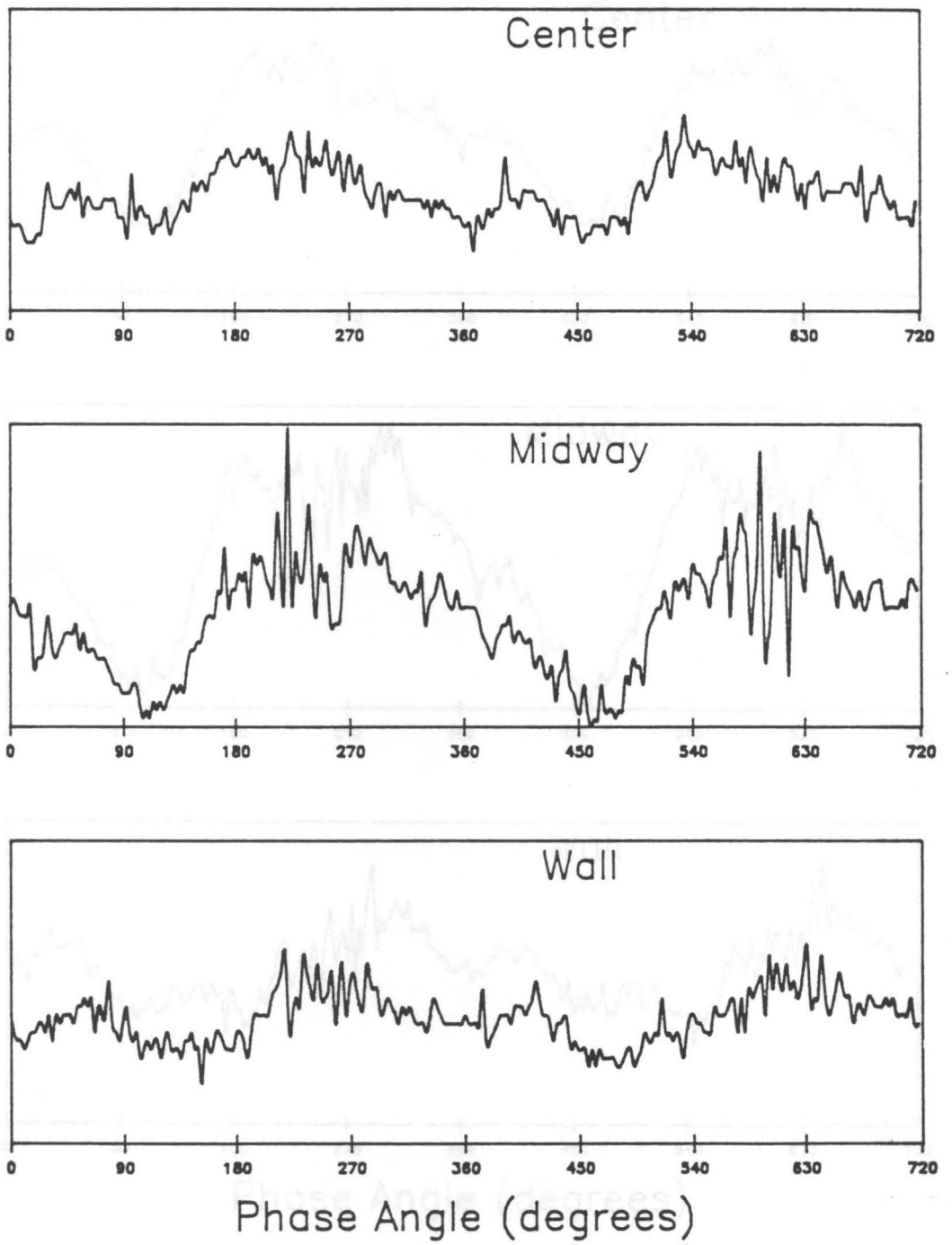

Figure 5.44. Output from the floor-mounted piezo-films for 88-μm Master Beads at K = 3: Output *versus* phase angle over two cycles. Top plot is for the center dot, center plot is for the dot 29 mm from the center, and bottom plot is for the dot 58 mm from the center.

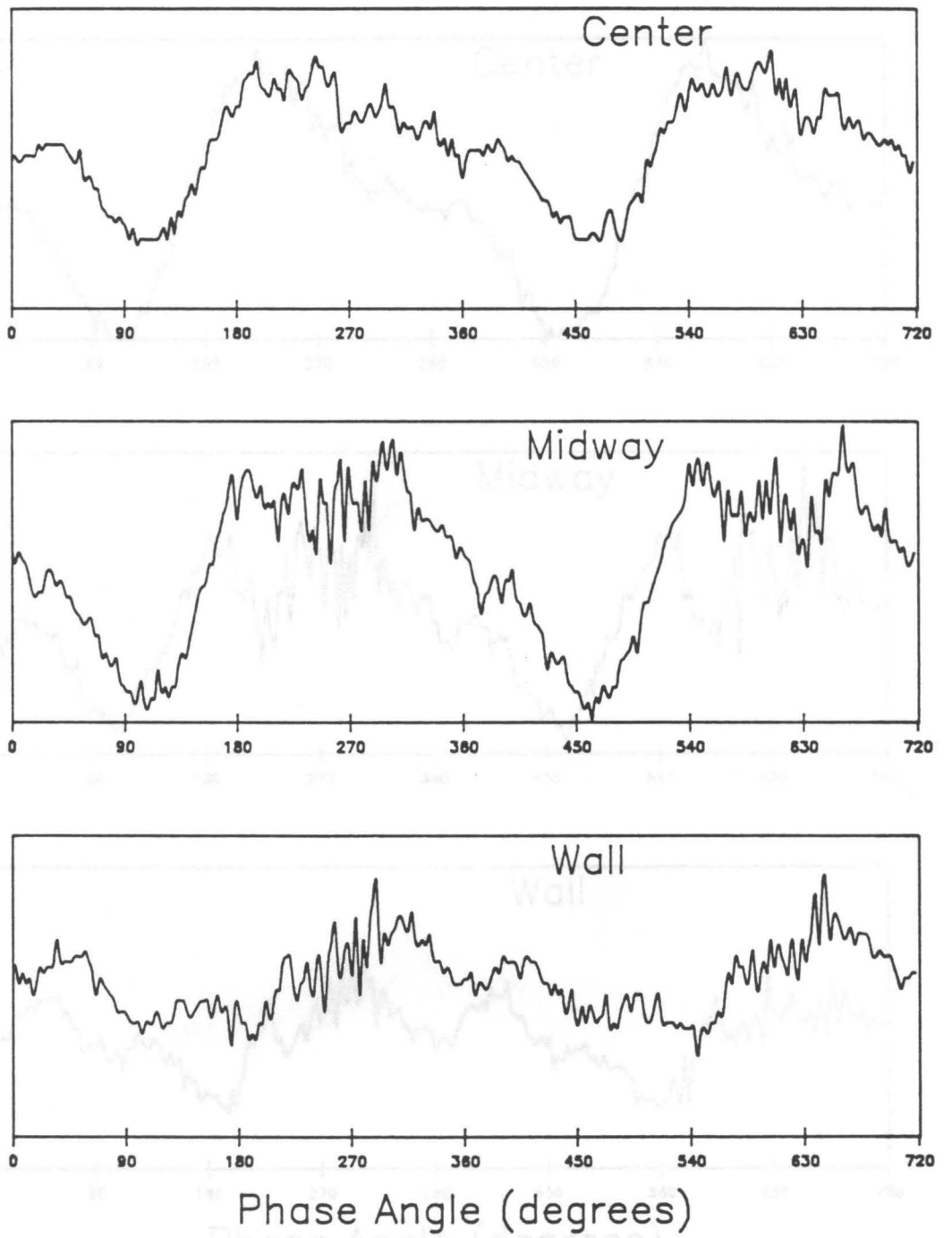

Figure 5.45. Output from the floor-mounted piezo-films for 88-μm Master Beads at K = 4: Output *versus* phase angle over two cycles. Top plot is for the center dot, center plot is for the dot 29 mm from the center, and bottom plot is for the dot 58 mm from the center.

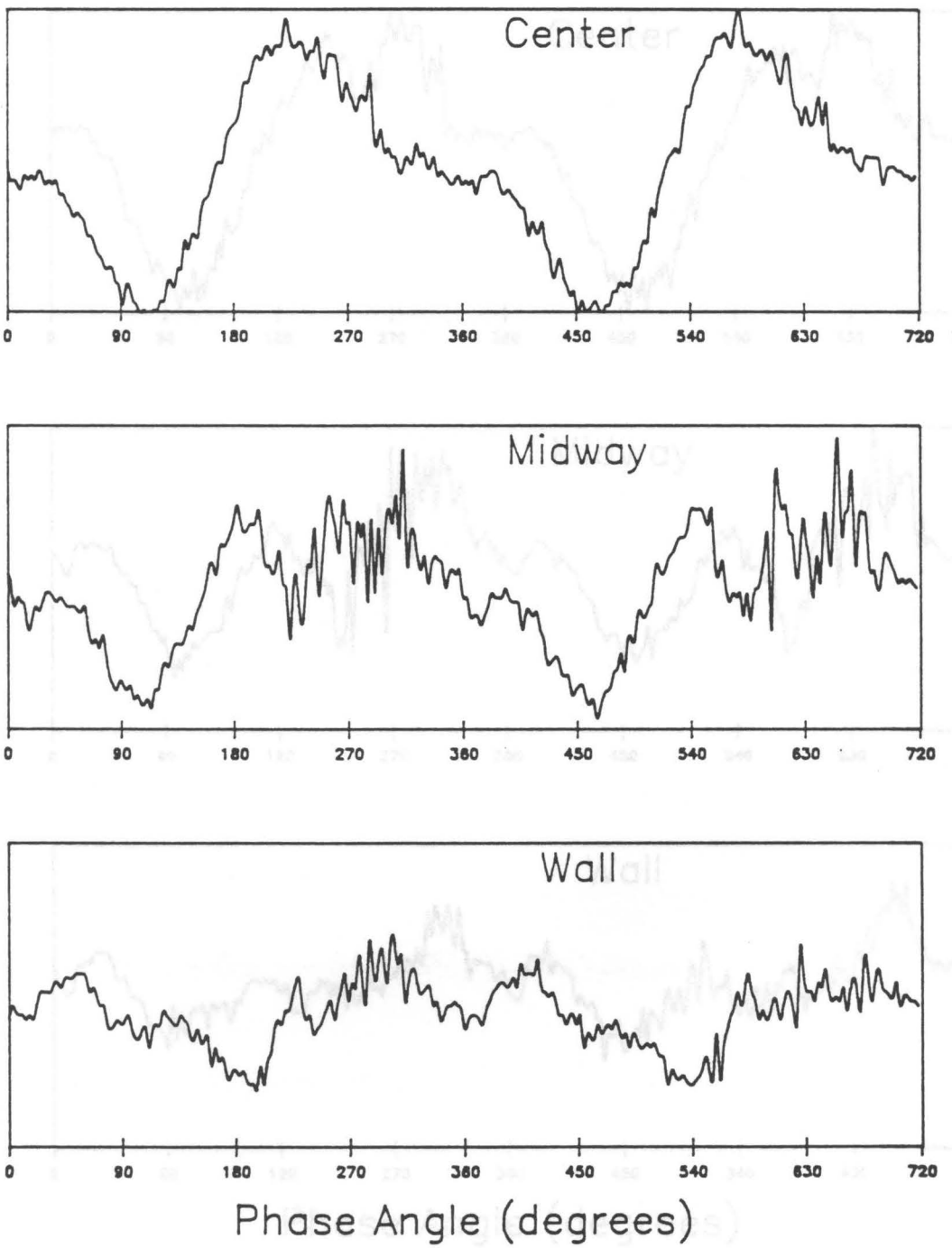

Figure 5.46. Output from the floor-mounted piezo-films for 88-μm Master Beads at K = 5: Output *versus* phase angle over two cycles. Top plot is for the center dot, center plot is for the dot 29 mm from the center, and bottom plot is for the dot 58 mm from the center.

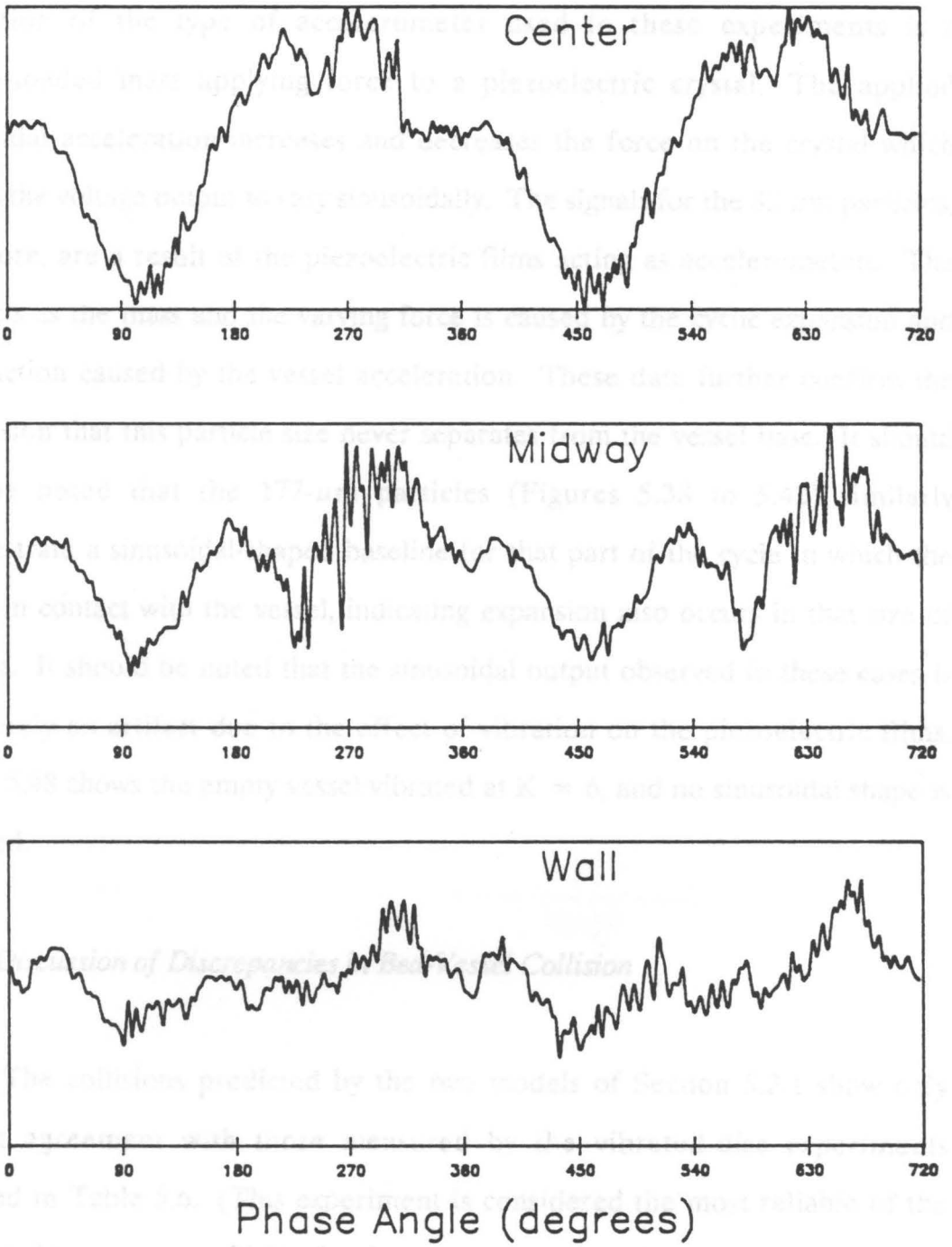

Figure 5.47. Output from the floor-mounted piezo-films for 88-μm Master Beads at K = 6: Output *versus* phase angle over two cycles. Top plot is for the center dot, center plot is for the dot 29 mm from the center, and bottom plot is for the dot 58 mm from the center.

signal of Figure 5.31, page 178). As mentioned in Section 3.3.2.1, the principle of operation of the type of accelerometer used in these experiments is a spring-loaded mass applying force to a piezoelectric crystal. The applied sinusoidal acceleration increases and decreases the force on the crystal which causes the voltage output to vary sinusoidally. The signals for the 88-μm particles, therefore, are a result of the piezoelectric films acting as accelerometers. The bed acts as the mass and the varying force is caused by the cyclic expansion and compaction caused by the vessel acceleration. These data further confirm the conclusion that this particle size never separates from the vessel base. It should also be noted that the 177-μm particles (Figures 5.38 to 5.42) similarly demonstrate a sinusoidal-shaped baseline for that part of the cycle in which the bed is in contact with the vessel, indicating expansion also occurs in that size of particle. It should be noted that the sinusoidal output observed in these cases is not merely an artifact due to the effect of vibration on the piezoelectric films. Figure 5.48 shows the empty vessel vibrated at K = 6, and no sinusoidal shape is detected.

5.2.5 Discussion of Discrepancies in Bed-Vessel Collision

The collisions predicted by the two models of Section 5.2.1 show only modest agreement with those measured by the vibrated-disc experiments reported in Table 5.6. (This experiment is considered the most reliable of the three used to measure collision for the reasons mentioned earlier in this section.) Both models tend to predict significantly later collisions than those measured for 707-μm particles at all K-values. The predictions are somewhat better for

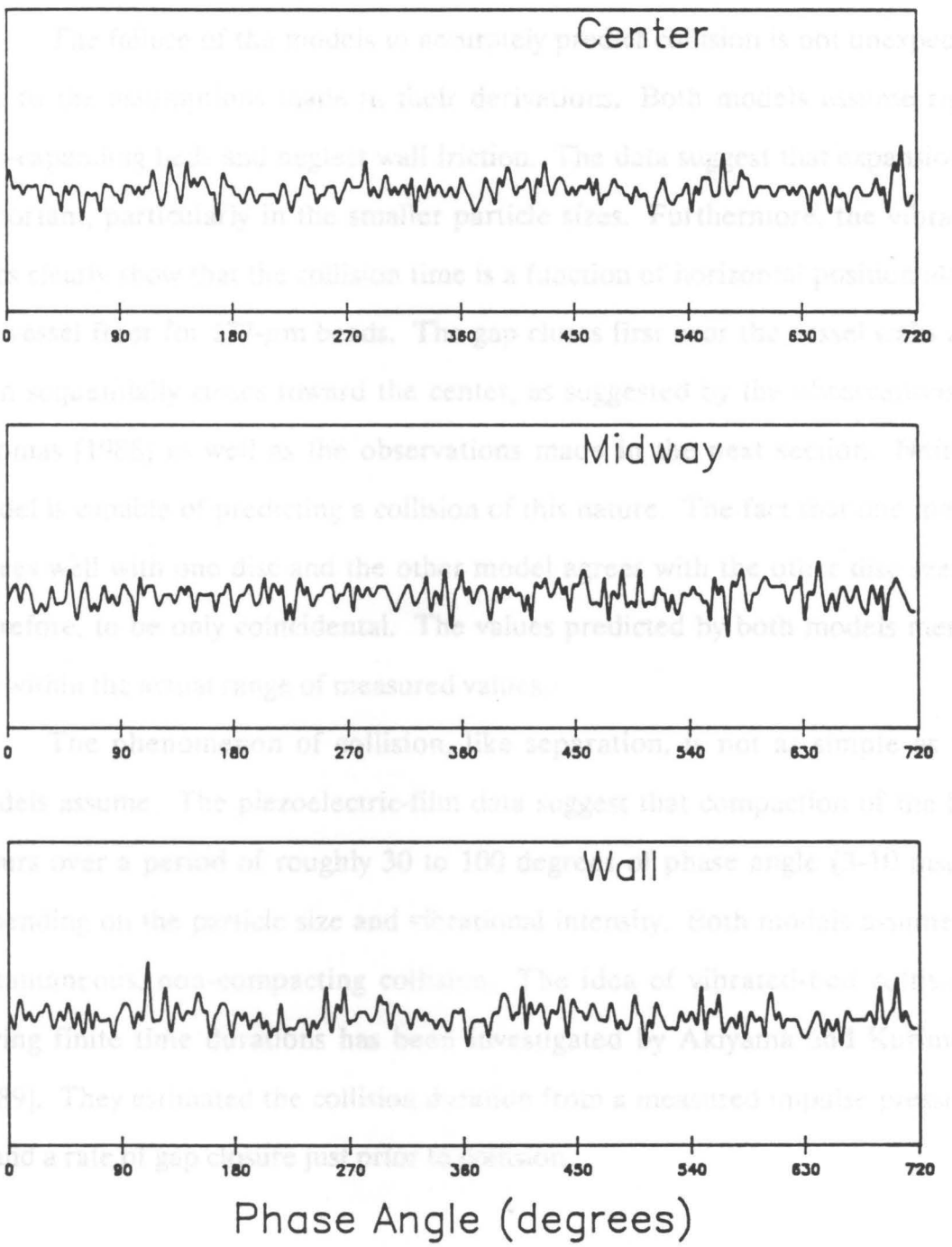

Figure 5.48. Output from the floor-mounted piezo-films for an empty vessel vibrated at K = 6.

177-μm particles. The Kroll model agrees well with the values for the edge disc, and the Thomas model agrees with the center disc.

The failure of the models to accurately predict collision is not unexpected due to the assumptions made in their derivations. Both models assume rigid, non-expanding beds and neglect wall friction. The data suggest that expansion is important, particularly in the smaller particle sizes. Furthermore, the vibrated discs clearly show that the collision time is a function of horizontal position along the vessel floor for 177-μm beads. The gap closes first near the vessel walls and then sequentially closes toward the center, as suggested by the observations of Thomas [1988] as well as the observations made in the next section. Neither model is capable of predicting a collision of this nature. The fact that one model agrees well with one disc and the other model agrees with the other disc seems, therefore, to be only coincidental. The values predicted by both models merely fall within the actual range of measured values.

The phenomenon of collision, like separation, is not as simple as the models assume. The piezoelectric-film data suggest that compaction of the bed occurs over a period of roughly 30 to 100 degrees of phase angle (3-10 msec), depending on the particle size and vibrational intensity. Both models assume an instantaneous, non-compacting collision. The idea of vibrated-bed collisions having finite time durations has been investigated by Akiyama and Kurimoto [1989]. They estimated the collision duration from a measured impulse pressure, σ, and a rate of gap closure just prior to collision,

$$\frac{ds}{dt}$$

(calculated from the Gutman model of Section 2.1.7.3) with the equation

$$\sigma t = - \rho_b L \frac{ds}{dt} \qquad [5.1]$$

In this equation, t is the duration of collision, ρ_b is the bulk density of the bed, and L is the bed depth. They report values of 2 to 4 msec at 25 Hz for bed depths of 40 mm at a K-value of 5 for particles in the range of 99 to 332 μm. This range agrees fairly well with the durations reported here.

5.3 Bed Compaction During Collision

Despite the assumption of instantaneous collision made by nearly all of the models discussed in Chapter 2, several investigators have conjectured or observed a compaction of the bed upon collision. Gutman [1974] postulated the propagation of a compressive stress wave passing up through the bed upon collision which would be reflected back down the bed as a tensile wave. He did not report observing this wave, although he took high-speed movies of his bed. Thomas [1988], however, reported observing what he termed a compaction wave passing through 177-μm Master Beads at a K-value of 4. His observations were made via high-speed movies. For these conditions, he reported that the compaction wave was not merely a horizontal wave propagating vertically up through the bed, but rather a diagonal wave with vertical and horizontal velocity components. He noted that the forward, horizontal edge of the wave corresponded to the point where the gap had just closed. (Gap closure occurs first at the side walls and moves toward the center under these conditions.) The

horizontal propagation velocity was, therefore, equal to the horizontal rate of gap closure. He assumed the vertical propagation to be a function of the rate at which the bed can expel gas, which would be a function of particle size. He noted no reflected tensile wave as Gutman had predicted, however. Based on these observations, a study has been conducted to further investigate this compaction-wave phenomenon.

5.3.1 Compaction-Wave Observations Based on High-Speed Movies

Since Thomas [1988] reported observing a compaction wave using high-speed movies, this technique has been adopted for this study. Movies are taken as described in Section 4.2.4. All of the movies are shot in a vessel with no partition (i.e., no "dummy" heat probe). Because of the difficulty in analyzing high-speed movies quantitatively, the experiments are designed to reveal qualitative information about the compaction-wave phenomenon.

The first series of experiments is designed to test the dependence of the angle of the compaction wave on particle size. For the situation depicted schematically in Figure 5.49, it can be shown that

$$\frac{V_V}{V_H} = \cot \alpha \qquad [5.2]$$

Due to the nature of the cotangent function, decreasing the angle α results in increasing the ratio of vertical propagation velocity to horizontal propagation velocity, and *vice versa.* This suggests that for conditions in which the vertical propagation is dominant, the compaction wave should be nearly horizontal

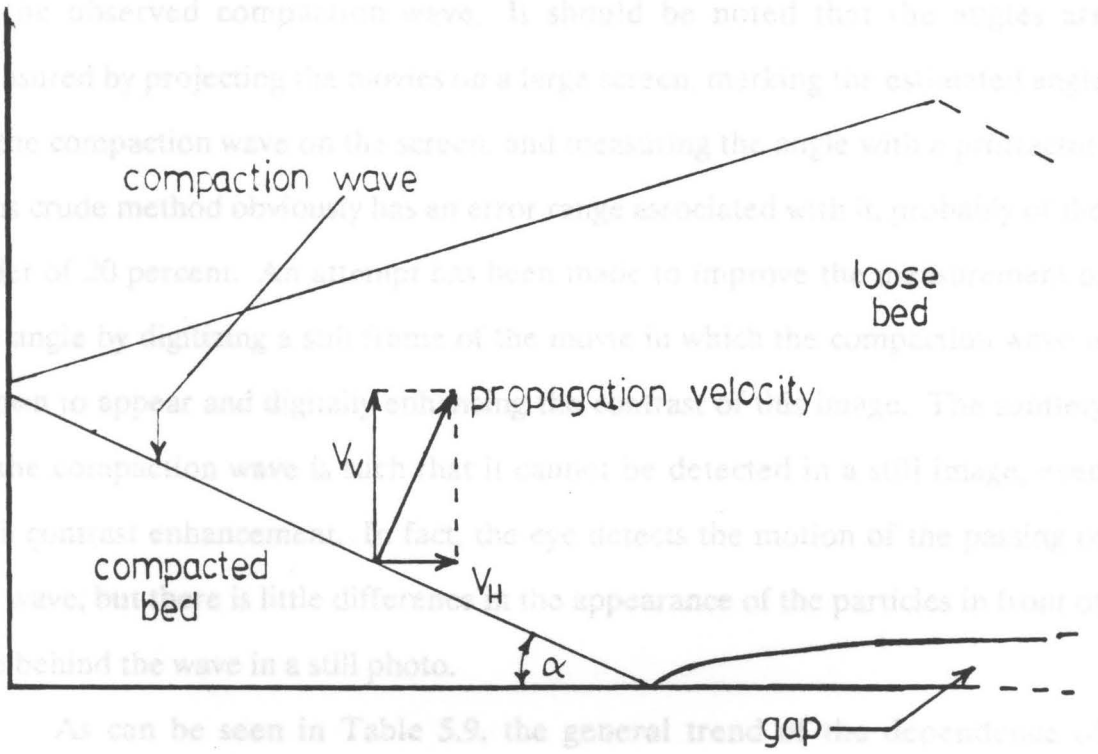

Figure 5.49. Schematic of compaction-wave propagation: Diagonal propagation of a compaction wave in a vibrated bed (the other half of the bed is the mirror image). Notation: V_V = vertical propagation velocity; V_H = horizontal propagation velocity; α = angle the compaction wave forms with the vessel base.

(angle α is small). If, as Thomas [1988] postulated, the vertical propagation velocity is a function of the ease with which gas can escape from the bed, large-particle beds should exhibit smaller-angle compaction waves than small-particle beds.

High-speed movies of Master Beads of five different sizes have been taken at approximately the same K-value. Table 5.9 summarizes the approximate angle of the observed compaction wave. It should be noted that the angles are measured by projecting the movies on a large screen, marking the estimated angle of the compaction wave on the screen, and measuring the angle with a protractor. This crude method obviously has an error range associated with it, probably of the order of 20 percent. An attempt has been made to improve the measurement of the angle by digitizing a still frame of the movie in which the compaction wave is known to appear and digitally enhancing the contrast of this image. The subtlety of the compaction wave is such that it cannot be detected in a still image, even with contrast enhancement. In fact, the eye detects the motion of the passing of the wave, but there is little difference in the appearance of the particles in front of and behind the wave in a still photo.

As can be seen in Table 5.9, the general trend of the dependence of compaction-wave angle on particle size is as expected. Since the angle-measurement technique is crude, no attempt is made to quantitatively relate the angle to the particle size. Rather, a discussion of observations made while watching the films of phenomena which affect the compaction wave is presented.

The film of 707-μm beads vibrated at K = 3.75 shows that the top surface of the bed, while approximately level on the average, actually consists of a series of hills and valleys spaced approximately an inch apart. Furthermore, this feature

Table 5.9. Approximate angle of propagation of compaction waves for Master Beads

Particle Size (microns)	Angle (degrees)
707	0
353	8-10
272	12-15
229	20-25
177	25-30

alternates in every other cycle; that is, where a high place occurs in one cycle, a low place will appear in the next cycle. Such behavior has also been reported by Fauve *et al.* [1989], who reported it as a standing wave of half of the frequency of bed vibration (thus the alternating peaks and valleys). They give no explanation for the behavior, but state that it is analogous to the Faraday instability of fluids. The proposed explanation for the observed alternating pattern is a small, local difference in compaction. In a vertical slice of the bed beneath a valley, the particles are marginally more compacted than in a slice under a peak. Due to this extra compaction, the normal force of the vessel base is transmitted better, causing this section to be thrown slightly higher in the next cycle. Once this section is thrown higher, it becomes more expanded, is slower to compact, and becomes a peak on the surface. This same section (now a peak) is not thrown as high in the succeeding cycle, thus has more time to compact on collision, and becomes a valley once more. A consequence of this phenomenon is that the compaction wave, while reported in Table 5.9 as being flat, actually has the same high and low features as the top surface and is merely flat on average. The features in the compaction wave are observed to be the opposite of those on the surface, however. Where a peak occurs in the surface, a low point is seen in the compaction wave directly beneath, as shown in Figure 5.50. This is because the expanded region beneath a peak takes longer to compact than a region beneath a valley, and thus the compaction wave lags behind. It should be noted that this K-value is not far from the value needed to cause this size of particle to go into the period-doubling regime, and thus this behavior may be the beginning of what leads to the period-doubling phenomenon.

The next smaller size filmed, 353-μm beads, exhibits very slight bunkering at K = 4. The same hill-and-valley effect as reported for 707-μm beads is

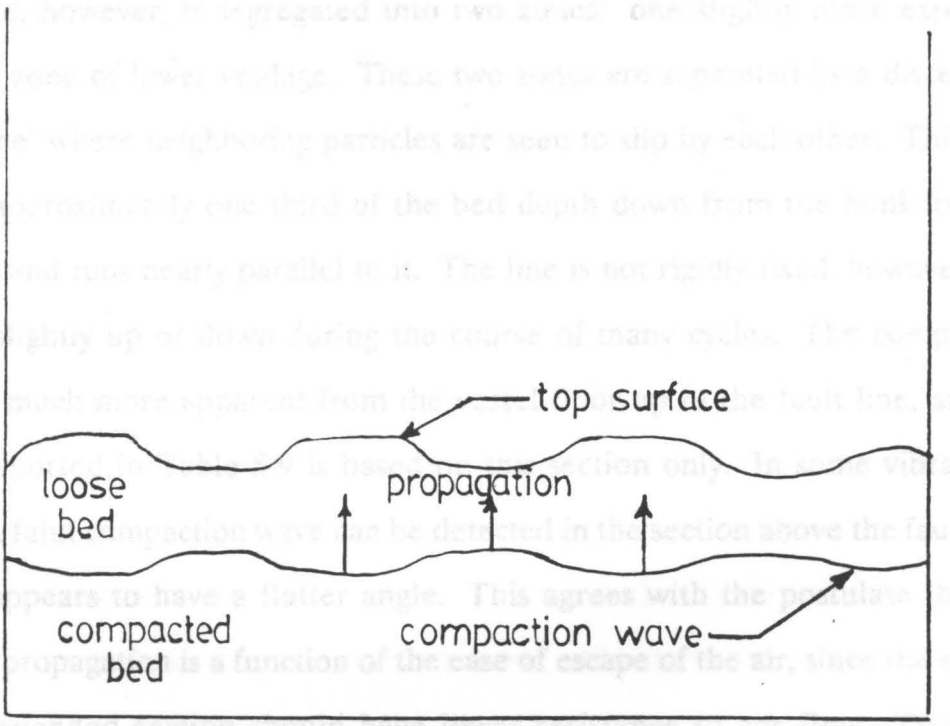

Figure 5.50. Schematic showing compaction wave for 707-μm Master Beads at K = 3.75: Wavy nature of the top surface and compaction wave is shown.

noticeable, but to a much smaller extent. The compaction wave, while exhibiting the inverse effect of the top surface, is no longer flat on the average. The estimated average angle for these conditions is between eight and ten degrees, as reported in the table.

The 272-μm particle bed exhibits a bunker at this vibrational intensity (K = 4). It does not have the hill-and-valley effect observed in the larger beads. This bed, however, is segregated into two zones: one slightly more expanded above a zone of lower voidage. These two zones are separated by a discernible "fault line" where neighboring particles are seen to slip by each other. This fault line is approximately one-third of the bed depth down from the bunkered top surface, and runs nearly parallel to it. The line is not rigidly fixed, however, and moves slightly up or down during the course of many cycles. The compaction wave is much more apparent from the vessel floor up to the fault line, and the angle reported in Table 5.9 is based on this section only. In some vibrational cycles, a faint compaction wave can be detected in the section above the fault line, and it appears to have a flatter angle. This agrees with the postulate that the vertical propagation is a function of the ease of escape of the air, since the slightly more expanded section should have lower resistance to gas flow. The same qualitative observations are made in the films of 229 and 177-μm beads at K = 4.3, but with the angles reported in Table 5.9. A high-speed movie of 88-μm Master Beads does not show any discernible compaction wave, but merely cyclic expansion and compaction. A fault line is apparent and even more pronounced to the point where it appears to be almost a small split in the bed. No gap is observed for these particles.

A second series of movies has been taken to investigate the dependence of the angle of the compaction wave on vibrational intensity for a fixed particle size.

Master Beads of 229 μm are chosen since they exhibit a relatively easily discernible compaction wave with a non-zero angle. If the vertical propagation velocity can be assumed to be approximately the same for particles of the same size, then the measure of the change in compaction-wave angle with K-value becomes a measure of the dependence of the rate of horizontal propagation (and thus gap closure) on vibrational intensity. This assumes that the voidage, and thus the resistance to gas flow, is about the same at different K-values.

Films of these particles at K-values of 3, 4.3, and 5 show the compaction-wave angle to be about the same within the limits of the admittedly crude measurement technique. In light of the observed voidage variation within a single bed mentioned above which causes a fault line, the assumption of constant vertical propagation rate seems to be invalid, however. (All of the experiments were planned and the films shot before any of the films were carefully viewed.) In fact, data from Thomas [1988] indicates that the amount of time that it takes for the maximum pressure peak for these solids to travel from the wall to the center is more than three times as long for K = 5 as for K = 3. If the maximum pressure peak corresponds to the compaction wave, this shows that the horizontal propagation rate does depend on K-value. The high-speed movies thus merely show that the ratio of vertical propagation to horizontal propagation is constant for a given particle size at different vibrational intensities. This suggests that the angle of the compaction wave is a fundamental property of a given particle. This conclusion has been substantiated by Professor J. Michael Duncan of this university's Department of Civil Engineering. In a discussion of the soil mechanics involved with vibrated beds, he suggested that the compaction wave is the passing of passive failure planes through the bed, and thus the angle is a function only of particle properties and the orientation of the principal stresses.

Since all of the beds with a non-zero compaction-wave angle also have at least a slight degree of bunker on the top surface, an experiment has been run to see if the angle of the top surface of the bed is related to the angle of the compaction wave. To test this, 707-μm beads are filmed at K = 2.2. At this low vibrational intensity, even this largest size of beads is bunkered. The violence of collision at this K-value is much less, and the compaction wave is equivalently more difficult to discern. The film shows that the compaction-wave angle is still zero or very close to it, as is the case for the same particles at K = 3.75 when the surface is not bunkered. This experiment suggests that the angle of the compaction wave does not depend on the angle of the top surface, and it also lends further credence to the theory that the compaction-wave angle is a property of the particle.

For the radically different situation of the same 707-μm particles at a vibrational intensity high enough to induce period-doubling, the angle of the compaction wave is greatly different. A film of these same beads at K = 5 shows a very steep compaction wave of about 60 degrees. The entire situation is changed under these conditions, however. The bed is observed to land at one wall and the gap sequentially closes from that wall all the way over to the other rather than from both sides toward the middle. The wall at which collision first occurs alternates in successive vibrational cycles so that the entire bed appears to rock back and forth from side to side. The explanation for this behavior is similar to that for the hill-and-valley behavior of the same particles at K = 3.75. The side of the bed which collides first becomes more compacted and is thrown up higher in the next cycle. This causes it to land later in the following cycle, consequently it is not compacted as well or thrown as high. This leads to the alternating phenomenon observed.

5.3.2 *Estimation of the Compaction-Wave Propagation Velocities*

Since the compaction wave is observed to have both horizontal and vertical velocity components, experiments are run to allow estimation of these components. The horizontal propagation can be calculated from the vibrated-disc data, with the assumption that the horizontal propagation corresponds to the rate of gap closure (which appears to be the case in the high-speed movies). As previously mentioned, for the 707-μm particles, the compaction wave is very nearly horizontal and thus has only vertical propagation. This is true, at least, for the K-values below which period-doubling occurs. Table 5.6, which reports collision angles for the vibrated-disc experiments, shows that the collision angle for this solid is nearly the same for the two discs at K-values up to 4. This table shows that the 177-μm particles do have a horizontal component of the compaction wave, however.

It can be deduced from Table 5.6 that the rate of gap closure depends on the K-value for 177-μm beads, with the closure rate decreasing as K-value increases. At K = 2, the gap closes about 8° later at the center than at the edge; at K = 4, the gap closes about 15° later at the center; at K = 6, the gap closes about 35° later at the center. Since the distance between the centers of the two discs is 39 mm, these values correspond to horizontal velocities of about 44, 23, and 10 meters per second, respectively. These values are only reliable within about 20 percent due to the error associated with reading the phase angles. Since no reliable collision data are available for 88-μm particles (and, in fact, no compaction wave is observed in high-speed movies for this particle), no estimate of a propagation velocity is made.

The vertical propagation velocity is estimated from passive piezo-films placed on a side wall of the vessel as described in Section 3.2.2.1. The data obtained from this experiment are very similar to the floor-mounted piezo-film data as can be seen in Figures 5.51 to 5.65. Since the response range is again quite broad, only a rough estimate of vertical propagation velocity can be made. Figures 5.51, 5.52, and 5.53 for 707-μm particles at K-values of 2, 3, and 4, respectively, indicate that the time taken for the compaction wave to pass from the bottom to the top piezo-dot is between 8 and 15 degrees of phase angle. Since the distance between these dots is 15.8 mm, this corresponds to a vertical propagation of about 10 to 18 meters per second. It appears that the velocity increases as the K-value increases, but the uncertainty is so great (on the order of 100 percent) that no real conclusions can be drawn.

For the 177-μm beads, the signal is weaker than for the 707-μm beads, and the background noise is relatively greater. Figure 5.58, at K = 4, indicates a time of about 14 degrees of phase angle for the passage of the compaction wave from the bottom piezo-film to the top one. This corresponds to a velocity of about 10 meters per second, but this value is no more accurate than an order of magnitude due to the uncertainty of reading the peaks in Figure 5.58. Note that this value, when used with the value for horizontal propagation cited previously of 23 meters per second, gives a value of 66.5° for α in Equation 5.2. This value does not agree at all with the observed angle of approximately 25° for this solid. If the values of the observed angle and the horizontal propagation velocity (which seems much more reliable than the vertical velocity) are used, Equation 5.2 gives a value of about 50 meters per second.

Figures 5.61 to 5.65 for 88-μm particles again show somewhat sinusoidal curves indicating again the expansion and compaction which occurs during the

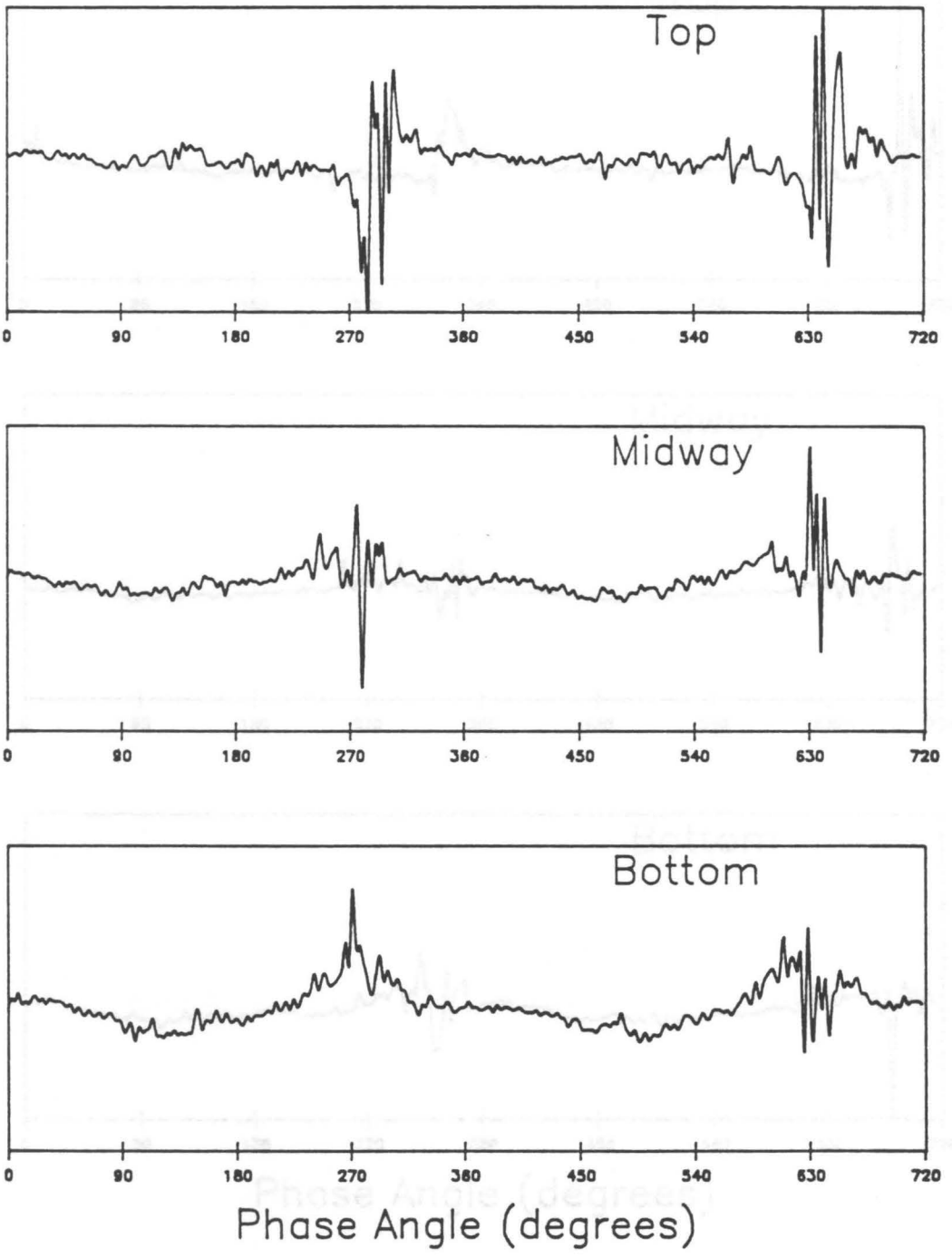

Figure 5.51. Output from the wall-mounted piezo-film for 707-μm Master Beads at K = 2: Output from the piezo-dots over two cycles. Top plot is for the top dot, the center plot is for the middle dot, and the bottom plot is for the lowest dot.

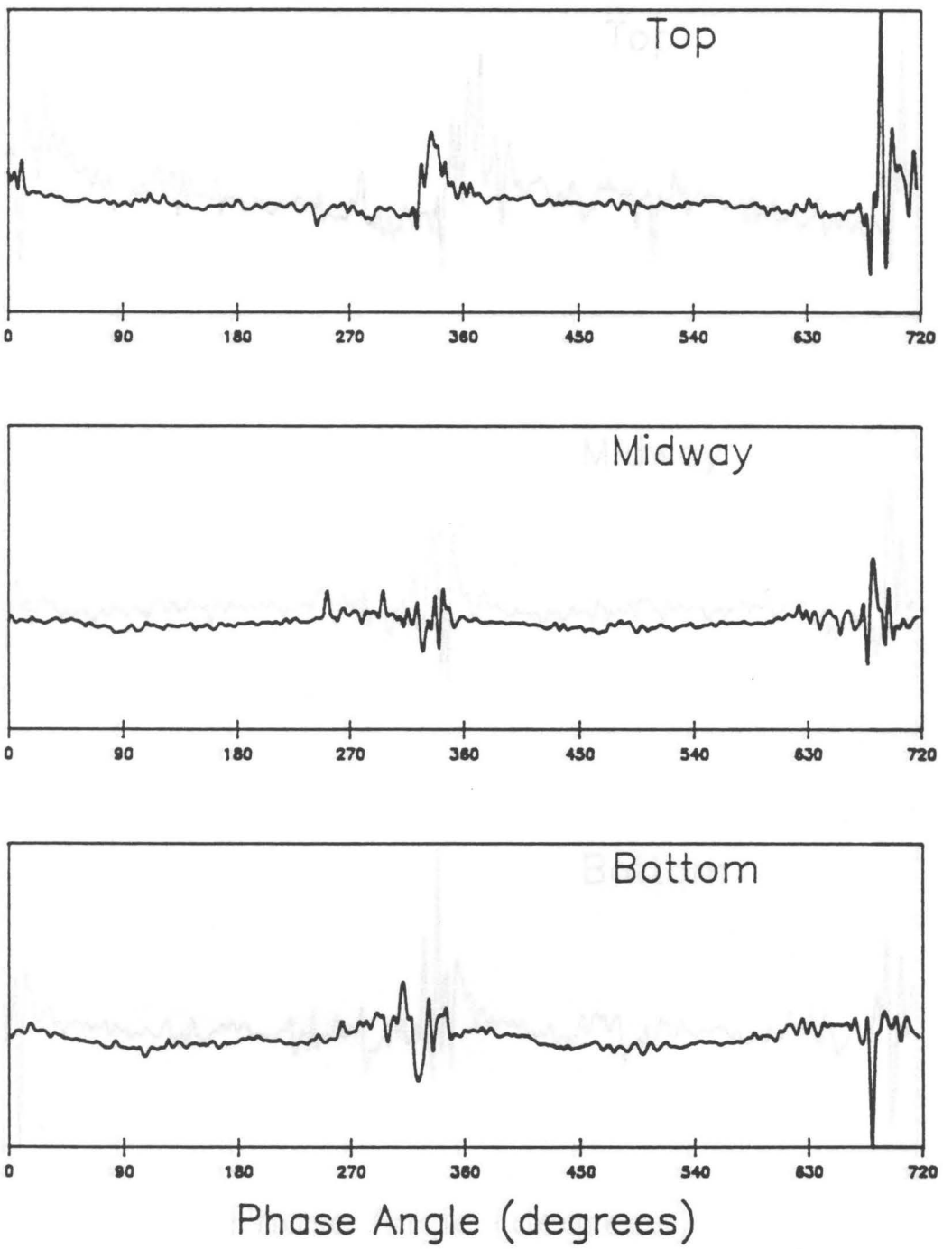

Figure 5.52. Output from the wall-mounted piezo-film for 707-μm Master Beads at K = 3: Output from the piezo-dots over two cycles. Top plot is for the top dot, the center plot is for the middle dot, and the bottom plot is for the lowest dot.

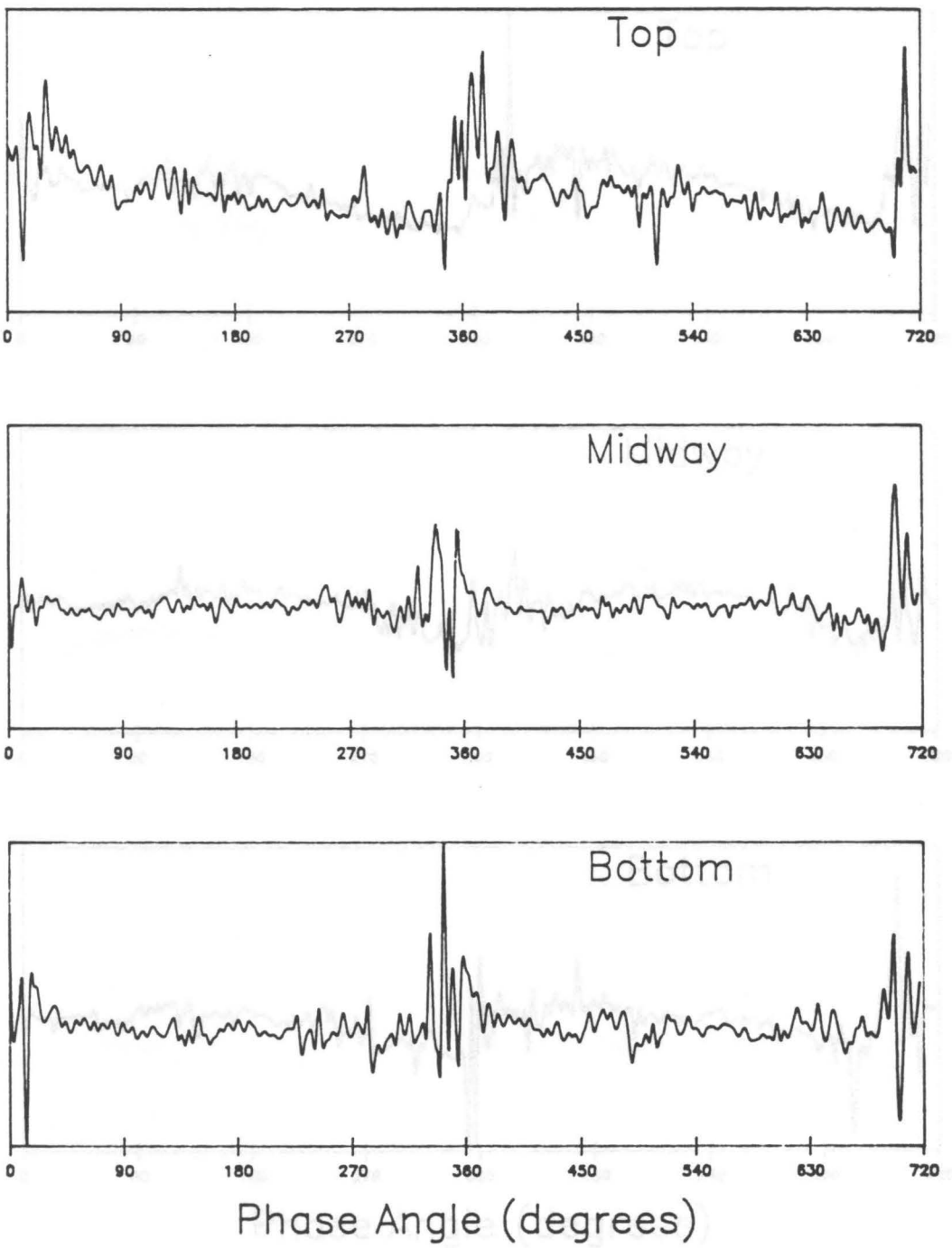

Figure 5.53. Output from the wall-mounted piezo-film for 707-μm Master Beads at K = 4: Output from the piezo-dots over two cycles. Top plot is for the top dot, the center plot is for the middle dot, and the bottom plot is for the lowest dot.

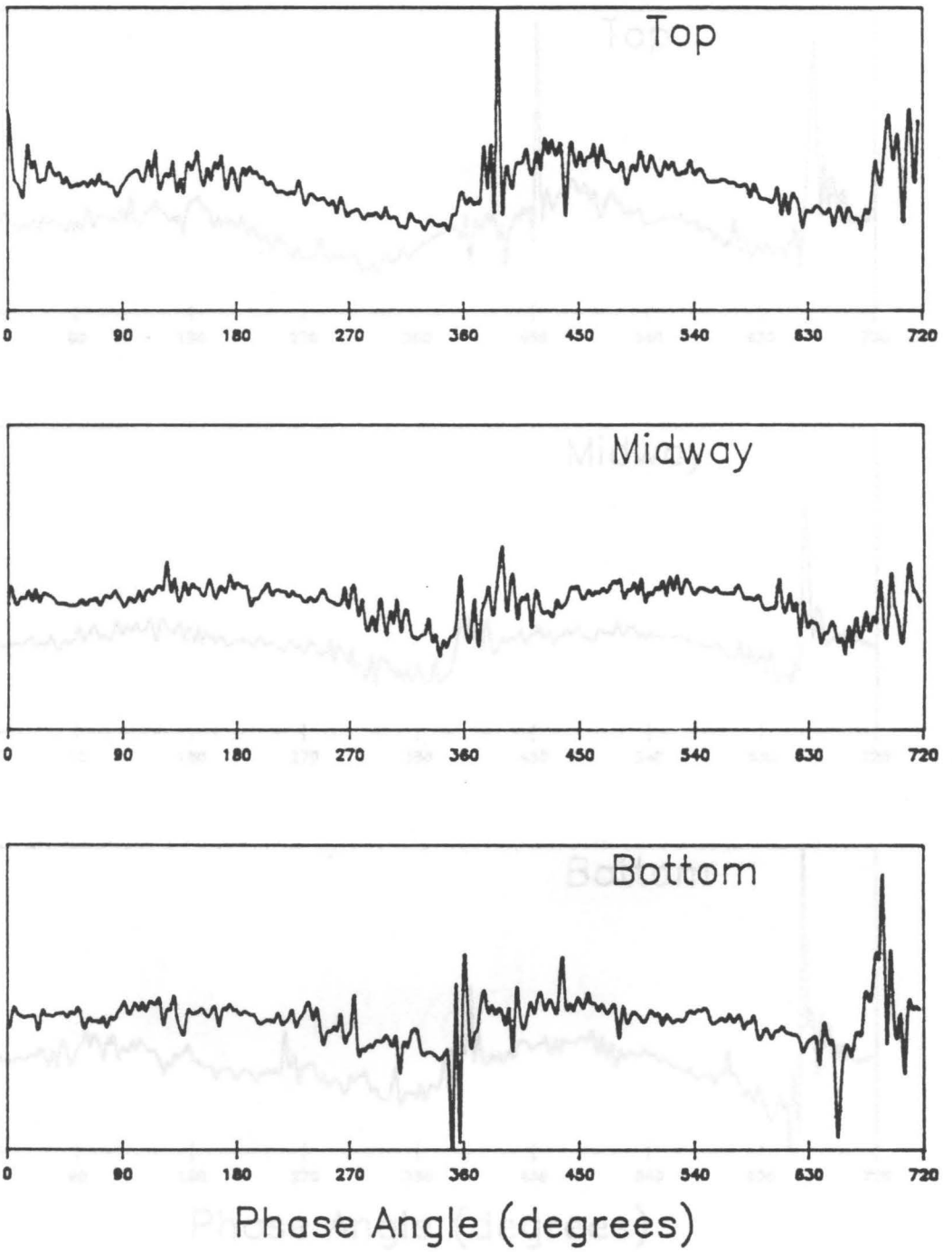

Figure 5.54. Output from the wall-mounted piezo-film for 707-μm Master Beads at K = 5: Output from the piezo-dots over two cycles. Top plot is for the top dot, the center plot is for the middle dot, and the bottom plot is for the lowest dot.

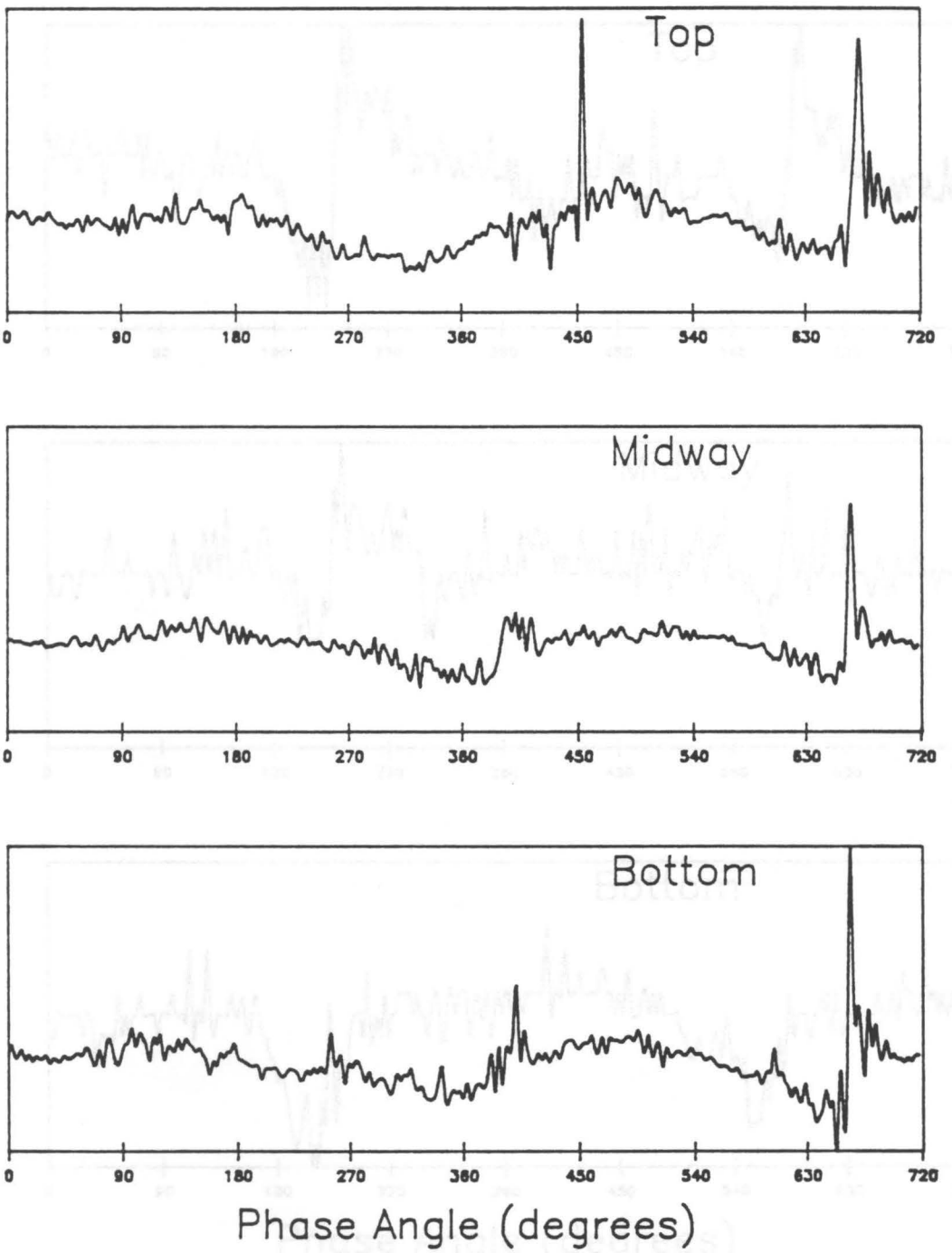

Figure 5.55. Output from the wall-mounted piezo-film for 707-μm Master Beads at K = 6: Output from the piezo-dots over two cycles. Top plot is for the top dot, the center plot is for the middle dot, and the bottom plot is for the lowest dot.

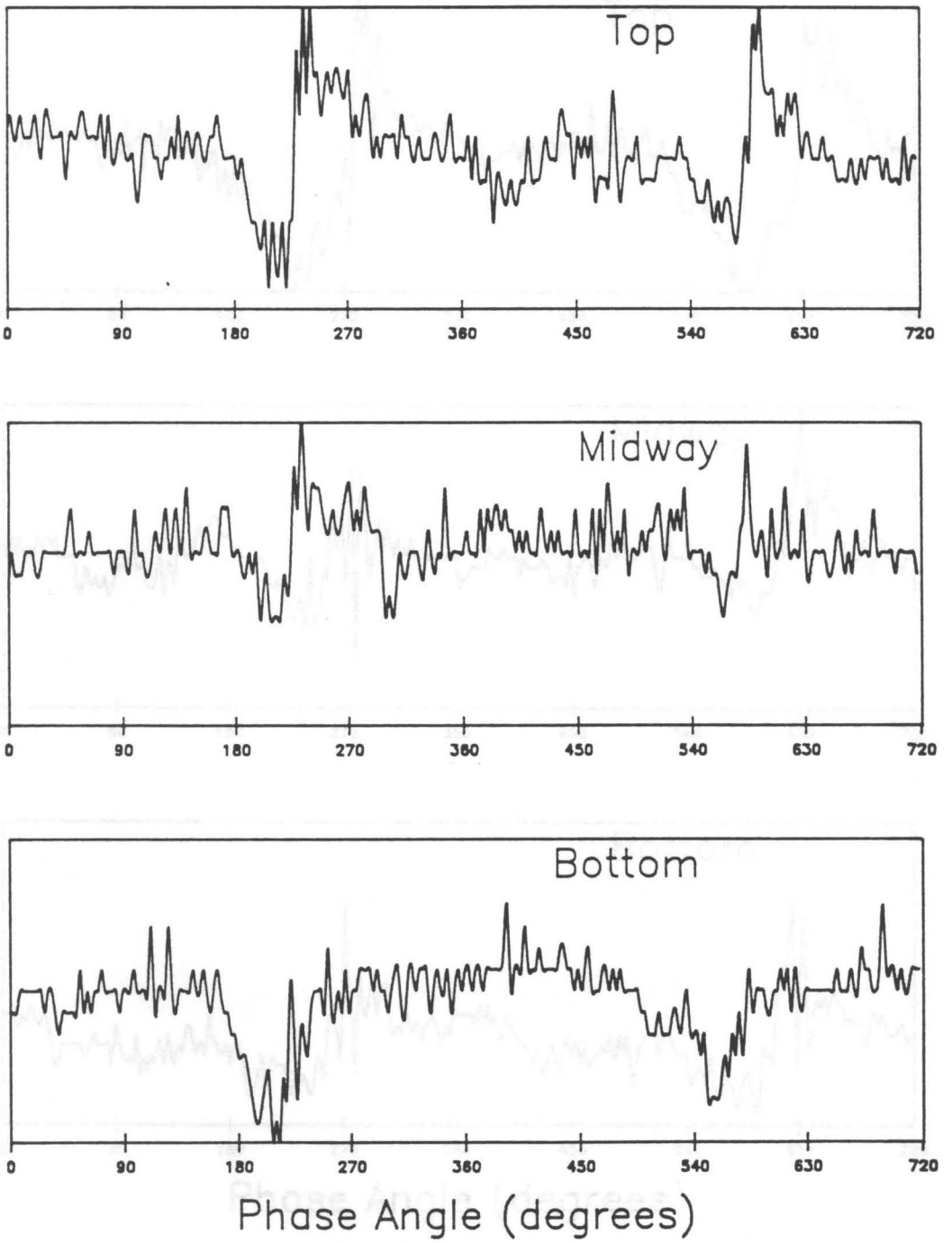

Figure 5.56. Output from the wall-mounted piezo-film for 177-μm Master Beads at K = 2: Output from the piezo-dots over two cycles. Top plot is for the top dot, the center plot is for the middle dot, and the bottom plot is for the lowest dot.

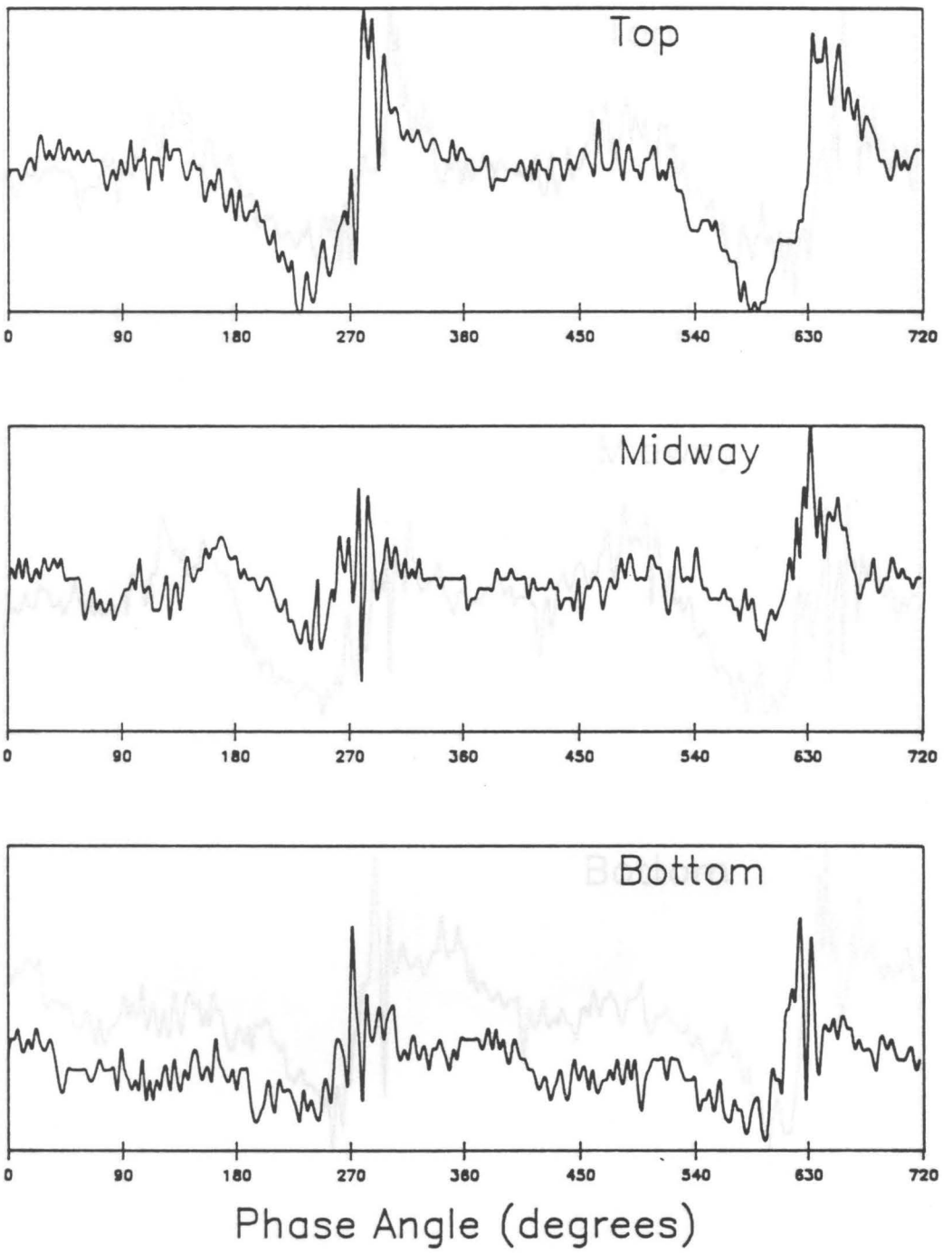

Figure 5.57. Output from the wall-mounted piezo-film for 177-μm Master Beads at K = 3: Output from the piezo-dots over two cycles. Top plot is for the top dot, the center plot is for the middle dot, and the bottom plot is for the lowest dot.

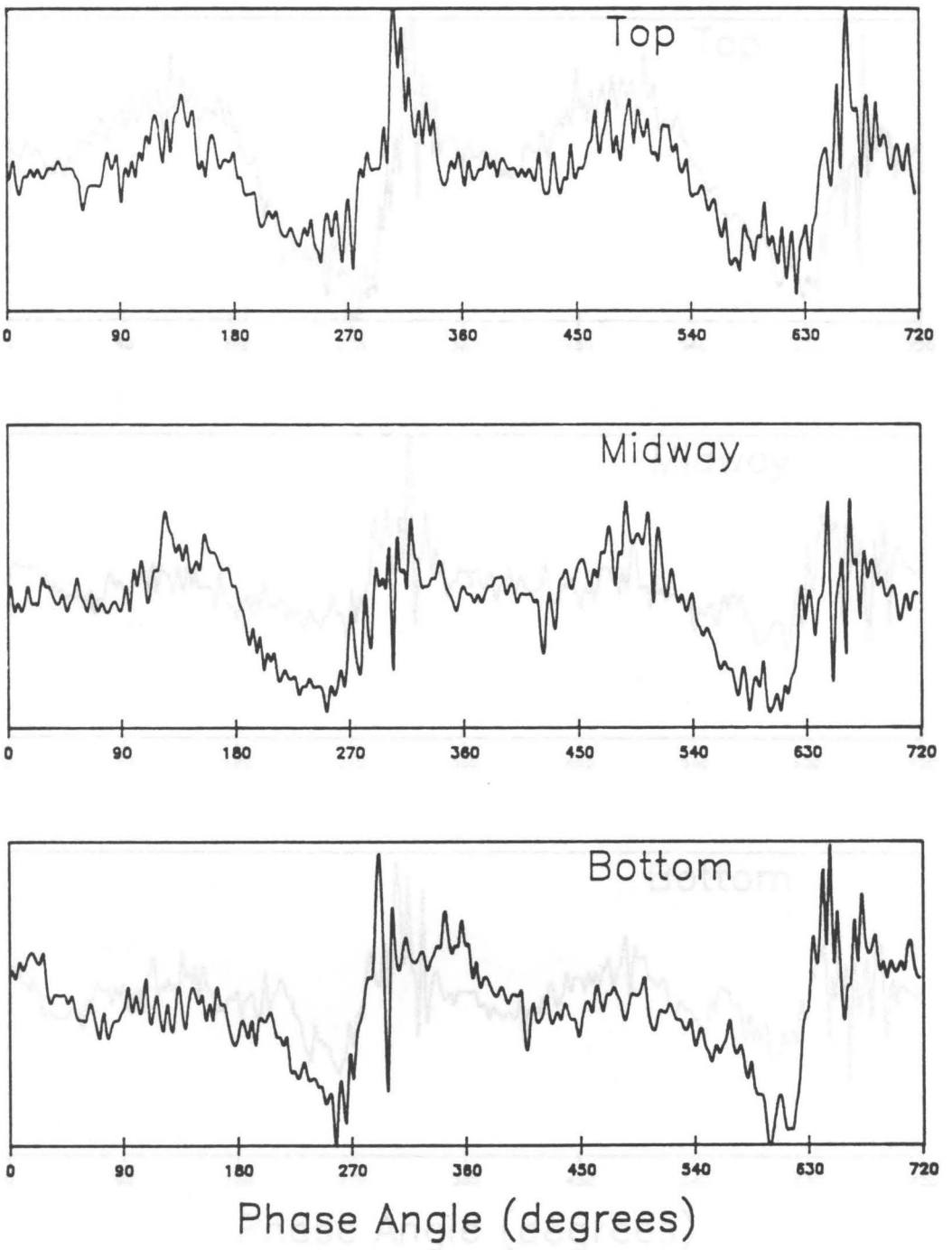

Figure 5.58. Output from the wall-mounted piezo-film for 177-μm Master Beads at K = 4: Output from the piezo-dots over two cycles. Top plot is for the top dot, the center plot is for the middle dot, and the bottom plot is for the lowest dot.

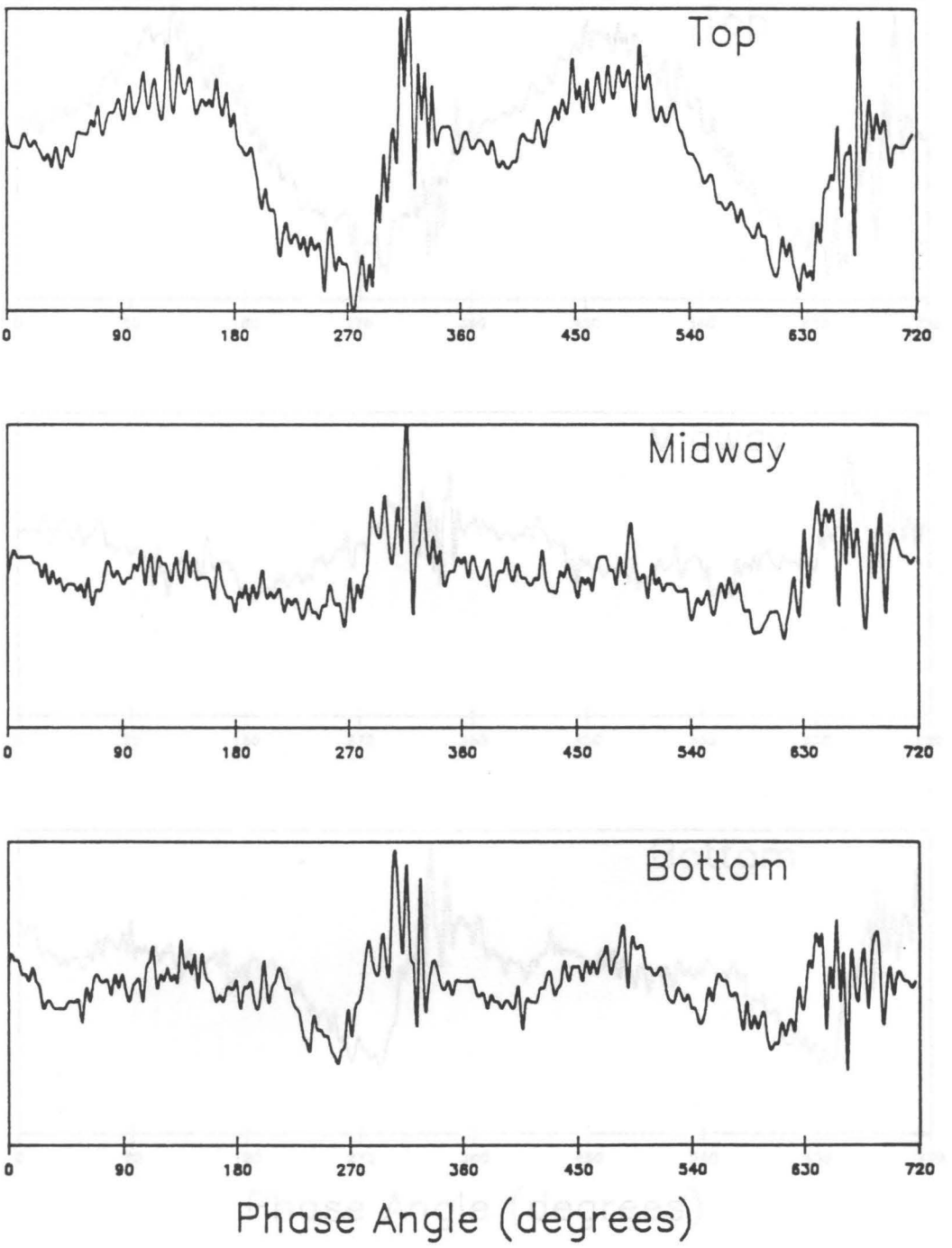

Figure 5.59. Output from the wall-mounted piezo-film for 177-μm Master Beads at K = 5: Output from the piezo-dots over two cycles. Top plot is for the top dot, the center plot is for the middle dot, and the bottom plot is for the lowest dot.

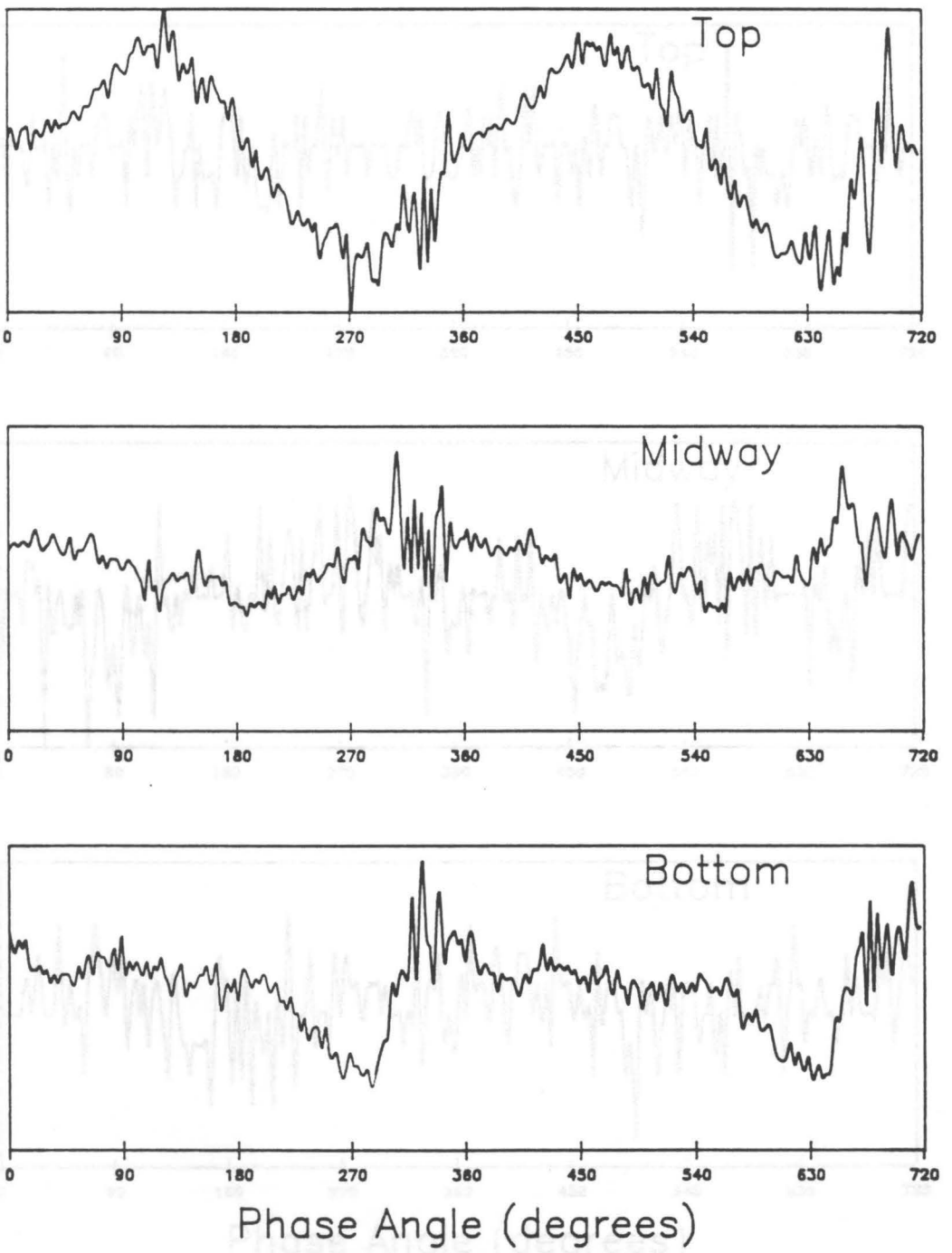

Figure 5.60. Output from the wall-mounted piezo-film for 177-μm Master Beads at K = 6: Output from the piezo-dots over two cycles. Top plot is for the top dot, the center plot is for the middle dot, and the bottom plot is for the lowest dot.

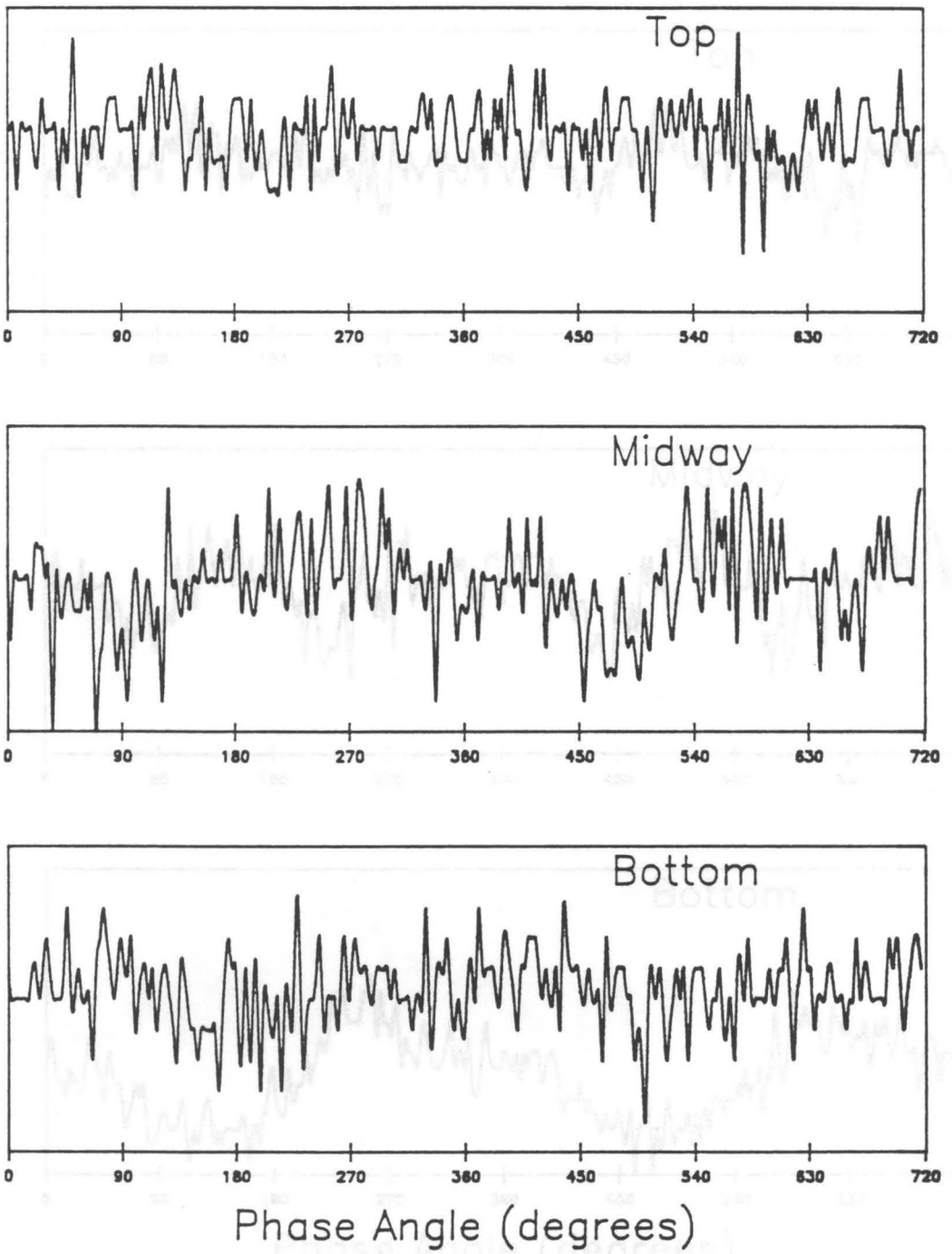

Figure 5.61. Output from the wall-mounted piezo-film for 88-μm Master Beads at K = 2: Output from the piezo-dots over two cycles. Top plot is for the top dot, the center plot is for the middle dot, and the bottom plot is for the lowest dot.

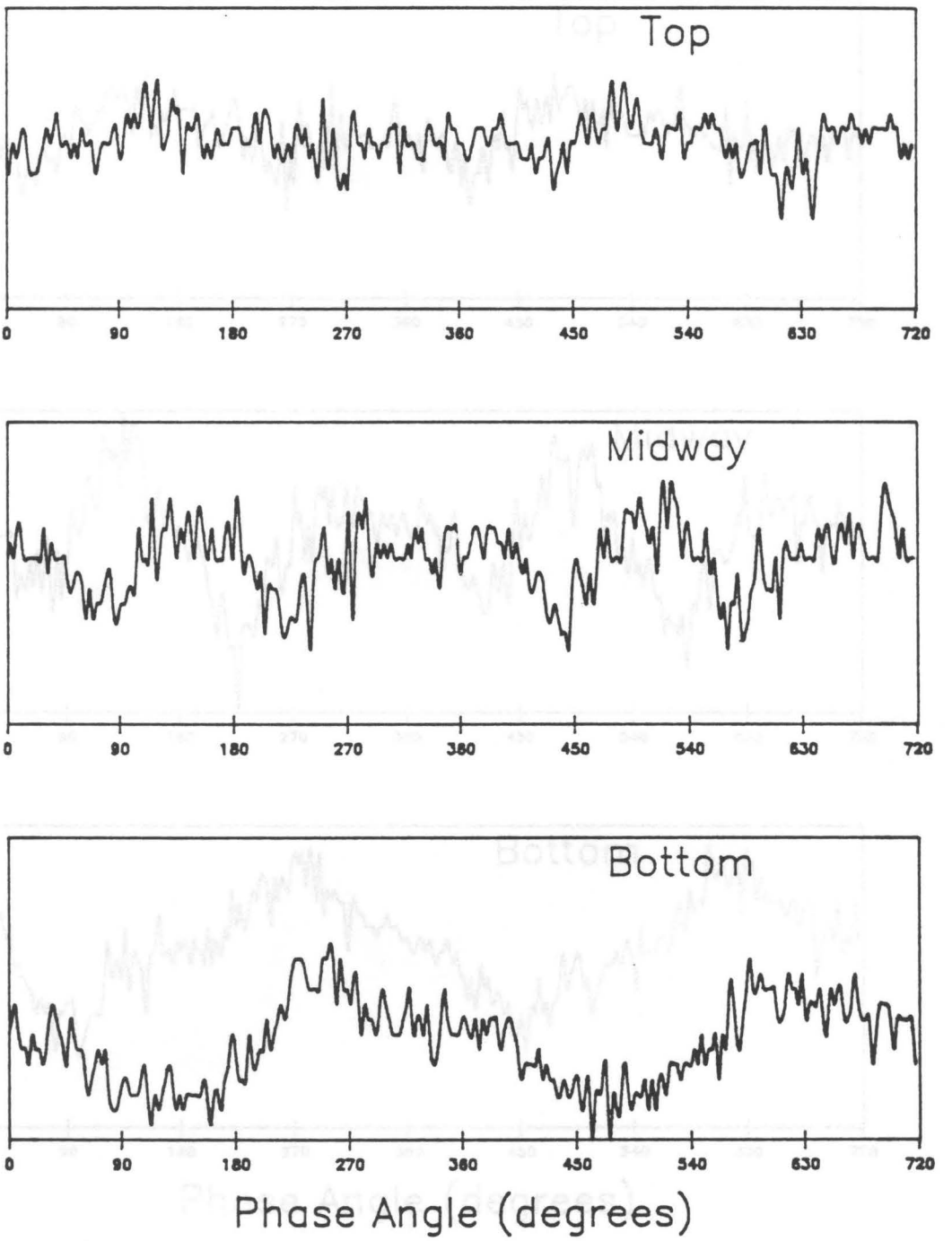

Figure 5.62. Output from the wall-mounted piezo-film for 88-μm Master Beads at K = 3: Output from the piezo-dots over two cycles. Top plot is for the top dot, the center plot is for the middle dot, and the bottom plot is for the lowest dot.

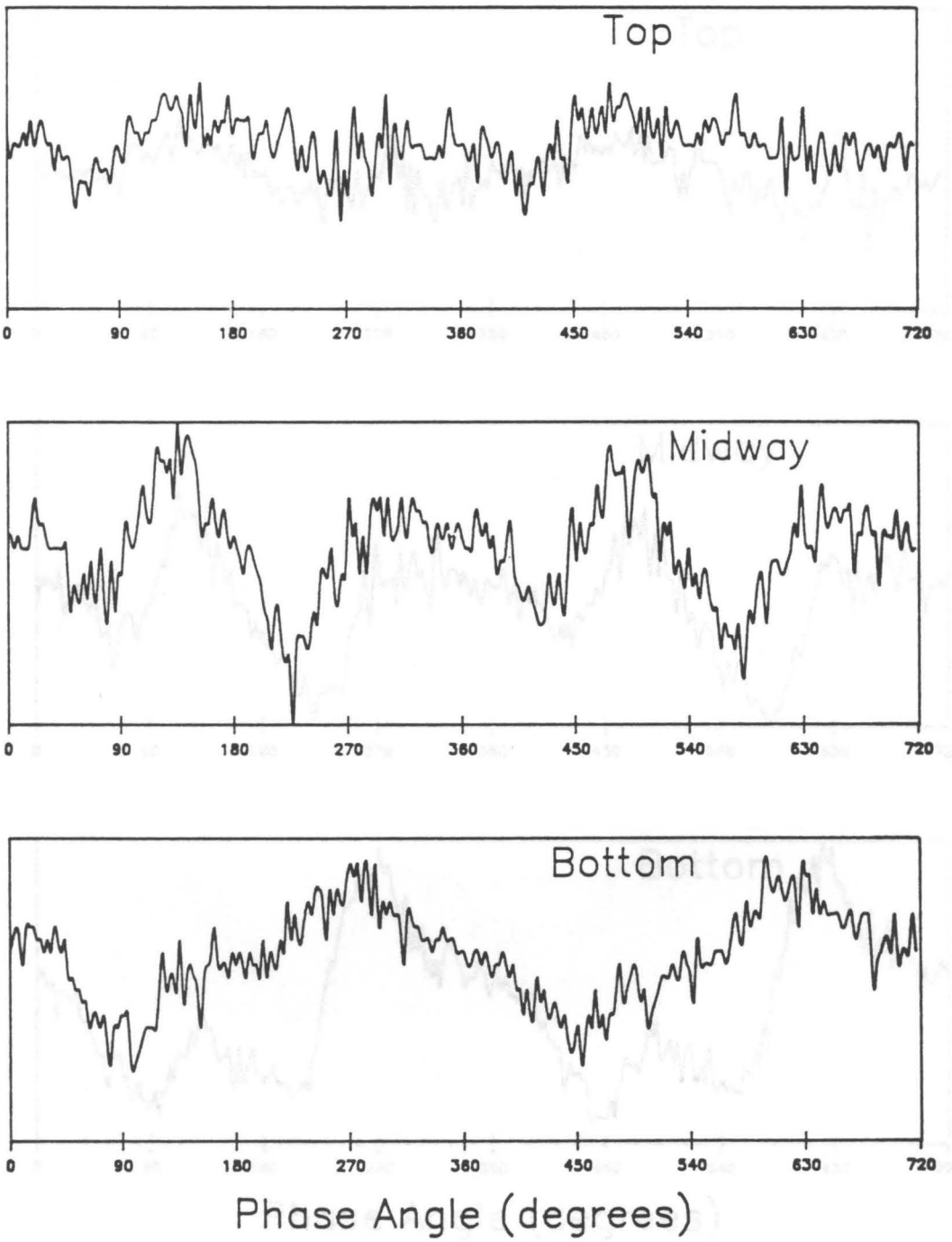

Figure 5.63. Output from the wall-mounted piezo-film for 88-μm Master Beads at K = 4: Output from the piezo-dots over two cycles. Top plot is for the top dot, the center plot is for the middle dot, and the bottom plot is for the lowest dot.

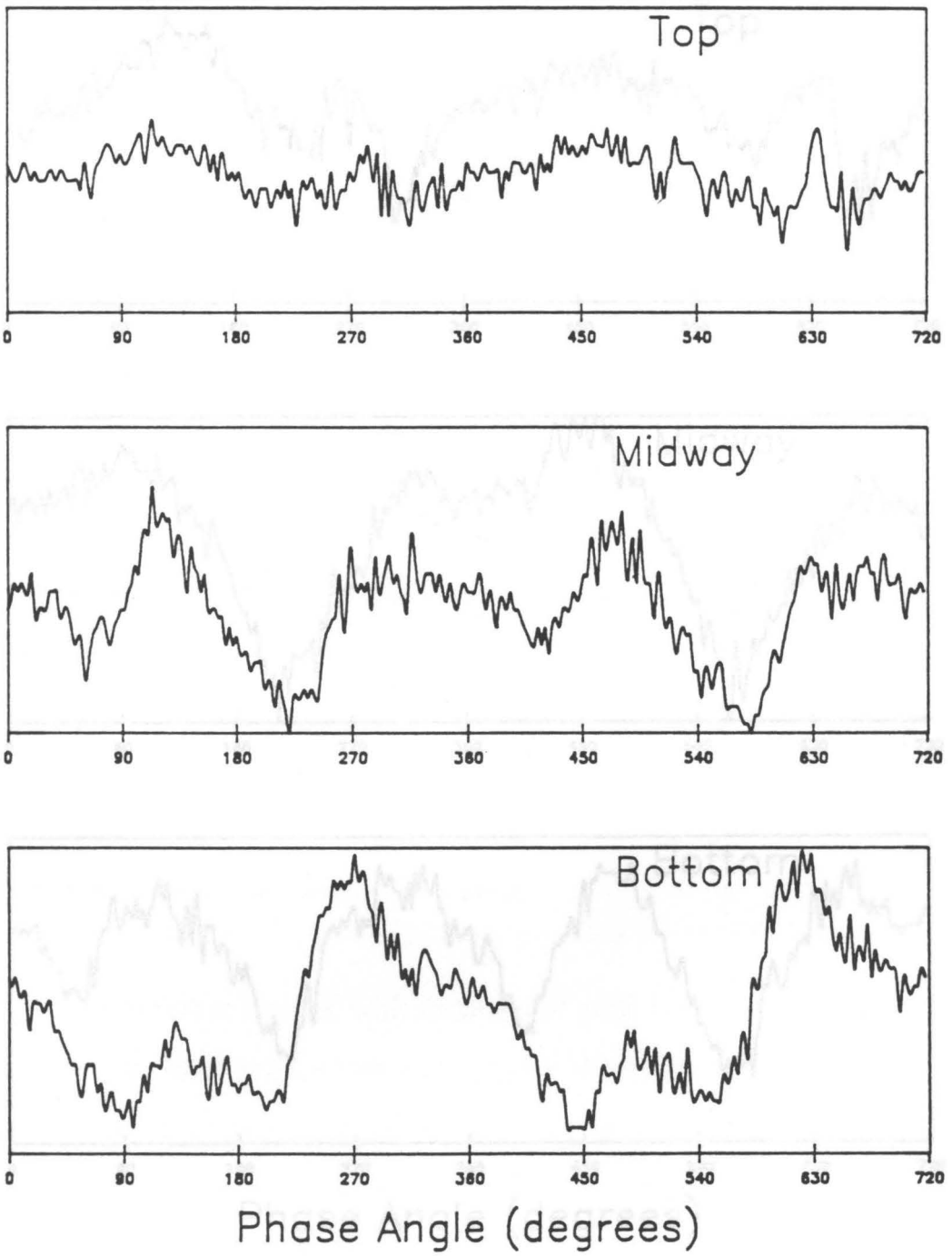

Figure 5.64. Output from the wall-mounted piezo-film for 88-μm Master Beads at K = 5: Output from the piezo-dots over two cycles. Top plot is for the top dot, the center plot is for the middle dot, and the bottom plot is for the lowest dot.

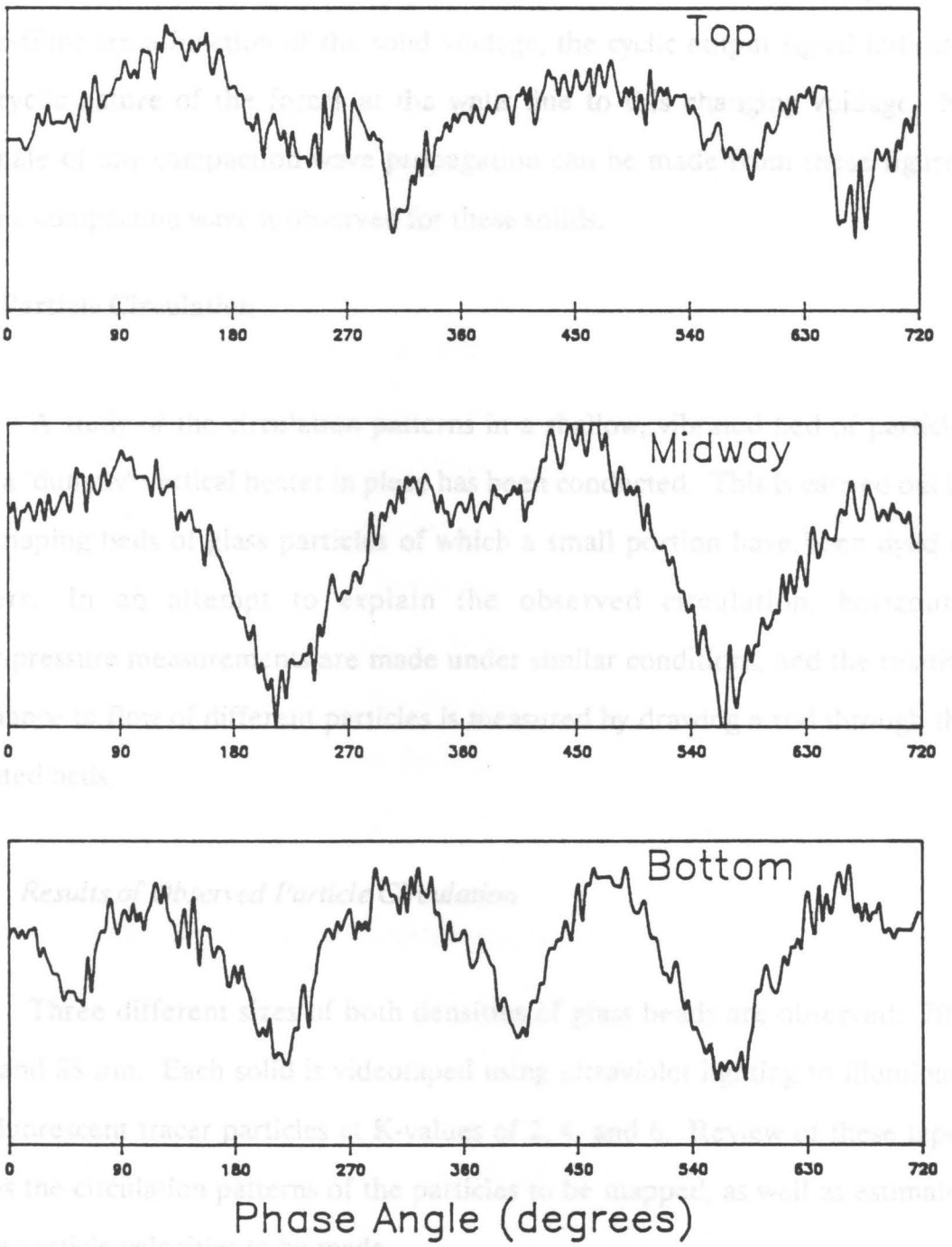

Figure 5.65. Output from the wall-mounted piezo-film for 88-μm Master Beads at K = 6: Output from the piezo-dots over two cycles. Top plot is for the top dot, the center plot is for the middle dot, and the bottom plot is for the lowest dot.

cycle for these solids. Since the horizontal stresses at the wall acting on the piezo-films are a function of the solid voidage, the cyclic output signal indicates the cyclic nature of the forces at the walls due to this changing voidage. No estimate of any compaction wave propagation can be made from these figures, and no compaction wave is observed for these solids.

5.4 Particle Circulation

A study of the circulation patterns in a shallow, vibrated bed of particles with a "dummy" vertical heater in place has been conducted. This is carried out by videotaping beds of glass particles of which a small portion have been dyed as tracers. In an attempt to explain the observed circulation, horizontal floor-pressure measurements are made under similar conditions, and the relative resistance to flow of different particles is measured by drawing a rod through the vibrated beds.

5.4.1 Results of Observed Particle Circulation

Three different sizes of both densities of glass beads are observed: 707, 177, and 88 μm. Each solid is videotaped using ultraviolet lighting to illuminate the fluorescent tracer particles at K-values of 2, 4, and 6. Review of these tapes allows the circulation patterns of the particles to be mapped, as well as estimates of the particle velocities to be made.

5.4.1.1 Observed Circulation Patterns

Observation of the videotapes shows that the circulation patterns can be divided into two general groups: one for beds which exhibit bunkering; and a quite different one for those which do not. Of the particle sizes chosen, the two smaller sizes tend to form a bunker when vibrated, and the larger size does not. The bunkered circulation pattern has appreciable horizontal particle movement, while the non-bunkered particles move almost strictly vertically. Figures 5.66-5.71 show the observed particle circulation patterns.

As can be seen in the figures, the circulation patterns are symmetric about the dummy heat probe. For the bunkered circulation, the general pattern is a horizontal flow from the side walls in toward the probe in the bulk of the bed, vertical flow from the bottom to the top near the center of the bed, and a much faster return avalanche flow down the top slope of the bunker toward the side walls. This avalanche flow takes place in a very narrow expanded region on the surface.

While this generalized description summarizes the flow in bunkered beds, certain trends can be noted from the figures. For the low-density beads, the flow of particles is somewhat less horizontal for the 177-μm size than for the 88-μm size. For 177-μm beads, the flow is only strictly horizontal at the very bottom of the bed and near the side walls. In the rest of the bed, the streamlines of flow move diagonally up and toward the center. For the 88-μm beads, the streamlines tend to be more horizontal and then make a sharper turn up toward the surface near the center. In both cases, the slope of the bunker decreases with increasing vibrational intensity. As this occurs, the particles tend to travel less of a distance down the top slope in the avalanche flow before they are pulled into the bulk of

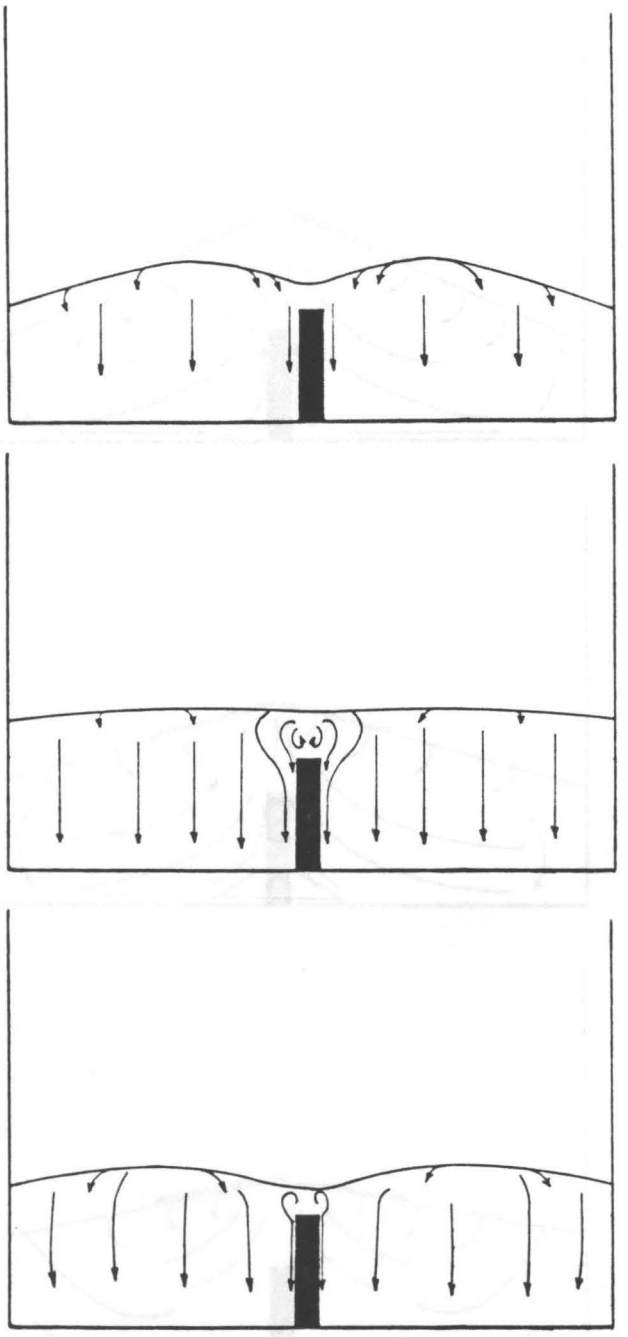

Figure 5.66. Observed particle circulation patterns for 707-μm low-density glass beads: Top drawing is for K = 2, center drawing is for K = 4, and bottom drawing is for K = 6. Note: particle return flow is up everywhere but the 2-3 layers near the wall. This return flow is not shown in the figure.

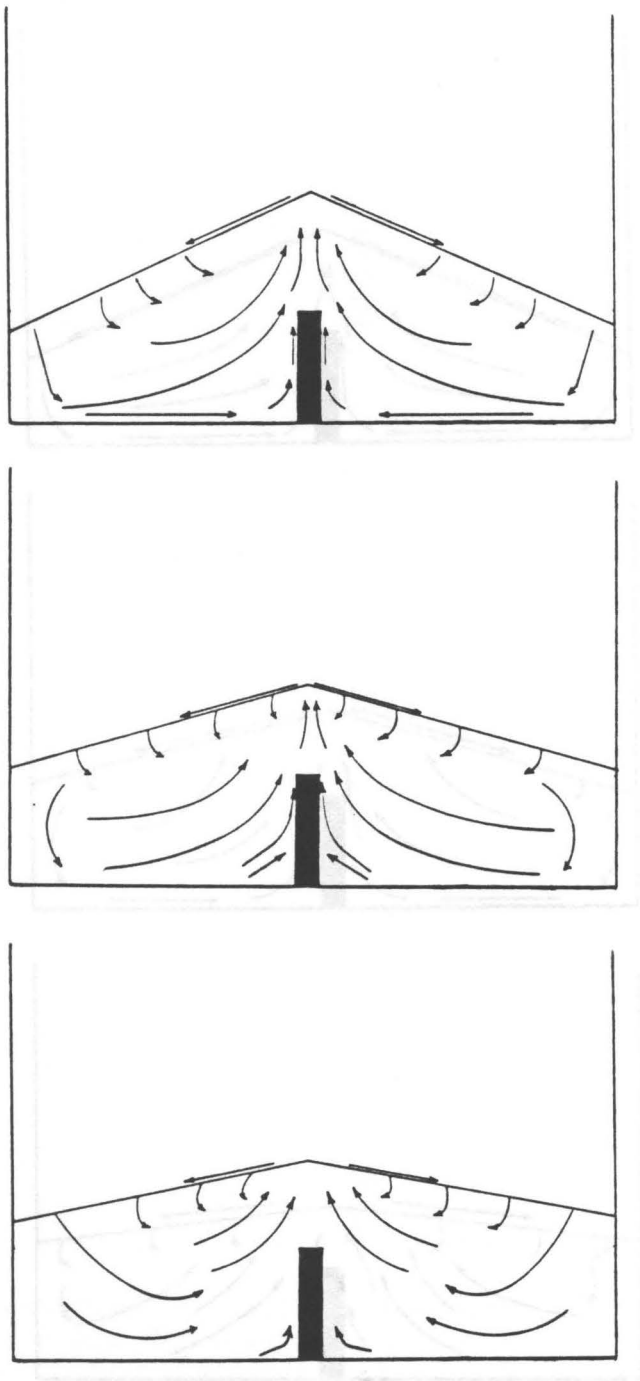

Figure 5.67. Observed particle circulation patterns for 177-μm low-density glass beads: Top drawing is for K = 2, center drawing is for K = 4, and bottom drawing is for K = 6.

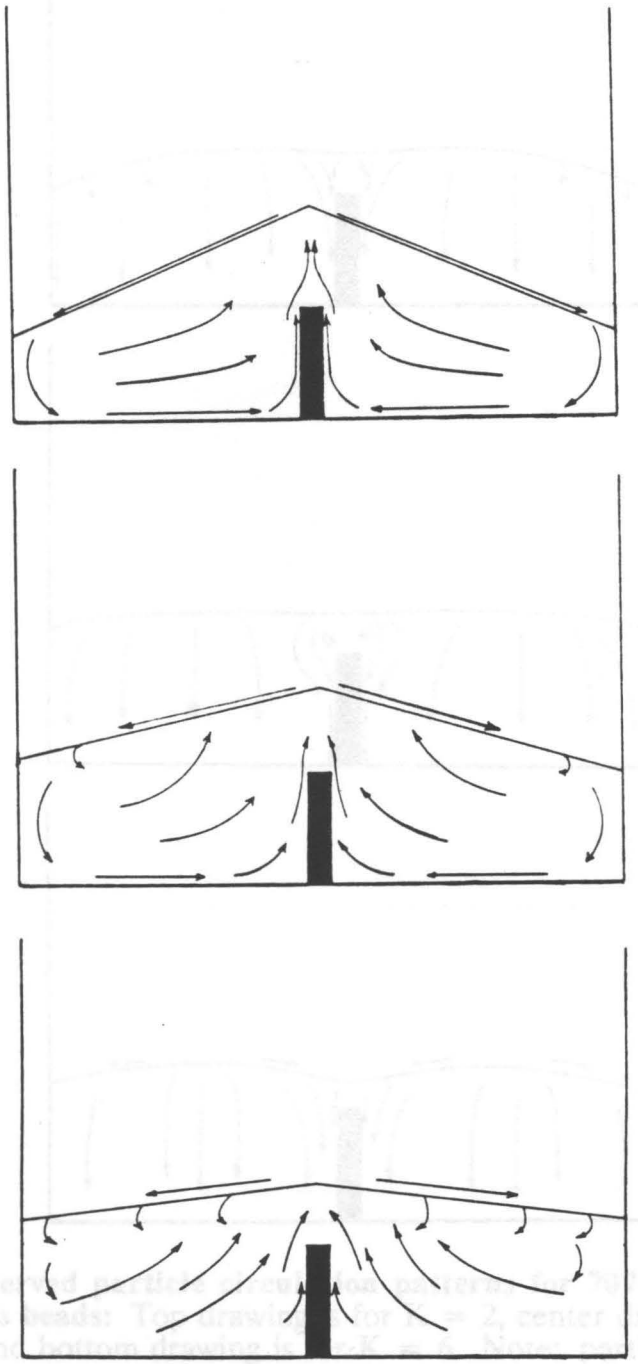

Figure 5.68. Observed particle circulation patterns for 88-μm low-density glass beads: Top drawing is for K = 2, center drawing is for K = 4, and bottom drawing is for K = 6.

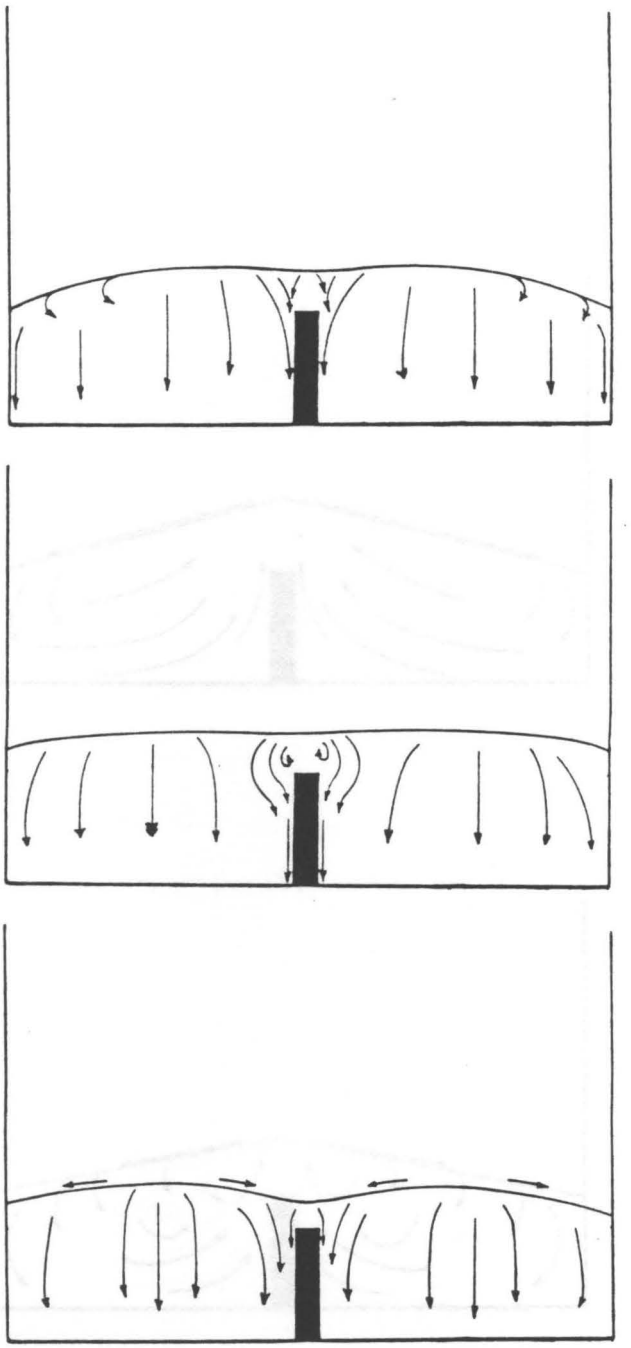

Figure 5.69. Observed particle circulation patterns for 707-μm high-density glass beads: Top drawing is for K = 2, center drawing is for K = 4, and bottom drawing is for K = 6. Note: particle return flow is up everywhere but the 2-3 layers near the wall. This return flow is not shown in the figure.

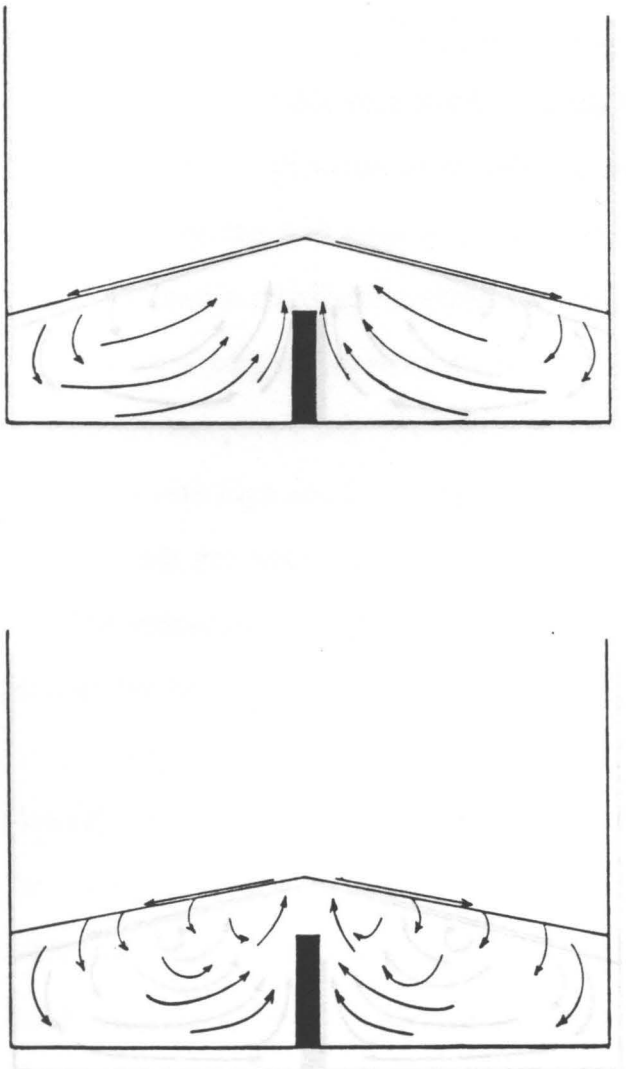

Figure 5.70. Observed particle circulation patterns for 177-μm high-density glass beads: Top drawing is for K = 2; bottom drawing is for K = 4. Circulation pattern is not stable at K = 6.

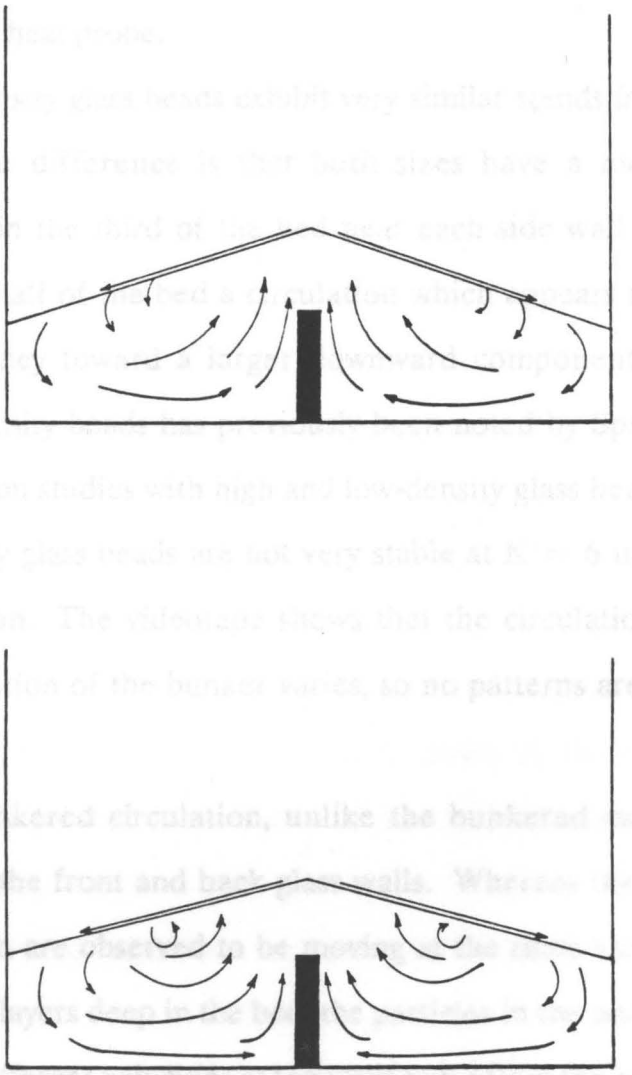

Figure 5.71. Observed particle circulation patterns for 88-μm high-density glass beads: Top drawing is for K = 2; bottom drawing is for K = 4. Circulation pattern is not stable at K = 6.

the bed. This trend is particularly observed for the 177-μm particles. Also, for both sizes the horizontal component of flow in the bulk of the bed is less pronounced as the vibrational intensity is increased. These trends agree well with observations made by Thomas [1988], who carried out similar experiments in a bed with no dummy heat probe.

The high-density glass beads exhibit very similar trends in the two smaller sizes. One notable difference is that both sizes have a more pronounced downward motion in the third of the bed near each side wall at K = 4. This motion gives each half of the bed a circulation which appears as a whirl with a vortex. The tendency toward a larger downward component of the particle motion for high-density beads has previously been noted by Sprung [1987], who performed circulation studies with high and low-density glass beads. Both 88 and 177-μm high-density glass beads are not very stable at K = 6 in the center-high bunker configuration. The videotape shows that the circulation pattern is not constant as the position of the bunker varies, so no patterns are shown in these cases.

The non-bunkered circulation, unlike the bunkered case, seems to be greatly affected by the front and back glass walls. Whereas the particles in the bunkered circulation are observed to be moving at the same velocity at the wall and several particle layers deep in the bed, the particles in the non-bunkered beds quite clearly have different velocities at the walls and within the bed.

Both densities of 707-μm glass beads have very similar circulation patterns at all vibrational intensities. The particles move vertically down at the front wall, move in toward the center of the bed upon reaching the bottom (into the paper in the figures, not horizontally), and then slowly move vertically up in the bulk of the bed. The downward flow at the walls occurs only in a very few particle layers, and

those layers which are not in direct contact with the wall move much more slowly. Since the vast majority of the bed is moving up in a return flow, this velocity is very low.

At K = 2, the dummy heat probe divides the bed into two halves, each of which has a slight bunker as seen in Figure 5.66. This causes a slight avalanche flow down the top slope of the bunker as shown, but once the particles move into the bulk of the bed no horizontal motion is observed. At K = 4, the bed is nearly flat and a circulation pattern forms above the dummy heat probe as shown which leads to some slight horizontal mixing. At K = 6 where the bed is in the period-doubling regime (see Section 5.1.2, p. 143), the dummy probe again splits the bed in half. In this case, the dummy probe acts as a wall. Instead of rocking back-and-forth from side wall to side wall as seen in the high-speed movies (with no dummy probe), the bed rocks between a side wall and the dummy probe. This effect creates a slight mound near the center of each half-bed which causes a slight horizontal motion near the top surface as shown in Figure 5.66. The greatly predominant motion in all cases is vertically down at the wall. Very little horizontal mixing is observed in non-bunkered circulation.

5.4.1.2 Observed Particle Velocities

Particle velocities can be estimated from the videotapes of particle circulation. Prior to videotaping, a centimeter scale has been painted onto the two-dimensional vessel, and the video camera has been set to superimpose a clock in the corner of the videotaped image. Horizontal particle velocities are estimated for low-density glass beads at K-values of 2 and 4 for particle sizes of 88 and 177 μm. Particle velocities are not estimated for 707-μm beads since the

observed circulation is apparently due to wall effects, and thus of little relevance to the particle velocities in the three-dimensional heat-transfer vessel. All estimates of particle velocities are based on 6-8 measurements and are repeatable within about 10-15 percent.

For the 177-μm beads, the velocity appears to be nearly constant along the major streamlines indicated in Figure 5.67. In other words, the horizontal velocity in the lower region of the bed and near the side walls is about the same as the resultant diagonal velocity nearer the dummy heat probe. For K = 2, this value is about 1.5 mm/s, and for K = 4 it is about 8 mm/s. This latter velocity agrees well with Thomas [1988], who estimated the velocity of these particles under similar conditions, but with no dummy heat probe. Thomas, however, gave 8 mm/s as an average, horizontal component of velocity, whereas this study shows that this is the horizontal velocity only in the regions with strictly horizontal flow. The flow stagnates as it approaches the dummy probe. At the very bottom of the bed where the flow remains horizontal, the velocity appreciably declines about 15 mm from the probe. The vertical velocity in the layer adjacent to the probe is much slower: about 0.25 mm/s at K = 2 and about 1.5 mm/s at K = 4.

The 88-μm beads, which tend to travel horizontally in a greater percentage of the bed, have a slightly different velocity profile. In this case, the horizontal velocity is greatest at the bottom of the bed with a small decrease in velocity in successively higher layers. For this solid, the circulation at K = 2 is very slow, with an estimated horizontal velocity of only about 0.8 mm/s at the bottom of the bed. An increase in vibrational intensity to 4 brings about a dramatic change, however. Under these conditions, the horizontal velocity at the bottom of the bed is about 8 mm/s. As in the case for the 177-μm particles, the velocity is much

slower in the immediate vicinity of the dummy probe. The vertical velocity in the adjoining layer is only about 10 mm/min. at K = 2, and about 1.3 mm/s at K = 4.

5.4.2 Results of Floor-Pressure Experiments

Sprung [1987] and Thomas [1988] have measured instantaneous floor pressure at three horizontal locations beneath a vibrated bed with a cylindrical dummy heat probe and with no dummy probe, respectively. Both of their results indicate that a horizontal pressure gradient exists from the side walls toward the center for all solids which exhibit bunkering during the part of the vibrational cycle when the bed is in free flight. Similar experiments have been performed in this study with a vertical barrier simulating the heat probe in place. A wide range of sizes of Master Beads is used for the experiments.

Figures 5.72 to 5.87 show results for particles ranging from 707 to 88 μm at K-values from 2 to 6 (up to K = 7 for 177-μm particles). The three curves in each plot represent pressures taken at the locations shown in Figure 3.9 (page 105), over two vibrational cycles. Note that the pressure scale (y-axis) has been changed from one particle size to another to enlarge the features, but that the scale is the same for all K-values at a single particle size. Two vibrational cycles are plotted to demonstrate the cyclic nature and high degree of reproducibility in these data in all cases except for situations in which period doubling occurs. In these instances, the two plotted cycles are different. The two-cycle period is also reproducible, but four cycles have not been plotted to prevent the x-axis from becoming too compressed.

For the 707 and 500-μm particles, there is little or no difference in the pressures of any of the three locations at any point in the cycle. These solids do

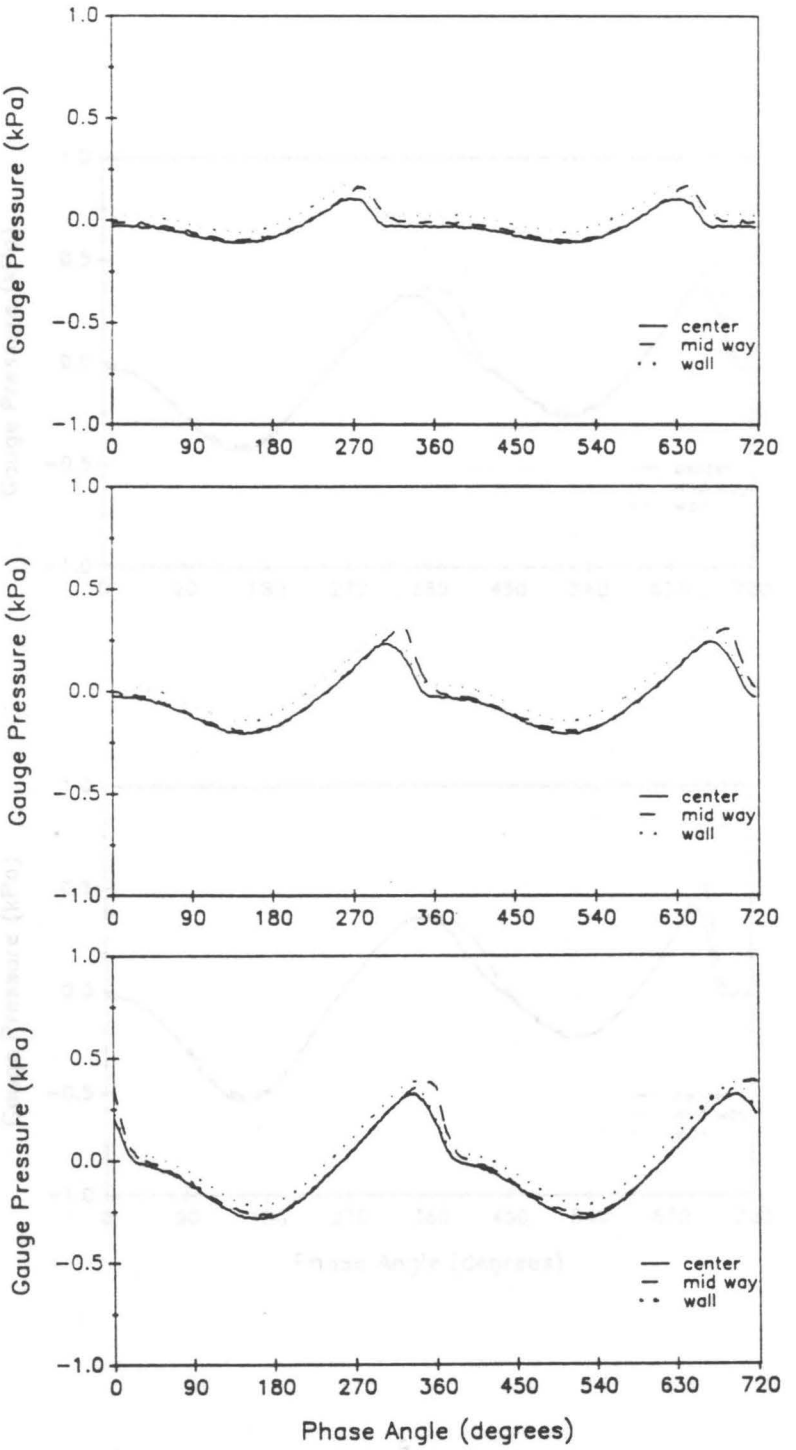

Figure 5.72. Floor pressure beneath 707-μm Master Beads at K = 2, 3, and 4: Solid line is for pressure beneath center of bed, dashed line is for pressure midway between the center and the wall, and dotted line is for pressure at the wall. Top plot is for K = 2, middle is for K = 3, bottom is for K = 4.

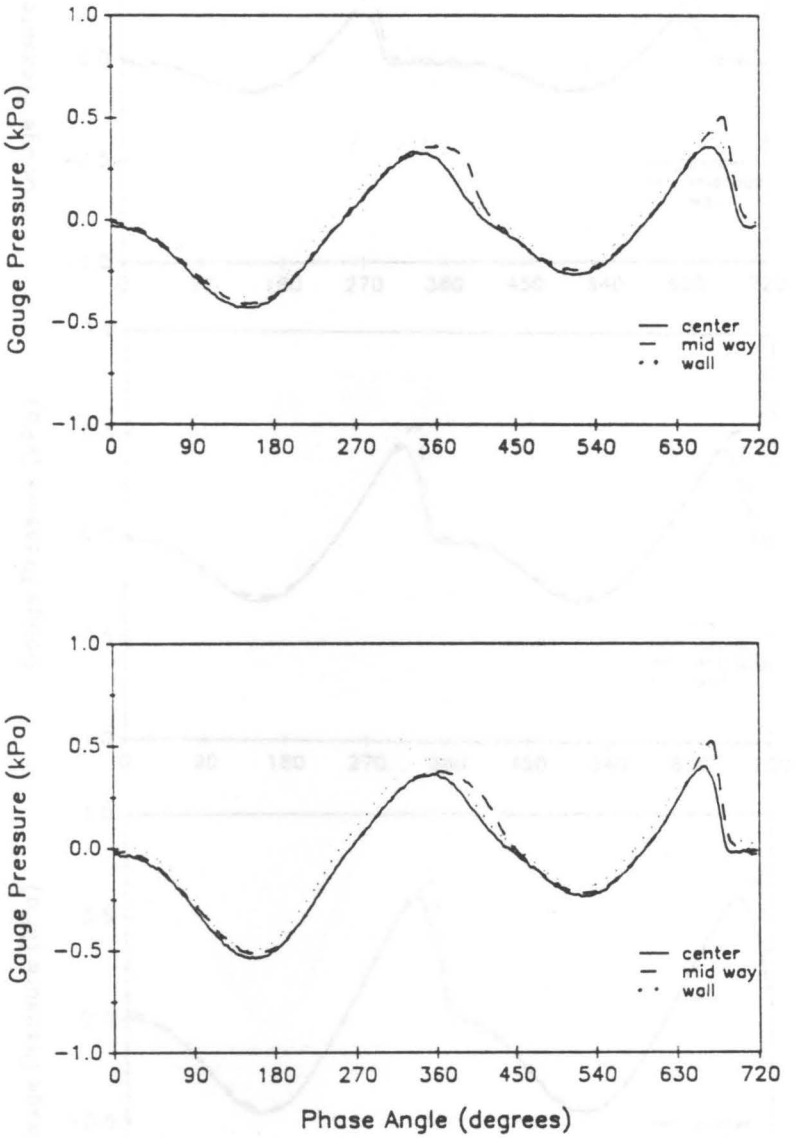

Figure 5.73. Floor pressure beneath 707-μm Master Beads at K = 5 and 6: Solid line is for pressure beneath center of bed, dashed line is for pressure midway between the center and the wall, and dotted line is for pressure at the wall. Top plot is for K = 5, bottom plot is for K = 6.

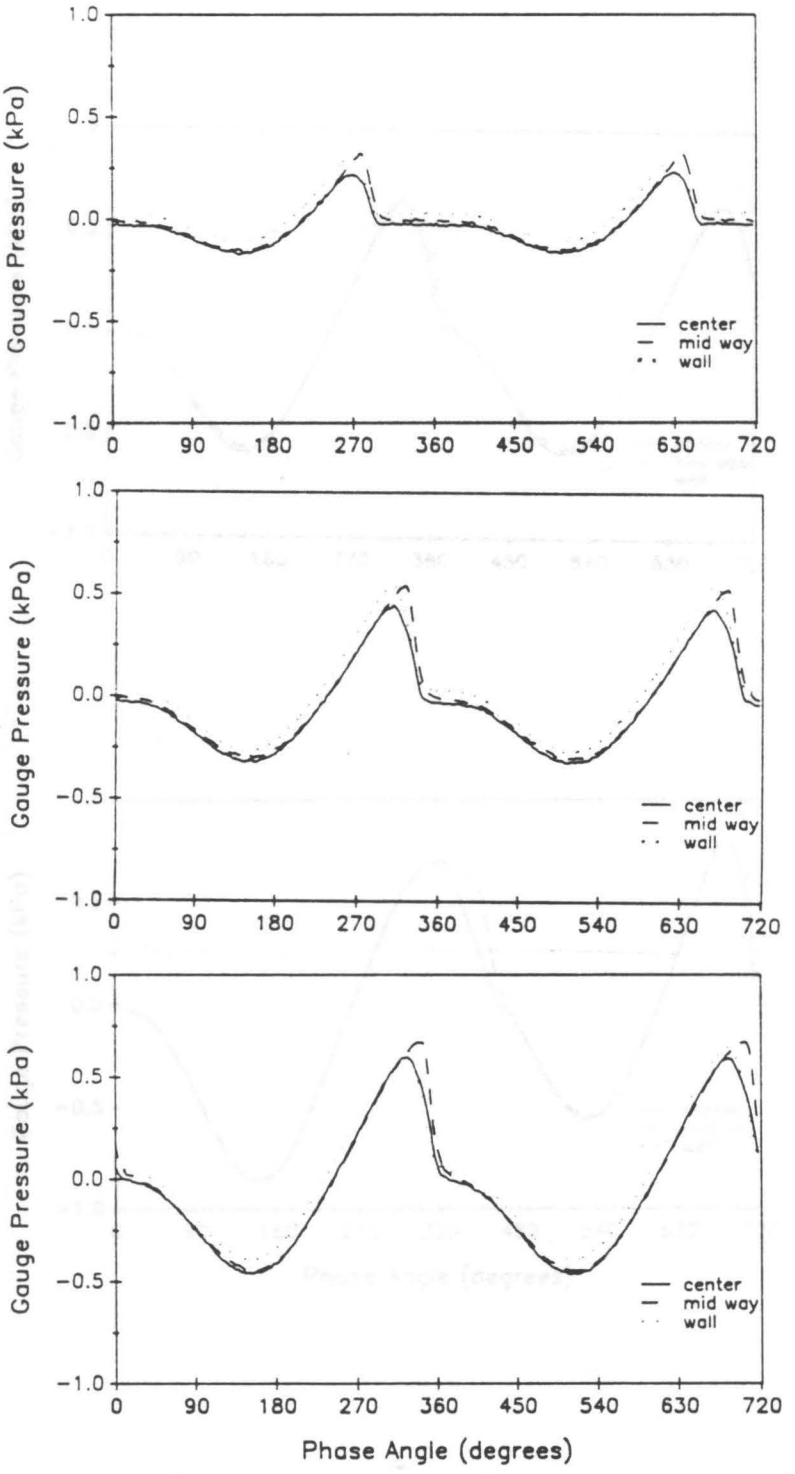

Figure 5.74. Floor pressure beneath 500-μm Master Beads at K = 2, 3, and 4: Solid line is for pressure beneath center of bed, dashed line is for pressure midway between the center and the wall, and dotted line is for pressure at the wall. Top plot is for K = 2, middle is for K = 3, bottom is for K = 4.

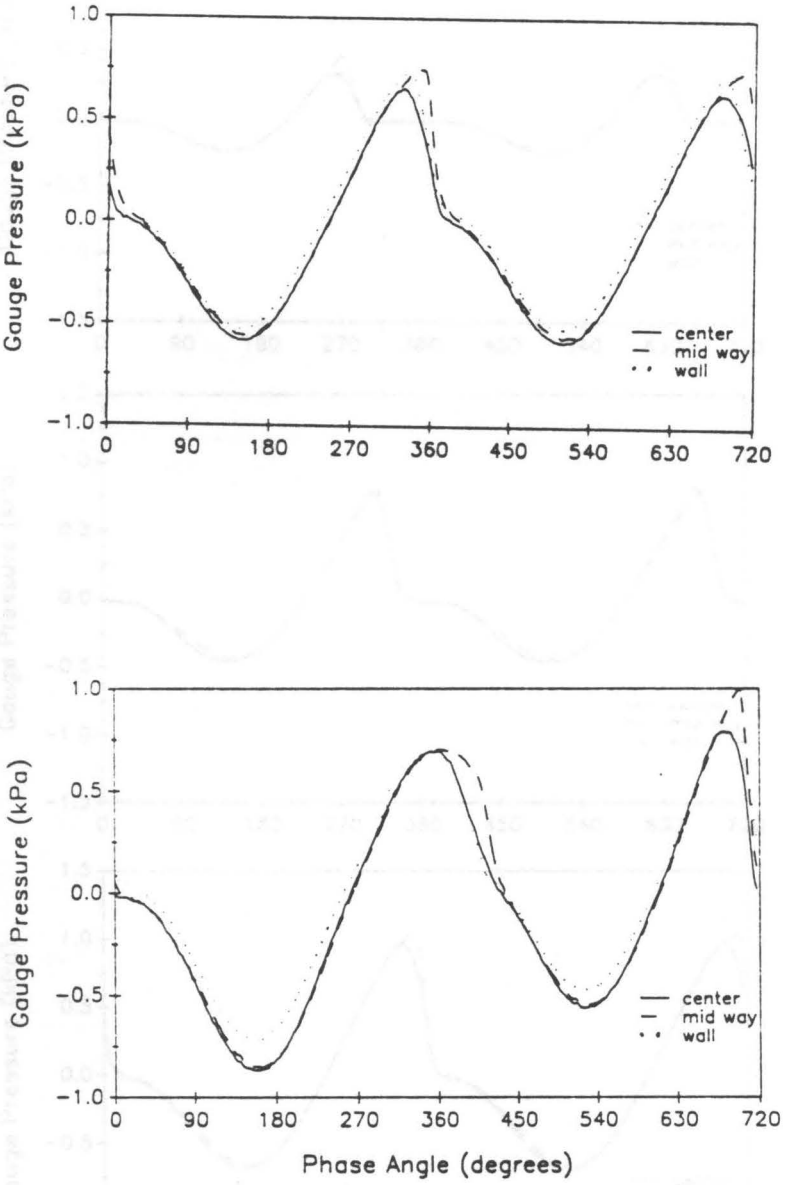

Figure 5.75. Floor pressure beneath 500-μm Master Beads at K = 5 and 6: Solid line is for pressure beneath center of bed, dashed line is for pressure midway between the center and the wall, and dotted line is for pressure at the wall. Top plot is for K = 5, bottom plot is for K = 6.

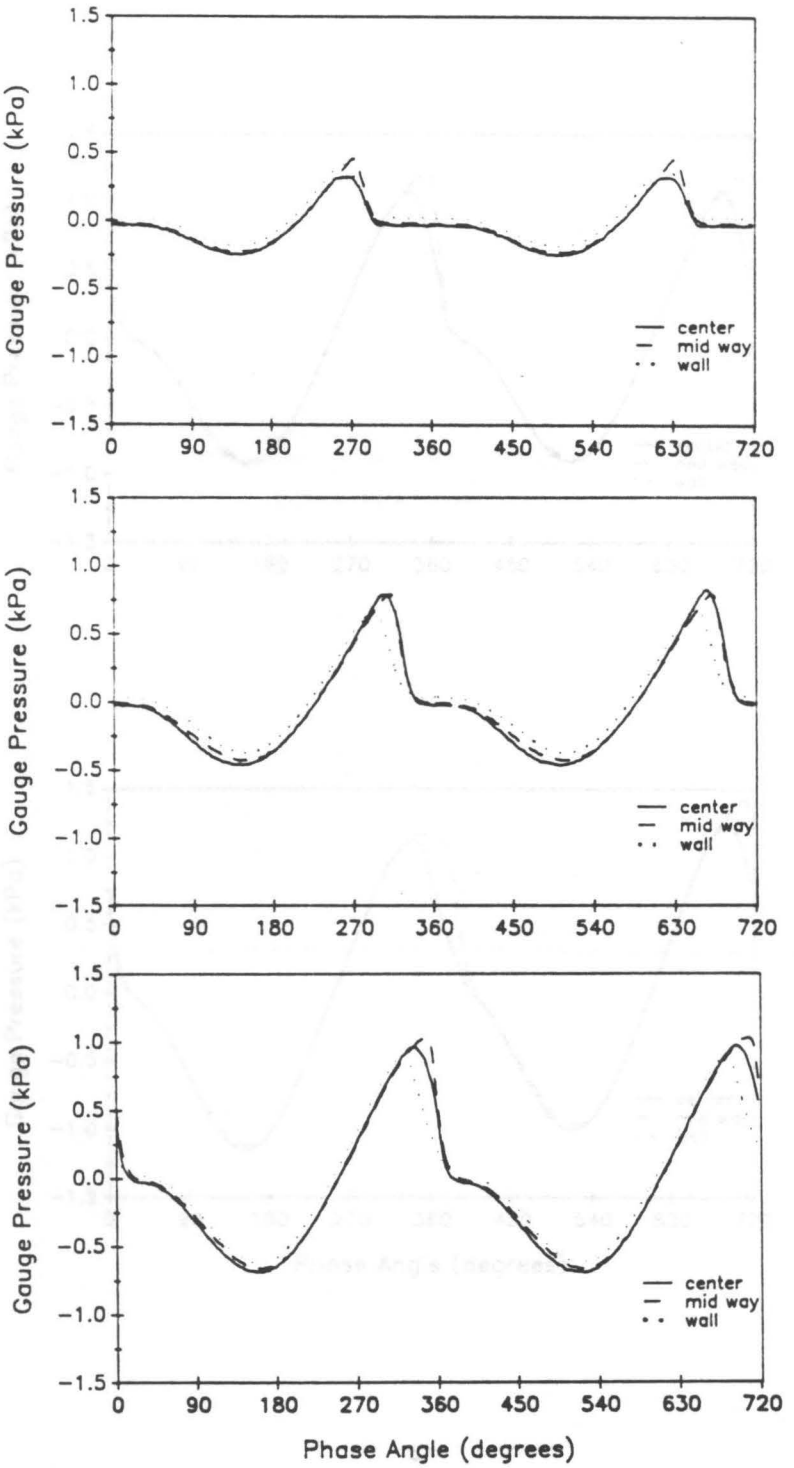

Figure 5.76. Floor pressure beneath 353-μm Master Beads at K = 2, 3, and 4: Solid line is for pressure beneath center of bed, dashed line is for pressure midway between the center and the wall, and dotted line is for pressure at the wall. Top plot is for K = 2, middle is for K = 3, bottom is for K = 4.

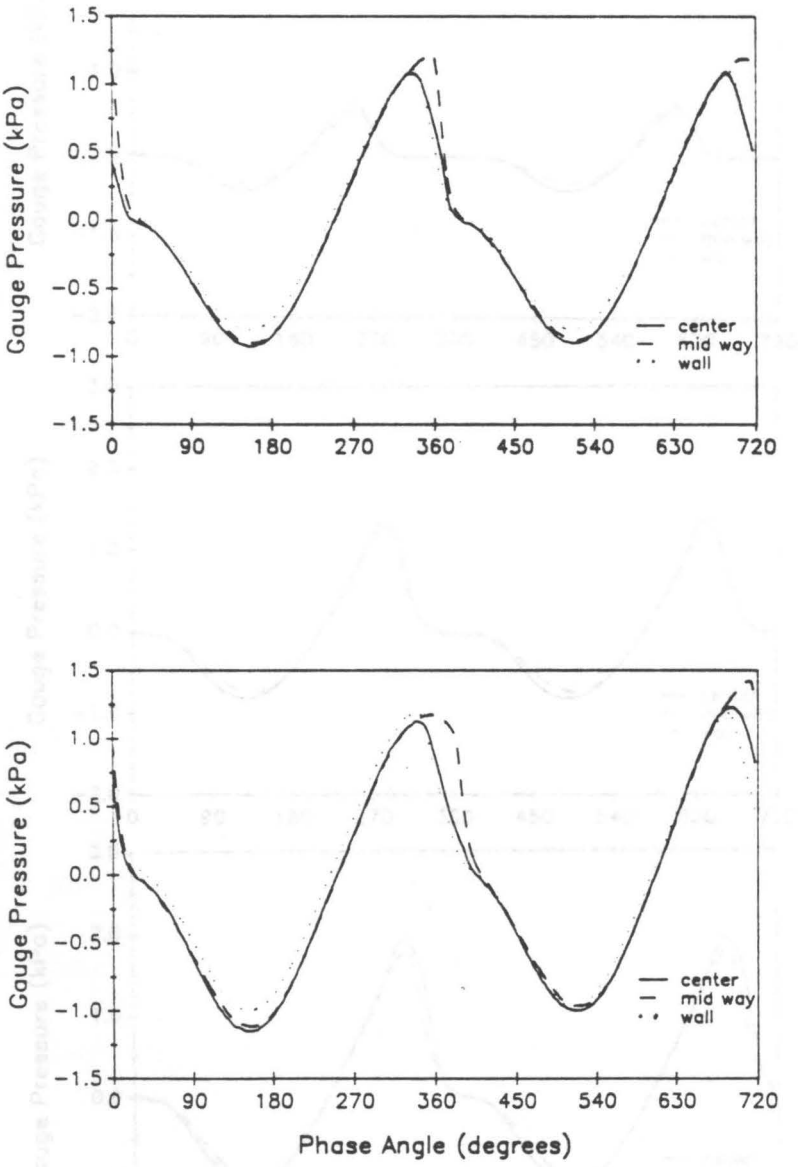

Figure 5.77. Floor pressure beneath 353-μm Master Beads at K = 5 and 6: Solid line is for pressure beneath center of bed, dashed line is for pressure midway between the center and the wall, and dotted line is for pressure at the wall. Top plot is for K = 5, bottom plot is for K = 6.

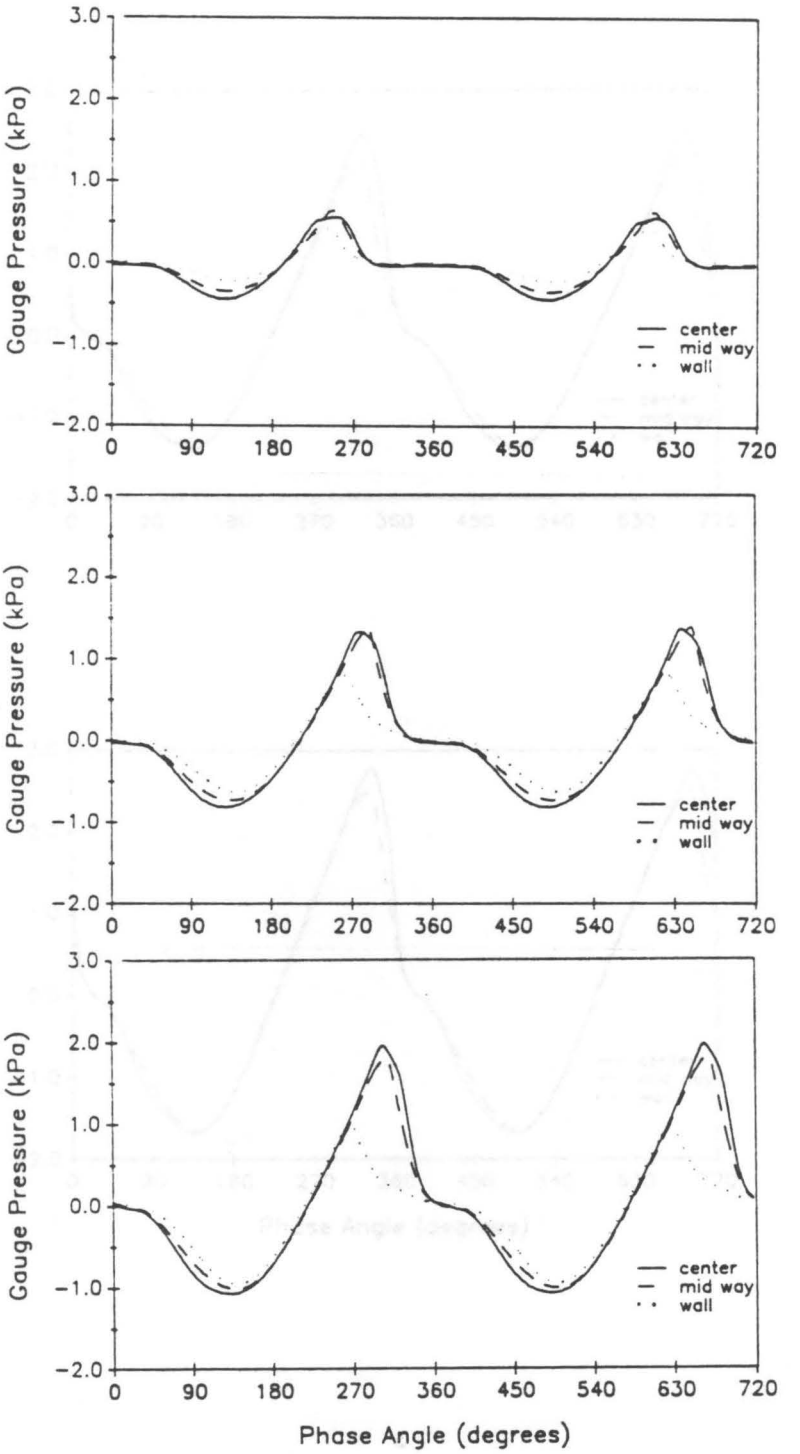

Figure 5.78. Floor pressure beneath 272-μm Master Beads at K = 2, 3, and 4: Solid line is for pressure beneath center of bed, dashed line is for pressure midway between the center and the wall, and dotted line is for pressure at the wall. Top plot is for K = 2, middle is for K = 3, bottom is for K = 4.

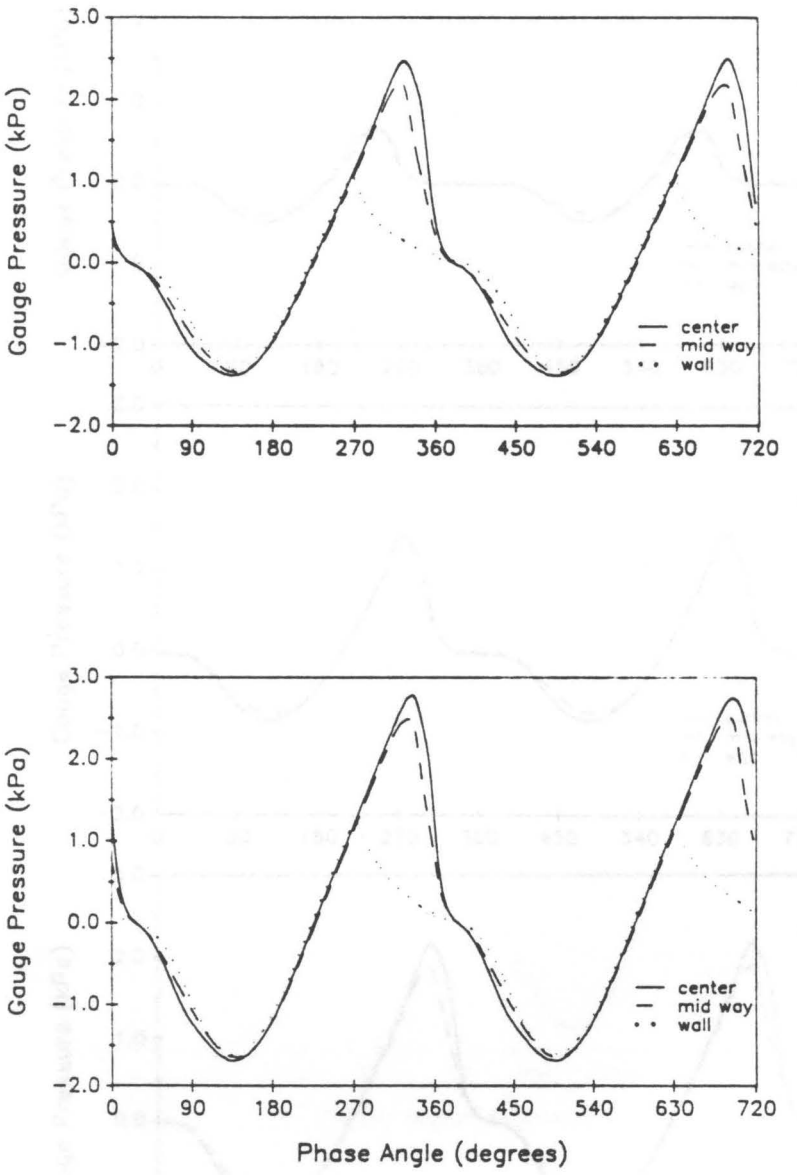

Figure 5.79. Floor pressure beneath 272-μm Master Beads at K = 5 and 6: Solid line is for pressure beneath center of bed, dashed line is for pressure midway between the center and the wall, and dotted line is for pressure at the wall. Top plot is for K = 5, bottom plot is for K = 6.

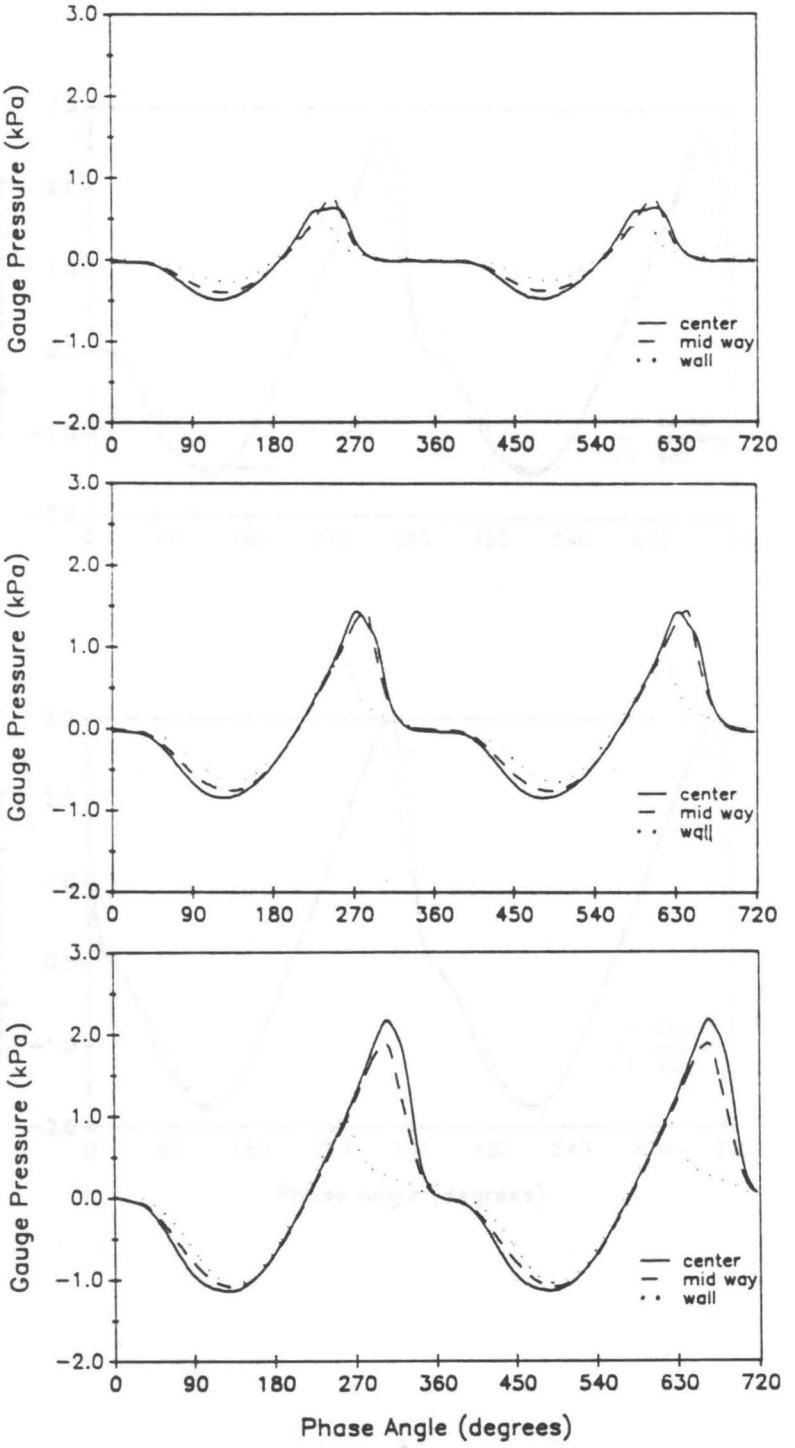

Figure 5.80. Floor pressure beneath 229-μm Master Beads at K = 2, 3, and 4: Solid line is for pressure beneath center of bed, dashed line is for pressure midway between the center and the wall, and dotted line is for pressure at the wall. Top plot is for K = 2, middle is for K = 3, bottom is for K = 4.

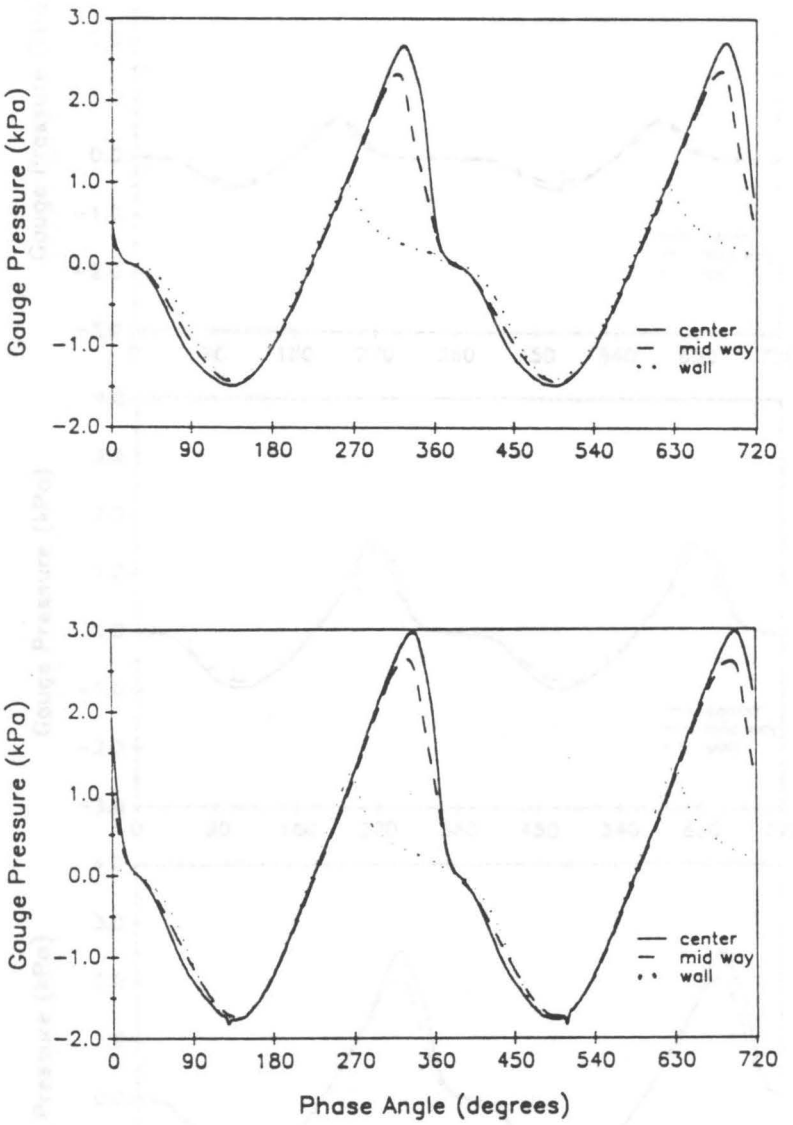

Figure 5.81. Floor pressure beneath 229-μm Master Beads at K = 5 and 6: Solid line is for pressure beneath center of bed, dashed line is for pressure midway between the center and the wall, and dotted line is for pressure at the wall. Top plot is for K = 5, bottom plot is for K = 6.

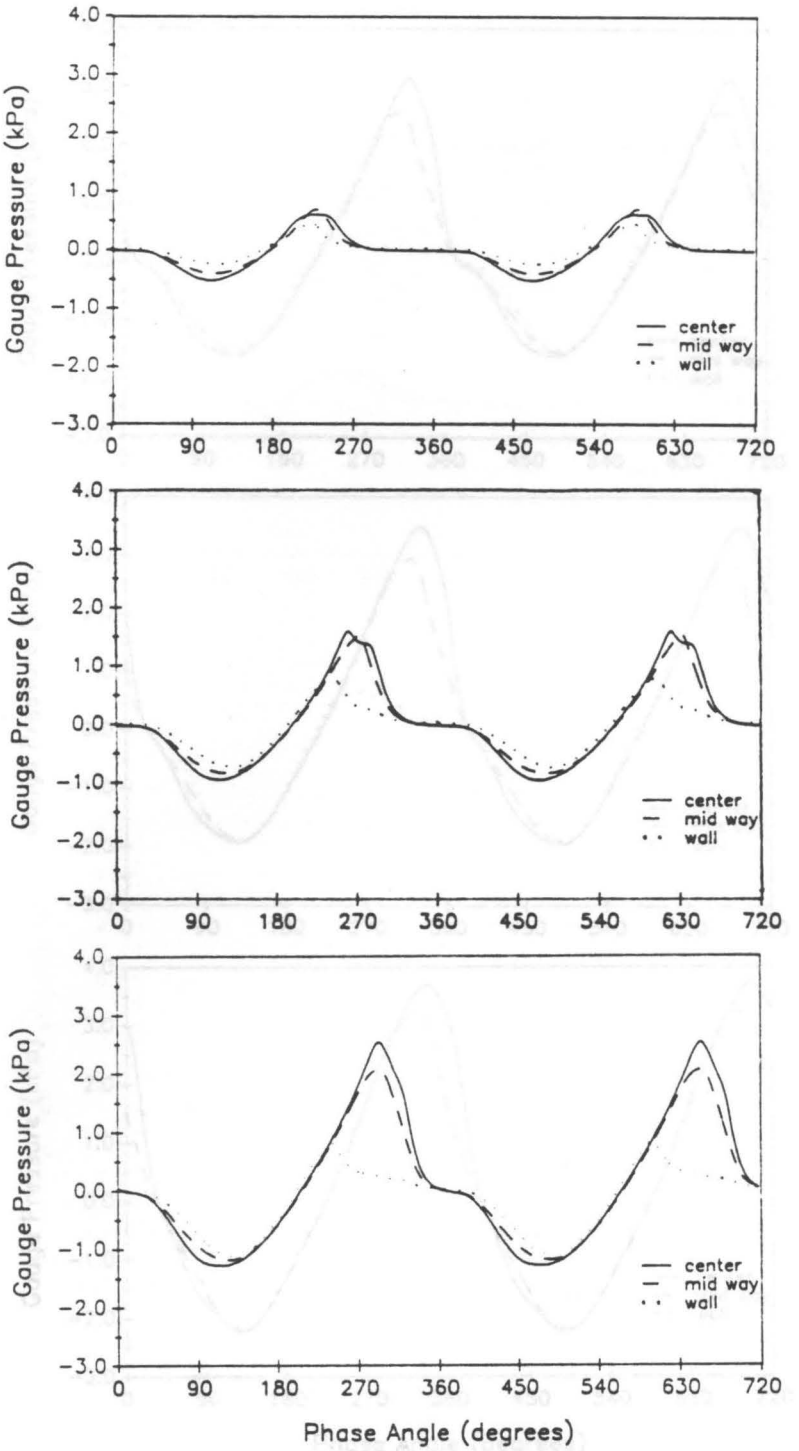

Figure 5.82. Floor pressure beneath 177-μm Master Beads at K = 2, 3, and 4: Solid line is for pressure beneath center of bed, dashed line is for pressure midway between the center and the wall, and dotted line is for pressure at the wall. Top plot is for K = 2, middle is for K = 3, bottom is for K = 4.

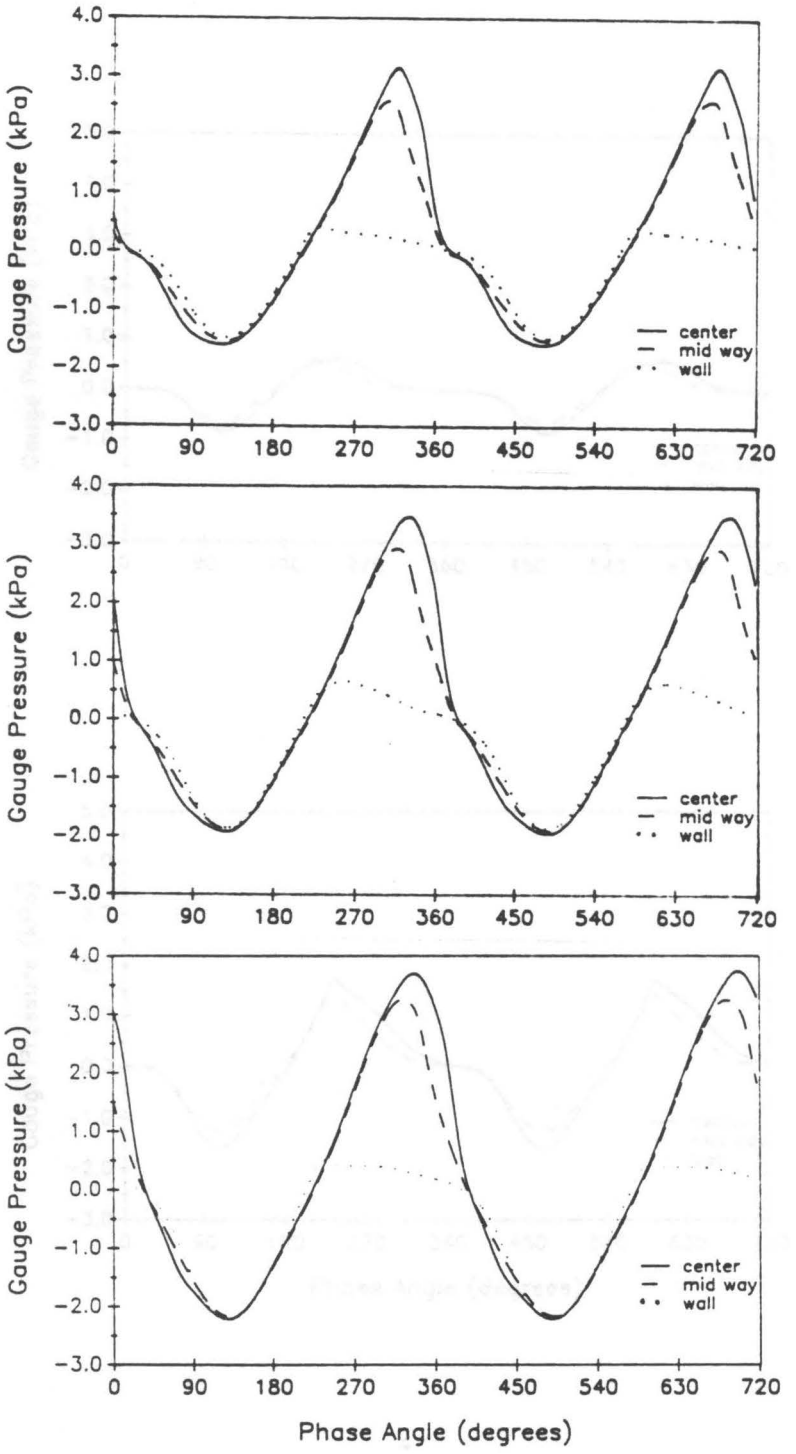

Figure 5.83. Floor pressure beneath 177-μm Master Beads at K = 5, 6, and 7: Solid line is for pressure beneath center of bed, dashed line is for pressure midway between the center and the wall, and dotted line is for pressure at the wall. Top plot is for K = 5, middle is for K = 6, bottom is for K = 7.

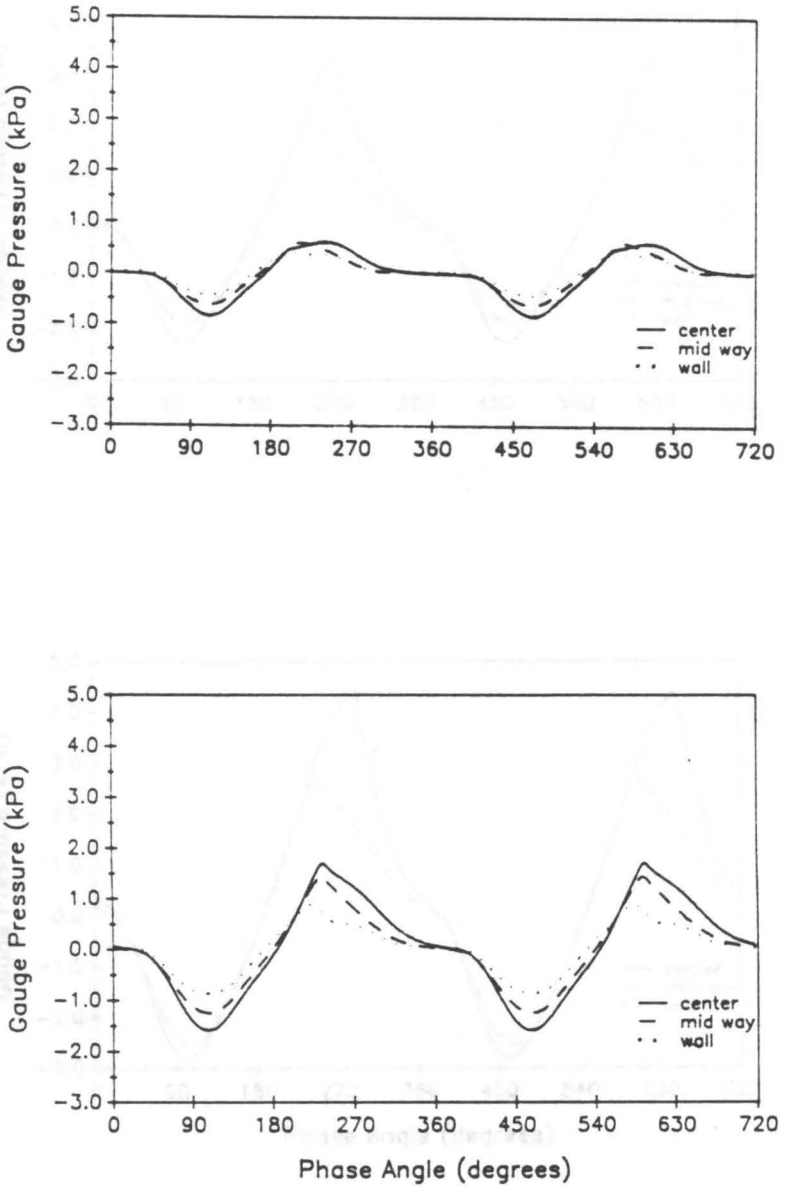

Figure 5.84. Floor pressure beneath 125-μm Master Beads at K = 2 and 3: Solid line is for pressure beneath center of bed, dashed line is for pressure midway between the center and the wall, and dotted line is for pressure at the wall. Top plot is for K = 2, bottom plot is for K = 3.

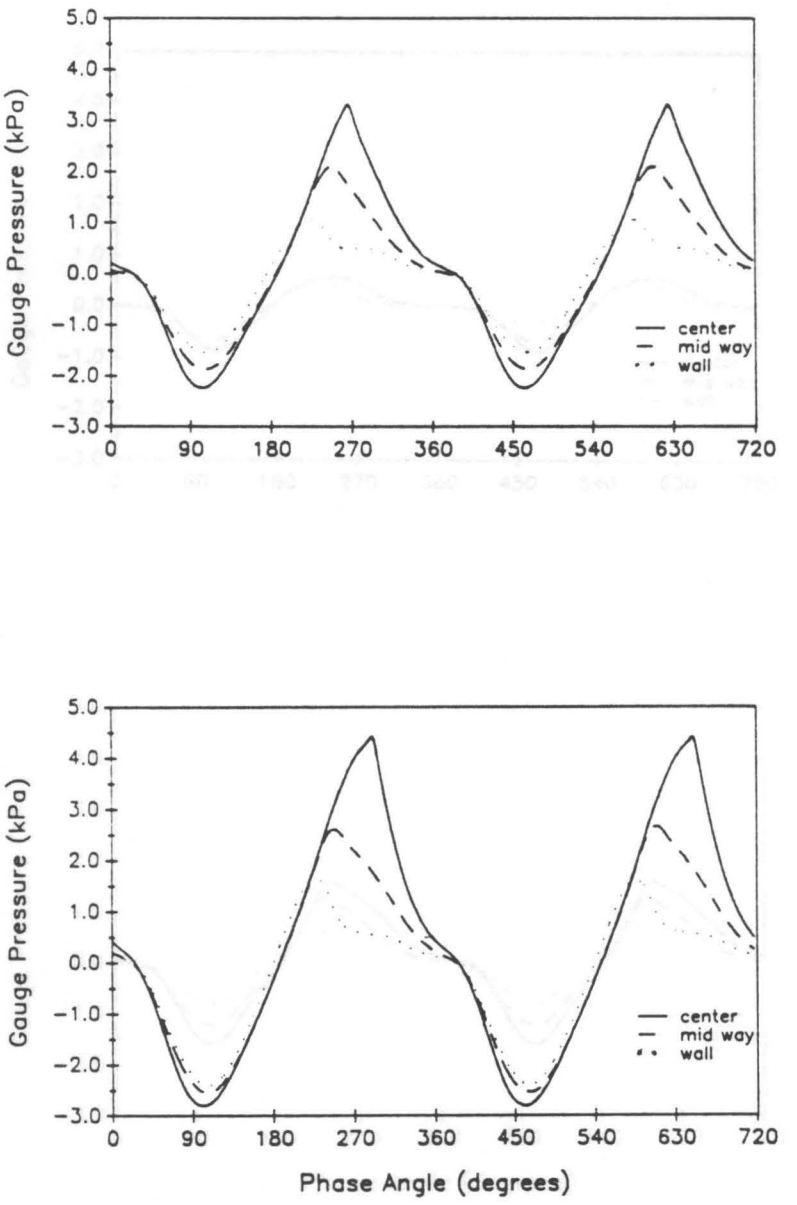

Figure 5.85. Floor pressure beneath 125-μm Master Beads at K = 4 and 5: Solid line is for pressure beneath center of bed, dashed line is for pressure midway between the center and the wall, and dotted line is for pressure at the wall. Top plot is for K = 4, bottom plot is for K = 5.

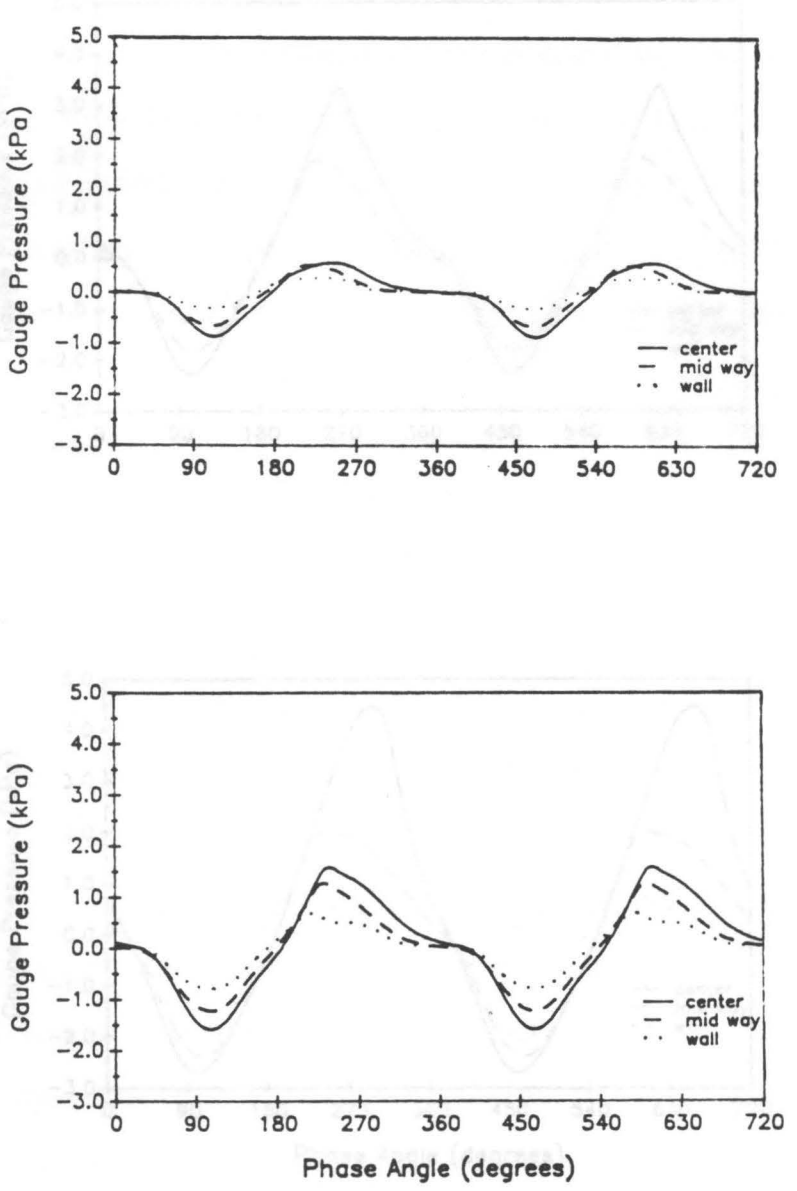

Figure 5.86. Floor pressure beneath 88-μm Master Beads at K = 2 and 3: Solid line is for pressure beneath center of bed, dashed line is for pressure midway between the center and the wall, and dotted line is for pressure at the wall. Top plot is for K = 2, bottom plot is for K = 3.

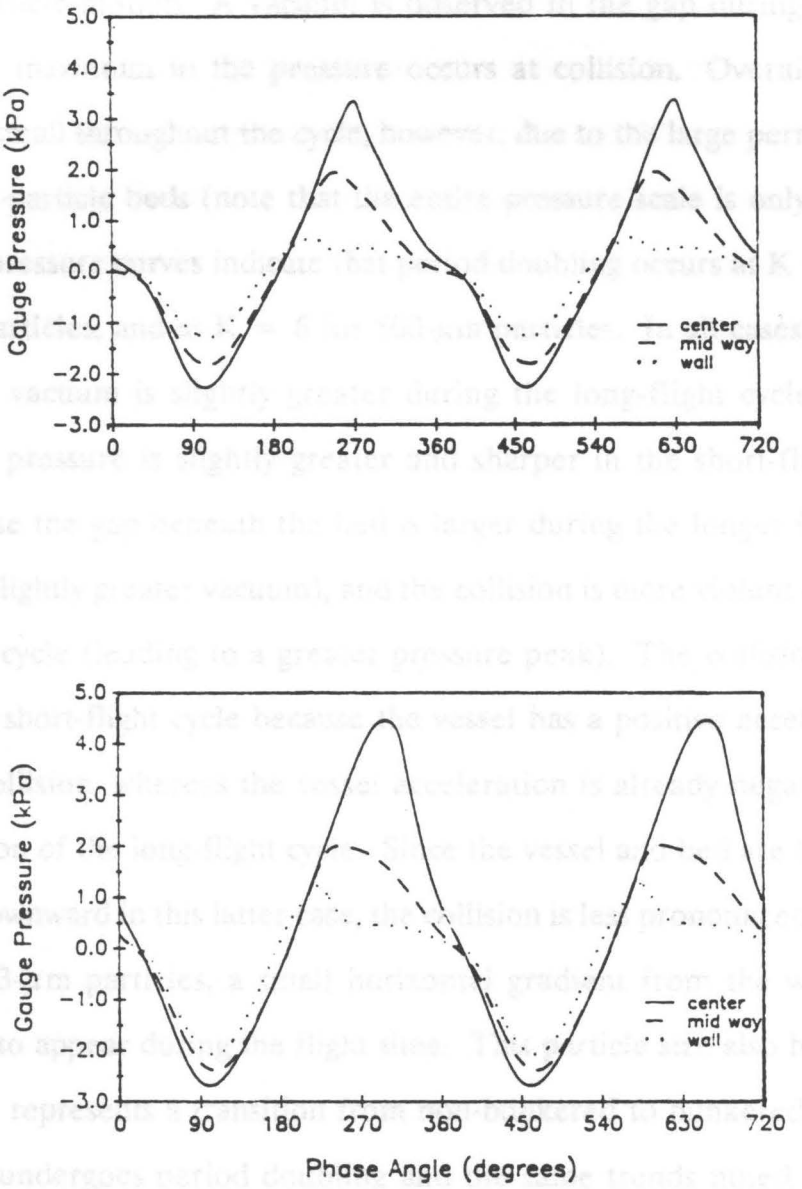

Figure 5.87. Floor pressure beneath 88-μm Master Beads at K = 4 and 5: Solid line is for pressure beneath center of bed, dashed line is for pressure midway between the center and the wall, and dotted line is for pressure at the wall. Top plot is for K = 4, bottom plot is for K = 5.

not bunker except at very low K-values, and they also do not exhibit any horizontal particle motion. A vacuum is observed in the gap during the flight period, and a maximum in the pressure occurs at collision. Overall pressure fluctuation is small throughout the cycle, however, due to the large permeabilities of these large-particle beds (note that the entire pressure scale is only -1 to +1 kPa). These pressure curves indicate that period doubling occurs at K = 5 and 6 for 707-μm particles, and at K = 6 for 500-μm particles. In all cases of period doubling, the vacuum is slightly greater during the long-flight cycle, and the positive peak pressure is slightly greater and sharper in the short-flight cycle. This is because the gap beneath the bed is larger during the longer flight time (leading to a slightly greater vacuum), and the collision is more violent during the shorter flight cycle (leading to a greater pressure peak). The collision is more violent in the short-flight cycle because the vessel has a positive acceleration at the time of collision, whereas the vessel acceleration is already negative at the time of collision of the long-flight cycle. Since the vessel and bed are both being accelerated downward in this latter case, the collision is less pronounced.

For 353-μm particles, a small horizontal gradient from the wall to the center begins to appear during the flight time. This particle size also has a slight bunker, and it represents a transition from non-bunkered to bunkered behavior. At K = 6, it undergoes period doubling and the same trends noted above are observed. As the particle size is further decreased for the cases of 272, 229, and 177-μm particles, the horizontal pressure gradient during the flight time and overall pressure fluctuation during the cycle increases. These solids are observed to have an increased degree of bunkering with decreasing particle size. The positive peak in the pressure curve is now sequential (from the wall toward the

center), confirming the noted trend in bunkered beds of gap closure from the wall toward the center.

In the finest solids (125 and 88-μm), the sharpest bunkers occur. These solids exhibit the highest horizontal pressure gradients and the greatest pressure fluctuations during a vibrational cycle due to their very low permeability. The same sequential collision from wall to center is evidenced in these curves. These solids do not have a stable center-high bunker at K-values above 5 due to the relatively high pressure gradients and associated gas flows out of the bed, and thus no data at K = 6 are shown for them.

5.4.3 Results of Resistance-to-Flow Experiments

In order to get some information about the relative resistance to flow, or "apparent viscosity," of different particles, an experiment in which the time needed to draw a rod through the vibrated bed at a given force is performed as described in Section 4.2.7. This information helps in determining the relative velocities particles should attain when under an external force such as a pressure gradient. Although the equipment is somewhat crude, it assists in interpreting qualitative trends in observed particle velocities. The greater the flow resistance of the bed, the longer the time it takes to draw the rod a set distance with a given force.

To test the sensitivity and reliability of the apparatus, a crude calibration has been performed with two liquids of known viscosity. Two trials are run with each liquid, water and glycerol, and the results are shown in Figure 5.88. The two tests for water perfectly overlap, while there is some spread in the tests for glycerol. It should be noted that the y-axis represents the output voltage from a

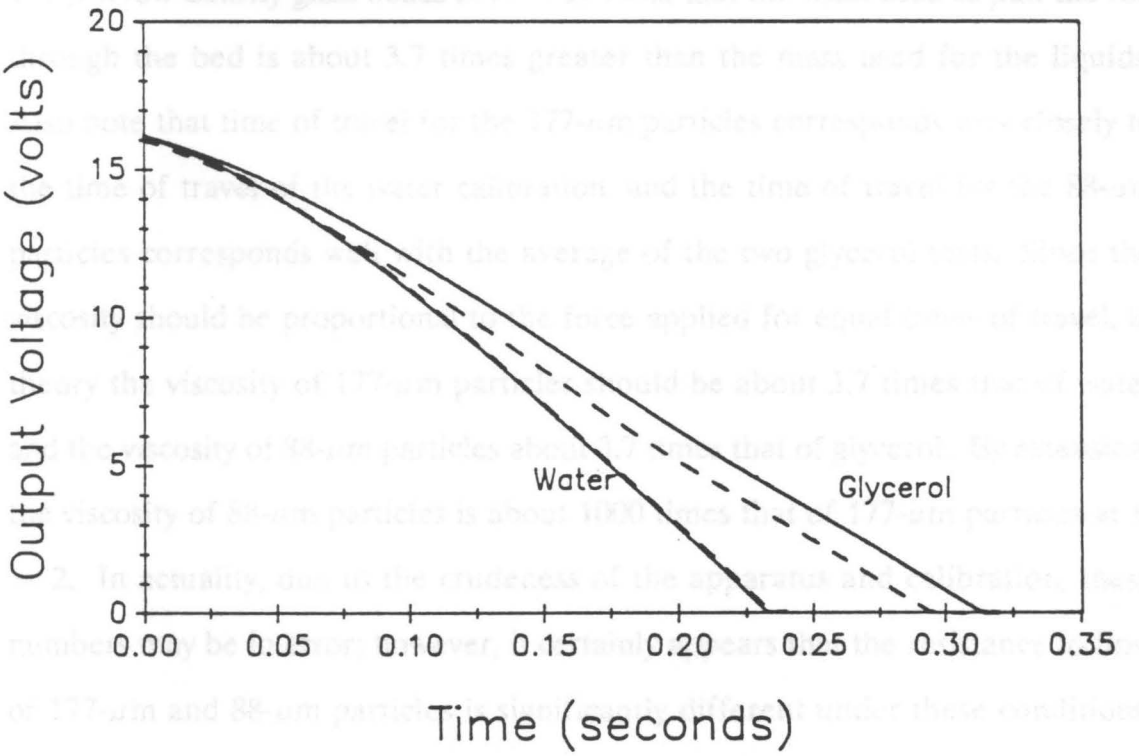

Figure 5.88. Calibration of the resistance-to-flow equipment: Resistance due to the viscosity of water and glycerol is measured. A mass of 15.69 grams is used to supply the force. X-axis represents time of travel of the rod assembly, and y-axis is proportional to displacement.

LVDT transducer, and as such this voltage is directly proportional to distance traveled. The total distance traveled in all cases is one inch. Since the viscosity of water at room temperature is 1 cP and the viscosity of glycerol is 1000 cP, this figure shows the difference in response of liquids with three orders of magnitude difference in viscosity.

Figure 5.89 shows the results of the relative flow resistances of 88 and 177-μm low-density glass beads at K = 2. Note that the mass used to pull the rod through the bed is about 3.7 times greater than the mass used for the liquids. Also note that time of travel for the 177-μm particles corresponds very closely to the time of travel of the water calibration, and the time of travel for the 88-μm particles corresponds well with the average of the two glycerol tests. Since the viscosity should be proportional to the force applied for equal times of travel, in theory the viscosity of 177-μm particles should be about 3.7 times that of water and the viscosity of 88-μm particles about 3.7 times that of glycerol. By extension, the viscosity of 88-μm particles is about 1000 times that of 177-μm particles at K = 2. In actuality, due to the crudeness of the apparatus and calibration, these numbers may be in error; however, it certainly appears that the resistance to flow of 177-μm and 88-μm particles is significantly different under these conditions. These curves have a stair-step appearance which is not seen in the liquid curves. This is due to the cyclic expansion and compaction of the bed. The horizontal section corresponds to that portion of the cycle in which the bed is in contact with the vessel and compacted, thus greatly restricting the movement of the rod. The section with the negative slope corresponds to the portion of the cycle when the bed is expanded and the rod can move relatively easily. Thus, counting the number of steps in each curve corresponds to counting the number of vibrational cycles over which the experiment is conducted.

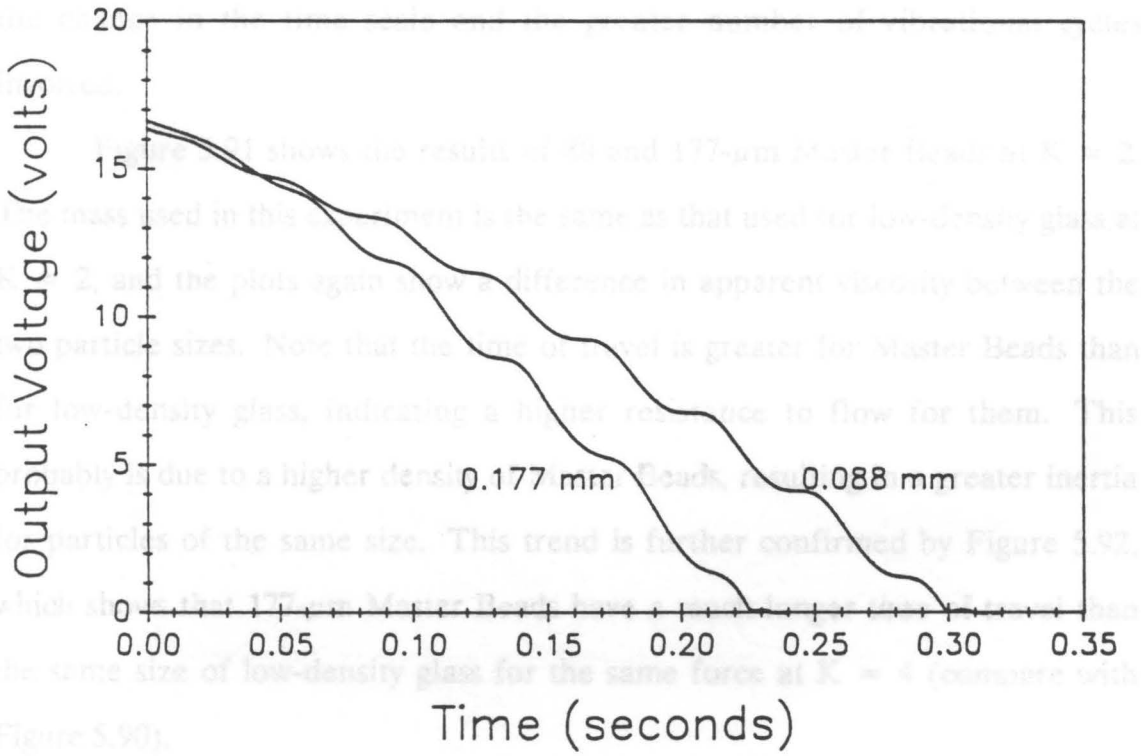

Figure 5.89. Relative resistance to flow of 88 and 177-μm low-density glass beads at K = 2: Mass used to supply the force is 57.77 grams. X-axis represents time of travel of the rod assembly, and y-axis is proportional to displacement.

Figure 5.90 shows the results for the same two solids at K = 4. Here the mass used to pull the rod through the bed is intermediate to that used in the previous two figures, and since the times of travel do not match up well, no reliable estimate of viscosity can be made. The large difference in the times of travel in the two solids suggests a very significant increase in apparent viscosity of 88-μm particles over 177-μm particles, however. Again the curves have a stair-step appearance for the same reason, but the steps are much smaller due to the change in the time scale and the greater number of vibrational cycles involved.

Figure 5.91 shows the results of 88 and 177-μm Master Beads at K = 2. The mass used in this experiment is the same as that used for low-density glass at K = 2, and the plots again show a difference in apparent viscosity between the two particle sizes. Note that the time of travel is greater for Master Beads than for low-density glass, indicating a higher resistance to flow for them. This probably is due to a higher density of Master Beads, resulting in a greater inertia for particles of the same size. This trend is further confirmed by Figure 5.92, which shows that 177-μm Master Beads have a much longer time of travel than the same size of low-density glass for the same force at K = 4 (compare with Figure 5.90).

5.4.4 Proposed Explanation of Observed Circulation

Observations of vibrated-bed circulation suggest that there are two distinct regimes: bunkered-bed circulation and non-bunkered circulation. Since the two cases are quite different and particle motion appears to be due to different forces, they are dealt with separately.

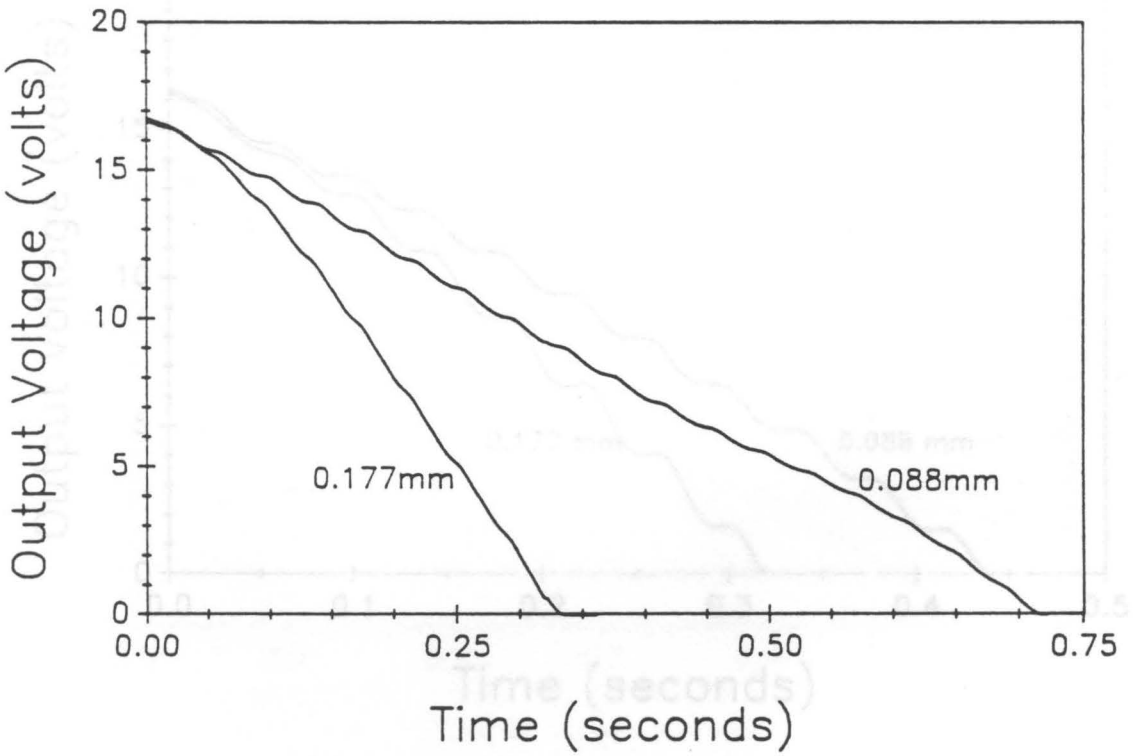

Figure 5.90. Relative resistance to flow of 88 and 177-μm low-density glass beads at K = 4: Mass used to supply the force is 23.30 grams. X-axis represents time of travel of the rod assembly, and y-axis is proportional to displacement.

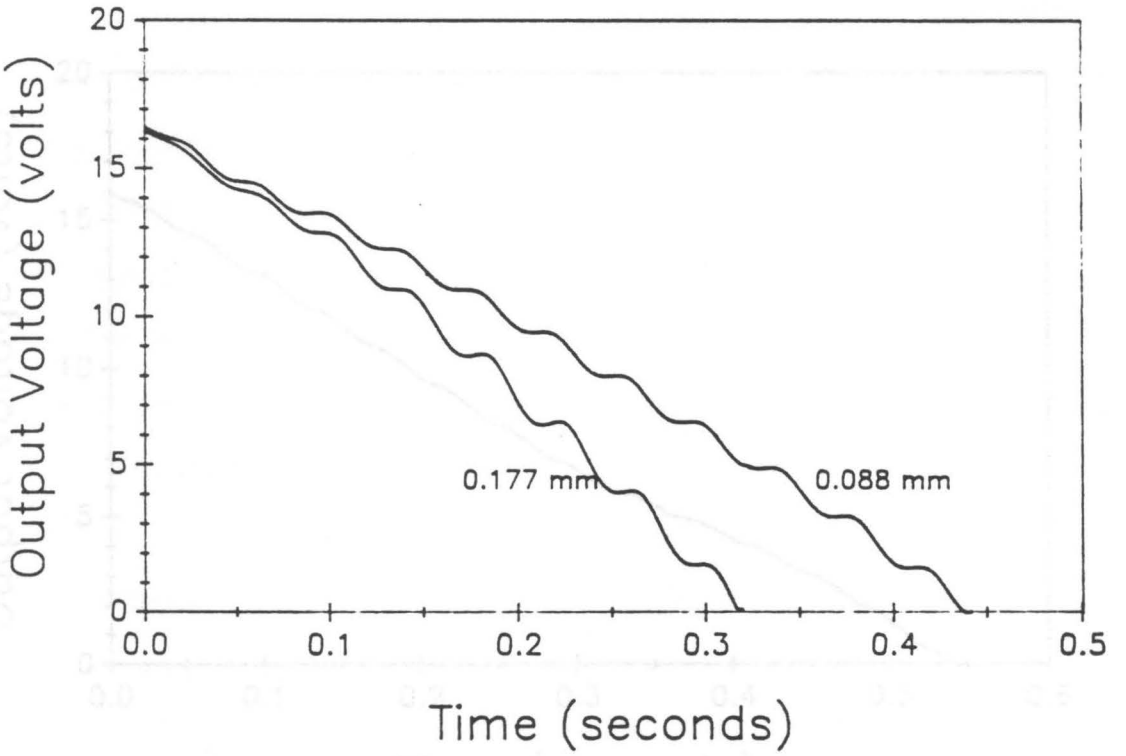

Figure 5.91. Relative resistance to flow of 88 and 177-μm Master Beads at K = 2: Mass used to supply the force is 57.77 grams. X-axis represents time of travel of the rod assembly, and y-axis is proportional to displacement.

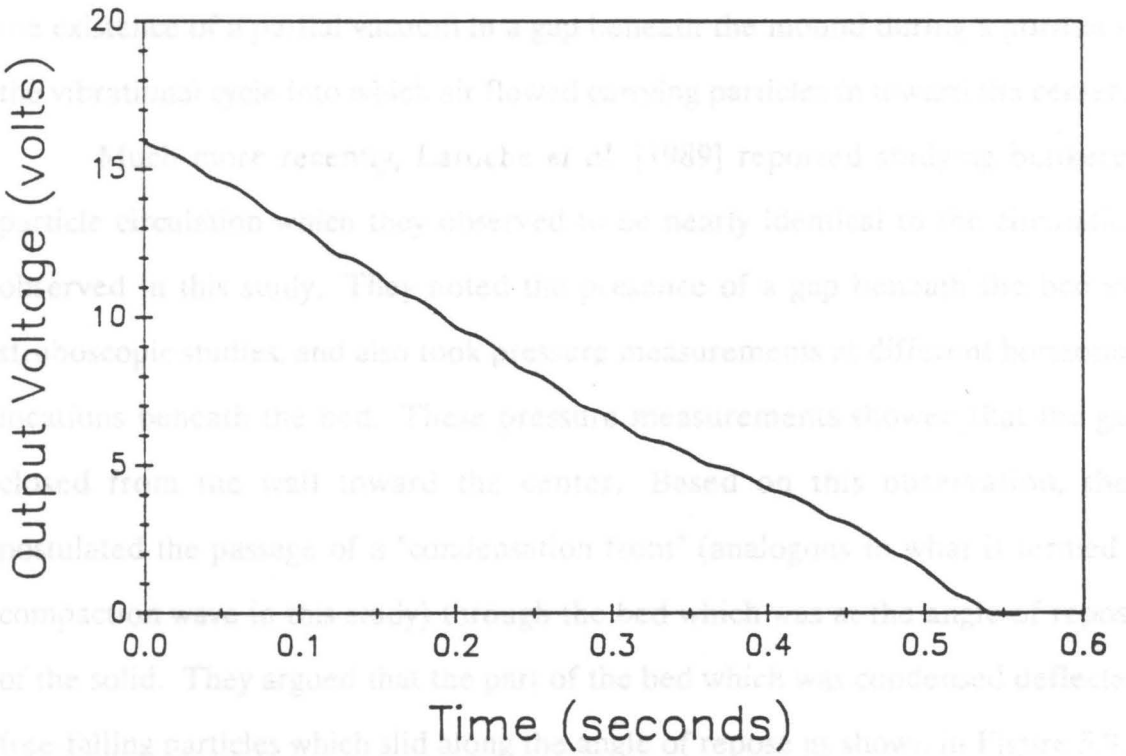

Figure 5.92. Resistance to flow for 177-μm Master Beads at K = 4: Mass used to supply the force is 23.30 grams. X-axis represents time of travel of the rod assembly, and y-axis is proportional to displacement.

5.4.4.1 Circulation in Bunkered Beds

Circulation in vibrated beds of relatively fine particles, which tend to form a non-flat or bunkered top surface, has been observed and described by several previous investigators. Faraday [1831] reported seeing fine particles mound up on a vibrated plate and noted that each mound had internal circulation: particles near the bottom were drawn in toward the middle, proceeded up at the center, and fell down the slope on all sides. He explained this motion by hypothesizing the existence of a partial vacuum in a gap beneath the mound during a portion of the vibrational cycle into which air flowed carrying particles in toward the center.

Much more recently, Laroche *et al.* [1989] reported studying bunkered particle circulation which they observed to be nearly identical to the circulation observed in this study. They noted the presence of a gap beneath the bed via stroboscopic studies, and also took pressure measurements at different horizontal locations beneath the bed. These pressure measurements showed that the gap closed from the wall toward the center. Based on this observation, they postulated the passage of a "condensation front" (analogous to what is termed a compaction wave in this study) through the bed which was at the angle of repose of the solid. They argued that the part of the bed which was condensed deflected free-falling particles which slid along the angle of repose as shown in Figure 5.93. This deflection caused by the condensation front, when averaged over many vibrational cycles, caused the overall macroscopic circulation pattern.

Observation of bunkered beds via high-speed movies taken in this study suggests that the passage of the compaction wave (or condensation front) is too fast to have any appreciable particle deflection along its surface. Furthermore, particles are observed to be moving with a horizontal as well as vertical

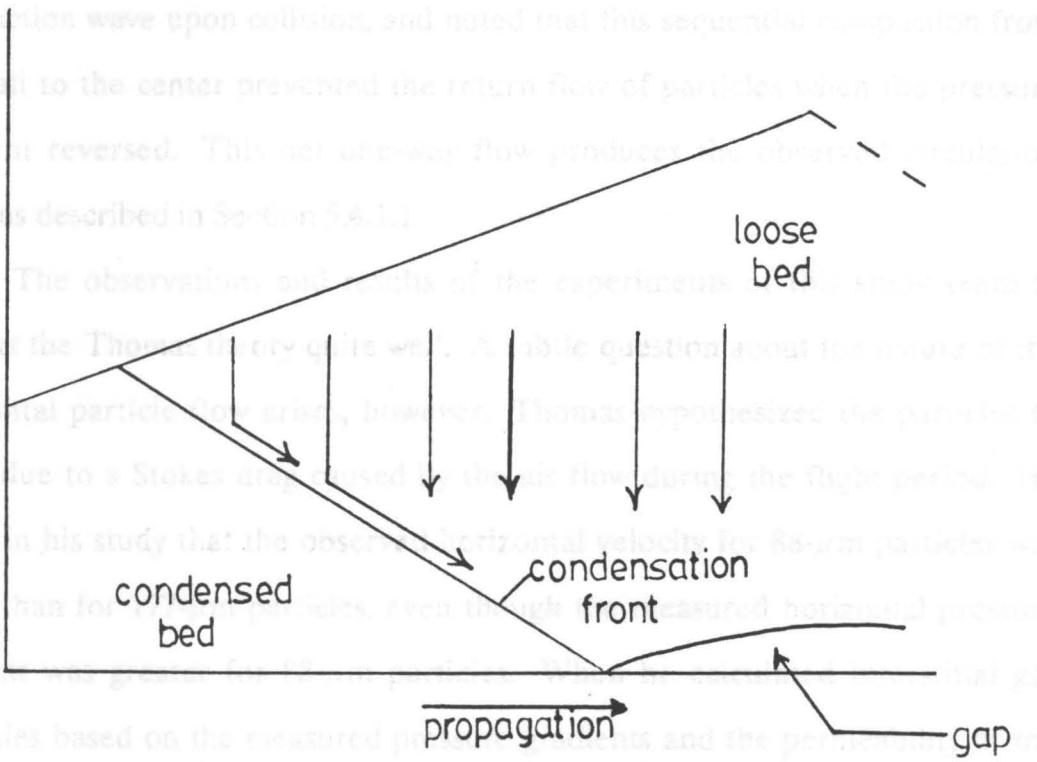

Figure 5.93. Proposed explanation for bunkered-bed circulation: The particles in free flight are deflected by the "condensation front" along the angle of repose. Adapted from Laroche *et al.* [1989].

component of velocity during the entire free-flight period of the cycle, which does not fit with the theory of Laroche as shown in Figure 5.93. This observation supports the theory of circulation in bunkered beds which was first put forth by Thomas [1988]. In this theory, horizontal particle motion is brought about by horizontal air movement caused by a pressure gradient. The results of Section 5.4.2 show that a horizontal pressure gradient does exist from the walls toward the center of the bed during the flight period. Thomas also noted the passage of a compaction wave upon collision, and noted that this sequential compaction from the wall to the center prevented the return flow of particles when the pressure gradient reversed. This net one-way flow produces the observed circulation patterns described in Section 5.4.1.1.

The observations and results of the experiments of this study seem to support the Thomas theory quite well. A subtle question about the nature of the horizontal particle flow arises, however. Thomas hypothesized the particles to move due to a Stokes drag caused by the air flow during the flight period. He noted in his study that the observed horizontal velocity for 88-μm particles was lower than for 177-μm particles, even though the measured horizontal pressure gradient was greater for 88-μm particles. When he calculated interstitial gas velocities based on the measured pressure gradients and the permeability of the beds, however, he found that the interstitial velocities supported the trend in the observed velocities, and thus he ascribed the motion to Stokes drag brought about by the interstitial air flow.

The resistance-to-flow experiments of Section 5.4.3 allow an alternative explanation. If the bed in the expanded state (*i.e.*, during the flight period) is thought of as a pseudo-fluid (behaves as a fluid), then it can flow under the influence of a pressure gradient. The velocity of flow in this case is a function of the size of the pressure gradient, as well as the resistance to flow or apparent viscosity of the bed. Since the results of the flow resistance measurements show that smaller particle beds are more "viscous," Thomas' observed trend in particle velocity can be explained by assuming the effect of increased flow resistance for 88-μm particles is larger than the effect of increased pressure gradient (relative to 177-μm particles).

In this study, low-density glass beads are observed to have a higher velocity for 177-μm particles than 88-μm particles at K = 2, but at K = 4 the velocities are approximately the same. Since Thomas calculated that the interstitial gas velocity of the 88-μm particles is lower than that for 177-μm particles at K = 4, the Stokes drag model cannot predict the observation that the velocities are the same. The pseudo-fluid model can explain the observed trends since the effect of increased pressure gradient can be assumed to compensate for the increased flow resistance for 88-μm beads at K = 4. Unfortunately, since the flow-resistance apparatus only gives relative rather than absolute "viscosities" for the vibrated particles, the validity of this assumption cannot be checked with a calculation, so the model cannot be further tested.

5.4.4.2 Circulation in Non-Bunkered Beds

Circulation in large-particle, non-bunkered beds has been described by Muchowski [1980]. He noted very similar circulation patterns to those observed

in this study, and explained them in terms of wall friction. He ascribed the downward motion at the walls to a smaller trajectory of the particles at the walls relative to those in the middle. Since these wall particles were not thrown as high due to friction, they had a net downward velocity over the course of many cycles. He observed that the effect of this frictional trajectory-damping extended only a small way into the bed, which agrees well with observations in this study and Thomas [1988]. He noted a much slower upward flow in the bulk of the bed.

This explanation fits the observations and experimental results obtained in this study well. Wall friction plays a much larger role in circulation for these particles because there is no pressure gradient to create a competing hydrodynamic force as is the case for finer particles. This is borne out by the evidence of the pressure curves for 707 and 500-μm particles in Section 5.4.2. The curves show no horizontal pressure gradient, and no horizontal particle movement is observed. Furthermore, the collision data indicate that the gap closes simultaneously for non-bunkered beds and high-speed movies show that the compaction wave is nearly horizontal with a strictly vertical propagation. All of the experiments show no driving force for horizontal motion, which agrees with observation.

The argument for wall friction being the cause of the downward motion at the wall rather than a preferential down-flow of gas there (as proposed by Chlenov and Mikhailov [1972]) has been supported by Thomas [1988]. He reported seeing the same circulation patterns for non-bunkered beds in a vacuum, a situation where particle movement cannot be due to gas flow. In fact, he reported that all particles, regardless of size, exhibit the characteristic non-bunkered circulation pattern in a vacuum. This simultaneously confirms the

theory that non-bunkered circulation is due to wall friction and bunkered circulation is due to hydrodynamic forces.

5.5 Summary of Particle-Dynamics Results

The most significant results on particle dynamics obtained in this study are capsulated in this section for emphasis.

The experiments on bed-vessel separation indicate that separation is delayed over what is predicted by the rigid, porous-piston models. This observation is attributed to a two-part separation. First, at the point of the cycle where the forces on the bed cancel and it becomes "weightless," it dilates slightly. This dilation causes the horizontal stress at the walls, which is preventing the bed from separating from the vessel base, to decay. When this horizontal stress is sufficiently small, actual bed-vessel separation occurs. It appears that separation never occurs for the finest (88 μm) particles, however. For these particles, the bed merely goes through cyclic expansion and compaction.

The study of bed-vessel collision indicates that beds having a non-bunkered top surface collide essentially simultaneously, while beds which are bunkered collide first at the side walls with the gap closing toward the center. There is evidence from the collision experiments that the bed undergoes compaction on collision, which supports the expansion theory mentioned above. High-speed movies show that this compaction occurs via the propagation of a stress wave which has horizontal and vertical components. The angle of the compaction wave appears to be a property of the vibrated solid, and it does not vary significantly with changing K-value for the same solid. The observed trend in the angle of the compaction wave is that it is nearly horizontal for large particles,

and the angle increases monotonically with decreasing particle size for all sizes observed.

Particle circulation is observed to have two distinct regimes in shallow vibrated beds: one for large particles which exhibit a flat, non-bunkered top surface; and one for smaller particles in which the top surface bunkers. The circulation in non-bunkered beds is observed to be vertically down at the walls in two or three particle layers, and up much more slowly in the bulk of the bed. This circulation is driven by wall friction. Little or no horizontal particle motion is observed, and overall mixing is relatively poor. Bunkered circulation, on the other hand, exhibits a large horizontal component of particle velocity in the bulk of the bed. This horizontal component is due to horizontal pressure gradients, which have been directly measured at the vessel floor, that cause hydrodynamic forces. During the flight period of the bed in which the particles are free to move, these forces are in the direction of the side walls toward the bed center. This agrees with observed particle flow. During compaction the pressure gradient reverses, but the particles are no longer free to move once compacted and there is no return particle flow. The rate at which particles circulate in bunkered beds appears to be tied to the magnitude of the pressure gradient and the flow resistance of the bed. The pressure gradient increases with increasing vibrational intensity, while the flow resistance decreases. The exact dependence of bed flow resistance on K-value is not measured, however, so particle circulation velocities cannot be predicted at this time.

Chapter 6 Heat Transfer Results and Discussion

This chapter addresses the findings of this study on heat transfer in vibrated beds. The first section examines the measured heat-transfer coefficients, including a discussion of observed trends and an analysis of errors. The second section contains a comparison of the measured values with published results, emphasizing the effect of heater geometry on heat transfer by comparison with a very similar study. The third section deals with proposed models for heat transfer in vibrated beds. Data from this study are used to test the applicability of these models to this system. The final section gives a brief summary of the findings on heat transfer.

6.1 Measured Heat-Transfer Coefficients

Heat-transfer coefficients are measured for eight size ranges of Master Beads and four size ranges each of high-density glass and low-density glass. Results for Master Beads and glass beads, and an analysis of the probable experimental error appear in the following subsections.

6.1.1 Heat-Transfer Coefficients for Master Beads

Heat-transfer coefficients are measured as described in Section 4.2.1 with the vertical-surface heating probe described in Section 3.3.1 placed horizontally in the bed. All measurements are made with the surface of the heating probe

between eighty and ninety degrees Celsius, and all measurements are made at steady-state.

The heat-transfer coefficient is calculated from Newton's law of cooling,

$$h = \frac{Q}{A_S(T_P - T_B)} \qquad [6.1]$$

In this equation, h is the overall surface-to-bed heat-transfer coefficient in Watts per square meter per degree Celsius (or Kelvin), Q is the electrical power dissipated by the heater in Watts, A_S is the area of the heater surface in square meters, T_P is the average of the heating probe temperatures in degrees Celsius, and T_B is the average of the bed temperatures in degrees Celsius.

Figure 6.1 shows the experimentally measured heat-transfer coefficients for 30-mm deep beds of Master Beads as a function of vibrational intensity parameter, K. All measurements are made with the bed in the center-high bunker configuration (if bunkering occurs) unless otherwise noted. With this vessel geometry, the center-high bunker tends to form a ridge which extends the length of the vessel just above the heating probe.

Several of the most noteworthy features of the data are:

1) For all sizes of particles measured, the heat-transfer coefficient increases initially from its value at K = 2.
2) For the largest particles (707 and 500 μm), the heat-transfer coefficient does not vary as greatly with K as in the case of the smaller particles, and flattens out at about K = 4.
3) The heat-transfer coefficients for the particles between 177 μm and 353 μm all increase very rapidly with K-value, and the curves do not

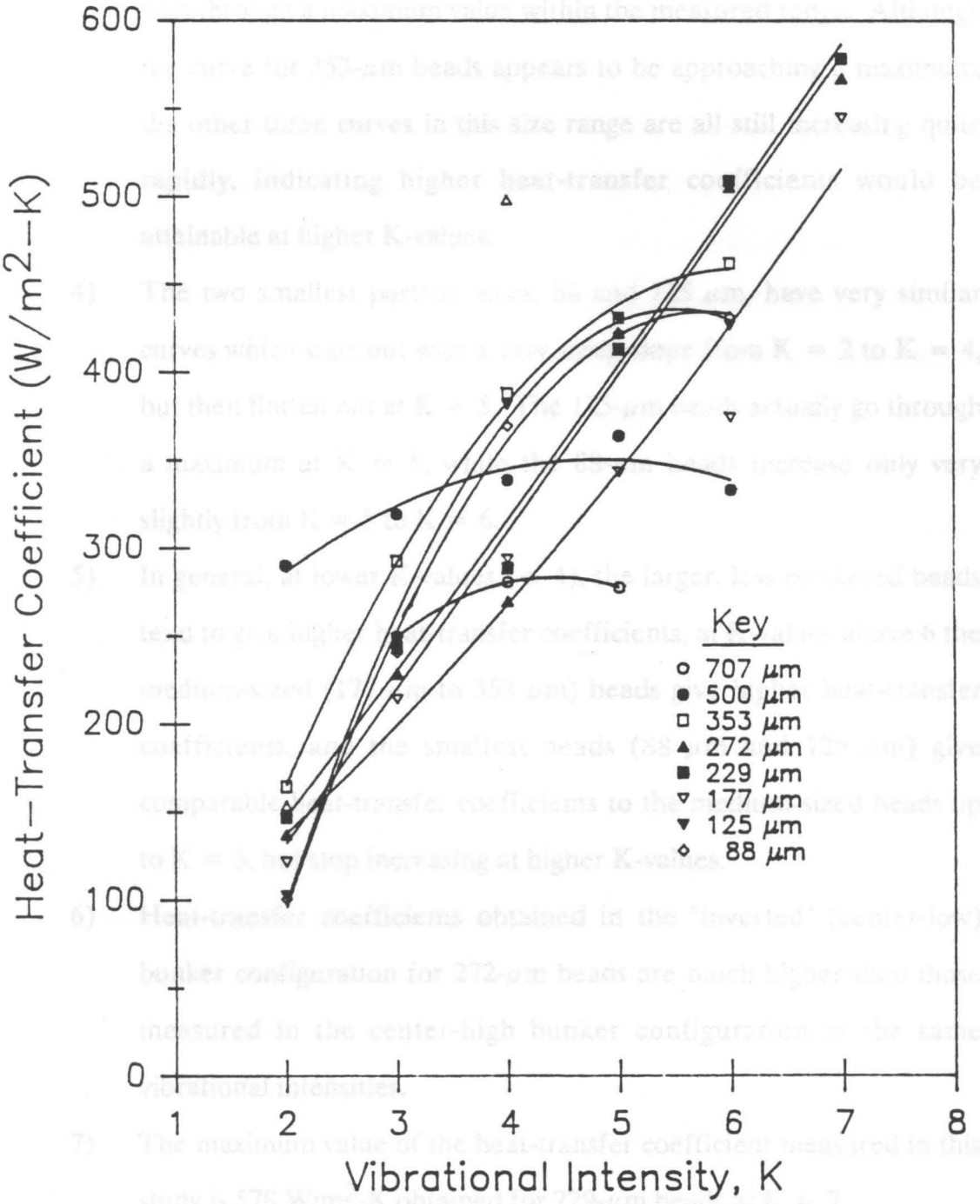

Figure 6.1. Heat-transfer coefficients for Master Beads: Measured heat-transfer coefficients of Master Beads *versus* K-value. Note: the two data points appearing as open triangles represent values obtained for 272-μm particles in the center-low bunker configuration.

pass through a maximum value within the measured range. Although the curve for 353-μm beads appears to be approaching a maximum, the other three curves in this size range are all still increasing quite rapidly, indicating higher heat-transfer coefficients would be attainable at higher K-values.

4) The two smallest particle sizes, 88 and 125 μm, have very similar curves which start out with a very steep slope from K = 2 to K = 4, but then flatten out at K = 5. The 125-μm beads actually go through a maximum at K = 5, while the 88-μm beads increase only very slightly from K = 5 to K = 6.

5) In general, at lower K-values (< 4), the larger, less-bunkered beads tend to give higher heat-transfer coefficients, at K-values above 6 the medium-sized (177 μm to 353 μm) beads give higher heat-transfer coefficients, and the smallest beads (88 μm and 125 μm) give comparable heat-transfer coefficients to the medium-sized beads up to K = 5, but stop increasing at higher K-values.

6) Heat-transfer coefficients obtained in the "inverted" (center-low) bunker configuration for 272-μm beads are much higher than those measured in the center-high bunker configuration at the same vibrational intensities.

7) The maximum value of the heat-transfer coefficient measured in this study is 578 W/m^2-K obtained for 229-μm beads at K = 7.

A bed of the largest beads, 707 μm, is not stable at high K-values. The bed rocks back and forth due to the fact that the time of flight of the bed is greater than a cycle; that is, the bed enters the period-doubling regime discussed in Section 5.1.2. Because of this, no steady-state could be attained at K > 5.

Furthermore, since for a given solid density the bulk density increases with increasing particle size, this bed is the heaviest and produces appreciable distortion of the accelerometer signal. Values of the heat-transfer coefficient have been measured for this solid at K-values of 1.5 and 2, but are not reported. The poor overall particle circulation for these large solids at low K creates temperature differences between the bed thermocouples on the same order as the temperature difference between the heating probe and average bed temperature, making an overall heat-transfer coefficient meaningless.

Table 6.1 presents, in tabular form, the data plotted in Figure 6.1. The heat-transfer coefficient reported is the average of 6 or 7 data points taken as described in Section 4.2.1. The 95-percent confidence interval reported is based on the assumption that the data are normally distributed. It is a statistical quantity which gives an indication of the spread of the data. As such, the relatively low values reported in the table indicate only that the data are repeatable. In fact, the accuracy of the data is much lower than the repeatability due to the effect of heat loss (see Section 6.1.3.1). Therefore, the values shown in the 95-percent confidence interval column cannot be taken as the accuracy of the reported values.

6.1.1.1 Discussion of Observed Trends for Master Beads

An increase in the vibrational intensity leads to increased particle circulation, which allows the particles to carry more heat away from the heater and thus improves heat transfer. In the case of the larger particles, however, this effect is less significant since they tend not to bunker and demonstrate only local rather than overall, large-scale circulation patterns. The heat-transfer curves for

Table 6.1. Measured Heat-Transfer Coefficients for Master Beads

Particle Size, $\overline{d}_p$ (microns)	Vibrational Intensity Parameter, K	Heat-Transfer Coefficient, h (W/m^2-K)	95% Confidence Interval for h (W/m^2-K)
707	3	249.5	±1.8
	4	280.7	±0.4
	5	277.5	±0.8
500	2	289.9	±12.0
	3	319.3	±1.7
	4	338.7	±0.8
	5	363.7	±2.7
	6	332.7	±0.5
353	2	164.1	±0.7
	3	292.6	±5.2
	4	387.9	±9.2
	5	430.7	±2.4
	6	461.6	±3.2
272	2	136.9	±0.8
	3	228.5	±0.5
	4	269.7	±1.2
	5	422.1	±2.0
	6	505.2	±3.2
	7	567.2	±3.1
	2*	153.2	±3.4
	4*	497.8	±6.8

*denotes data obtained in "center-low" bunker configuration

(table continued on following page)

Table 6.1 (continued)

Particle Size, d_p (microns)	Vibrational Intensity Parameter, K	Heat-Transfer Coefficient, h (W/m^2-K)	95% Confidence Interval for h (W/m^2-K)
229	2	146.8	±1.0
	3	243.4	±1.6
	4	288.8	±2.7
	5	413.2	±3.1
	6	508.6	±5.1
	7	578.4	±3.9
177	2	121.5	±0.6
	3	214.0	±0.7
	4	293.7	±1.7
	5	343.2	±0.9
	6	374.1	±4.4
	7	544.6	±10.7
125	2	102.9	±1.2
	3	249.0	±4.5
	4	381.8	±3.7
	5	431.1	±1.3
	6	426.6	±1.0
88	2	100.7	±0.8
	3	240.5	±2.7
	4	369.4	±1.9
	5	421.8	±1.0
	6	430.9	±1.9

these larger particles, therefore, have the relatively flat shape one would expect for a particle size which receives only very limited benefit of increased circulation due to increased vibrational intensity. The slight drop off in heat-transfer coefficient for the 500-μm particles at K = 6 can be explained by an observation made with the two-dimensional bed. At this high vibrational intensity, these particles are observed to shear away from a small portion of the top of the heating surface as shown in Figure 6.2. This effect introduces an additional resistance to heat transfer, an air space, over the small part of the heater exposed and therefore results in a slight reduction in heat-transfer coefficient. Thomas [1988] evaluated the effect of air gaps around heating surfaces and this effect is discussed in Section 6.2.1.

The next group of particles, those between 177 and 353 μm, exhibits on the whole a rather straightforward trend. All of these particles show an increase in heat-transfer coefficient with increasing K-value. This can be explained by the increase of overall particle circulation with increasing K-value, as noted before. The largest particle in this group, the 353-μm particle, begins to exhibit some of the character of the larger particles by K = 6, where the rate of increase appears to be lessening. The 272 and 229-μm particles exhibit a nearly linear increase in heat-transfer coefficient with K, and the 177-μm particles give similar results except for seemingly anomalous values at K = 5 and 6.

The observed trend for the finest particles, the 88 and 125-μm sizes, can be directly explained by observations of particle circulation. These fine particles, when viewed in a two-dimensional vessel with glass front walls, are not truly stable over long periods of time at high K-values. The circulation patterns vary over time and are very sensitive to slight shifts in the bunker position, which is nearly flat above K = 5. At times the particle motion near the dummy probe is

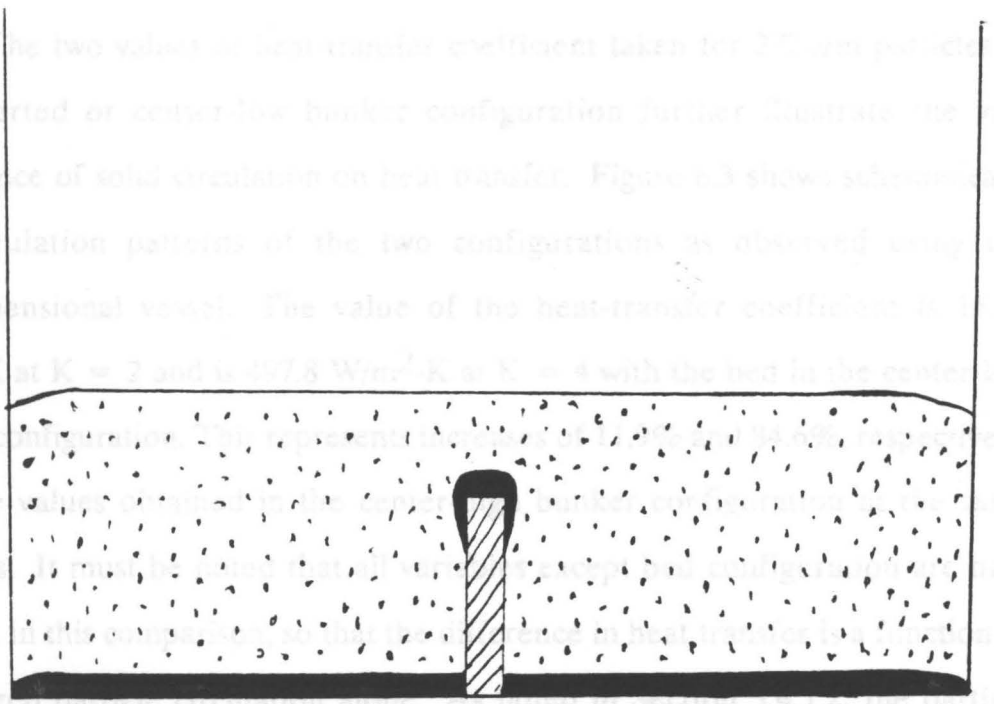

Figure 6.2. Schematic of bed separation from heater at high K: 500-μm Master Beads separate slightly from the heating surface at K = 6 during a portion of the vibrational cycle.

observed to be quite sluggish in spite of the high level of vibrational intensity. In the heat-transfer vessel, these variations in circulation are not apparent, however, since one can only observe the top of the bed. The curve of the heat-transfer coefficient for these solids shows a sharp increase with K-value up to K = 5 because the circulation improves with K-value in this region. Above this, the instabilities produce no further increase in circulation, so the heat transfer is not improved.

The two values of heat-transfer coefficient taken for 272-μm particles in the inverted or center-low bunker configuration further illustrate the vast importance of solid circulation on heat transfer. Figure 6.3 shows schematically the circulation patterns of the two configurations as observed using the two-dimensional vessel. The value of the heat-transfer coefficient is 153.2 W/m^2-K at K = 2 and is 497.8 W/m^2-K at K = 4 with the bed in the center-low bunker configuration. This represents increases of 11.9% and 84.6%, respectively, over the values obtained in the center-high bunker configuration at the same K-values. It must be noted that all variables except bed configuration are held constant in this comparison, so that the difference in heat transfer is a function of the altered particle circulation alone. As noted in Section 5.4.1.2, the particle velocity for the center-high configuration stagnates as it nears the dummy heat probe, and this effect is not noted for the center-low configuration. The particle velocity at the dummy probe is much greater in this case.

6.1.2 Heat-Transfer Coefficients for Glass Beads

Measurements of the heat-transfer coefficients are made for the glass beads in the same manner as the Master Beads. Figure 6.4 and Table 6.2 give

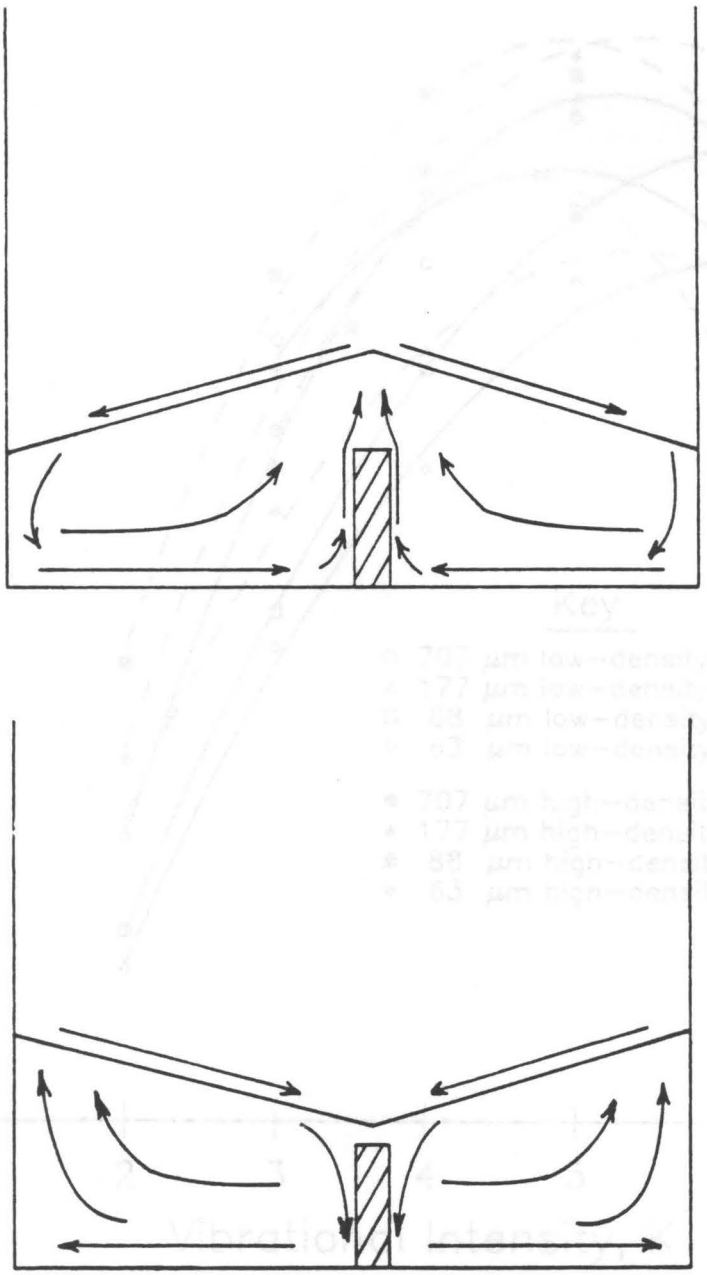

Figure 6.3. Circulation patterns for center-high and center-low bunker configurations: Schematic of observed circulation patterns for these two configurations.

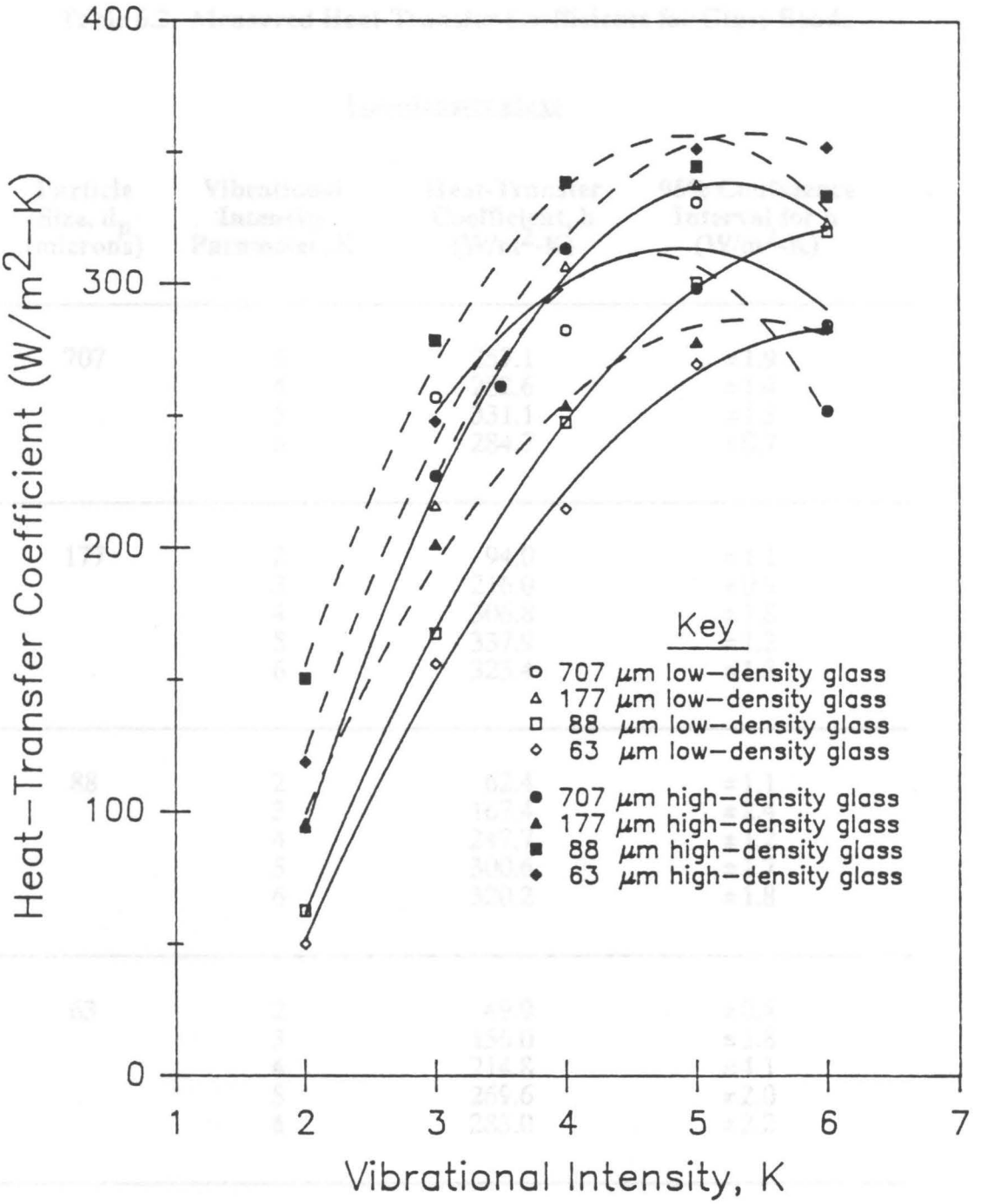

Figure 6.4. Heat-transfer coefficients for glass beads: Measured heat-transfer coefficients for glass beads *versus* K-value. Note: Open symbols are for low-density glass; closed symbols are for high-density glass.

Table 6.2. Measured Heat-Transfer Coefficients for Glass Beads

Low-density glass

Particle Size, d_p (microns)	Vibrational Intensity Parameter, K	Heat-Transfer Coefficient, h (W/m^2-K)	95% Confidence Interval for h (W/m^2-K)
707	3	257.1	±1.9
	4	282.6	±1.4
	5	331.1	±1.3
	6	284.7	±0.7
177	2	94.0	±1.1
	3	216.0	±0.9
	4	306.8	±1.8
	5	337.9	±1.2
	6	323.4	±1.3
88	2	62.4	±1.1
	3	167.4	±2.4
	4	247.7	±1.2
	5	300.6	±1.7
	6	320.2	±1.8
63	2	49.9	±0.4
	3	156.0	±1.8
	4	214.8	±4.1
	5	269.6	±2.0
	6	283.0	±2.2

(table continued on following page)

Table 6.2 (continued)

High-density glass

Particle Size, d_p (microns)	Vibrational Intensity Parameter, K	Heat-Transfer Coefficient, h (W/m^2-K)	95% Confidence Interval for h (W/m^2-K)
707	3	227.3	±5.1
	3.5	261.3	±4.6
	4	313.4	±0.8
	5	298.4	±1.5
	6	252.1	±5.6
177	2	95.5	±0.7
	3	201.4	±0.2
	4	254.2	±0.7
	5	278.2	±1.8
	6	283.9	±2.7
88	2	150.4	±1.7
	3	278.6	±0.6
	4	338.8	±1.6
	5	344.9	±0.6
	6	333.5	±0.8
63	2	118.8	±0.9
	3	248.0	±1.0
	4	313.8	±3.3
	5	351.4	±0.8
	6	352.1	±0.8

the values for four size ranges of each type of glass bead. Again, several things should be noted:

1) All solids show an initial increase of heat-transfer coefficient with increasing K.
2) All of the curves go through a maximum or show a marked decrease in the slope of the curve at high K-values.
3) For the high-density glass, the two smallest sizes (63 μm and 88 μm) give the highest heat-transfer coefficient at every value of K.
4) For the low-density glass, the same two sizes give the lowest heat-transfer coefficients at every K except 6, where the 88-μm size gives a greater value than the 707-μm size.

6.1.2.1 Comparison of Heat Transfer of Glass Beads with Master Beads

In comparison with the Master Beads of the same size, the 707-μm glass beads have slightly higher heat-transfer coefficients. This is true for every K-value in the case of the low-density beads, and for every one but K = 3 for the high-density glass. As with the Master Beads, measurements have been made at K = 1.5 and K = 2 but discarded due to inordinate spread in the bed temperatures caused by poor overall particle circulation. Unlike the Master Beads, however, a thermal steady-state could be achieved at K = 6 for both densities, even though the beds demonstrated the same unstable "rocking" caused by bed throws of greater than one cycle. These values are reported, therefore.

In the case of the 177-μm size, the values for the low-density glass and Master Beads are virtually identical up to K = 5, at which point the value for the Master Beads jump dramatically and the low-density glass levels off. The

high-density glass of the same size has comparable values at K = 2 and 3, but at higher K-values exhibits significantly lower heat transfer.

For the 88-μm size, the high-density glass has comparable heat-transfer coefficients to the Master Beads at low K-values, but levels off at K = 4 whereas the Master Beads continue to increase. The low-density 88-μm beads give consistently lower heat-transfer coefficients at all K-values. The smallest size range of glass beads, 63 μm, has no equivalent size in Master Beads. In this range, the high-density glass is consistently well above the low-density glass in the value of heat-transfer coefficient, and in fact produces the highest measured value, 352 W/m^2-K at K = 6, of any glass bead in this study. This is noteworthy since, as noted before, some previous work with different-sized particles of the same type has shown a maximum in heat-transfer coefficient at a particle size between about 100-200 μm, and then a reduction in heat-transfer coefficient with smaller particles, as is the case with the Master Beads and low-density glass beads in this study.

The heat-transfer coefficients measured for the low-density glass beads are somewhat surprising in view of the heat-transfer properties of the solid. The density, thermal conductivity, and heat capacity of low-density glass are all less than those of Master Beads. The thermal diffusivity α ($\alpha = k_s/\rho_s C_p$), which is the transport property for thermal diffusion, is nearly twenty times higher for Master Beads than low-density glass (1.3×10^{-5} m^2/s versus $7.5 \times 10^{-7} m^2/s$, using the values from Section 4.1.2). Furthermore, the thermal heat capacity ($\rho_s C_p$), another often-cited thermal property of solids, also favors Master Beads (2.75×10^6 J/m^3-K *vs.* 1.88×10^6 J/m^3-K). This property indicates the amount of heat per volume (and thus per particle for particles of equal size) a solid can transfer for a given temperature rise of the particle. In spite of this, however, the

low-density glass beads actually show better heat transfer for 707-μm particles and comparable heat transfer at most K-values for 177-μm particles.

The heat-transfer coefficients for glass beads are less easy to measure than Master Beads due to the susceptibility of the glass beads to static electricity. This causes the beads to form an insulating layer of particles over the heating probe surface, and in order to combat this, the bed has to be humidified. The humidification seems to lessen the problem, but the system for humidifying (a modified home vaporizer) is crude and may not totally rectify the problem. This may, in part, explain the poor performance of the two smallest sizes of low-density glass beads, which are the most affected by static, relative to the surprisingly good performance of the same sizes of high-density glass.

6.1.3 Possible Errors in Measured Heat-Transfer Coefficients

As with any experimental work, the values obtained for the heat-transfer coefficients are subject to errors. An examination of Equation 6.1

$$h = \frac{Q}{A_S(T_P - T_B)}$$

shows that the main areas for concern with error are the heat input into the bed, Q, and the temperature of the bed, T_B. The surface area of the heater, A_S, is very readily and accurately measured, and the probe temperature, T_P, is quite uniform. Therefore, these two quantities should not introduce any appreciable error in the values of h. The next two subsections, then, investigate the effect of errors in Q and T_B, respectively, on the measured heat-transfer coefficients.

6.1.3.1 Heat Loss from the Heating Probe

Even though the amount of heat put into the heating probe is quite accurately known, the heat-loss term can introduce error into the calculated heat-transfer coefficients. This is due to the fact that Equation 6.1 implicitly assumes that all of the heat supplied to the heater is passed to the bed through the probe surface. In fact, even though the probe is designed to reduce heat loss, some conduction to the insulating channels and probe supports is inevitable. This conduction results in the temperature of these surfaces being elevated so that they act as heat-transfer surfaces in addition to the probe surface, and also results in a lowered heat flux through the copper heat-probe surfaces. Due to the presence of the guard heaters, no heat from the heating probe is conducted out of the bed; all of the heat put into the heating probe passes to the bed, but not all via the surface of the probe.

This heat loss, in effect, causes the value of the heat-transfer coefficient which is measured to be higher than the actual heat-transfer coefficient. This effect can be analyzed mathematically, however, by making certain assumptions:

1) The epoxy which joins the copper with the Lexan at all joints has a uniform thickness of 0.1 mm, and this layer provides the only thermal resistance at the copper-Lexan junctions.
2) Since the surfaces of the channels and supports are vertical, the heat-transfer coefficient from them is the same as from the probe.
3) Since the heat-transfer coefficient to the bed is very high relative to conduction in Lexan, the upper surface of the top channel is at bed temperature (it is not a heat-transfer surface), and only the sections

of channel directly above or below the heating probe act as heat-transfer surfaces.

4) Since the channels are hollow, heat conducts into them only through an area equal to the cross-section of the walls.

5) The floor of the vessel, and thus the bottom of the bottom channel, are at bed temperature.

6) The heat fluxes into the support from the heating probe and guard heater sides are equal since the temperatures of both are held the same. This implies that the heat flux across the middle of the support is zero, and that the heating probe loses heat only to the half of the support nearest it.

7) Heat conduction in both channels occurs only in the vertical direction, and only in the horizontal direction (from heating probe end toward guard heater end) in the supports, with no temperature difference across the thickness of any Lexan piece.

A derivation of the equations necessary to correct the value of the heat-transfer coefficient, based on these assumptions, is made in the Appendix. The solution is iterative, requiring initial guesses for the heat-transfer coefficient and the temperatures of the Lexan pieces at the point closest to the heating probe. The equations converge fairly quickly, however, requiring only three or four iterations in most cases. The largest error in calculation of the heat-transfer coefficient should occur in one of two extreme cases:

1) when the heat-transfer coefficient is very high so that heat input to the probe is high, and thus heat loss is high, or

2) when the heat-transfer coefficient is low so that heat is not taken away from the probe efficiently, and thus can conduct into the Lexan more readily.

In fact, the second case produces the largest percentage of error as the following analysis shows. A good example of the first case is the 229-μm Master Beads at K = 7, which have the highest heat-transfer coefficient obtained in this study. One particular data point from this run gives the following measured values:

Average Probe Temperature	82.2° C
Average Bed Temperature	50.8° C
Heat Input to the Probe	47.0 W
Heat-Transfer Coefficient	581.6 W/m^2-K

Using the method outlined in the Appendix, the corrected value of the heat-transfer coefficient is 532.8 W/m^2-K, so that the measured value is about nine percent high relative to the corrected value. About 3.2 percent of the heat input to the probe is lost to each of the top and bottom channels, and about 1.9 percent of the heat is lost to the supports.

An example of a low heat-transfer coefficient is the 63 μm high-density glass at K = 2. Although the low-density glass gives a lower heat-transfer coefficient in the same size range, the problem of the susceptibility of the low-density glass to static electricity (as noted earlier) makes the high-density glass a more representative case. Values measured during this run give:

Average Probe Temperature	83.0° C
Average Bed Temperature	40.7° C
Heat Input to the Probe	13.0 W
Heat-Transfer Coefficient	119.1 W/m^2-K

These values lead to a corrected heat-transfer coefficient of 97.5 W/m^2-K. The measured value in this case is about 22 percent higher than the corrected value. The heat lost to the top and bottom channels and the supports is about 7, 7.2, and 3.9 percent, respectively.

An example of a heat-transfer coefficient in between these two extremes should give a more representative error. The 500-μm Master Beads at K = 3 are chosen for this purpose. The values measured for this solid are:

Average Probe Temperature	84.4° C
Average Bed Temperature	48.8° C
Heat Input to the Probe	29.3 W
Heat-Transfer Coefficient	319.9 W/m^2-K

The corrected value of the heat-transfer coefficient for this case is 283.5 W/m^2-K, which means the uncorrected value is about thirteen percent high.

The assumptions made for this analysis, for the most part, are for the worst case, so that the calculated error percentages are probably somewhat high. Assumption 2, for example, that the heat-transfer coefficient is the same for the channels as for the probe almost surely does not hold for low K-values of fine particles, as in the second case above. Observation of these particles in the two-dimensional bed with the dummy heat probe in place shows that much of the

bottom channel is adjacent to a "dead zone" in the particle circulation. This lower particle circulation for the bottom channel would lead to a lower value of h for it than for the probe, and thus less heat lost to it. As can be seen above, the heat lost to the bottom channel is the major contribution to the calculated error in the heat-transfer coefficient.

Assumption 7 is also a slightly pessimistic assumption. Assuming that the conduction in the probe supports is a one-dimensional problem greatly simplifies the analysis, but actually the thickness of the members, especially the supports, is large enough that a gradient exists. A measure of isothermality across a thickness is the Biot modulus, which compares the relative effects of convection and conduction on heat transfer. This dimensionless number is given by

$$Bi = \frac{h\ x}{k}$$

where h is the convective heat-transfer coefficient in W/m^2-K, x is a characteristic length (usually the thickness for a rectangular slab) in meters, and k is the thermal conductivity of the solid in W/m-K. Biot numbers much less than unity indicate isothermality across the thickness because the conduction is much higher than convection. Higher Biot numbers indicate that the assumption of isothermality across the solid is worse. The assumption of isothermality, and thus the analysis based on a one-dimensional approach as presented in the Appendix, should be worst for the highest Biot number. This occurs for the case of the supports (which are much thicker than the channels) at the highest convective heat transfer (*i.e.*, the 229-μm Master Beads at K = 7 presented earlier). This case is examined with two dimensional heat-transfer theory, therefore, to test the

applicability of the one-dimensional analysis.

Two-dimensional problems of this nature are addressed by VandenBerghe and Diller [1989]. In order to use their technique, the dimensions defined by Figure 6.5 are needed. Half of the support is analyzed, and the entire length is used this time, so that the boundary conditions are the same as for the case solved by VandenBerghe and Diller. The governing equation is

$$\frac{1}{w^2}\frac{\partial^2\theta}{\partial\rho^2} + \frac{1}{d^2}\frac{\partial^2\theta}{\partial\eta^2} = 0 \qquad [6.2]$$

where $\theta = \dfrac{T_P - T(\rho,\eta)}{T_P - T_B}$, $\rho = \dfrac{x}{w}$, and $\eta = \dfrac{y}{d}$.

The boundary conditions are

$$\theta = 0 \quad \text{at} \quad \rho = 0$$

$$\theta = 0 \quad \text{at} \quad \rho = 1$$

$$\frac{\partial\theta}{\partial\eta} = 0 \quad \text{at} \quad \eta = 0$$

$$\frac{\partial\theta}{\partial\eta} + Bi_d\,\theta = Bi_d \quad \text{at} \quad \eta = 1$$

(Bi_d is Biot number based on d).

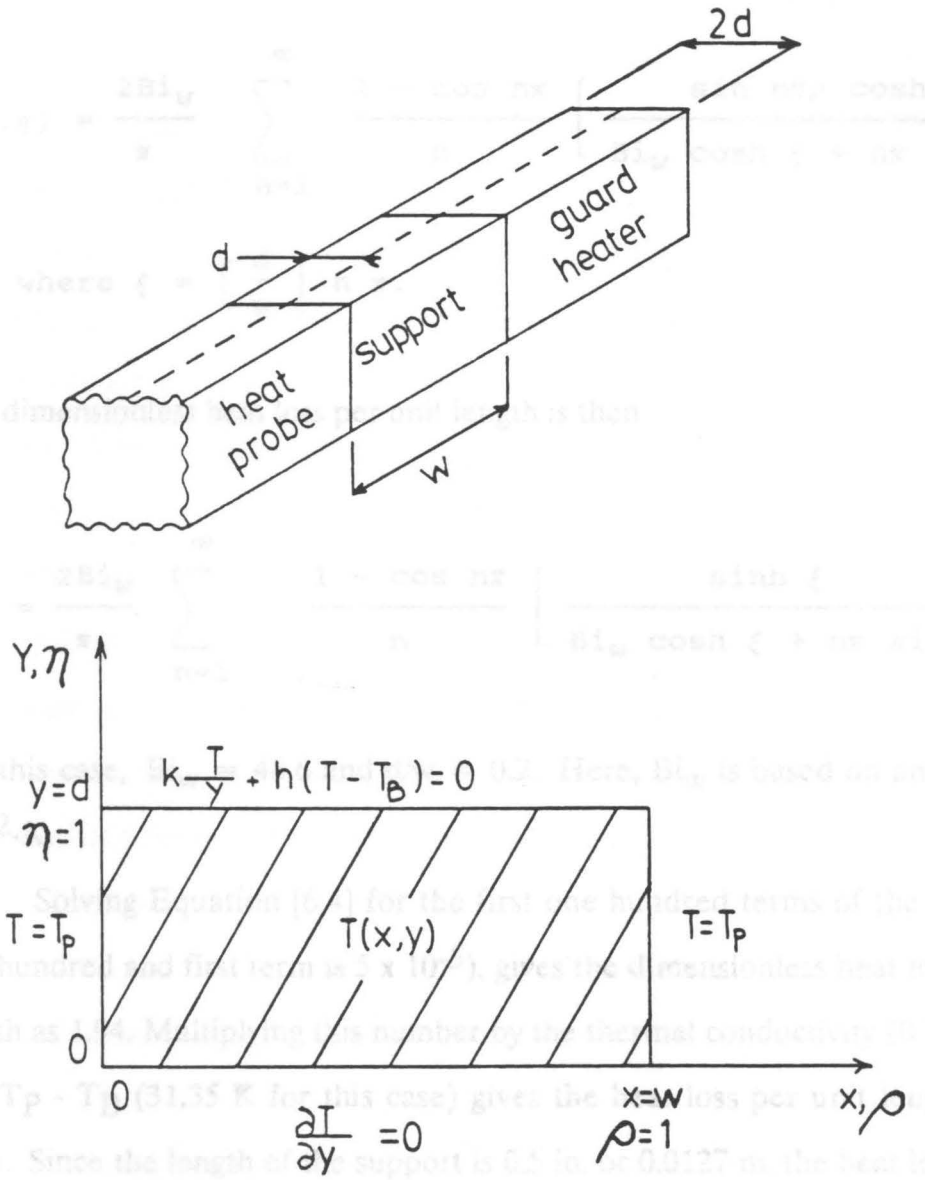

Figure 6.5. Schematic for two-dimensional heat-loss analysis: The dimensions needed (top) and coordinate system with boundary conditions (bottom) for the two-dimensional heat-loss problem. Adapted from VandenBerghe and Diller [1989].

The solution to this system is

$$\theta(\rho,\eta) = \frac{2Bi_w}{\pi} \sum_{n=1}^{\infty} \frac{1 - \cos n\pi}{n} \left[\frac{\sin n\pi\rho \cosh \xi}{Bi_w \cosh \xi + n\pi \sinh \xi} \right] \qquad [6.3]$$

$$\text{where } \xi = \left[\frac{d}{w} \right] n \pi .$$

The dimensionless heat loss per unit length is then

$$q = \frac{2Bi_w}{\pi} \sum_{n=1}^{\infty} \frac{1 - \cos n\pi}{n} \left[\frac{\sinh \xi}{Bi_w \cosh \xi + n\pi \sinh \xi} \right] \qquad [6.4]$$

For this case, Bi_w = 48.6 and d/w = 0.2. Here, Bi_w is based on an h of 581.6 w/m^2-K.

Solving Equation [6.4] for the first one hundred terms of the series (the one hundred and first term is 5 x 10^{-5}), gives the dimensionless heat loss per unit length as 1.94. Multiplying this number by the thermal conductivity (0.19 W/m-K) and T_P - T_B (31.35 K for this case) gives the heat loss per unit length as 11.5 W/m. Since the length of the support is 0.5 in. or 0.0127 m, the heat loss per half support is 0.15 W. This means the heat loss for the two halves of both supports is 0.6 W, compared to 0.88 W calculated from the one-dimensional analysis. This indicates that the one-dimensional analysis gives a value about 32 percent too high for this worst case. A similar calculation for a low heat-transfer coefficient case, that of 63-μm high-density glass at K = 2, gives a heat loss to the supports of 0.47 W for the two-dimensional case *versus* 0.51 W for the one-dimensional case.

Here the assumption of isothermality introduces only about an 8 percent additional error. Since the heat lost to the supports is the smallest contributor to total heat loss in all cases and the one-dimensional assumption is more valid for the channels due to their much smaller thickness, the one-dimensional analysis is adequate although slightly pessimistic.

As seen from the three cases presented, the error in the reported heat-transfer coefficients due to heat loss is a function of the heat-transfer coefficient. The percentage error is smaller for cases of high heat transfer and larger for low heat transfer. The range is about nine to twenty-two percent, based on the one-dimensional analysis. Since this analysis has been shown to slightly overestimate the heat loss and some of the other assumptions are for the worst case, this range is probably somewhat high. Also, the low heat-transfer case presented is somewhat unrepresentative since most of the solids used have heat-transfer coefficients at least twice as high. In light of these considerations, a more realistic range of error in heat-transfer coefficient due to heat loss is about ten to fifteen percent for most solids.

6.1.3.2 Measurement of the Bed Temperature

Vibrated beds generally do not have large temperature gradients due to solid mixing. As noted in Chapter 5, however, for some cases such as low K-values or large particles, the solid mixing is not as high and the temperature may vary at different locations within the bed. This situation is particularly true when both of these conditions are met, and it is for this reason that no heat-transfer coefficient has been reported at K = 2 for the 707-μm particles.

The bed temperature used in the calculation of the heat-transfer coefficient is the average of nine thermocouple readings. These thermocouples have been positioned throughout the bed to give a representative sampling of different circulation cells, as shown in Figure 3.3. page 96. They typically do not differ by more than a few degrees. The thermocouples nearest to the heat probe tend to give slightly higher readings, while those further away are slightly lower. The difference is generally only about ten percent of the difference between the probe temperature and the average bed temperature. If the heat-transfer coefficients were based only on the temperatures nearest the heater, they would be approximately five to ten percent higher. If they were based on the lowest temperatures, they would be approximately the same amount lower in most cases.

6.2 Comparison of Measured Values with Published Results

Values of the measured heat-transfer coefficients are compared to previously measured values under similar conditions. In the following subsection, particular attention is given to the results of Thomas [1988] obtained with a cylindrical heater under nearly identical conditions. Following that, the results of this study are compared with other published results.

6.2.1 Effect of Heater Geometry on Heat-Transfer Coefficients

As mentioned previously in Section 2.2, one of the biggest problems in comparing the results of different investigators of heat transfer in vibrated beds is the number of variables which affect heat transfer. Frequency of vibration, vibrational intensity, bed depth, heater geometry, heater orientation, solid

circulation rates and patterns, particle size and type, and vessel shape and size have all been shown to affect the heat-transfer rate, and compounding the problem is the fact that many of these variables are inter-related. This tends to make the results from any given study very dependent on the apparatus, methods, and conditions used in the study and thus of limited general or practical applicability. This study has been primarily aimed at investigating the effect of just one of these variables--heater geometry--and therefore the conditions have been held as closely as possible to those of another study, Thomas [1988], varying only the heating probe employed.

Thomas [1988] chose to investigate the heat transfer from a horizontal, cylindrical surface to a shallow vibrated bed of particles. This geometry, of course, represents one commonly encountered in heat transfer work--that of horizontal heating (or cooling) tubes. The geometry for this study has been chosen to represent another commonly encountered device, the vertical heat fin. Both heating probes are somewhat idealized cases of the devices they are intended to represent, being designed to have very isothermal surfaces and greatly reduced heat losses, but both sufficiently resemble their respective devices to be of practical interest.

Since so many of the variables are identical in the two studies, only the differences will be noted. The vessel used by Thomas was a 170-mm cylinder, whereas the vessel in this study is not quite cylindrical, but nearly so (see Figure 3.3 and description in Section 3.2.1). Also, there was a gap of 13.7 mm between Thomas' cylindrical heating probe and the vessel floor (except for in the case of the small glass beads, when a barrier was placed beneath the probe for bed stability). This study has a channel beneath the heating probe which acts as a physical barrier to particle movement beneath the probe.

Both of these alterations lead to possibly important differences in one of the previously mentioned parameters affecting heat transfer in vibrated beds--particle circulation. Thomas, however, reported "dead zones" beneath his heat probe which acted as a *de facto* barrier to particle interchange between the two halves of the bed, and actually placed a physical barrier beneath his probe for the small glass-bead work. The presence of the channel beneath the heater in this study may therefore not affect circulation as greatly as it would seem.

The effect of the other alteration, that of the slight difference in vessel geometry, is difficult to appraise. Beds of the same particles vibrated at the same K-values have very similar shapes in both vessels. In both studies, the beds have been kept almost exclusively in the center-high bunkering formation (for the particles which bunker), and the observable circulation patterns are nearly identical. Unfortunately, little can be said about the internal circulation based only on observation of the heat-transfer vessels since only the movement on the surface can be seen. To observe much about the circulation patterns, the two-dimensional vessel, which represents a cross-sectional slice of the heat-transfer vessel, must be used. Since the cross-sections of both Thomas' heat-transfer vessel and the heat-transfer vessel used in this study are the same, this technique is not useful in evaluating any possible differences in the two. On the basis of the surface observations, however, it is assumed that the slight difference in vessel geometry introduces little difference in particle circulation.

Making allowance for these two apparently minor differences, therefore, allows for a direct comparison between the results of this study and those of Thomas [1988]. Figures 6.6 and 6.7 give the results obtained by Thomas for his cylindrical probe. Table 6.3 provides a direct comparison of the results obtained by Thomas with this study. In general, the vertical-surface heater shows

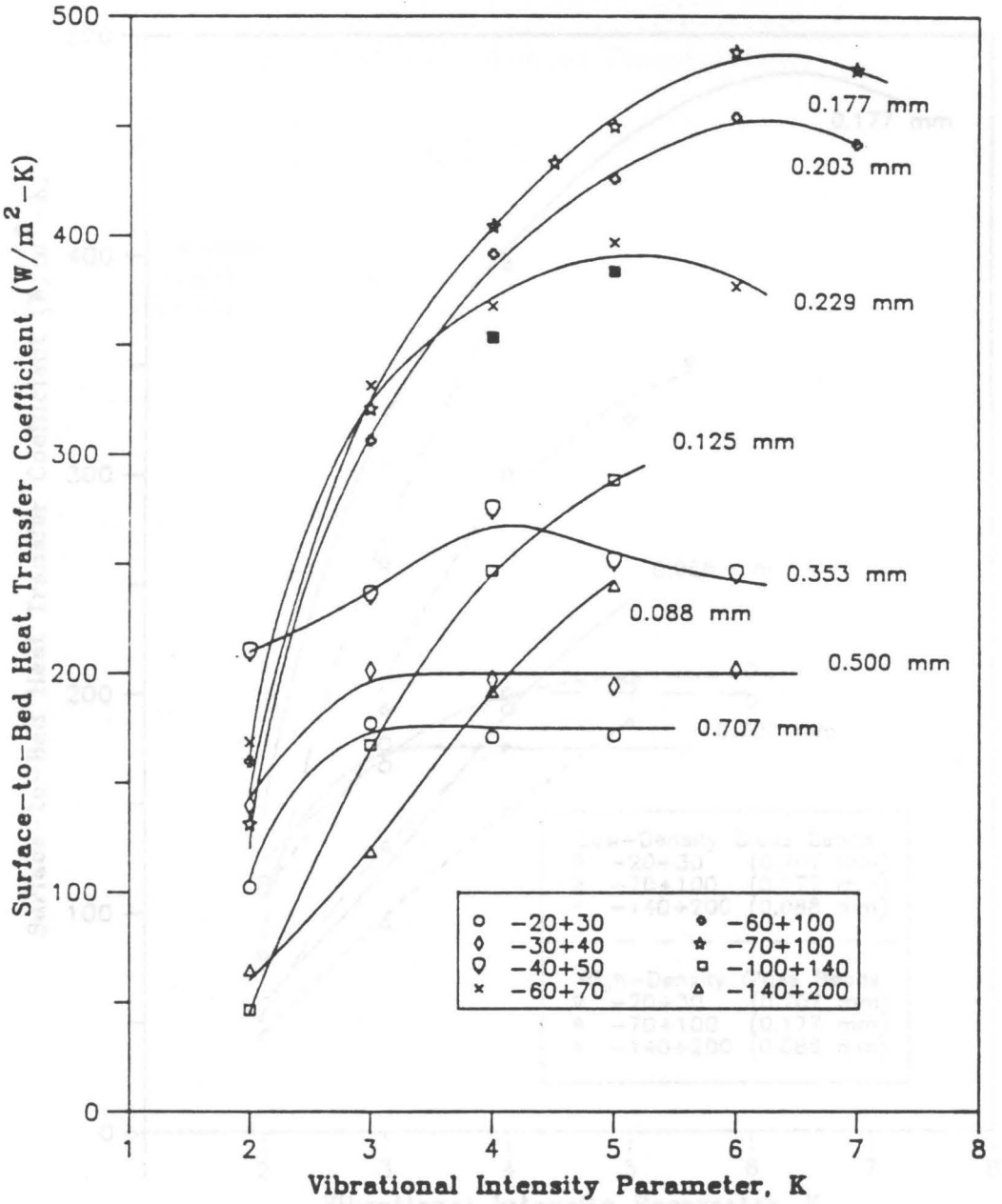

Figure 6.6. Measured heat-transfer coefficients from a horizontal cylinder to a vibrated bed of Master Beads: Heat-transfer coefficient *versus* K-value. Note: darkened squares represent data taken for 125-μm beads in the "wall-high" bunker configuration. All other data taken in the center-high configuration. From Thomas [1988].

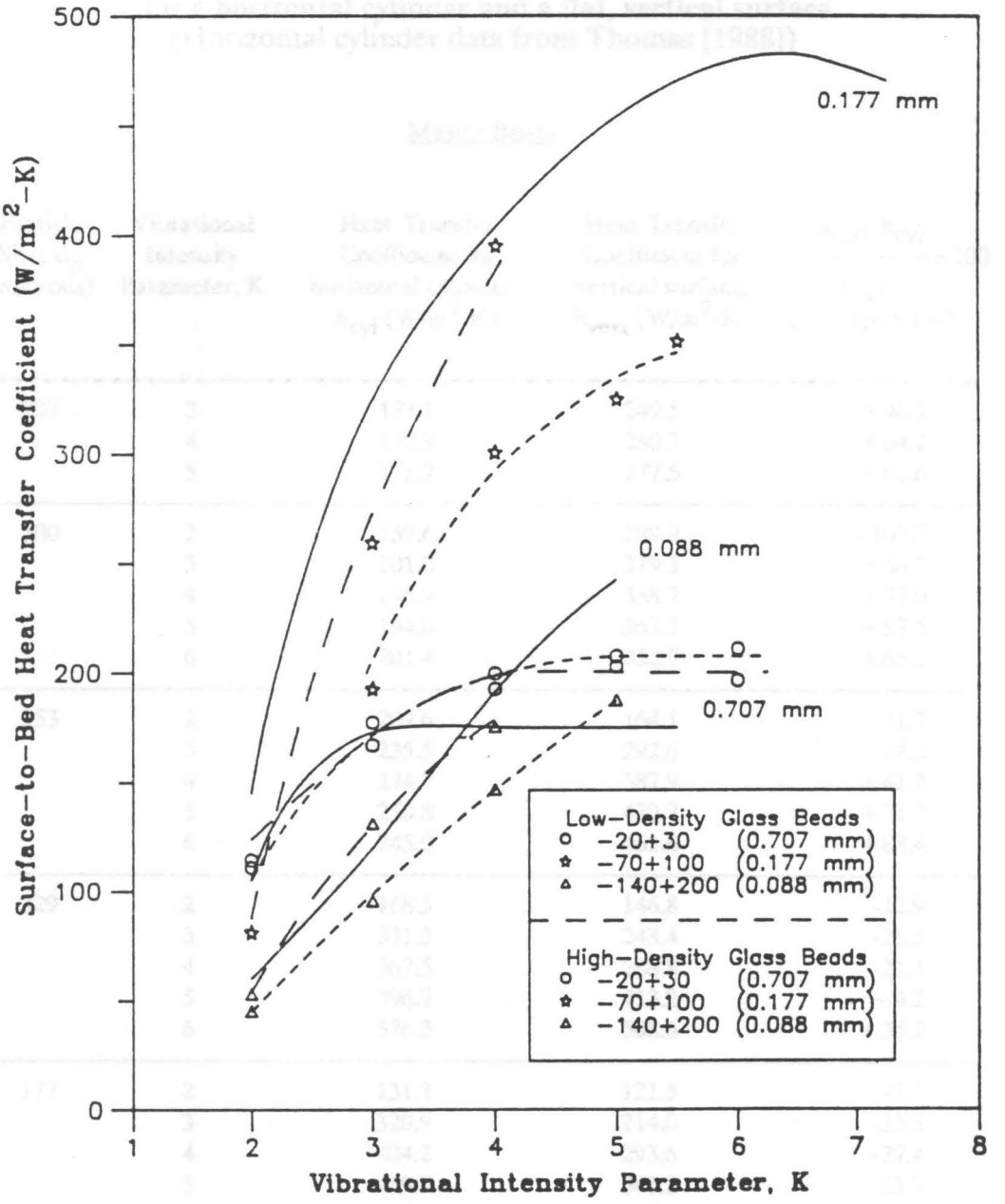

Figure 6.7. Measured heat-transfer coefficients from a horizontal cylinder to a vibrated bed of glass beads: Heat-transfer coefficient *versus* K-value. Long dashed lines are for high-density glass, short dashed lines are for low-density glass, and solid lines are for Master Beads (for comparison--data points not shown). From Thomas [1988].

Table 6.3. Comparison between measured heat-transfer coefficients for a horizontal cylinder and a flat, vertical surface
(Horizontal cylinder data from Thomas [1988])

Master Beads

Particle Size, $\bar{d}_p$ (microns)	Vibrational Intensity Parameter, K	Heat-Transfer Coefficient for horizontal cylinder, h_{cyl} (W/m^2-K)	Heat-Transfer Coefficient for vertical surface, h_{vert} (W/m^2-K)	$\frac{h_{vert}-h_{cyl}}{h_{cyl}} \times 100$ (percent)
707	3	177.1	249.5	+40.9
	4	170.9	280.7	+64.2
	5	171.7	277.5	+61.6
500	2	139.6	289.9	+107.7
	3	201.2	319.3	+58.7
	4	196.9	338.7	+72.0
	5	194.0	363.7	+87.5
	6	201.4	332.7	+65.2
353	2	209.6	164.1	-21.7
	3	235.5	292.6	+24.2
	4	274.7	387.9	+41.2
	5	250.8	430.7	+71.7
	6	245.0	461.6	+88.4
229	2	168.5	146.8	-12.9
	3	331.3	243.4	-26.5
	4	367.5	288.8	-21.4
	5	396.7	413.2	+4.2
	6	376.3	508.6	+35.2
177	2	131.3	121.5	-7.5
	3	320.9	214.0	-33.3
	4	404.2	293.6	-27.4
	5	449.9	343.2	-23.7
	6	483.7	374.1	-22.6
	7	475.6	544.6	+14.5

(table continued on following page)

Table 6.3 (continued)

Particle Size, $\bar{d}_p$ (microns)	Vibrational Intensity Parameter, K	Heat-Transfer Coefficient for horizontal cylinder, h_{cyl} (W/m^2-K)	Heat-Transfer Coefficient for vertical surface, h_{vert} (W/m^2-K)	$\frac{h_{vert}-h_{cyl}}{h_{cyl}} \times 100$ (percent)
Master Beads				
125	2	46.2	102.9	+122.7
	3	167.2	249.0	+48.9
	4	246.7	381.8	+54.8
	5	288.2	431.1	+49.6
88	2	64.2	100.7	+56.8
	3	118.4	246.5	+103.1
	4	191.5	369.4	+92.9
	5	239.8	421.8	+75.9
Low-density glass				
707	3	177.3	257.1	+45.0
	4	192.6	282.6	+46.7
	5	207.3	331.1	+59.7
	6	210.7	284.7	+35.1
177	3	192.6	216.0	+12.1
	4	300.9	306.8	+2.0
	5	325.0	337.9	+4.0
88	2	44.8	62.4	+39.3
	3	95.4	167.4	+75.5
	4	146.6	247.7	+69.0
	5	187.2	300.6	+60.6
High-density glass				
707	3	166.9	227.3	+36.2
	4	199.6	313.4	+57.0
	5	202.8	298.4	+47.1
	6	196.3	252.1	+28.4
117	2	81.0	95.5	+17.9
	3	259.5	201.4	-22.4
	4	395.2	254.2	-35.7
88	2	52.7	150.4	+185.4
	3	131.1	278.6	+112.5
	4	175.2	338.8	+93.4

significant improvement in heat transfer over the cylindrical heater for large particles ($\overline{d}_p \geq 350\ \mu m$) and small particles ($\overline{d}_p \leq 125\ \mu m$), but for the intermediate range ($125\ \mu m < \overline{d}_p < 350\ \mu m$), the improvement is small or else the cylindrical heater is actually better.

In the case of the large particles, this trend can be explained in terms of the air gaps which form around horizontal surfaces placed in vibrated beds. These gaps have been noted not only by Thomas [1988], but also by Sprung [1987], Bukareva et al. [1969], Muchowski [1980], and others. Elimination of such gaps is one of the main reasons for the selection of the vertical surface in this study. As shown in Figure 6.8, these gaps form above and below the cylindrical probe during a portion of the vibrational cycle and constitute an additional resistance to heat transfer.

Thomas, in fact, explained the shape of his heat-transfer curves, nearly all of which either go through a maximum or hit a plateau and level out (except for the particles which had bed stability problems at higher K-values), as primarily due to two opposing effects. As the vibrational intensity is increased for a given particle size, the particle circulation is increased which improves heat transfer, but at the same time the size of the air gaps is increased which is detrimental to heat transfer. Thomas estimated that the average fractional coverage of his heat probe by air gaps reached its maximum value at $K = 3$ and remained fairly constant at higher K-values for the 707-μm particles. Since these large particles exhibit very little overall circulation, as noted earlier, their heat-transfer curves directly reflect the growth and then leveling off of the air-gap coverage. With the vertical-surface heater, no gaps form except for at very high K-values. This heating probe thus demonstrates appreciably better heat transfer at all values of K for the larger particles.

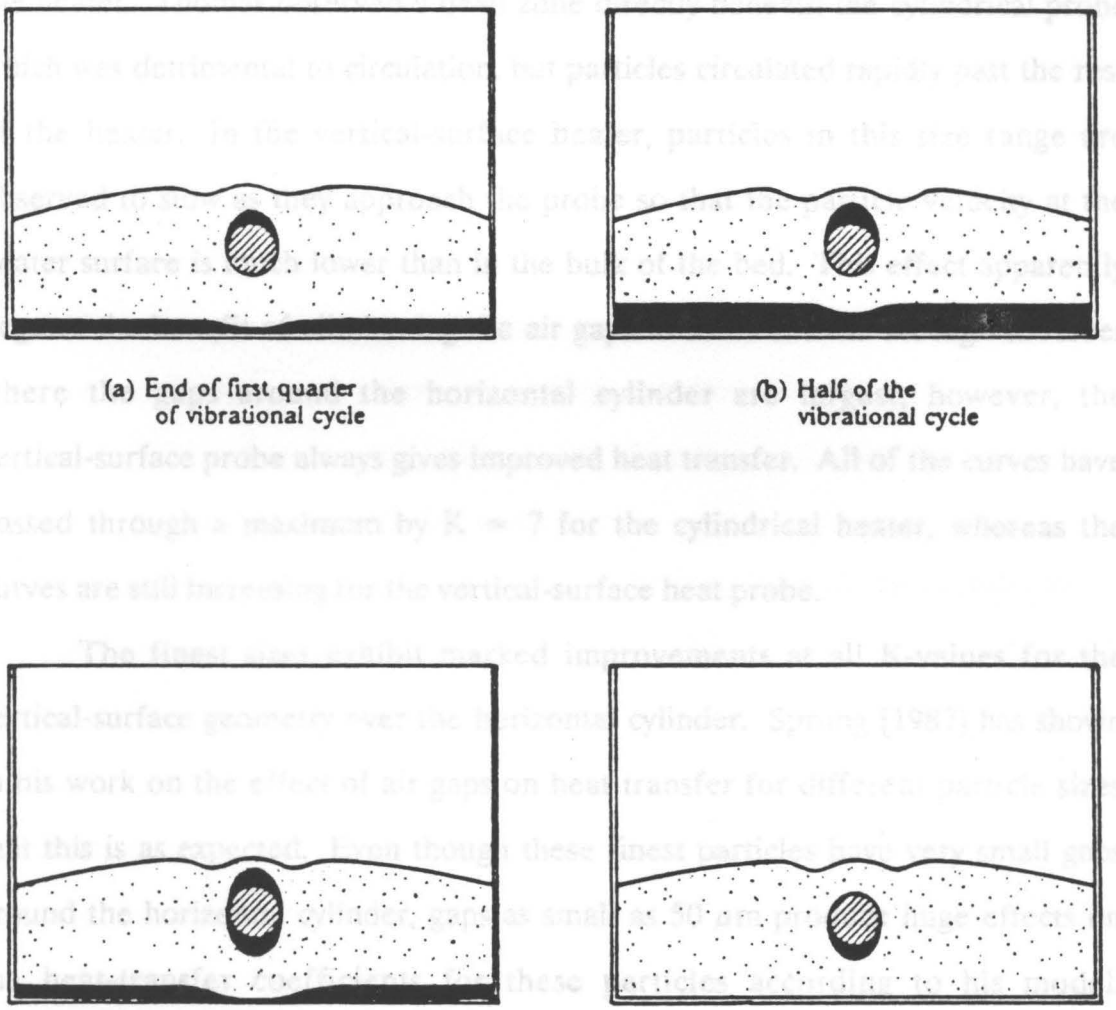

Figure 6.8. Formation of air gaps around a horizontal, cylindrical surface: Air-gap formation in a vibrated bed of 707-μm Master Beads at K = 4. Air gaps are the dark region at the vessel floor and near the dummy heat probe. From Sprung [1987].

The explanation of the comparison between the two geometries for the medium-sized particles can be found in the particle circulation in the vicinity of the heater. Thomas observed a dead zone directly beneath the cylindrical probe which was detrimental to circulation, but particles circulated rapidly past the rest of the heater. In the vertical-surface heater, particles in this size range are observed to slow as they approach the probe so that the particle velocity at the heater surface is much lower than in the bulk of the bed. This effect apparently negates the benefit of eliminating the air gaps to some extent. At high K-values where the gaps around the horizontal cylinder are largest, however, the vertical-surface probe always gives improved heat transfer. All of the curves have passed through a maximum by K = 7 for the cylindrical heater, whereas the curves are still increasing for the vertical-surface heat probe.

The finest sizes exhibit marked improvements at all K-values for the vertical-surface geometry over the horizontal cylinder. Sprung [1987] has shown in his work on the effect of air gaps on heat transfer for different particle sizes that this is as expected. Even though these finest particles have very small gaps around the horizontal cylinder, gaps as small as 50 μm produce huge effects on the heat-transfer coefficients for these particles according to his model. Therefore, the elimination of gaps by the vertical-surface probe improves heat transfer in spite of the observed sluggish circulation for these fine particles.

6.2.2 Comparison with Other Results

Many other investigators have measured heat-transfer coefficients in vibrated beds. Of course, this study is not nearly as similar in terms of the parameters which affect heat transfer with any other study as it is with the

Thomas [1988] study, but a couple of other investigations warrant comment. Bukareva *et al.* [1969] and Gutman [1976b] both report results of heat transfer from a vertical flat heater to a vibrated bed of solids.

The Bukareva *et al.* [1969] study was conducted with quartz sand of 280-355 μm. They investigated the effect of vibrational frequency on heat transfer, reporting values obtained between 25 and 60 Hz. The bed depth used was 70 mm and the vessel had an inside diameter of 110 mm, so both the depth and L/D were appreciably greater than those in this study. Gutman [1976b] reported results for several size ranges of glass ballotini at 20 and 50 Hz with a bed depth of 80 mm and a vessel diameter of 150 mm. Again, both bed depth and L/D were greater than those in this study.

As shown in Figure 6.9, the results published in these two papers agree well with results from this study in spite of the differences in conditions. From the Bukareva *et al.* [1969] study, the curves reported for 25 and 30 Hz are plotted; the curves at 20 Hz for 90-135 μm and 210-325 μm ballotini are plotted from the Gutman study. The intermediate-sized particles (177 μm) of both densities of glass are plotted from this study. It can be seen that both curves fall between the curves for the other two studies.

Note that the range of vibrational intensities reported is rather narrow, but that all of the curves increase monotonically over this range. The curve at 30 Hz from the Bukareva *et al.* [1969] study appears to be leveling off, but it should be noted that they drew a curve through the points as if it were not in their paper. All of the curves shown in Figure 6.9 resulted from a second-order regression of the data. Neither of the two studies reported a maximum in heat-transfer coefficient for the vertical heater over the range of vibrational intensities studied, which agrees with the results from this study over the same range.

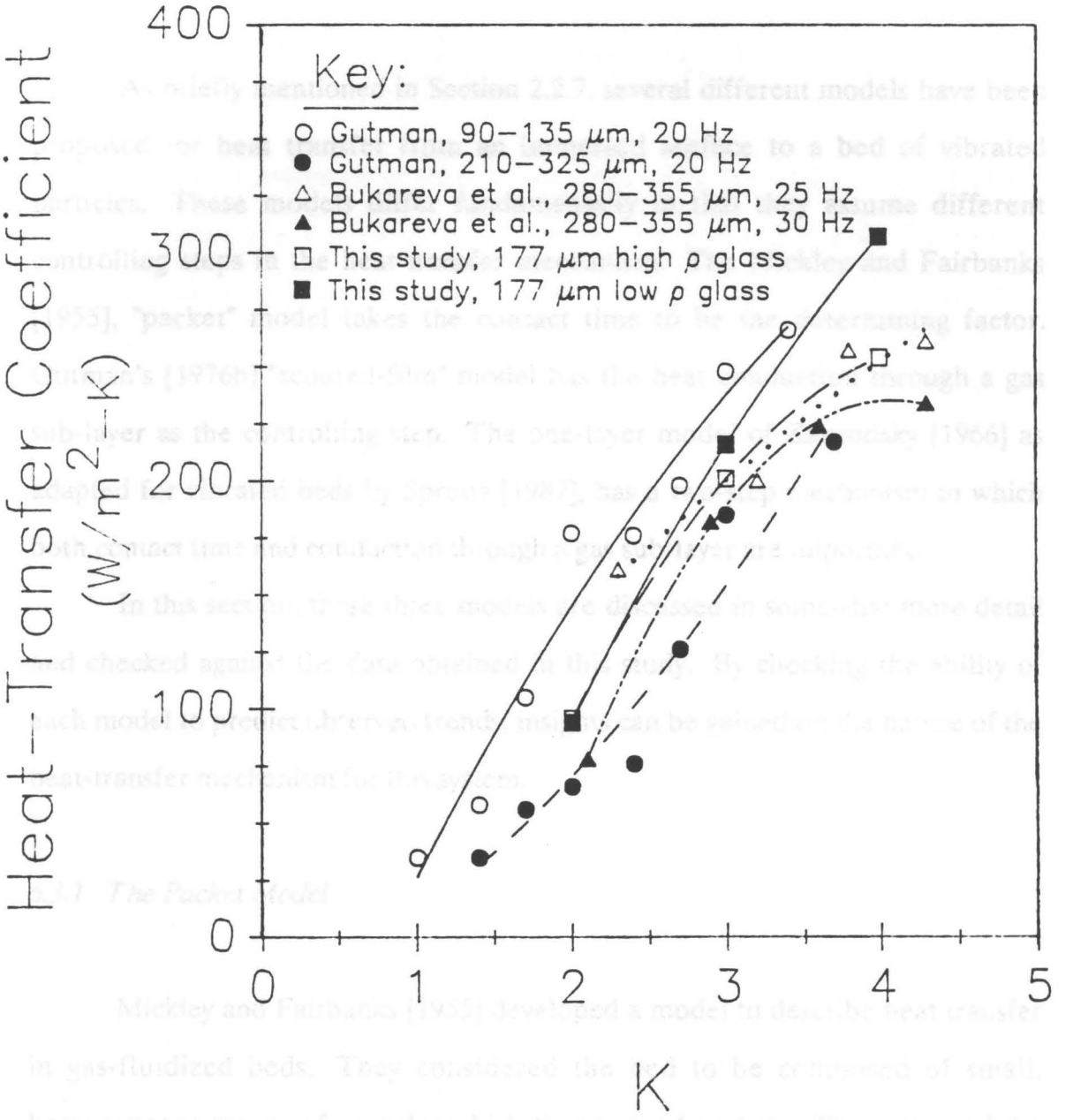

Figure 6.9. Comparison of heat-transfer coefficient data taken with flat, vertical-surface heaters: Plots of data from three studies. Particles in the Gutman [1976b] study were glass spheres, particles in the Bukareva *et al.* [1969] study were quartz sand, and particles plotted from this study are glass beads of two densities. Data from Gutman [1976b], and Bukareva *et al.* [1969].

6.3 Comparison of Results with Theoretical Models

As briefly mentioned in Section 2.2.7, several different models have been proposed for heat transfer from an immersed surface to a bed of vibrated particles. These models differ fundamentally in that they assume different controlling steps in the heat-transfer mechanism. The Mickley and Fairbanks [1955], "packet" model takes the contact time to be the determining factor. Gutman's [1976b] "scoured-film" model has the heat conduction through a gas sub-layer as the controlling step. The one-layer model of Zabrodsky [1966] as adapted for vibrated beds by Sprung [1987], has a two-step mechanism in which both contact time and conduction through a gas sub-layer are important.

In this section, these three models are discussed in somewhat more detail and checked against the data obtained in this study. By checking the ability of each model to predict observed trends, insights can be gained on the nature of the heat-transfer mechanism for this system.

6.3.1 The Packet Model

Mickley and Fairbanks [1955] developed a model to describe heat transfer in gas-fluidized beds. They considered the bed to be composed of small, homogeneous groups of particles which they termed packets. They assumed the void fraction, density, heat capacity, and thermal conductivity of the packet to be that of the bed at rest. They noted that such packets need not be permanent, but merely exist for some finite amount of time.

For a packet at temperature T_B and a flat surface at temperature T_P, the unsteady-state diffusion of heat into the packet after contact time τ is

$$Q_m = \frac{A_m}{\sqrt{\pi}} \sqrt{k_m \rho_m C_m} \; \tau^{-\frac{1}{2}} \left[T_P - T_B \right] \qquad [6.5]$$

where Q is the instantaneous rate of heat flow, A is the contact area, k is the thermal conductivity, ρ is the density, C is the heat capacity, and the subscript m refers to properties of the packet. The local, instantaneous heat-transfer coefficient h_i is given by

$$h_i = \frac{Q_m}{A_m (T_P - T_B)} = \frac{1}{\sqrt{\pi}} \sqrt{k_m \rho_m C_m} \; \tau^{-\frac{1}{2}} \qquad [6.6]$$

The problem now becomes one of finding an expression for τ so that Equation [6.6] can be integrated to give an average heat-transfer coefficient. To do this, Mickley and Fairbanks defined a local heat-transfer coefficient, h_x, by the equation

$$h_x = \int_0^\infty h_i(\tau) \; \psi \; (\tau) \; d\tau \qquad [6.7]$$

where $\psi(\tau)$ represents the fraction of total time the heating surface is in contact with packets of ages between τ and $\tau + d\tau$. Defining a local stirring factor, S_x, as

$$S_x = \frac{1}{\pi} \left[\int_0^\infty \tau^{-\frac{1}{2}} \; \psi \; (\tau) \; d\tau \right]^2 \qquad [6.8]$$

allows Equations [6.6] and [6.7] to be reduced to

$$h_x = \sqrt{k_m \rho_m c_m S_x} \qquad [6.9]$$

Fortunately, the vertical flow pattern observed near the heater in this study leads to a very simple expression for S_x which has been solved by Mickley and Fairbanks. For the situation shown in Figure 6.10 (which is the observed flow pattern in this study),

$$S_x^{\frac{1}{2}} = \frac{1}{\sqrt{\pi}} \int_0^{\infty} \tau^{-\frac{1}{2}} \psi(\tau)\, d\tau = \frac{1}{\sqrt{\pi}} \left[\frac{v}{x} \right]^{\frac{1}{2}} \qquad [6.10]$$

Equation [6.9] now becomes

$$h_x = \frac{1}{\sqrt{\pi}} \sqrt{k_m \rho_m c_m} \left[\frac{v}{x} \right]^{\frac{1}{2}} \qquad [6.11]$$

The average heat-transfer coefficient is obtained by integrating this local heat-transfer coefficient over the length, L, of the heater. This leads to

$$h = \frac{1}{L} \int_0^{L} h_x\, dx = \frac{2}{\sqrt{\pi}} \sqrt{k_m \rho_m c_m} \left[\frac{v}{L} \right]^{\frac{1}{2}} \qquad [6.12]$$

Equation [6.12] can now be used to calculate heat-transfer coefficients based on data taken in this study. If the packet properties are taken to be the sum of the solid properties times 1 - ε and the gas properties (taken as air at 85° C) times ε, for an assumed voidage of 0.41, these are

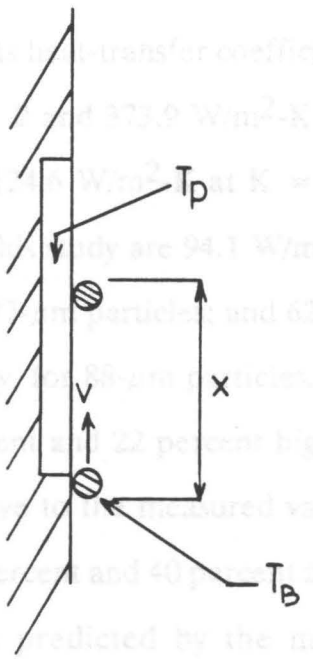

Figure 6.10. Schematic for vertical flow of a packet past a heated surface: Adapted from Mickley and Fairbanks [1955].

k_m = 0.84 W/m-K

ρ_m = 1475.4 kg/m^3

C_m = 750.1 J/kg-K

for low-density glass. Estimates of a vertical particle velocity at the heater surface are reported for low-density glass of 177 and 88 μm at K = 2 and 4 in Section 5.4.1.2. Assuming that the particle velocities correspond to packet velocities allows for calculation of the heat-transfer coefficients at these conditions.

This model predicts heat-transfer coefficients for 177-μm low-density glass of 152.6 W/m^2-K at K = 2 and 373.9 W/m^2-K at K = 4. The values predicted for 88-μm particles are 124.6 W/m^2-K at K = 2 and 348.1 W/m^2-K at K = 4. The values measured in this study are 94.1 W/m^2-K and 306.8 W/m^2-K at K = 2 and 4, respectively, for 177-μm particles; and 62.4 W/m^2-K and 247.7 W/m^2-K at K = 2 and 4, respectively, for 88-μm particles. This model, therefore, predicts values which are 62 percent and 22 percent high for 177-μm particles at K = 2 and 4, respectively, relative to the measured values. The percent errors for the 88-μm particles are 100 percent and 40 percent at K = 2 and 4, respectively.

While the trends predicted by the model are correct (*i.e.*, that the heat-transfer coefficient increases with K-value in both cases and the heat-transfer coefficient is less for 88-μm particles than 177-μm particles), the consistently large overprediction by the model seems significant. Although the estimates of particle velocities at the heater surface are crude, since the particle velocities have a square-root dependence in this model, it is unlikely that these estimates produce errors as large as those calculated. Therefore, it appears that this model neglects a resistance to heat transfer which generally reduces the rate at which heat is transferred. The obvious resistance which is not included in this

model is the conduction through a gas sub-layer to the packet. Although Mickley and Fairbanks explicitly stated that they observed no significant resistance by a gas film in their work on gas-fluidized heat transfer, it appears from this study that conduction through a gas film as well as reduction in contact time may be important for heat transfer in vibrated beds.

6.3.2 The Scoured-Film Model

Gutman [1974, 1976b] proposed a model for heat transfer in vibrated beds predicated on the gas sub-layer between the heater and nearest particles forming the major resistance to heat transfer. He rejected the Mickley and Fairbanks model described above based on his observations of particle velocities at the vessel walls which were far too low to give the heat-transfer coefficients he measured. He did not report measuring particle velocities at the heater surface.

Gutman assumed that at the heating surface, the average distance between particles touching the wall was d_r in both the horizontal and vertical directions for a static bed (see Figure 6.11). For these particles, the air film is thin and (he assumed) proportional to the particle diameter, d_p. The thickness of the film for these particles in contact with the wall can then be represented by $c_1 d_p$, with c_1 a constant. He also assumed that the projected area of the particle on the heater surface can be approximated by a square d_p x d_p. Between these hypothetically evenly-spaced contacting particles, the air film is much thicker, as seen in Figure 6.11a. He designated this thickness δ_o. With these assumptions, he calculated the average air-film thickness, $\overline{\delta}_{st}$ over the entire heater surface for a static bed to be

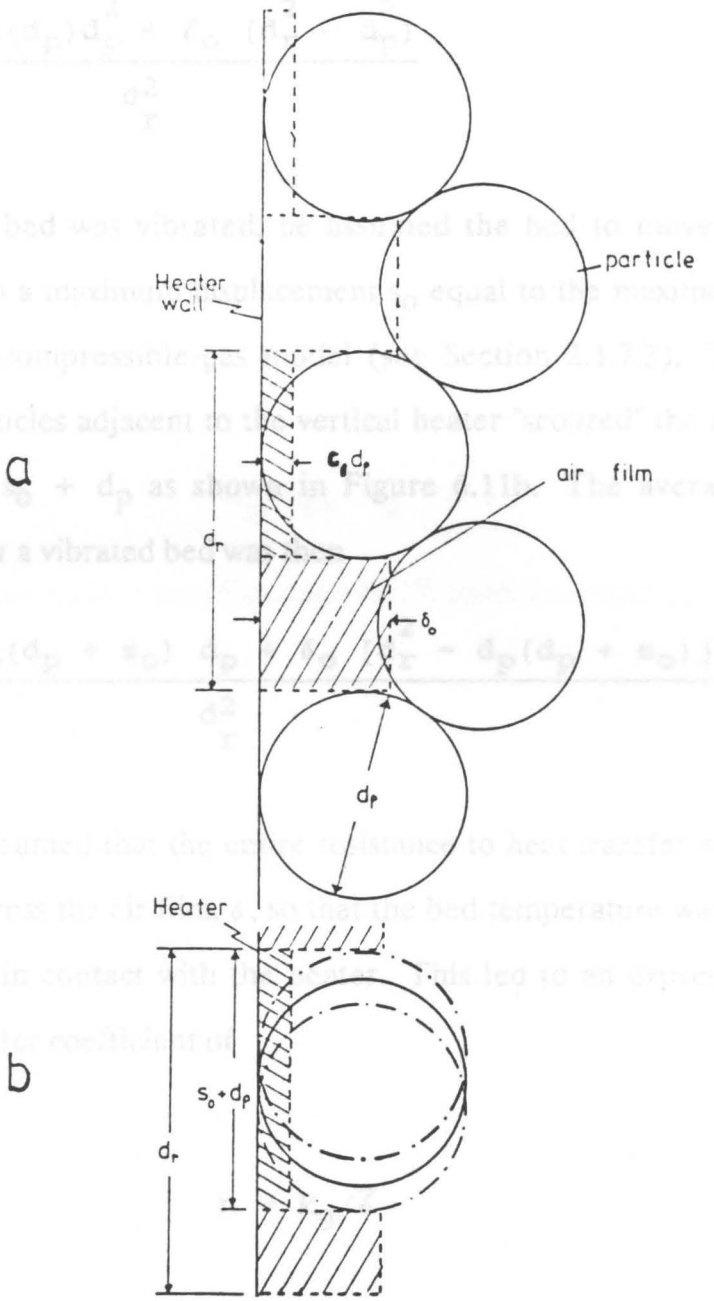

Figure 6.11. Packing of spherical particles next to a vertical heater: a) static particle bed; b) vibrated bed with particle moving up and down past the surface, "scouring" the gas sub-layer. Notation: d_p = particle diameter; $c_1 d_p$ = sub-layer thickness of particles in contact with the wall; d_r = the assumed particle spacing; δ_o = sub-layer thickness of closest particles not in contact with the wall; and s_o is the maximum bed displacement. From Gutman [1974].

$$\overline{\delta}_{st} = \frac{(c_1 d_p) d_p^2 + \delta_o \, (d_r^2 - d_p^2)}{d_r^2} \qquad [6.13]$$

When the bed was vibrated, he assumed the bed to move as a single, porous piston with a maximum displacement s_o equal to the maximum floor gap predicted by his compressible-gas model (see Section 2.1.7.3). This vertical motion of the particles adjacent to the vertical heater "scoured" the air film for a vertical distance $s_o + d_p$ as shown in Figure 6.11b. The average air- film thickness, $\overline{\delta}_{vib}$, for a vibrated bed was then

$$\overline{\delta}_{vib} = \frac{c_1 d_p (d_p + s_o) \; d_p + \delta_o \, [d_r^2 - d_p (d_p + s_o)]}{d_r^2} \qquad [6.14]$$

Next, he assumed that the entire resistance to heat transfer resulted from the conduction across the air film, δ, so that the bed temperature was isothermal, even in the layer in contact with the heater. This led to an expression for the average heat-transfer coefficient of

$$h = k_g / \overline{\delta} \qquad [6.15]$$

where k_g is the thermal conductivity of the gas and $\overline{\delta}$ is the average sub-layer thickness. Combining Equations [6.13], [6.14], and [6.15] allowed him to write an expression for the relation between the heat-transfer coefficients for vibrated and static beds:

$$h_{vib} = h_{st}/(1 - c_2 s_o) \qquad [6.16]$$

where

$$c_2 = \frac{d_p(1 - c_1 d_p h_{st}/k_g)}{d_r^2 - d_p^2} \qquad [6.17]$$

His data showed that

$$d_p/h_{st}\ k_g << 1,$$

and since c_1 is small, he reasoned Equation [6.17] could be approximated by

$$c_2 \approx d_p/(d_r^2 - d_p^2) \qquad [6.18]$$

Also, for $c_2 s_o << 1$, he noted that Equation [6.16] can be approximated by

$$h_{vib} = h_{st}\ (1 + c_2 S_o) \qquad [6.19]$$

He concluded from Equation [6.19] that since h_{st} and c_2 are constant for a given particle, h_{vib} should be a linear function of the peak gap height.

This model does not lend itself well to prediction of heat-transfer coefficients since d_r (the distance between particles in contact with the wall), which is needed to calculate c_2, is unknown. Gutman obtained values for c_2 from an experimental fit of his data. Also, some of the logic in the derivation seems faulty since the assumption that $c_2 s_o << 1$, which is necessary to transform Equation [6.16] into Equation [6.19], also implies (from Equation [6.19]) that h_{vib}

$\approx h_{st}$. This certainly is not the case, and his data show h_{vib} to be eight times h_{st} at K-values as low as 4. In light of this, no attempt is made to quantitatively predict results from this model.

The trends which he reports show an increase in heat-transfer coefficient with decreasing particle diameter, and also an increase in heat transfer with increasing K-value. Both of these trends agree with those noted in this study. However, an increase in K-value does more than merely increase s_o. Observations in this study (and many others) indicate that increasing vibrational intensity generally increases particle circulation rates. Increased circulation rates lead to decreased contact times at the heater surface. Therefore, even though his derivation neglects the effect of particle contact time with the heater surface, his results do not preclude that contact times are important in vibrated-bed heat transfer due to the fact that increased vibrational intensity not only scours the gas film more efficiently, but also increases particle circulation.

6.3.3 The One-Layer Model

Zabrodsky [1966] proposed a model for heat transfer from an immersed surface to a gas-fluidized bed which had a two-part mechanism. This model accounted for the resistance due to conduction through a gas sub-layer as well as for contact time. Sprung [1987] adapted this model to vibrated-bed heat transfer, and it is his analysis presented here. In this model, it is assumed that heat is transferred only from the heater to the nearest layer of particles (and hence the name). The gas sub-layer between the particles and the heater, as well as the rate of exchange of particles in the first layer with the bulk of the bed, determine the rate of heat transfer.

Figure 6.12 depicts this model schematically. Note that Sprung [1987] used a horizontal, cylindrical heater and thus b in the figure represents the additional air gap he noted around his heater. This additional air gap is not relevant to the vertical-surface geometry. Also note that the model is derived based only on v_n, which is the component of particle velocity normal to the heater surface.

From Sprung's analysis, the amount of heat dQ transferred in time dt can be expressed as

$$dQ = \frac{k_g}{\delta_g} \frac{\pi d_p^2}{4} \left[T_P - T_{par}\right] dt = C_s \rho_s \frac{\pi d_p^2}{6} dT_{par} \qquad [6.20]$$

where k_g is the thermal conductivity of the gas, δ_g is the thickness of the gas sub-layer, d_p is the particle diameter, T_p is the temperature of the heating probe, T_{par} is the temperature of the particles in the first layer, C_s is the heat capacity of the solid, and ρ_s is the density of the solid. Next, Sprung integrated over the time that the particle stayed in the first layer and rearranged the result to give

$$T_{par} - T_B = (T_p - T_B) \left[1 - \exp \left[\frac{-1.5\ k_g}{\delta_g C_s \rho_s d_p} \tau \right] \right] \qquad [6.21]$$

where T_B is the temperature in the bulk of the bed and τ is the residence time in the first layer (or contact time). For a dense, cubic packing of spheres, the particle spacing d is given by

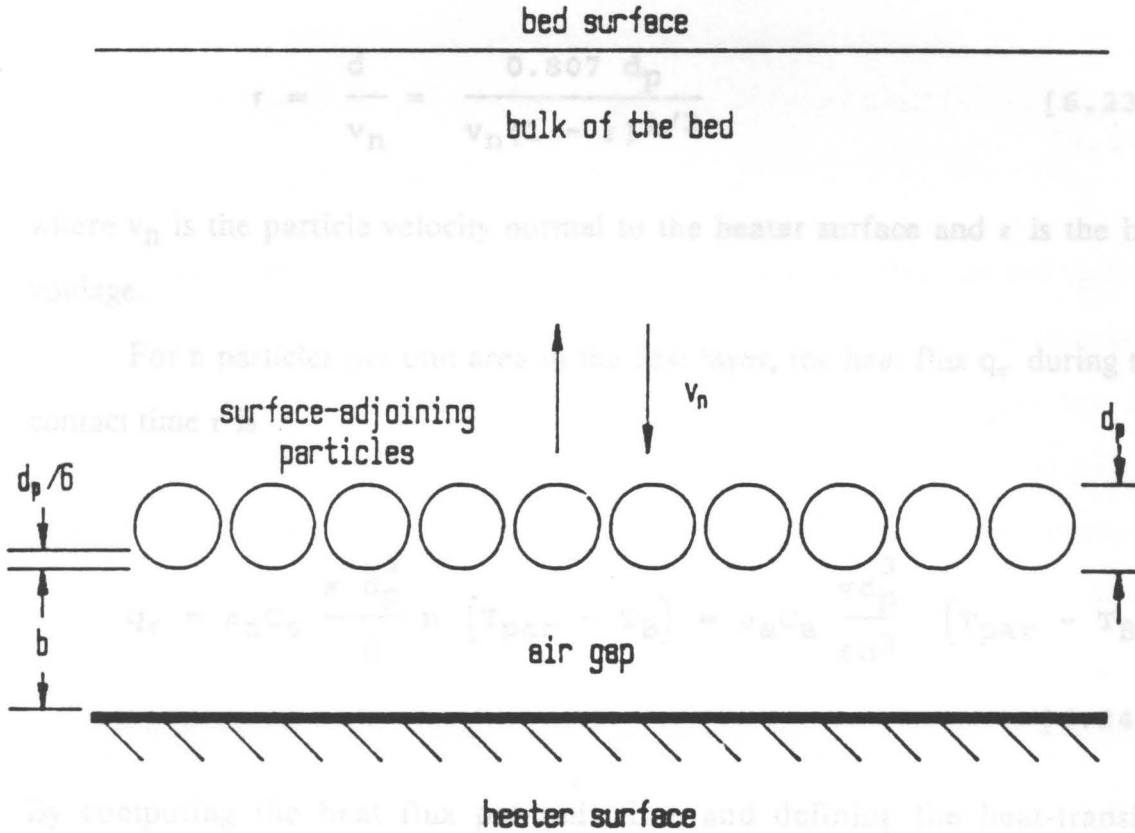

Figure 6.12. Schematic representation of the one-layer model: Representation of the one-layer model as presented by Sprung [1987]. Notation: d_p = particle diameter; b = air-gap thickness; v_n = particle velocity normal to heater surface; $d_p/6$ = air sub-layer thickness. Adapted from Sprung [1987].

$$d = d_p \left[\frac{1 - 0.476}{1 - \varepsilon} \right]^{1/3} = \frac{0.807\ d_p}{(1 - \varepsilon)^{1/3}} \qquad [6.22]$$

The contact time is related to the particle spacing (and thus the particle diameter) by

$$\tau = \frac{d}{v_n} = \frac{0.807\ d_p}{v_n(1 - \varepsilon)^{1/3}} \qquad [6.23]$$

where v_n is the particle velocity normal to the heater surface and ε is the bed voidage.

For n particles per unit area in the first layer, the heat flux q_τ during the contact time τ is

$$q_\tau = \rho_s C_s \frac{\pi\ d_p^3}{6}\ n \left[T_{par} - T_B\right] = \rho_s C_s \frac{\pi d_p^3}{6d^2} \left[T_{par} - T_B\right] \qquad [6.24]$$

By computing the heat flux per unit time and defining the heat-transfer coefficient h for the temperature difference between the heater and the bulk of the bed, Sprung derived

$$h = \rho_s C_s v_n\ (1 - \varepsilon) \left[1 - \exp\left[\frac{-1.2\ k_g}{\delta_g \rho_s C_s v_n (1-\varepsilon)^{1/3}} \right]\right] \qquad [6.25]$$

There is a problem in the direct application of this model to the current study, however. The model assumes that particle renewal occurs in the direction normal to the heater surface, but observation of particle circulation in the system indicates that particle flow in the vicinity of the heater is parallel to the surface. Sprung suggests that for this case

$$\tau = \frac{L}{v_p} \qquad [6.26]$$

where L is the dimension of the heater over which the particles pass and v_p is the particle velocity parallel to the surface. This approach leads to calculated heat-transfer coefficients which are far lower than those measured, however. For the case of 177-μm low-density glass at K = 4, this model predicts a heat-transfer coefficient of only 119 W/m^2-K which is much less than half of the measured value of 306.8 W/m^2-K. For the same particles at K = 2, the predicted value is more than an order of magnitude low. Such poor agreement suggests that this approach to accounting for contact times in cases of parallel flow is not adequate. Unlike the packet model discussed earlier, this model is very sensitive to contact times, and a more sophisticated method of measuring contact times than that used in this study is needed. Since the model is not easily adapted to this study's results, no conclusions can be drawn from it.

6.4 Summary of Heat-Transfer Results

The main findings on heat transfer in vibrated beds from this study are summarized in this section.

The measurement of heat-transfer coefficients from a vertical-surface heater to vibrated beds of particles indicates a dependence of heat transfer on both particle size and vibrational intensity. For Master Beads, large particles (500 μm and larger), show an initial increase in heat transfer as the vibrational intensity increases and then level off. This trend is due to the relatively weak dependence of non-bunkered circulation on K-value and a lack of large-scale horizontal mixing. Medium-sized particles (177-353 μm) exhibit a much greater improvement in heat-transfer coefficient with increasing K-value due to the greater effect of vibrational intensity on bunkered circulation. The smallest particles show a similar trend in heat transfer up to $K = 5$, at which point the curves level off. This is due to observed instabilities in circulation at the highest K-values for these particles which lead to no net increase in circulation rate. Heat-transfer measurements in glass beads show that the thermal properties of the solid are not very important since the observed trends are actually opposite to those expected in some cases.

Analysis of the errors in heat-transfer coefficient measurements indicates that the largest source of error is the heat lost to the top and bottom channels of the heat-probe assembly. The percentage error is found to be a function of heat-transfer coefficient with larger errors for low values and smaller ones for high values. The range of error is found to be 10-15 percent for most solids.

The vertical-surface heater geometry is found to be generally superior to that of a horizontal cylinder based on comparison of results from this study with those of another study under nearly identical conditions. Elimination of air gaps with the vertical-surface heater causes it to give higher heat transfer at all K-values for both large and very small particles. Sluggish circulation in the vicinity of the vertical-surface heat probe causes the heat transfer to be only

marginally better or actually worse than the horizontal cylinder for medium-sized particles, however. Values of heat transfer from this study compare quite closely with published results from other studies using vertical-surface heaters.

The strong dependence of heat-transfer coefficients on circulation rates suggests that models which involve particle-heater contact times may be best suited to this system. An analysis of the packet model, however, shows that an additional resistance to heat transfer, such as conduction through a gas film, may also be important. The scoured-film and one-layer models are found to be less applicable to this study because of problems with model formulation and uncertainties in measured contact times.

Chapter 7 Conclusions and Recommendations for Further Study

This chapter presents the major conclusions drawn from the results of this study, and suggests recommendations for further study based on questions which arise that are beyond the scope of the current work.

7.1 Conclusions from This Study

This investigation has examined the particle dynamics and circulation as well as the heat transfer from an immersed, vertical surface in a shallow bed of vibrated particles. Vibrational frequency has been held constant at 25 Hz, and the vibrational amplitude has been varied to give K-values ranging from 2 to 7. Three types of particles (Master Beads, low-density glass, and high-density glass) have been employed in particle sizes ranging from 63-707 μm fractions. The bed depth has been kept at 30 mm for all experiments. This section presents the conclusions from experimental results obtained under these conditions.

7.1.1 Bed Dynamics

The study of vibrated-bed dynamics has yielded the following conclusions:

1) The bed-vessel separation does not necessarily occur at the point in the cycle predicted by porous, plastic, single-mass models. This point is delayed over what is predicted, and the amount of delay increases as particle size decreases. In fact, for the smallest (88 μm) particles

studied, no bed-vessel separation is detected for K-values as high as 6. This delay, or lack of separation, is attributed to an increase in porosity of the bed at the point of the cycle where the bed becomes "weightless." Such expansions are not accounted for by the single-mass models, and therefore the separation phase angle predicted is too small, particularly for smaller particles.

2) For large particles, high vibrational intensities create a situation in which the bed remains in flight for longer than a complete vibrational cycle. When this occurs, the succeeding flight period is shorter so that the two flight times are unequal. This phenomenon, in which the period of repetition of separation and collision is two vibrational cycles instead of one, is termed period-doubling. It has been observed in this study for particles as small as 353 μm for K = 6.

3) The bed-vessel collision for large-particle, non-bunkered beds occurs essentially simultaneously. The collision for bunkered beds occurs first at the side walls and moves sequentially toward the center.

4) There is a small, but discernible, compaction of the bed upon collision. This compaction takes place over a finite time which results in the propagation of a compaction wave through the bed. For non-bunkered beds, this wave is horizontal and passes through the bed from bottom to top. For beds which bunker, the angle of the compaction wave becomes steeper as particle size is decreased. This angle is a property of the vibrated solid and is not a function of vibrational intensity.

5) Two distinct types of particle circulation are observed in shallow vibrated beds: one for non-bunkered beds and another for bunkered beds. Circulation in non-bunkered beds is observed to be a downward motion of particles at the walls in a very few particle layers with a much slower return flow upward in the bulk of the bed. Little horizontal particle motion occurs, and overall mixing is relatively poor. This circulation is driven by wall friction.

6) Circulation in bunkered beds is characterized by a significant horizontal component of particle movement. The particles in the bulk of the bed are observed to move from the side walls toward the center, vertically up at the center, and cascade down the incline of the top surface to the side walls. This horizontal motion within the bulk of the bed is driven by hydrodynamic forces which are caused by horizontal pressure gradients. These gradients are from the side walls toward the center of the bed during the portion of the cycle when the bed is in flight and the particles are free to move. Upon collision, the particles are compacted from the wall to the center; there is no return flow of particles due to this sequential compaction even though the pressure gradient reverses.

7) The horizontal pressure gradient, as well as the overall pressure change within a vibrational cycle, increase as particle size decreases. This is due to a reduced bed permeability for smaller particles. For the same particle size, the horizontal pressure gradients and overall pressure change during the cycle increase with increasing vibrational intensity.

8) Vibrated beds of different particles have different relative resistance to flow. For the same particle type, decreasing the particle size increases the flow resistance at constant K-value. Increasing the K-value reduces the flow resistance for the same particle size and type.

9) Particle circulation rate increases with increasing K-value. The increase is less significant for non-bunkered particles which are driven by wall friction. For bunkered particles, the horizontal velocity is a function of the horizontal pressure gradient (which increases with K-value), and the resistance to flow (which decreases with K-value). The observed increase in particle circulation with increasing K-value is much more pronounced for bunkered circulation, particularly for the finest beads.

10) The finest particles do not exhibit stable circulation patterns at the highest vibrational intensities. These instabilities, produced by the high pressure gradients at high K-values, result in little or no net improvement in particle motion near the dummy heater relative to that observed at moderate K-values.

7.1.2 Heat Transfer

The study of heat transfer from an immersed, vertical surface to a shallow vibrated bed has yielded the following conclusions:

1) Heat-transfer coefficients measured from the vertical-surface heat probe to the vibrated bed of Master Beads show a dependence on both particle size and vibrational intensity. The dependence on size

is largely due to the differences in circulation patterns of large-particle, non-bunkered beds and smaller-particle, bunkered beds. Large-particle beds show an initial increase in heat transfer with increasing vibrational intensity, but this increase levels off due to the relatively weak dependence of wall-friction induced circulation at high K-values.

2) Particle sizes which create a bunkered bed exhibit a very strong dependence of heat transfer on the vibrational intensity. This increase is due to the observed increase in particle circulation with increased K-values for these particles. For those particles which do not have flow-stability problems at the highest K-values, no maximum in heat-transfer coefficient is observed. For the finest particles, the same sharp increase in heat transfer at low-to-moderate K-values occurs, but the flow instabilities at high K-values cause the heat-transfer coefficient to reach a maximum value.

3) Heat-transfer coefficients measured for glass beads show that there is little dependence of particle thermal properties on heat transfer. Low-density glass, which has inferior thermal properties compared to Master Beads, has the same or even greater heat-transfer coefficients for many cases of identical particle size and vibrational intensity.

4) Analysis of the heat lost from the vertical-surface heat probe shows that the largest source of error in the heat-transfer coefficient measurements is due to conduction to the insulating channels above and below the probe. The percentage error varies with the

heat-transfer coefficient being larger for low values and smaller for high ones. Based on the analysis, the reported values are 10-15% higher than the actual values for most solids.

5) Comparison with another very similar study of heat transfer in shallow vibrated beds shows that the vertical-surface heater geometry is generally superior to a horizontal, cylindrical geometry. Specifically, the vertical-surface heater yields higher values for both large particles and very fine particles at all values of vibrational intensity for Master Beads and glass beads. For particles which exhibit bunkered-bed behavior, yet are larger than about 150 μm, the improvement is slight or the horizontal cylinder actually gives better heat transfer for low to moderate K-values. At high K-values, the vertical-surface heat probe always gives higher values. This is largely due to an adverse effect of air gaps formed around the horizontal cylinder which is not present for the vertical surface.

6) The noted strong dependence of measurable heat transfer on particle circulation suggests that the contact time between particles and the heating surface is a major factor in the heat-transfer mechanism. A packet model, which assumes that contact time is the only controlling step in the heat-transfer mechanism, predicts values which are 22-100 percent higher than the measured values of heat-transfer coefficient based on observed particle velocities. This consistent overprediction by the model suggests that an additional resistance to heat transfer, notably conduction through a thin gas film to the packet, probably plays a role in the heat-transfer mechanism. Insufficient data on particle contact times do not allow for the

quantitative analysis of the one-layer model, which accounts for both particle contact times and resistance due to a gas film, however.

7.2 Recommendations for Further Study

The following areas are suggested for further study:

1) Since the results from this study indicate that a change in bed porosity occurs during the vibrational cycle and that this variation has a significant effect on observed bed behavior, a device to measure the instantaneous porosity during the cycle would be an immense aid. Previous measurements [Gutman, 1974; Rippie *et al.*, 1978] have been crude or uncalibrated. The change in voidage is known to be small, so a very sensitive device is needed. A parallel-plate capacitance device is suggested. Care is needed in the design of such a device, however. The periodic formation of the gap beneath the bed creates a large change in average voidage if this gap occurs in the electric field of the capacitor. This problem can be avoided by surrounding the charged plate to be monitored with other charged plates, which direct the electric field lines of the monitored plate straight through the bed to the ground plate and "mask it" from seeing the gap. Such an approach has been suggested by Louge [1989].

2) The measurement of relative flow resistances of different vibrated particles is reported in this study. While this data is useful in explaining qualitative trends in observed circulation rates, absolute

"apparent viscosities" should allow for more quantitative prediction of particle velocities along with a knowledge of pressure gradients.

3) A better measurement of the particle-surface contact time is needed for use in proposed heat-transfer models. Such measurements could be made by filming just the region of the dummy probe with the high-speed movie camera set on a relatively low speed. If a shutter speed of 250 frames per second were used, this would slow down the motion ten times when played back at 25 fps. At this speed, an accurate measurement of the velocity could be made, as well as a determination if any short time-scale effects take place at the heater surface which do not appear on a videotape.

4) This study has concentrated on the analysis of just one circulation pattern observed in bunkered beds: that of the center-high bunker. Observations have shown that this pattern leads to a reduced flow rate in the vicinity of the vertical surface. Two other possible stable configurations have been noted. The wall-high bunker was shown by Sprung [1987] to improve heat transfer. The center-low bunker has been demonstrated in a few cases [two data points in this study] to increase heat transfer relative to the center-high bunker. These two configurations could be more thoroughly studied, as well as better ways to control which bunker configuration the bed assumes, in order to increase heat transfer and better predict performance in large, sealed, vibrated beds.

5) Although the circulation patterns and heat transfer for a single, vertical heat fin are useful starting points, scale-up would require a knowledge of particle circulation and heat transfer for multiple fins.

A series of vertical heaters would presumably segregate a shallow vibrated bed into smaller circulation cells, and the effect of this segregation is not confidently predictable from this study. Therefore, a study containing multiple vertical barriers, preferably with variable spacing, is suggested. For simplicity of fabrication, only one of these barriers needs to be a heat probe; the others can be dummy heaters used to simulate the flow patterns of multiple heat fins.

6) Investigate the heat transfer in a shallow vibrated bed with a vertical heater for a case with continuous feed of solids. Net solid flow may serve to increase particle velocity near the heater, leading to higher heat-transfer coefficients. Such a system could find applications in drying or for pre-heating of solids.

Bibliography

Akiyama, T., and H. Kurimoto, *Chem. Eng. Sci.*, **43**, (1988), 2645.

Akiyama, T., and H. Kurimoto, *Chem. Eng. Sci.*, **44**, (1989), 427.

Akiyama, T., and T. Naito, *Chem. Eng. Sci.*, **42**, (1987), 1305.

Akiyama, T., H. Kurimoto, and K. Nakasaki, *Chem. Eng. Sci.*, **44**, (1989), 1594.

Bachmann, D., *Verfahenstechnik Z.V.D.I. Beiheft*, **No. 2**, (1940), 43. [Cited by Gutman, 1974].

Bagnold, R. A., *Proc. Roy. Soc. London A*, **225**, (1954), 49.

Bagnold, R. A., *Proc. Roy. Soc. London A*, **295**, (1966), 219.

Benge, G. Gregory, Private communication of work in progress, Department of Chemical Engineering, Virginia Polytechnic Institute and State University, Blacksburg, Virginia, (1990).

Bird, R. B., W. E. Stewart, and E. N. Lightfoot, *Transport Phenomena*, John Wiley & Sons, Inc., New York, New York, (1960).

Bretsznajder, S., M. Jaszczak, and W. Pasiuk, *Int. Chem. Eng.*, **3**, (1963), 496.

Briggs, Robert A., "*Gas and Solid-Mixing Behavior in a Vibrated-Bed Microreactor with Rapid Switching of Catalyst Between Gas Atmospheres*", M.S. Thesis, Virginia Polytechnic Institute and State University, Blacksburg, Virginia, (1987).

Buevich, Yu. A., and V. L. Galontsev, *Inzh.-Fiz. Zh.*, **34**, (1978), 394.

Buevich, Yu. A., and N. M. Kharisova, *Inzh.-Fiz. Zh.*, **34**, (1978), 604.

Buevich, Yu. A., A. F. Ryzhkov, and N. M. Kharisova, *Inzh. Fiz. Zh.*, **37**, (1979), 626.

Bukareva, M. F., V. A. Chlenov, and N. V. Mikhailov, *Int. Chem. Eng.*, **9**, (1969), 119.

Bukareva, M. F., V. A. Chlenov, and N. V. Mikhailov, *Int. Chem. Eng.*, **10**, (1970), 384.

Carman, P. C., *Trans.-Inst. Chem. Eng.*, **15**, (1937), 150.

Cheah, Chun-Wah, "*Heat Transfer Between a Supernatant Gas and a Flowing Vibrofluidized Bed of Solid Particles*", M. S. Thesis, Virginia Polytechnic Institute and State University, Blacksburg, Virginia, (1986).

Cheah, C. W., D. E. Hirt, Y. A. Liu, and A. M. Squires, *Powder Technol.*, **55**, (1988), 269.

Chlenov, V. A. and N. V. Mikhailov, *Dokl. Akad. Nauk SSSR*, **154**, (1964), 703.

Chlenov, V. A., and N. V. Mikhailov, *Inzh.-Fiz. Zh.*, **9**, (1965a), 196.

Chlenov, V. A., and N. V. Mikhailov, *Russ. J. Phys. Chem.*, **39**, (1965b), 250.

Chlenov, V. A., and N. V. Mikhailov, *Vibrokipyashchii Sloi*, (Vibrofluidized Bed), Nauka, Moscow, (1972). [Cited by Pakowski, *et al.*, 1984].

Choc, M., *Strojirenstvi*, **25**, 8, (1975). [Cited by Pakowski *et al.*, 1984].

Choc, M., *Teplomassoobmen*, **V**, 6, Minsk, (1976). [Cited by Pakowski *et al.*, 1984].

Danielsen, S., and S. Hovmand, in *Drying'80, Vol. 1: Developments in Drying*, Ed. Mujumdar, A. S., Hemisphere Publishing Co., Washington, D.C., (1980), 194.

Douady, S., S. Fauve, and C. Laroche, *Europhys. Lett.*, **8**, (1989), 621.

Faraday, M., *Phil. Trans. Roy. Soc. London*, (1831), 299.

Fauve, S., S. Douady, and C. Laroche, *Journal de Physique*, Colloque C3, supplement au no. 3, **50**, (1989), C3-187.

Geldart, D., *Powder Technol.*, **7**, (1973), 285.

Ginzburg, A. S., and V. I. Syroedov, *Inzh.-Fiz. Zh.*, **9**, (1965), 744.

Grace, J. R., *Can. J. Chem. Eng.*, **64**, (1986), 353.

Gray, W. A., and G. T. Rhodes, *Powder Technol.*, **6**, (1972), 271.

Gutman, R. G., "*Vibrated Beds of Powders*", Ph.D. Dissertation, University of Cambridge, Cambridge, United Kingdom, (1974).

Gutman, R. G., *Trans. Instn. Chem. Engrs.*, **54**, (1976a), 174.

Gutman, R. G., *Trans. Instn. Chem. Engrs.*, **54**, (1976b), 251.

Gutman, R. G., and J. F. Davidson, *Chem. Eng. Sci.*, **30**, (1975), 89.

Harwood, C. F., *Powder Technol.*, **16**, (1977), 51.

Hirt, Douglas E., "*Heat Transfer Between a Supernatant Gas and a Flowing Vibrofluidized Bed of Solids*", M. S. Thesis, Virginia Polytechnic Institute and State University, Blacksburg, Virginia, (1984).

Hirt, D. E., C. W. Cheah, Y. A. Liu, and A. M. Squires, *Powder Technol.*, **55**, (1988), 257.

Incropera, F. P. and D. P. DeWitt, *Fundamentals of Heat Transfer*, John Wiley & Sons, Inc., New York, New York, (1981).

Kal'tman, I. I., and A. I. Tamarin, *Inzh.-Fiz. Zh.*, **16**, (1969), 630.

Kapustin, E. A., V. I. Prosvirnin, and I. V. Butorina, *Teor. Osny. Khim. Tekh.*, **14**, (1980), 720.

Karmazin, V. D., *Tekhnika i Primenenie Vibriruyushchego Sloya* (Technology and Application of Vibrating Bed), Naukova Dumka, Kiev, (1977). [Cited by Pakowski *et al.*, 1984].

Konyakhin, A. P., A. P. Fomin, A. D. Uchitel, and V. P. Krishtop, *Koks i Khimiya*, **10**, (1979), 15.

Kossenko, G. D., E. G. Reshetnikov, N. I. Syromjatnikov, and B. G. Sapozhnikov, *Inst. Fuel Symp. Series No. 1: Fluidised Combustion*, **1**, (1975), B4-1.

Kroll, W., *Forschung auf der Gebiete des Ingenieurwesen*, **20**, (1954), 2.

Kroll, W., *Chemie-Ing.-Techn.*, **27**, (1955), 33.

Laroche, C., S. Douady, and S. Fauve, *J. Phys. France*, **50**, (1989), 699.

Lawrence, L. R., and J. K. Beddow, *Powder Technol.*, **2**, (1968), 125.

Louge, Michel, Private communication, Department of Mechanical Engineering, Cornell University, Ithaca, New York, (1989).

Lyul'ko, V. G., L. V. Krasnichenko, V. D. Kishko, and V. I. Litvinenko, *Poroshkovaya Metallurgiya*, **199**, No. 7, (1979), 1.

Malhotra, K., and A. S. Mujumdar, *Can. J. Chem. Eng.*, **63**, (1985), 22.

Malhotra, K., and A. S. Mujumdar, *Ind. Eng. Chem. Res.*, **26**, (1987), 1983.

Mickley, H. S., and D. F. Fairbanks, *AIChE J.*, **1**, (1955), 374.

Muchowski, E., *Int. Chem. Eng.*, **20**, (1980), 564.

Muchowski, E., and E. Mä nnchen, *Int. Chem. Eng.*, **20**, (1980), 577.

Osinskii, V. P., B. S. Sazhin, and E. A. Chuvpilo, *Khimicheskoe i Neftyanoe Mashinostroenie*, **11**, (1969), 14.

Pakowski, Z., and A. S. Mujumdar, *Proceedings of ASME-JSME Thermal Engineering Joint Conference*, Honolulu, (1983).

Pakowski, Z., A. S. Mujumdar, and C. Strumillo, in *Advances in Drying Vol. 3*, Ed. Mujumdar, A. S., Hemisphere Publishing Co., Washington, D.C., (1984), 245.

Ratkai, G., *Powder Technol.*, **15**, (1976), 187.

Ringer, D. U., in *Drying '80, Vol. 2: Proceedings of the Second International Symposium on Drying*, Ed. Mujumdar, A. S., Hemisphere Publishing Co., Washington, D.C., (1980), 144.

Rippie, Edward G., Douglas C. Kriesel, and Harald Rettig, *J. Pharm. Sci.*, **67**, (1978), 1121.

Ripple, C. D., R. V. James, and J. Rubin, *Powder Technol.*, **8**, (1973), 165.

Ryzhkov, A. F., and A. P. Baskakov, *Inzh.-Fiz. Zh.*, **27**, (1974), 15.

Ryzhkov, A. F., and A. P. Baskakov, *Fluid Mechanics-Soviet Research*, **4**, (1975), 75.

Ryzhkov, A. F., A. P. Baskakov, and V. A. Munts, *Heat Transfer-Soviet Research*, **8**, (1976), 136.

Sapozhnikov, B. G., and N. I. Syromyatnikov, *Heat Transfer-Soviet Research*, **1**, (1969), 22.

Sapozhnikov, B. G., and N. I. Syromyatnikov, *The Soviet Chem. Ind.*, **2**, (1970), 81.

Sapozhnikov, B. G., Ye. G. Reshetkov, G. D. Kosenko, and N. M. Kharisova, *Heat Transfer-Soviet Research*, **8**, (1976), 141.

Savage, Stuart B., *J. Fluid Mech.*, **194**, (1988), 457.

Shvetsov, V. V., A. D. Alekseev, and V. I. Redekop, *Khim.-Farmat. Zh.*, **10**, (1976), 131.

Sprung, Renato, "*Studies in Vibrofluidized Beds and Synthesis of Silica Catalysts*", Ph.D. Dissertation, Virginia Polytechnic Institute and State University, Blacksburg, Virginia, (1987).

Sprung, R., B. Thomas, Y. A. Liu, and A. M. Squires, in *Fluidization V - Proceedings of the Fifth Engineering Foundation Conference on Fluidization*, Eds. Ostergaard, K., and A. Sorensen, Engineering Foundation, New York, New York, (1986), 409.

Strumillo, C., and Z. Pakowski, in *Drying '80, Vol. 1: Developments in Drying*, Ed. Mujumdar, A. S., Hemisphere Publishing Co., Washington, D.C., (1980), 211.

Suzuki, K., H. Hosaka, R. Yamazaki, and G. Jimbo, *J. Chem. Eng. Japan*, **13**, (1980a), 117.

Suzuki, K., A. Fujigami, R. Yamazaki, and G. Jimbo, *J. Chem. Eng. Japan*, **13**, (1980b), 495.

Takahashi, H., A. Suzuki, and T. Tanaka, *Powder Technol.*, **2**, (1968), 65.

Tamarin, A., I. Kal'tman, and L. Vasil'ev, *Metallovedenie i Termicheskaya Obrabotka Metallov*, **3**, (1968), 10.

Thomas, Benku, "*Shallow Vibrated Particulate Beds - Bed Dynamics and Heat Transfer*", Ph.D. Dissertation, Virginia Polytechnic Institute and State University, Blacksburg, Virginia, (1988).

Thomas, Benku, and Arthur M. Squires, in *Fluidization VI - Proceedings of the International Conference on Fluidization Sponsored by the Engineering Foundation*, Eds. Grace, J. R., L. W. Shemitt, and M. A. Bergougnou, Engineering Foundation, New York, New York, (1989), 375.

Thomas, B., Y. A. Liu, R. T. Chan, and A. M. Squires, *Powder Technol.*, **52**, (1987), 77.

Thomas, B., M. O. Mason, Y. A. Liu, and A. M. Squires, *Powder Technol.*, **57**, (1989), 267.

Ur'ev, N. B., *Kolloid. Zh.*, **40**, (1978), 915.

VandenBerghe, T., and T. E. Diller, *Experimental Thermal and Fluid Science*, **2**, (1989), 236.

Volovik, Yu. I., G. G. Moseychuk, and N. A. Isayev, *Heat Transfer-Soviet Research*, **7**, (1975), 146.

Whiting, Gary K., "*Development of a Microreactor System for Unsteady-State Fischer-Tropsch Synthesis*", Ph.D. Dissertation, Virginia Polytechnic Institute and State University, Blacksburg, Virginia, (1985).

Williams, J. C., and G. Shields, *Powder Technol.*, **1**, (1967), 134.

Yoshida, T., and Y. Kousaka, *Kagaku Kogaku*, **30**, (1966), 1019. [Cited by Gray and Rhodes, 1972].

Yoshida, T., and Y. Kousaka, *Kagaku Kogaku*, **5**, (1967), 159. [Cited by Strumillo and Pakowski, 1980].

Zabrodskii, S. S., I. L. Zamnius, S. A. Malyukovich, and A. I. Tamarin, *Inzh.-Fiz. Zh.*, **14**, (1968), 448.

Zabrodsky, S. S., *Hydrodynamics and Heat Transfer in Fluidized Beds*, The M.I.T. Press, Cambridge, Massachusetts, (1966). [Cited by Sprung, 1987].

Zaitsev, E. D., V. I. Redekop, and V. V. Shvetsov, *Khim.-Farmat. Zh.*, **10**, (1976), 81.

Appendix. Derivation of the Equations for Determining the Effect of Heat Loss on the Heat-Transfer Coefficient

In Section 6.1.3.1, a list of assumptions is presented which makes possible a mathematical analysis of the effect of heat loss to the Lexan channels and supports. The total heat supplied to the bed, in the form of electric power, can be broken down as follows:

$$Q = Q_P + Q_{BC} + Q_{TC} + Q_S \qquad [A.1]$$

where Q is the total heat, Q_P is the heat transferred to the bed through the heating-probe surface, Q_{BC} is the heat conducted to the bottom channel, Q_{TC} is the heat conducted to the top channel, and Q_S is the heat conducted to the supports. Note that Equation 6.1 assumes that Q and Q_P are equal for the calculation of heat-transfer coefficients, but that actually some heat is conducted to the Lexan members.

In order to develop expressions for the terms on the right-hand-side of Equation A.1, consider an element of surface somewhere on the heater assembly (including Lexan members) which is sufficiently small that the temperature difference across the element is negligible compared to the difference between its temperature and the bed temperature. If the area of this element is dA, then the amount of heat, dQ, transferred from the element to the bed can be obtained from Newton's Law of Cooling

$$dQ = h\, dA\, (T - T_B) \qquad [A.2]$$

where h is the heat-transfer coefficient (which has been assumed to be the same for all vertical surfaces), T is the temperature of the surface element, and T_B is the bed temperature. This expression can be integrated to give Q if an expression for T can be obtained.

If the element of surface is somewhere on the surface of the copper probe itself, then $T = T_P$ since the probe is isothermal. This leads to an expression for the heat transferred through the probe surface of

$$Q_P = hA(T_P - T_B) = h(4W_PL_P)(T_P - T_B) \qquad [A.3]$$

where A has been taken to be the width of the probe, W_P, times the length of half of the probe, L_P, times four (there are four of these half-surfaces--two on each side). Due to the symmetry of the heat-probe assembly, the analysis is based on one half of one side as shown in Figure A.1.

If the surface element is on one of the non-isothermal Lexan members, however, an expression for T as a function of position is needed. Take first the situation in the bottom channel as shown in Figure A.2. If the element is a distance x from the top of the channel, has width Δx, and is at temperature T_x, a steady-state heat balance can be written. Since, at steady-state, the heat put into the element must equal the heat out, for a heat flux in due to conduction of q_x and out of $q_{x+\Delta x}$, the balance becomes

$$L_P t_C(q_x - q_{x+\Delta x}) - hL_P\,\Delta x(T_x - T_B) = 0 \qquad [A.4]$$

with the dimensions defined in Figure A.2. By defining

$$\Delta q = q_{x+\Delta x} - q_x \qquad [A.5]$$

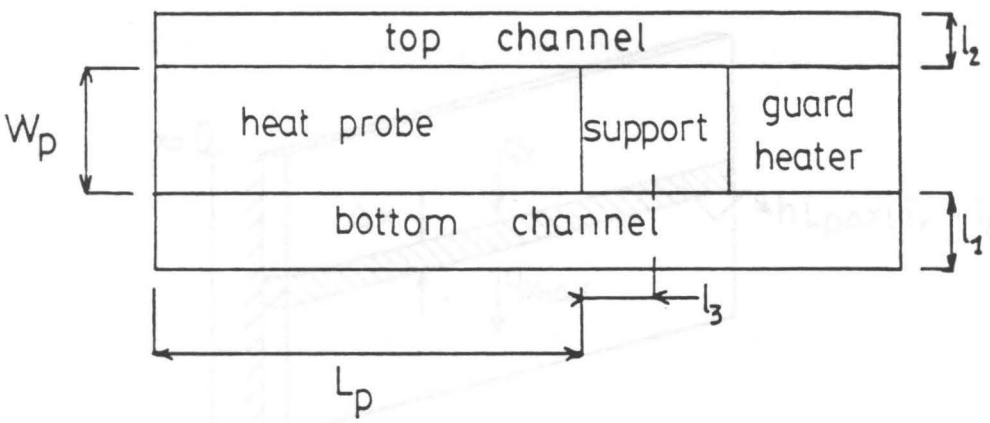

Figure A.1. Schematic of half of the heat-probe assembly: Definition of dimensions used in the one-dimensional heat-loss analysis.

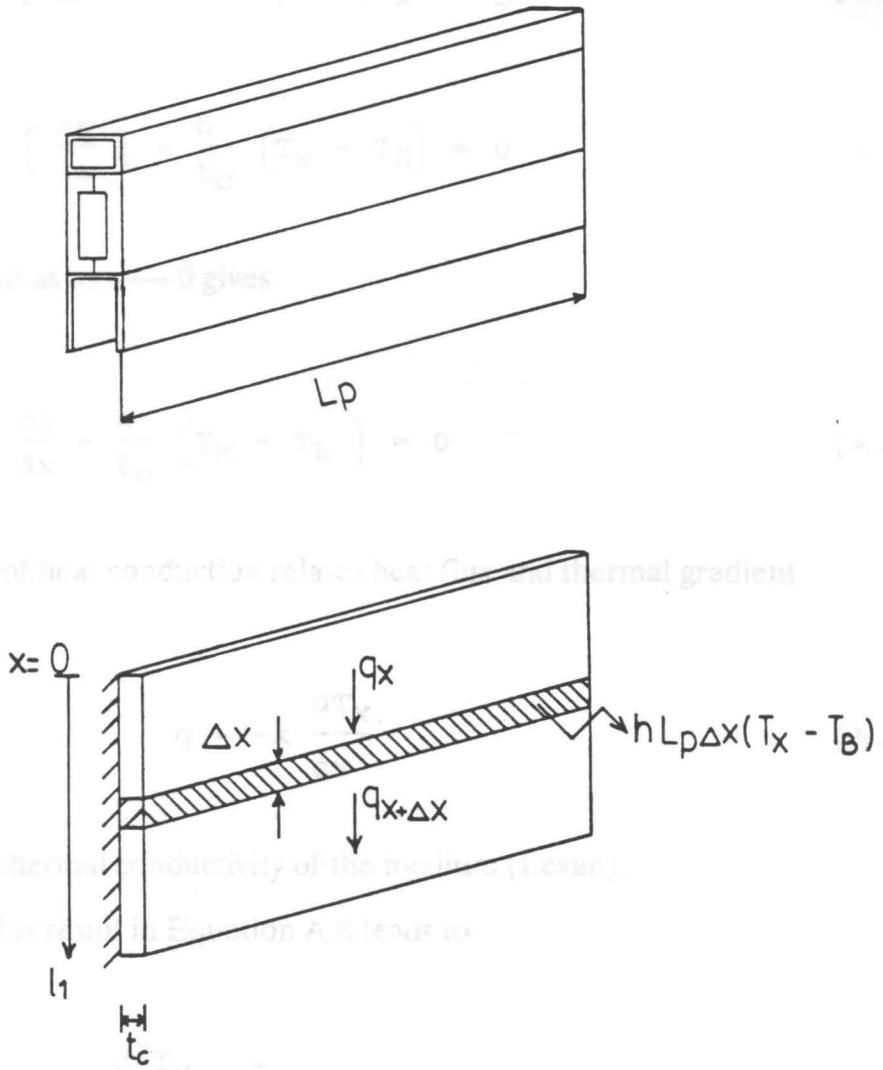

Figure A.2. Heat balance on "leg" of bottom channel: Cross-section of the heater assembly with blow-up of bottom-channel leg for analysis.

Equation A.4 can be rearranged to give

$$L_p t_c(-\Delta q) - hL_p\Delta x\ (T_x - T_B) = 0 \qquad [A.6]$$

or

$$-\left[\frac{\Delta q}{\Delta x}\right] - \frac{h}{t_c}\left[T_x - T_B\right] = 0 \qquad [A.7]$$

Taking the limit as $\Delta x \longrightarrow 0$ gives

$$-\frac{dq}{dx} - \frac{h}{t_c}\left[T_x - T_B\right] = 0 \qquad [A.8]$$

Fourier's Law of heat conduction relates heat flux and thermal gradient

$$q = -k\frac{dT_x}{dx} \qquad [A.9]$$

where k is the thermal conductivity of the medium (Lexan).

Using this result in Equation A.8 leads to

$$k\frac{d^2T_x}{dx^2} - \frac{h}{t_c}(T_x - T_B) = 0 \qquad [A.10]$$

Following convention, this equation can be made dimensionless by the introduction of the following variables

$$\theta_{BC} = \frac{T_x - T_B}{T_{0,BC} - T_B} \text{ and } \phi_{BC} = \frac{x}{l_1} \qquad [A.11]$$

where $T_{0,BC}$ is the temperature of the bottom channel at x = 0. Substituting these variables into Equation A.10 yields

$$\frac{d^2\theta_{BC}}{d\phi_{BC}^2} - \frac{h\ l_1^2}{kt_c}\ \theta_{BC} = 0 \qquad [A.12]$$

By defining

$$\lambda_1^2 = \frac{h\ l_1^2}{kt_c} \qquad [A.13]$$

this becomes

$$\frac{d^2\theta_{BC}}{d\phi_{BC}^2} - \lambda_1^2\ \theta_{BC} = 0 \qquad [A.14]$$

The general form of the solution to Equation A.14 is

$$\theta_{BC} = c_1\ \exp(\lambda_1\phi_{BC}) + c_2\ \exp(-\lambda_1\phi_{BC}) \qquad [A.15]$$

where c_1 and c_2 are arbitrary constants to be determined by application of the boundary conditions. The boundary conditions are

$$T_x = T_{0,BC} \text{ at } x = 0$$

$$\text{and} \quad T_x = T_B \quad \text{at } x = l_1 \qquad [A.16]$$

which become, in dimensionless form,

$$\theta_{BC} = 1 \quad \text{at } \phi_{BC} = 0$$

$$\text{and} \quad \theta_{BC} = 0 \quad \text{at } \phi_{BC} = 1 \qquad [A.17]$$

Using these conditions to solve for c_1 and c_2 leads to

$$c_1 = \frac{1}{1 - \exp(2\lambda_1)} \qquad [A.18]$$

$$\text{and} \quad c_2 = \frac{-\exp(2\lambda_1)}{1 - \exp(2\lambda_1)}$$

Substituting these expressions into Equation A.15 gives

$$\theta_{BC} = \frac{\exp(\lambda_1 \phi_{BC}) - \exp[\lambda_1 (2 - \phi_{BC})]}{1 - \exp(2\lambda_1)} \qquad [A.19]$$

which is the dimensionless temperature profile in the bottom channel.

The analysis of the top channel is identical once the variables of Equation A.11 have been redefined to the geometry of the top channel.

$$\theta_{TC} = \frac{T_x - T_B}{T_{0,TC} - T_B} \quad \text{and} \quad \phi_{TC} = \frac{x}{l_2} \qquad [A.20]$$

For the top channel, x = 0 corresponds to the bottom edge of the top channel and the length of the leg is l_2. This leads to an expression for the dimensionless temperature profile in the top channel of

$$\theta_{TC} = \frac{\exp(\lambda_2 \phi_{TC}) - \exp[\lambda_2 (2-\phi_{TC})]}{1 - \exp(2\lambda_2)} \qquad [A.21]$$

where λ_2 is defined by

$$\lambda_2^2 = \frac{h\, l_2^2}{k\, t_c} \qquad [A.22]$$

with l_2 being the height of the top channel.

The derivation of the temperature profile in the supports is similar to that of the channels, but is slightly different since the supports are solid. Because of this, each cross-section of width Δx has two surfaces which lose heat to the bed rather than just one as in the case of the hollow channels. Figure A.3 gives a schematic top view of one-half of one of the supports. Note that only the half of the support nearest the heating probe needs to be considered since the heat flux at the mid-point of the support is zero (see Assumption 6, Section 6.1.3.1). The analysis leads to

$$k \frac{d^2 T_x}{dx^2} - \frac{2h}{t_s} (T_x - T_B) = 0 \qquad [A.23]$$

With the introduction of

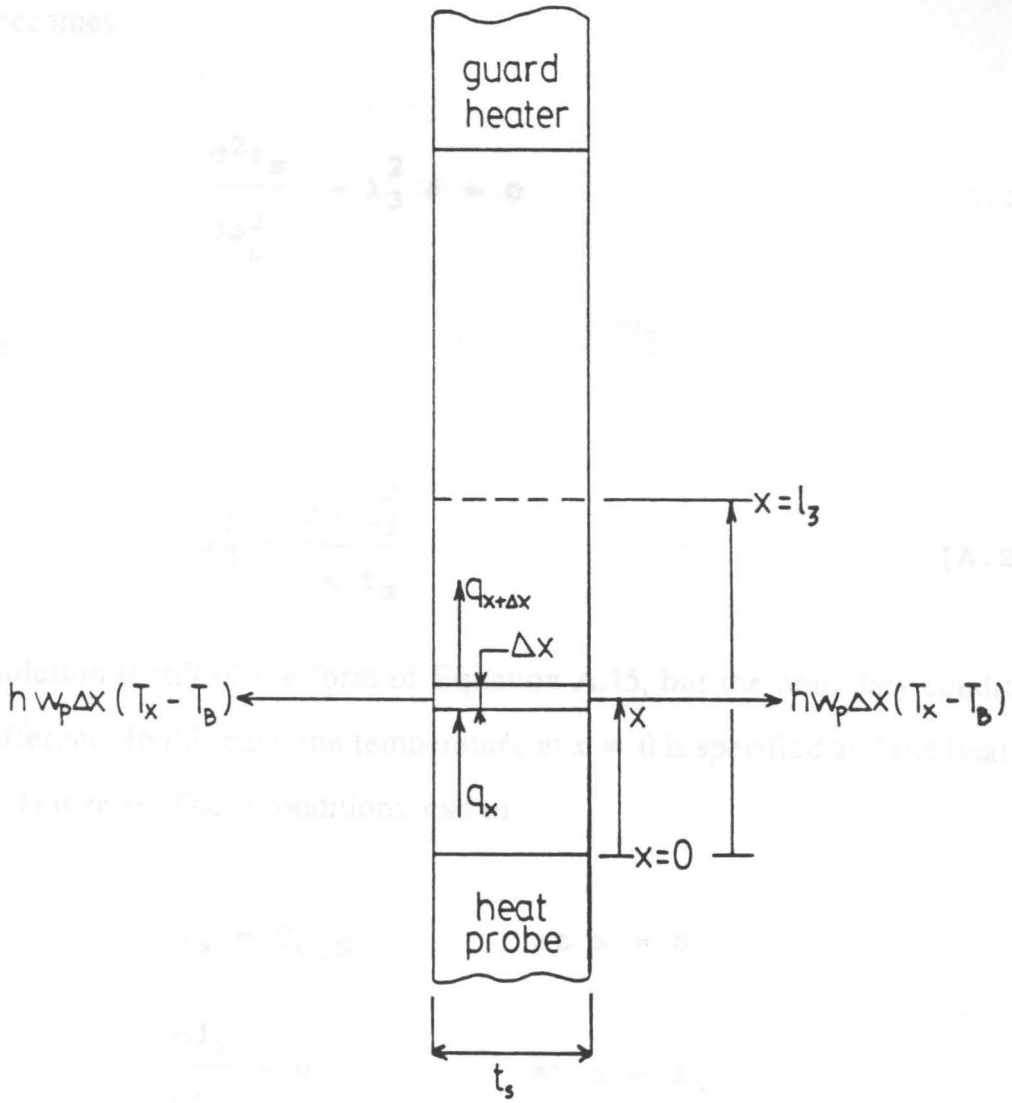

Figure A.3. Heat balance on a probe support: Only the half nearest the heat probe needs to be considered since the heat flux across the mid-line is zero due to the guard heater. The length of this half-support is l_3.

$$\theta_s = \frac{T_x - T_B}{T_{0,S} - T_B} \quad \text{and} \quad \phi_s = \frac{x}{l_3} \qquad [A.24]$$

this becomes

$$\frac{d^2\theta_s}{d\phi_s^2} - \lambda_3^2 \theta = 0 \qquad [A.25]$$

where

$$\lambda_3^2 = \frac{2h\ l_3^2}{k\ t_s} \qquad [A.26]$$

The solution is still of the form of Equation A.15, but the boundary conditions are different. In this case, the temperature at $x = 0$ is specified and the heat flux at $x = l_3$ is zero. These conditions lead to

$$T_x = T_{0,S} \qquad \text{at } x = 0$$

and

$$\frac{dT_x}{dx} = 0 \qquad \text{at } x = l_3 \qquad [A.27]$$

or

$$\theta_s = 1 \quad \text{at } \phi = 0 \qquad [A.28]$$

and

$$\frac{d\theta_s}{d\phi_s} = 0 \quad \text{at } \phi_s = 1$$

These conditions give the following values for the constants

$$c_1 = \frac{1}{1 + \exp(2\lambda_3)} \qquad [A.29]$$

and $$c_2 = \frac{\exp(2\lambda_3)}{1 + \exp(2\lambda_3)}$$

The dimensionless temperature profile in the supports is then given by

$$\theta_s = \frac{\exp(\lambda_3 \phi_s) + \exp[\lambda_3 (2-\phi_s)]}{1 + \exp(2\lambda_3)} \qquad [A.30]$$

Since expressions for temperature as a function of position have now been derived for all of the Lexan members, Equation A.2 can be integrated to give expressions for the remaining terms on the right-hand-side of Equation A.1. For the bottom channel

$$Q_{BC} = 4\, hL_p \int_0^{l_1} \left[T_x - T_B \right] dx \qquad [A.31]$$

For the top channel

$$Q_{TC} = 4\, hL_p \int_0^{l_2} \left[T_x - T_B \right] dx \qquad [A.32]$$

For the supports

$$Q_S = 4hW_p \int_0^{l_3} \left[T_x - T_B \right] dx \qquad [A.33]$$

Since Equations A.31 - A.33 call for the temperature profiles in dimensional form, the dimensionless temperature profiles must be re-dimensioned. Take, for example, the case for the bottom channel. From Equation A.19

$$\theta_{BC} = \frac{\exp(\lambda_1 \phi_{BC}) - \exp[\lambda_1 (2-\phi_{BC})]}{1 - \exp(2\lambda_1)}$$

and from Equation A.11

$$\theta_{BC} = \frac{T_x - T_B}{T_{0,BC} - T_B} \quad \text{and} \quad \phi_{BC} = \frac{x}{l_1}$$

Solving Equation A.11 for T_x gives

$$T_x = (T_{0,BC} - T_B)\ \theta_{BC} + T_B \qquad [A.34]$$

so Equation A.19 becomes (substituting in for ϕ_{BC} also)

$$T_x = (T_{0,BC} - T_B) \left[\frac{\exp(\lambda_1 x/l_1) - \exp[\lambda_1 (2-x/l_1)]}{1 - \exp(2\lambda_1)} \right] + T_B \qquad [A.35]$$

The integral from Equation A.31 then becomes

$$(T_{0,BC} - T_B) \int_0^{l_1} \left[\frac{\exp(\lambda_1 x/l_1) - \exp[\lambda_1(2-x/l_1)]}{1 - \exp(2\lambda_1)} \right] dx \qquad [A.36]$$

Upon integration, Equation A.36 gives

$$\frac{l_1 (T_{0,BC} - T_B)}{\lambda_1[1-\exp(2\lambda_1)]} \left[2 \exp(\lambda_1) - \exp(2\lambda_1) - 1 \right] \qquad [A.37]$$

Similarly, the integrals for the top channel and supports are

$$\frac{l_2 (T_{0,TC} - T_B)}{\lambda_2[1-\exp(2\lambda_2)]} \left[2 \exp(\lambda_2) - \exp(2\lambda_2) - 1 \right] \qquad [A.38]$$

for the top channel and

$$\frac{l_3 (T_{0,S} - T_B)}{\lambda_3[1+\exp(2\lambda_3)]} \left[\exp(2\lambda_3) - 1 \right] \qquad [A.39]$$

for the supports.

Now expressions for all of the terms on the right-hand-side of Equation A.1 have been derived. For the sake of compactness of notation, define Integral 1 to be the integral for the bottom channel, Integral 2 to be the integral for the top channel, and Integral 3 to be the integral for the supports. With this notation, Equation A.31, for example, becomes

$$Q_{BC} = 4h\, L_p\, (\text{Integral 1}) \qquad [A.40]$$

Using this notation and the results from Equations A.3 and A.31-A.33, Equation A.1 becomes

$$Q = 4h\left[W_P L_P (T_P - T_B) + L_P\ (\text{INTEGRAL 1} + \text{INTEGRAL 2}) + W_P\ (\text{INTEGRAL 3})\right] \qquad [A.41]$$

or, solving for the heat-transfer coefficient, h,

$$h = Q/4\left[W_P L_P (T_P - T_B) + L_P\ (\text{INTEGRAL 1} + \text{INTEGRAL 2}) + W_P\ (\text{INTEGRAL 3})\right] \qquad [A.42]$$

Since all of the integrals are functions of λ (see Equations A.37-A.39) and all of the λ values are functions of h (see Equations A.13, A.22, and A.26), Equation A.42 is implicit in h and must be solved iteratively. Furthermore, the values of $T_{0,BC}$, $T_{0,TC}$, and $T_{0,S}$ which appear in Equations A.37, A.38, and A.39, respectively, are not known. They can be calculated, however, by using Assumption 1 of Section 6.1.3.1.

Take, for example, the case of the bottom channel. The steady-state heat conduction across the uniform layer of epoxy leads to

$$\frac{d^2T_x}{dx^2} = 0 \qquad [A.43]$$

which has a solution of the form

$$T_x = C_1 + C_2 x \qquad [A.44]$$

The appropriate conditions for this situation are

$$\frac{dT_x}{dx} = -q_{BC}/k_e \qquad \text{(from Fourier's Law)} \qquad [A.45]$$

and

$$T = T_P \quad \text{at } x = 0$$

where q_{BC} is the heat flux into the bottom channel and k_e is the thermal conductivity of the epoxy. These conditions lead to the temperature profile across the epoxy layer

$$T_x = T_P - (q_{BC}/k_e)\, x \qquad [A.46]$$

Evaluation of this expression at $x = l$ (where l is the thickness of the epoxy layer) gives

$$T_{0,BC} = T_P - (q_{BC}/k_e)\, l \qquad [A.47]$$

Similarly, expressions for the top channel and supports are

$$T_{0,TC} = T_P - (q_{TC}/k_e)\, l \qquad [A.48]$$

and

$$T_{0,S} = T_P - (q_S/k_e)\, l \qquad [A.49]$$

respectively. The values of the heat fluxes can be obtained by

$$q_{BC} = Q_{BC}/A_{BC} = Q_{BC}/4L_p t_c \qquad [A.50]$$

$$q_{TC} = Q_{TC}/4L_p t_c \qquad [A.51]$$

$$q_s = Q_s/4W_p t_s \qquad [A.52]$$

This results in another iterative solution since, for example, the value of Q_{BC} depends on $T_{0,BC}$, as shown in Equation A.40 (recalling that Integral 1 is defined by Equation A.37).

The process for determining a corrected value of the heat-transfer coefficient, then, is as follows:

1) For the first iteration, take the value of h to be the one experimentally measured.
2) Calculate values for λ_1, λ_2, and λ_3 from Equations A.13, A.22, and A.26, respectively.
3) Calculate values for Integral 1, Integral 2, and Integral 3 from Equations A.37, A.38, and A.39, respectively, using a first guess of $T_{0,BC}$, $T_{0,TC}$, and $T_{0,S}$ all equal to T_P.
4) Use Equation A.42 to get a correction for h.
5) Use this new value of h to obtain values for the lost heat terms by using Equation A.31-A.33.
6) Use these values of lost heat to obtain values of heat fluxes in Equations A.50-A.52.
7) Use these values of heat fluxes to calculate $T_{0,BC}$, $T_{0,TC}$, and $T_{0,S}$ from Equations A.47, A.48, and A.49, respectively.

8) Repeat steps 2 through 7 using the new values of h, $T_{0,BC}$, $T_{0,TC}$, and $T_{0,S}$.

After three or four iterations, the values of h, $T_{0,BC}$, $T_{0,TC}$, and $T_{0,S}$ have all usually stopped changing in the first two decimal places, and this is taken to be convergence. The values of the constants used in this derivation which are necessary for the calculation are listed below:

W_P = 0.0127 m

L_P = 0.0508 m

l_1 = 0.010033 m

l_2 = 0.004953 m

l_3 = 0.007302 m

t_c = 0.0007 m

t_s = 0.00635 m

k = 0.19 W/m-°C (from Perry's, 5th ed. value for polycarbonate

k_e = 0.335 W/m-°C (from 3M, manufacturer of the epoxy)

l = 0.0001 m

The values for h, Q, T_P, and T_B depend on the data point chosen. Section 6.1.3.1 gives corrected values of heat-transfer coefficient and percentage error for several data points using this approach.

The vita has been removed from the scanned document